The weldability of high and ultra-high strength steel.

Anderson, Cheryl Marie

The Weldability of High and Ultra-High Strength Steel

Cheryl Marie Anderson

Submitted to the University of Wales in fulfilment for the degree of Doctor of Engineering

University of Wales - Swansea

2003

Supervisors

University of Wales Swansea
Prof. J D Parker

Corus UK
Mr. W Waddell

DECLARATION

This work has not previously been accepted in substance for any degree and is not being concurrently submitted in candidature for any degree.

Signed... ... . (candidate)

Date... ... ... 25/4/03 ... ...

STATEMENT 1

This thesis is the result of my own investigations, except where otherwise stated.
Other sources are acknowledged by footnotes giving explicit references.
A bibliography is appended.

Signed... ... ... (candidate)

Date... ... ... 25/4/03 ... ...

STATEMENT 2

I hereby give my consent for my thesis, if accepted, to be available for photocopying and for interlibrary loan, and for the title and summary to be made available to outside organisations.

Signed... ... ... (candidate)

Date... ... ... 25/4/03 ... ...

ACKNOWLEDGEMENTS

I would like to acknowledge the financial support received from the EPSRC and Corus UK during this research programme and the use of the facilities at the Welsh Technology Centre provided by Dr B J Hewitt – Technical Director Corus UK. I would like to thank my project supervisors, Professor J D Parker and Mr W Waddell for their constructive support and technical assistance throughout this research project. I would also like to express my gratitude to Professor B Wilshire for the advice given during the last four years and the use of the facilities in the Materials Department, University of Wales Swansea.

I am very grateful for the assistance that I received from many colleagues in the Welsh Technology Centre. In particular I would like to thank: Mr S Smith, Mr K Chilvers, Mr T B Jones, Mr H Merckle, Mr J Aitchison, Mr M Westacott, Mr W Abbott and Mr C Broome and his staff in the WTC workshop. I would also like to thank my colleagues in the Steel Institute, University of Wollongong: Professor R Dippennaar for the use of the facilities and Dr P Manohar and Mr B DeJong for their help and support both during and after the time I spent at the Steel Institute.

To my friends, especially James and Debbie, thank you for your help and encouragement over the last four years.

To Mum and Dad, you have been the inspiration behind my whole academic career. Thank you for all your support, advice and encouragement – you have really kept me going. And to Nic and Ed, thank you for being there for your big sister.

EXECUTIVE SUMMARY

Weight reduction in body-in-white structures is necessary to make automobiles more fuel-efficient. A range of high and ultra-high strength strip steels have been developed, that will play a key role in achieving lower weights since the steels have the potential to achieve equivalent strength and crashworthiness at thinner gauges. However, the full potential of these advanced alloys can only be realised if they can be integrated into production facilities that rely on resistance spot welding as the predominant means of component joining. In particular, spot welds manufactured in these modern high strength steels will need to meet the strength and fracture resistance requirements that are based on automotive manufacturers' familiarity with low alloy steels.

Dual phase steels are a range of modern alloys causing considerable excitement due to their combination of high strength, high ductility and improved crashworthiness in automotive components, compared to mild steel. Their commercial production routes rely on a metallurgical understanding of how chemical composition and thermomechanical treatments interrelate to produce appropriate microstructures. Their often complex alloy compositions mean that there is potential for significant changes to take place in the microstructure on resistance welding.

This research programme has considered the important relationships from which resistance spot-welds, produced in high strength steels, derive their properties. This includes an investigation into the continuous cooling transformation behaviour of four dual phase alloys, in comparison to low alloy grades, and measurement of the mechanical properties associated with their microstructures. The thermal profiles generated within spot welds have been measured using a thermocouple technique. Advanced resistance spot welding processes, that can modify the metallurgical condition of a spot-weld, have been investigated with some success, both in terms of reductions in weld hardness following pulsed welding schedules, and an understanding of the effect of such schedules on the thermal cycle.

CONTENTS

1. INTRODUCTION

Automotive manufacturers are faced with three key demands from their customers: improved safety, greater fuel efficiency and increased specification. These requirements must be met without any significant increase in the overall vehicle cost. One important means of improving fuel consumption is to reduce vehicle weight. However, with increased levels of weight adding features, such as air conditioning, being required as standard, attention has turned to the body-in-white to provide the necessary reductions. A concern with decreases in the mass of the car body itself is that there could be a penalty in terms of crashworthiness, a critical issue to consumers and an ever more prevalent one since the introduction of the well publicised European crash tests EuroNCAP[1].

One development that counters these conflicting concerns is the introduction of high strength materials to effect weight reduction of body-in-white components[2, 3]. Not only do higher strength materials allow thin strip steel to be used but they can also result in improved component performance compared with mild steel equivalents. In terms of choice of materials there have been two main contenders. Aluminium alloys have had recent high profile use in ranges by Audi whilst other manufacturers have chosen high strength steels. A critical issue is that of integrating new products into existing production facilities. Many manufacturers already make extensive use of steel in their plants and a change to aluminium would require large investments both in terms of equipment and training. The chosen solution must not result in an uneconomical product for consumers and this makes aluminium a less favourable choice for many manufacturers. Further, with European legislation[4] due to come into force, which will require manufacturers to recycle 95% of their cars by 2015, the ease with which a material can be recycled is now of critical importance. Steel products are highly recyclable and whilst many aluminium alloys can also be recycled a mixture of materials is more difficult to process.

Clearly a steel solution to the issue of down gauging is attractive to manufacturers. In recent years a range of advanced steel alloys have been developed which address the requirement for a higher strength : weight ratio through different technologies. In particular dual phase ferrite-martensite steels have caused considerable excitement because whilst offering an excellent combination of strength and ductility they also exhibit significantly improved crashworthiness in automotive components compared to their mild steel counterparts[5-7].

Of the many manufacturing operations that any new steel grade must satisfy, welding is one of the most critical. A range of welding processes is used in the production of a body-in-white but the most predominant technique is resistance spot welding. This readily automated technique is ideally suited to high volume production and as such accounts for approximately 80% of the welds made in a car. This amounts to approximately seven million spot welds a day on a typical modern automotive manufacturing line.

Clearly it is important that any new grades can be joined using this process. However, concerns have been raised about how readily dual phase steels will integrate into existing welding facilities. The characteristic microstructures of dual phase steels are developed through a combination of alloy additions and careful thermomechanical processing. The alloy additions make the steels more sensitive to the rapid heating and cooling rates generated by welding processes, in particular resistance spot welding, with significantly modified microstructures being present in the welds compared to the parent material. In automotive applications it is less likely that high strength steels will be welded to themselves and more likely that they will be joined to mild steel components. This reduces the alloy composition of the resultant spot weld nugget, reducing the sensitivity to fast cooling rates, but the heat-affected zones in the dual phase steel remain sensitive to the spot welding thermal cycles. The modified microstructures are thought likely to affect the weld properties and whilst there is no difficulty in producing welds of the desired diameter in dual phase steels, some reports have suggested that these steels are failing the traditional chisel test, often used on production facilities to provide a rough indicator of weld quality. A further issue that needs clarification is, therefore, the most suitable means of defining weld quality.

In order to control the weld microstructures some attempts have been made at modifying the welding parameters used to effect a post weld heat treatment online or a reduction in the rate of heat input through the use of pulsed welding. These experiments have, however, been trial and error in nature and there is no clear understanding of how welding parameters affect heat input and cooling rate.

Clearly, if the potential benefits of dual phase steels are to be realised a detailed research programme is required which addresses the important issues described above. The present work involved a critical review of literature of current knowledge on the factors affecting

weld quality in high strength steels and possible modifications to the weld schedules used for higher alloy grades. On the basis of this review, a series of investigations has been defined, which covers: (i) the continuous cooling transformation behaviour of dual phase steels, both in terms of their microstructures and properties and (ii) a detailed assessment of the resistance spot welding process, in order to identify suitable modifications to standard weld programmes, which offer improvements to spot weld characteristics.

2. REVIEW OF LITERATURE

This critical review of literature considers the most important issues in modern automotive welding processes as well as those high and ultra high strength steels that offer the potential for the down-gauging of body-in-white components. Microstructure – property interactions are considered in the context of welding and current knowledge regarding the role of continuous cooling transformations in the development of these microstructures evaluated.

2.1 Industrial Welding Practice for Automotive Applications

This section presents a review of important automotive welding processes, resistance spot welding parameter selection and the wide range of factors used to monitor spot weld quality.

2.1.1 Industrial Welding Processes

One of the critical considerations for any advanced steel alloy is whether it can be integrated into current automotive production regimes without major changes to processing parameters. In particular, it should be possible to join modern grades to other ferrous alloys via current fabrication techniques. The main technique used in automotive manufacture is resistance spot welding. However, there is a move towards laser welding, for some areas of the body-in-white, by manufacturers who wish to take advantage of the improved rigidity afforded by the use of this technique. Other techniques, such as Metal Inert Gas (MIG) welding and weld bonding, a combination of adhesive and resistance spot welding, are used to some degree but are not such important techniques for the manufacture of the body-in-white.

Resistance Spot Welding

Resistance spot welding is one of the earliest resistance welding processes but is still one of the most widely used. The principle set-up is illustrated in Figure 2.1. Two or more sheets of material are overlapped and a pair of electrodes squeezed together at a pre-set force. A current is passed between the electrodes, which causes heating due to interfacial resistance and the bulk resistance of the parent material. This causes the eventual melting of the sheet, fusing the two surfaces together. The force and current cycle are depicted schematically in Figure 2.2. The four stages of the cycle are:

- **Squeeze**

The electrodes press the sheets together ensuring good fit. The squeeze time must be sufficient for the force to build up to the pre-set level.

- **Weld**

The current is passed between the electrodes and resistance heating occurs initially at the point of greatest local resistance. This is often the sheet-to-sheet interface but the electrode-to-sheet interface is also considered to generate some heat. If sufficient current is applied, the material will melt and a nugget will develop. The size of this nugget is dependent on a number of factors:

Weld Current - Joule's Law indicates the relationship between the applied current and the heat generated:

$$H = kI^2Rt \qquad [2.1]$$

where **H** = heat energy in Joules
R = total resistance in circuit in Ohms
k = constant
t = time in seconds
I = current in Amperes

Clearly, the greater the applied current the more heat will be generated and the greater the amount of material melted.

Weld Time - The length of time for which the current is applied should be sufficient for the weld nugget to grow to the desired size. This factor is related to current and, with reference to Joule's Law, the trend is that to achieve a given weld size, the weld time can be decreased as the current is increased. In industry, with tight production schedules high currents and low weld times are often chosen to speed up the welding process.

Electrode Force – The electrode force is principally imposed to maintain sufficient contact between the sheet surfaces during welding. This minimises the expulsion of molten metal and thus helps to preserve weld nugget integrity. In addition it prevents burning of the sheet surfaces.

- **Hold Time**

The electrode force is maintained for a set time after the current flow has stopped in order to consolidate the weld nugget during solidification. The length of the hold time

potentially has an effect on the cooling rate of the weld due to the water-cooling of the electrodes. This forced cooling draws heat out of the weld parallel to the direction of current flow, thus longer hold times could possibly speed up the cooling of the nugget.

- **Off Time**

If the cycle is to be repeated periodically an off time is pre-programmed. During this time the electrodes are retracted allowing repositioning / substitution of the sheets before the process is repeated.

Practically, each part of the weld process is measured in cycles, where 1 cycle = 1/50 of a second or 0.02s (for a 50Hz AC supply). For different steels the time of each step, and the other parameters used (current, force etc.) are subject to variation in order to obtain the desired weld diameter. A further consideration is current shunting, which occurs if the weld spacing is insufficient and reduces the amount of current available to make each new spot weld. In practice, a car panel or other component could have several spot welds adjacent to each other and therefore this effect would need to be compensated for.

Resistance spot welding equipment has received heavy investment by the automotive sector due to the advantages of automation and rapid processing speed that it offers as a process. Therefore any new material will have to be readily spot welded if it is going to be introduced by manufacturers into their process lines. For high strength steels this means establishing the welding parameters that achieve satisfactory nugget formation and weld properties. It is desirable, however, that these conditions do not greatly increase the overall weld time from current typical settings. With modern automotive production lines producing around seven million spot welds a day, any increase in the time to produce one weld would significantly decrease productivity.

Laser Welding

Laser technology has, in recent years, been applied in many ways to automobile production. In particular it provides a sophisticated cutting technique and can also be used for welding, both in body-in-white manufacture and in the production of tailor welded blanks.

In outline, laser welding makes use of a high-powered laser beam to melt, and thus facilitate the bonding of, two or more surfaces. The high energy input means that some of the molten metal evaporates leading to a deep hole filled with vapour. This is termed the 'keyhole' effect and it achieves a full penetration weld with the minimum amount of melting of the parent metal. The keyhole moves along the workpiece with the beam creating a continuous weld.

In terms of welding, lasers offer advantages over resistance spot welding in three main ways:

- Joints are continuous, which increases torsional rigidity and stiffness thus improving fatigue properties.
- Heat input is reduced creating a narrower heat-affected zone, less distortion and the potential for better surface appearance.
- Joint flexibility is increased - single sided access is possible and being a non-contact joining method areas that cannot physically be reached by electrode arms can be welded. However, areas inside the body-in-white are still difficult to reach and currently laser welding finds more use in external components.

Laser welding equipment is currently expensive so its use is not likely to predominate in the near future, particularly for automotive models produced on existing manufacturing lines. The technique was extensively used in the ULSAB project[8] but this collaboration was more about illustrating the high-tech application of steels than addressing the immediate introduction of advanced production techniques. In addition, despite the use of a number of modern fabrication techniques in the ULSAB, there were still over two thousand spot welds. This clearly shows the importance of resistance spot welding to the automotive industry. Overall laser welding offers several advantages that are likely to increase its presence in the automotive sector in the future in suitable areas, particularly as the capital costs decrease.

2.1.2 Resistance Spot Welding Parameter Selection

In determining the most important parameters to be controlled during spot welding, Karagoulis[9] initially identified over fifty that could apply. These included material properties, mechanical factors, such as the condition of welding guns and supplementary equipment, and the specific parameters that can be adjusted during spot welding. It is this latter group of factors that is now considered.

The Effect of Current

The general effect of an increase in current is an increase in weld size. This is simply due to the rise in heat generation as the current is increased, facilitating melting of more of the steel (see equation [2.1]). The effect of each unit increase in current is enhanced by the higher alloy compositions of high strength steels that increase their bulk resistivity. This leads to narrower welding current ranges, that is, the range between the minimum acceptable weld size and splash, where molten metal is ejected from a spot weld. Increasing the weld size in a given material has a subsequent effect on weld properties. Larger welds have, in general, higher static and dynamic strengths, although the relationship is not directly proportional. Further, within a weldability lobe, currents chosen from close to the lower limit have been shown to have a different effect on notch shape[10] to those chosen from the higher end.

One issue not frequently addressed is the use of direct current (DC) as opposed to alternating current (AC) in spot welding. Particular advantages include the use of smaller transformers on the welding robots and greater control over the welding currents. In his work comparing A.C. and D.C. welding, Brown[11] concludes that welding lobes, with similar dimensions, can be obtained with up to 27% less current with DC compared to AC. This clearly indicates a potential cost saving in terms of energy usage. However, as the majority of welding equipment currently installed in manufacturing plants is AC based it seems unlikely that automobile producers will be willing to reinvest unless further benefits can be determined. However, some manufacturers, BMW being a notable example, already use DC welding and new production lines will require new equipment selection. If it could be proven that DC welding produces optimum results in high strength steel it is possible that new lines could incorporate such techniques.

The Effect of Electrode Force

The electrode force is responsible for maintaining intimate contact between sheets being spot welded. There are, therefore, serious consequences to insufficient force being applied. Constant, sufficient pressure is important in preventing splash at lower than expected currents. If the electrode force is not high enough, the molten metal is released from the nugget resulting in a reduction in weld properties on solidification. For high strength steels it has been suggested that up to 50% more force will be required for satisfactory welding[12]. Problems with this could be that the welding guns used in plant environments cannot supply the required force in which case an alternative solution will be necessary. The pressure applied also affects void formation. If the electrode force is not high enough void formation may occur at the centre of the weld nugget. Other factors do influence this process, such as surface conditions, but if the electrode force is too low porosity may be a problem. This effect has been measured in higher carbon steel[13] and estimated via a factorial experiment in C-Mn[14] and rephosphorised steel.

The effect of electrode force on the position of the weldability lobe has been clearly shown for rephosphorised[15] and HSLA steel[16]. Both papers indicate a shift to higher currents as the force is increased. This results from a change in the sheet-to-sheet resistance before spot welding. At a lower force, the tiny peaks and troughs in the surface of the steel render the sheet-to-sheet interface the point of highest resistance encouraging heating, and subsequent melting, to occur at this point. The increase in force flattens some peaks, increasing the contact between the sheet surfaces and the resistance is thus reduced.

The Effect of Weld Time

Although Karagoulis[9] did not consider weld time to be a key variable, in terms of plant based spot welding, other researchers have highlighted its significance. Williams[12] noted that it was necessary to decrease weld time, for high strength steels in general, in order to achieve a given weld size. Gould[14] estimated a linear relationship between weld time and weld hardness for a rephosphorised steel and this was reinforced by Dickinson and Natale[16] who identified an increased weld time's role in reducing the hardness of the heat-affected zone of a spot weld. The reason for this reduction in hardness was thought to be due to the increased length of time it takes for the energy, imparted by the welding process, to be dissipated by the steel. The longer the time taken, the more the heat has a

chance to conduct into the surrounding material and thus the subsequent cooling rate is reduced due to a lower temperature gradient between the nugget and the bulk of the component. However, no measurements have been reported that support this claim.

This potentially positive effect is welcomed by many researchers, but, as Mitchell and Chang[17] point out, excessively long weld times, that increase production time to any great extent are not going to be welcomed by the automotive sector. Therefore, in order to increase the time allowed for heat absorption, without drastically increasing the weld time, pulsed welding has been considered. This type of welding has been considered a number of times by British Steel, now Corus UK[12, 13, 15] and the results indicate that an increase in the number of pulses results in plug failures at lower weld sizes. However, no mechanism has been described for the change in failure mode. Despite this it is not clear why this approach has not been pursued further. In particular it has not been applied to advanced dual phase steel alloys to any significant extent. Quantification of the possible benefits of pulsed welding is required with a view to confirming it, or not, as a suitable method of welding high alloy steel grades.

The Effect of Hold Time

Hold time sensitivity is a condition found in a number of modern high strength steels that rely on increased alloy content for their strength. Potentially, a decrease in the cooling rate of a spot weld could reduce the amount of brittle microstructural constituents such as martensite that are formed, which would influence weld properties. Current welding schedules that make use of hold times of around 25-30 cycles result in cooling rates reported to be anywhere between 2000°C/sec[49] and 100,000°C/sec[14], the higher cooling rates being more likely in thinner gauge material. However, these cooling rates are often predicted by computer models that have many simplifying assumptions built in and there is little practical data available to support these estimations. One of the main reasons for the high cooling rates are the water cooled electrodes being held in place over the weld nugget during the hold time. The copper electrodes rapidly draw heat from the weld resulting in extreme cooling rates. One potential method of reducing the temperature gradients is thus to reduce the hold time allowing the weld nugget to cool more slowly. The concern with this technique is that if the electrodes are not held in place long enough, the nugget will expand resulting in porosity, as previously outlined. This porosity is not considered critical to properties by some[18] but, for example, Gould[14] expressed concern

that this distribution of pores can lead to a low energy fracture path through the weld nugget.

Further indications of the effect of hold time have been presented by Sawhill and Furr[18] and Nishi et al[19]. Both papers illustrated how an increase in hold time leads to a significant increase in hardness. In the former case, an increase of 110 V.P.N. was seen in the weld nugget between a hold time of 10 cycles and one of 30 cycles. After this the hardness levelled off, possibly because a critical cooling rate is reached using the 30 cycle hold time.

Clearly there are two opposing factors here, the requirement for weld consolidation and the desire for a slow cooling rate. It seems unlikely that hold time will be the only parameter that requires modification in order to produce appropriate high strength steel welding schedules. However, it may have a role in a combined approach to specifying welding parameters.

Effect of Post Weld Heat Treatments

Post weld heat treatments (PWHTs) are commonplace in fusion welding processes but their usefulness in terms of spot welding is yet to be accepted on a wide scale. Peterson[20], as an example, considers this type of treatment to be capable of producing strong but tough spot welds. However, Mitchell and Chang[17] suggest that "the use of quench and temper cycles is completely unacceptable in the automotive field due to a loss of productivity." It is certainly true that, with the time to make one spot weld measured in fractions of a second even a seemingly small increase in the time, for example 5 cycles or 0.1s, would, percentage wise, lead to a significant increase in production times. However, these latter views were published in 1975 and present day manufacturers are keen to make use of the weight saving possibilities of new high strength steels, which may require such schedules to allow them to be spot welded satisfactorily.

Published work on the subject of spot welding PWHTs is very limited and even where data has been reported it is not always clear how the values for current and time in the post weld pulses have been decided upon. However, a very early paper[21] contains considerable detail of procedure and results. Simmie and Hipperson[21] compared the hardness profile of 'as welded' nuggets, machine tempered welds and furnace tempered

welds. The results of the machine tempered welds lay somewhere between the as welded and furnace-tempered results, see Figure 2.3 for an example. The key result from this paper is that, in order to be effective, the tempering treatment should not begin until the transformation to martensite has been completed, although it is recognised that tempering should begin as soon after this time as possible. Tanuma and Hasimoto[22] did some further work on furnace tempering. They found a steady decrease in hardness with 30 minute furnace treatments ranging from 200-900°C, but cross tensile strength was optimised at around 300°C. Both cross-tensile and tensile shear strength deteriorated at treatments above 600°C. However, furnace tempering at these temperatures is not practical for application in a production environment. Some more recent work[12] included a brief look at PWHTs in niobium treated steel. An increase in post heat time over three samples (from 0 to 0.2 to 0.4 seconds) was seen to result in the conversion of the failure mode from interface with no heat treatment, to partial plug for either of the two PWHTs. This work cannot be considered conclusive because of the small number of results.

2.1.3 Weldability of Alloy Steels

In order to make use of a given steel grade, in automotive production, it is important that the performance of resistance spot welds, made in that material, is satisfactory. To this end a series of tests have been developed, and where possible standardised, to provide manufacturers with greater assurances about the acceptability of a steel grade in terms of its spot weldability. Thus, all other factors being acceptable, a given steel is generally considered interchangeable with existing grades if these standards are met. Different companies place a greater emphasis on different properties. Kiyagawa et al[23] sent out a questionnaire, regarding the issue of quality of spot welds, to various automotive manufacturers in Japan. Questions asked covered such areas as the characteristics of a good quality spot weld and how welding parameters should be chosen. The thirteen replies received indicated a variety of parameters considered important in determining quality, including nugget diameter, static and dynamic strength and fracture mode. As different classes of steel achieve their strength through different mechanisms the tests developed to indicate acceptable weldability in mild steel may not provide accurate results in the case of a higher strength steel. For this reason the merits of a number of different tests, including the nature of the information that they provide, have been considered.

Weldability Lobe

Weldability lobes are determined from a number of weld growth curves, which are produced by measuring the increase in weld size with an increase in current for a fixed set of welding parameters, such as weld time and weld force. They give a visual representation of the range of welding conditions over which a given material will produce acceptable spot welds. This is an important consideration for industry who would not find acceptable a material that will only produce satisfactory welds with a very specific welding schedule, as conditions on a production line are subject to a certain amount of variability.

One area of uncertainty with regard to the measurement of weld size for lobe construction is the definition of the lower and upper limit on the plot. Corus UK's procedure for lobe determination suggests $3.5\sqrt{t}$ (where t is the sheet thickness) and splash for the lower and upper limits respectively. The French standard[16], NF A 87-001 indicates that the minimum acceptable nugget size is 6mm. No thickness limits were specified but the steels under consideration were 1.2 to 3mm thick. An older American paper[24], uses "the current required to produce a weld with a tensile shear strength equal to 65% of the maximum value (level that causes splash)" as the lower limit. The upper limit has as many definitions. Most standards consider those conditions that cause splash to be the upper limit but Karagoulis[9], in a paper based on General Motors practice in the U.S., mentions that above the splash limit a further "upper" limit is reached when electrode sticking or sheet indentation greater than 30% occurs. In practice, production lines often use splash as an indication that sufficient current to create a weld has been used and despite many researchers' view that it is not ideal no written challenge of the practice could be found.

The wider a weldability lobe the greater the range of conditions over which acceptable welds can be formed. However, there is further disagreement over what the minimum range of current should be. Ford's specification[17] requires a 2kA range from the lower limit, set at a specific size depending on material thickness, to the splash upper limit whereas the French standard has the lower requirement of 1.5kA.

It is important to define the required limits with manufacturers so that, in developing welding procedures, acceptable lobes can be determined. However, the existing weld lobe

criteria were developed for mild and low alloy steels and the benefits of modern advanced steel grades have been developed partly through increases to the alloy content. This increase in alloy composition increases the bulk resistivity of the grade, which imparts a greater sensitivity to current than the lower alloy counterparts. Therefore, it is unlikely that high and ultra high strength steel, with higher alloy compositions, will be able to produce weld lobes of a similar size to mild steel grades. However, large weld lobes have been a requirement of automotive manufacturers because of their concerns about the consistent performance of their welding equipment, particularly welding electrodes. It may be necessary for improvements to be made in this area if manufacturers want to take advantage of the benefits of modern high strength steels.

Mode of Failure

The relative importance of failure mode – plug or interface – is a contentious issue and one that is of particular importance when considering high strength steels. Plug failures are those that occur by the pulling of the weld from one sheet of steel leaving a hole in the other sheet. An interface failure is one where the failure occurs through the weld itself. The occurrence, and relevance, of partial plugs, which are a mixture of the two failure modes, has also become a consideration as many high strength steels fail predominantly in this way. A recent American standard[25] goes even further highlighting nine different categories of failure modes from full plug through to full interfacial failure, although most of these are different morphologies of partial plug failures.

Perhaps the most critical issue is whether an interfacial failure signifies a brittle weld compared to a plug failure. Pollard and Goodenow[24] considered there to be two reasons for an interfacial failure: low strength and low ductility. They concluded, therefore that an interfacial failure is not always a brittle one. Ferasse et al[10] further observed that in a cross tension test interfacial failures exhibited the same properties as small plugs suggesting that failure mode was not the only factor involved in determining strength. Partial plugs were also considered by Sawhill and Furr[18] who determined that it was the size of the plug, and not the percentage of the total weld size that failed as a plug, that was important. Nishi et al[19] disagreed and quantified the critical percentage plug as 85%. At this or a greater percentage plug, they found that U tension strength was satisfactory.

It is thought likely that the absolute size of the plug is important in terms of properties. A larger plug would have a larger circumference to be pulled, leading to greater energy absorption on failure. A smaller plug would not absorb as much energy. However, in a weld producing a smaller absolute plug size the proportion of the weld that fails interfacially would make a contribution to the overall weld strength and energy absorption. Thus, the relative weld strength of a 5mm full plug and a 5mm partial plug is not clear. In terms of process efficiency, percentage plug is very important. If the 'best' weld failure that can be achieved is, for example, 50% plug then in order to obtain a given plug size more current would have to be used (all other conditions being equal and assuming no interfacial contribution) to generate a weld twice the area of the required plug. This is clearly not desirable, or practical, from an energy or cost perspective.

The relationship between mode of failure and weld performance has not been clearly defined. Further, the reason for failures as partial plugs has not been established. It is possible that the direction of the columnar grain growth affects the direction of the failure path. For example, a weld would start to fail interfacially, along a columnar grain boundary that is parallel to the sheet surface. On reaching the intersection with a perpendicular columnar grain, with boundaries at right angles to the sheet surface, the direction of the failure path would change. This mechanism is thought likely to be affected by segregation along grain boundaries but it is less likely that segregation occurs in modern low alloy high strength steels. No evidence of a mechanism relating microstructure to partial plug failures has been reported.

A number of factors are known to affect the likelihood of a plug failure[12]:

- The type of test used. One reason that plugs are not always considered valid quality indicators is that the result depends on test type and further that within a single test type the failure mode is often dependent on the skill of the operator.
- The degree of restraint on the weld, that is, the ratio of weld size to steel thickness. It is generally thought to be easier to obtain plugs in thinner steel due to the failure path being shorter through the steel thickness than through the weld diameter. However, this is not a fixed factor and it is possible to obtain plug failures in thicker steel.
- The relative strengths of the weld, heat-affected zone and the base metal. In this area microstructure plays an important part with more brittle, martensitic structures tending to lead to interfacial failures.

- Inclusions in the steel[23]. If the cooling rate is slow enough lower melting point inclusions can make their way to the centre of the nugget creating a weak point at the interface. This can lead to an interfacial failure but inclusions are not thought to be an important consideration where steel is made using modern techniques.

A further consideration is the 'notch effect.' Figure 2.4[10] is an illustration of a spot weld with two key areas indicated: the notch tip and the diffusion zone. The diffusion zone is the area outside the weld nugget that has fused via diffusion mechanisms rather than by the steel melting on welding. In this work by Ferrasse et al[10], higher welding currents were seen to the diminish the diffusion zone and the notch was seen to have a more square shape than at lower currents, where the notch was sharp in appearance. It is the sharper notch that was found more likely to lead to an interfacial failure. Further, the microstructure present at the tip of the notch was shown to have an effect on failure mode. By increasing the length of the diffusion zone, that is, the distance between the notch and the weld microstructure, the chance of interfacial failure was reduced. This was thought to be due to a decrease in the stress level in the weld nugget.

A further influence on the notch is the ratio of electrode size to weld size[17]. It has been shown in mild steel that if the weld size is significantly smaller than the electrode tip a sharp notch and a likelihood of interfacial failure will result. Conversely, as the weld size approaches and exceeds the electrode size a blunter notch will form leading to a higher chance of pulling a plug. This effect has also been observed in rephosphorised steel[12]. These results are in agreement with the guidelines provided in BS1140[26].

Despite questions over the reliability of plug failures as a useful indicator of weld performance, in a manufacturing environment simple chisel and peel tests are still performed in an attempt to ensure that weld quality is satisfactory. These tests are frequently carried out by non-technical people and, as such, the easiest measure of acceptability is failure as a full plug. If high strength steels are to be widely adopted the current requirement for plug failures will need to be addressed. In addition, it is considered that providing a fundamental understanding of the mechanisms leading to acceptable weld performance, and optimisation of welding parameters, may reduce manufacturers' reliance on this test.

Peel and Chisel Tests

These are simple tests that allow both the measurement of weld size and determination of failure mode. In the manufacturing environment chisel tests are often performed to check that equipment is working correctly, with a plug or pullout failure indicating acceptance. Measurement of the bonded area is usually made with callipers following failure. An advantage to chisel testing is that it can potentially be used as a non-destructive test. The tester prises the sheets apart to check that the area is bonded and then taps the sheets back into place. More sophisticated non-destructive methods of testing, for example, ultrasonic testing, are being developed but widespread introduction is limited by the number of trained personnel. Non-technical staff can perform chisel tests with the results considered easy to interpret. The main limitations of this test are that the results do not provide any numerical information on weld performance and more importantly the results obtained are dependent on exactly how the operator carries out the test. As operator procedure, not only for chisel tests but also across the spectrum of quality tests, has been shown to affect the mode of failure it is relevant to consider stress distribution on testing. Figure 2.5a illustrates the chisel test whilst Figure 2.5b[20] indicates the stress distribution on the weld. From the latter it can be seen that the stress is concentrated on one side of the weld.

Despite the limitations, chisel tests are firmly fixed in plant practice, mainly due to their simplicity. If manufacturers are to accept a material that does not perform to this standard they will need evidence of the reliability of the welds from other tests, possibly ultrasonic testing. Further, the requirement for online testing has arisen out of a need to check the reliability of welding conditions set through practical welding tests. Evidence of the mechanisms by which welding schedules are translated into weld properties will reassure manufacturers of the reliability of the programmes developed for modern high strength steels. It is also important to comment that plug failures may not always be possible in high alloy steels, and it may be necessary to modify the alloy composition or suggest an alternative welding process for use in the application of interest.

The peel test results in the same distribution of stress as the chisel test but, whilst the test can be done manually it is also possible to mechanise it within the laboratory. This achieves two things: it removes the 'operator' factor from the results and it allows a simple determination of the strength required to cause the weld to fail. Further, as high

strength steels become more common place, a mechanical test is likely to become more favoured due to the strength increases making manual chisel tests impractical.

Lap Shear and Cross Tension Tests

These two tests place a static load on the spot weld to be tested, the results being both determination of failure mode and a numerical value for the failure load. The tests stress a spot weld in different ways and different manufacturers seem to place different emphasis on their significance.

The shear test is performed on a welded lap joint, with dimensions being chosen according to thickness. BS1140: 1993[26] lays down some standard sizes which, in the main, agree with those given in the American standard ANS/AWS/SAE/D8.9-97[25], although the American version has fewer steps in its thickness scale. It is important to that 'shims' are present at either end of the test piece. They are specified in both the Corus internal guidelines[27] and the American standard, and are designed to ensure that the samples are tested in pure shear. Figure 2.6 is a schematic diagram of the stress distribution applied during lap shear testing.

Sawhill and Furr[18] observed that acceptable weld tensile test results indicate that the toughness of the weld is also acceptable. This work was done on a range of fifteen high strength steels, however, this range did not include modern grades such as dual phase and transformation induced plasticity steels that tend to have higher carbon contents. Further, in work on HSLA steel, Mitchell and Chang[17] found that values of tensile-shear strength are not indicative of the "ductility" of a weld. Welds that failed through the interface and those that failed as a plug both had similar tensile-shear strengths. However, tensile shear strength values can be used to indicate ductility when compared with material tensile strength in the following ratio:

$$\text{Ductility Ratio} = \frac{\text{Cross Tension Strength}}{\text{Lap Shear Strength}} \qquad [2.2]$$

Pollard and Goodenhow[24] considered the idea of a ductility ratio further and concluded that it is not an intrinsic measure of weld ductility since it varies with the weld current. Further, the ductility ratio was seen to increase with steel thickness. This ratio could be useful for comparing two materials of equal thickness, welded under the same conditions to determine if either has superior post weld ductility. However, this is not likely to be a

useful indicator for steel selection during the design of down-gauged components where the purpose of the change in the steel grade in use is to change the thickness.

Aside from the standard plug / interface failure criteria, spot welds should have a minimum shear strength of at least that calculated according to BS1140. In this standard it is stated that the minimum shear strength should be:

$$P_s = 2.6t \,.\, d \,.\, P_{TS} \qquad [2.3]$$

where P_s = shear strength of weld (N) d = weld diameter (mm)

t = sheet thickness (mm) P_{TS} = tensile strength of steel (N/mm^2)

The cross tension test loads a spot weld in a different way to that previously seen. This test used two pieces of steel crossed symmetrically at 90° and joined with a single spot weld in the centre. The stress distribution is given in Figure 2.7 and it can be seen that the stress is more evenly distributed on both sides of the spot weld. This might be more likely to lead to plug failure and previous work[10] has indicated greater ease of pulling plugs in cross tension tests. However, the use of plugs as quality indicators is not confirmed as the most reliable measure for modern high strength steels.

Lap shear and cross tension test different aspects of the spot welds' strength. In work carried out on a rephosphorised steel[15] it was noted that cross tension strength was lower than tensile shear strength. Further the cross tension strength showed a stronger correlation with spot weld size although later work on a dual phase steel[19] showed clear trends for both measures of strength. This illustrates one reason why weld bonding, a combination of spot welding and adhesive bonding, has been introduced. The adhesive compensates for the lower shear strength of the spot weld, which in turn has the superior cross tension strength. Weld bonding is also known to improve component stiffness.

Impact Testing

The aim of an impact test is to determine the performance of a weld, in terms of failure load and failure energy, under impact conditions such as could be experienced in a crash. The test can either be done with a shear or cross tension sample and the simplest method of performing the test is to use a single spot weld and a modified Izod impact testing facility. The main limitation of this test is that the mechanism of energy absorption is different for a single weld and the type of weld arrays actually used in an automobile[28].

This is mainly because in service the material around the weld is likely to absorb more of the impact energy than is possible in the case of a single spot welded joint. However, the testing of a welded array would require more specialist equipment and is therefore more costly to carry out.

Fatigue Testing

Fatigue tests evaluate another aspect of in-service conditions. In general, tests are performed on specimens as defined for lap shear tests and the standard output is a Load – Cycle curve, which indicates the number of cycles, at a given load that a weld can withstand before failure. No account was found of failure mode being taken into account when considering fatigue performance.

In work by Sperle[29] it was determined that the performance of non-load carrying spot welds increased with base metal tensile strength, which means that non-critical components can be welded to high strength steels with an improved fatigue life compared to a similar set up using, for example, mild steel. Previous work by Jones[15] indicated that fatigue strength increased with weld size. However, Sawhill and Furr[18] concluded that spot weld fatigue strength was more dependent on the direction of loading, had little to do with material properties and was thus not very useful in quantifying a new material's likely performance. Although not mentioned in any previous work it is thought that material characteristics may influence fatigue properties. If the microstructure is brittle then it is expected that fewer cycles would be required to propagate a crack sufficiently to cause failure compared with a more ductile microstructure. In general however, spot welds are not used in fatigue critical areas due to the increase in stress at the notch tip increasing the likelihood of a fatigue failure.

Hardness Testing

Hardness testing, whilst not measuring a property directly of interest in-service, does have empirical relationships with other properties such as toughness[30], ductility ratio[24] and failure mode[20]. Standard procedure is to section a spot weld and make microhardness indentations at regular intervals across the weld to reveal the hardness profile. This property is invariably affected by microstructure[22]. For example, a martensitic or bainitic structure would produce much higher hardness readings than a predominantly ferritic structure. Parameters that can affect hardness are hold time[18] and thickness[24]. However,

the effect of thickness is in turn related to the cooling rate experienced by the steel under test. As such, hardness can be considered to indicate the localised cooling rate.

Carbon Equivalent

The alloy content of high strength steels is generally higher than high strength low alloy (HSLA) grades. Although individual elements have an effect on different aspects of the weldability of steel alloys, it is a parameter that combines a number of them that is frequently quoted when considering the overall effect of alloy composition. The Carbon Equivalent (CE) is a calculated parameter, having a value between 0 and 1. A simple equation for CE combines the carbon and manganese content of a steel grade as follows:

$$CE = C + \frac{Mn}{6} \qquad [2.4]$$

For example, according to this formula a typical ultra low carbon steel might have a CE of 0.04, whereas a dual phase steel (UTS 800MPa) might have a CE of 0.38. It can be seen that dual phase steels are unlikely to give the same response to a set of welding conditions as low carbon steels and it has been suggested[31] that a CE of more than 0.3 indicates potential weldability problems.

Work by Mitchell and Chang[17] suggested a more complex relationship than that given above, taking into account the influence of a greater number of elements along with some material factors:

$$CE = C + \frac{Mn}{30} + \frac{Cr + Mo + Zr}{10} + \frac{Ti}{2} + \frac{Cb}{3} + \frac{V}{7} + \frac{UTS\ (Nmm^{-2})}{6200} + \frac{Gauge\ (mm)}{500} \qquad [2.5]$$

Again a figure of 0.3 was considered the dividing line between plug failure (<0.3) and interfacial failure (>0.3). This formula was applied to a number of peel tests with greater success in predicting failure mode (92% correct) than applying carbon content alone (81% correct). Herai and Takahashi[49] proposed a simpler relationship, removing the influence of manganese from the equation:

$$CE = C + \frac{Si}{40} + \frac{Cr}{20} \qquad [2.6]$$

However, given the known influence of manganese as an austenite stabiliser[32], and its common appearance in advanced steel alloys, it seems unlikely that an equation without a manganese term will be suitable for use for modern high strength steel grades.

The Ito-Bessyo carbon equivalent equation[33] has been suggested as the most suitable for use with low carbon steels:

$$CE = C + \frac{Si}{30} + \frac{(Mn+Cu+Cr)}{20} + \frac{Ni}{60} + \frac{Mo}{15} + \frac{V}{10} + 5B \qquad [2.7]$$

This equation contains the main alloying elements used in modern high strength steels, which makes it more likely than other equations to represent the behaviour of advanced steel grades.

Nishi et al[19] used the combined value of carbon and phosphorus to relate the failure mode, following a peel test, to alloy composition. This relationship was tested on high strength low alloy steels but the lack of a manganese term makes the equation less relevant for modern steel grades. Work by Gould[14] found that carbon and phosphorus have an influence on weld hardness. It also indicated that manganese has a significant influence on hardness, which increases concern about the applicability of an equation without a manganese term, to advanced high strength grades.

.

2.2 Metallurgy of High Strength Steel

This section considers ferrous metallurgy from three perspectives: the individual constituents that are found in low carbon alloy steels; specific examples of high and ultra high strength steels that are enhanced through the careful control of both composition and microstructure; and the effect of different microstructural constituents on weld properties.

2.1.1 Ferrous Metallurgy

An important characteristic of steel alloys is the range of microstructures and subsequent properties available through heat treatment alone. A number of different microstructural constituents form the basis of these microstructures and these are considered below.

Ferrite

Ferrite is an equilibrium phase, which can have many different morphologies, a comprehensive review of which has been carried out[34]. Fully ferritic microstructures are only observed when the carbon content is very low. Above about 0.02wt%C a mixture of ferrite with an iron carbide constituent usually forms. The properties of fully ferritic structures depend primarily on grain size. The Hall-Petch relationship:

$$\sigma_y = \sigma_o + k_y d^{-1/2} \qquad [2.8]$$

σ_y - yield stress d - grain size

σ_o k_y - constants

indicates the inverse relationship between yield stress and grain size. In commercial steels much effort has been put on finding ways of refining the grain size in order to improve strength. A further advantage of a fine ferrite structure is improved formability and ductility. These characteristics make ferritic steels particularly useful for forming applications such as automotive panels. However, such microstructures are not found in high strength steels, which have carbon contents that surpass those that allow purely ferritic microstructures to form.

Pearlite

Pearlite is the product of a eutectoid reaction, that is, it is produced when austenite transforms to ferrite and cementite (Fe_3C) via a solid state transformation. It appears in steels with a carbon content of more than about 0.02%. The transformation usually

requires fairly slow cooling rates and under equilibrium conditions transformation should occur at 723°C according to the phase diagram. However, due to the diffusional nature of the transformation, pearlite formation is often suppressed to lower temperatures. During cooling, carbon atoms diffuse away from the regions transforming to ferrite resulting in carbon-rich austenite that subsequently transforms to cementite. If the cooling rate is fast enough (but not so fast as to generate displacive transformation products) there is less time for this diffusion to take place so the formation of pearlite doesn't start until a lower temperature is reached. The pearlite forms as parallel lamellae of alternate ferrite and cementite, which grow co-operatively, producing a two phase structure. The fine nature of the lamellae makes pearlite difficult to resolve optically and it tends to appear as a black or dark grey phase in optical images.

Fully pearlitic steels are only seen when the eutectoid composition (0.8%C) is observed. Most low carbon steels consist of some primary ferrite with a pearlite second phase with higher carbon steels (>0.8%C) having primary cementite and pearlite microstructures.

An important dimension with respect to the mechanical properties of pearlite is the interlamellar spacing. A reduction in this parameter increases the strength and hardness of the steel. An effective method of achieving a fine interlamellar spacing is to increase the cooling rate. However, care must be taken as pearlite can reduce toughness due to the interfaces between the lamellae providing easy nucleation sites for cracks during impact.
It is thought unlikely that pearlite will be observed in spot weld microstructures in high strength steels as the high cooling rates present during welding are more likely to generate non-diffusional microstructures.

Austenite (Retained Austenite)

Austenite is an equilibrium phase that is usually present in a low carbon steel microstructure between about 723 and 1400°C, except in ultra low carbon steels where it only exists above 910°C. In order to retain it in room temperature microstructures careful alloying is required, in addition to the presence of elements known to suppress the transformation to ferrite. Such elements include carbon, which, with a higher solubility in austenite than ferrite, favours the retention of austenite. Other examples include manganese, nitrogen, and nickel and chromium combinations[32].

The most important property of austenite is the insensitivity of its impact properties to temperature, due to its face-centred cubic structure. This property is made good use of in austenitic stainless steels, which are used for low temperature applications.

Austenite can also be retained in room temperature microstructures through quenching and is often found in quenched martensitic microstructures where the fast cooling rate has fixed the carbon in solution with the γ-iron. This retained austenite is thermodynamically unstable and, on mechanical deformation, will transform to martensite. This property is made use of in transformation induced plasticity (TRIP) steels. Retained austenite is often seen in weld microstructures, as the fast cooling rates can result in the incomplete transformations described above.

Acicular Ferrite

Acicular ferrite is a plate-like ferrite phase that nucleates intragranularly. Bhadeshia[35] has commented that it is essentially intragranularly nucleated bainite. It has an interwoven or basket weave structure[34] and the nucleation is usually associated with non-metallic inclusions.

The formation of acicular ferrite is promoted by a large grain size that decreases the volume fraction of grain boundaries available to provide nucleation sites. As it is one of the last phases to form, after other forms of ferrite, the presence of grain boundary phases such as ferrite allotriomorphs can also encourage acicular ferrite formation in preference to bainite.

Acicular ferrite is associated with high impact energy. This is thought to be due to the chaotic, interwoven nature of the grains that substantially increase the energy required for fracture.

Bainite

Bainitic microstructures are generally split into two groups, upper and lower bainite[36]. Upper bainite transforms at around 550-400°C. The characteristic microstructure consists of small plates of ferrite which grow in groups known as sheaves, separated by cementite

films, which precipitate following the rejection of carbon into the remaining austenite as the ferrite plates grow.

Lower bainite transforms at temperatures of between 400 and 250°C, with transformations taking place right down to the martensite start temperature. This phase also consists of ferrite plates but the key difference between the two microstructures is the nature of the carbides present. Due to the lower transformation temperature, much of the carbon in lower bainite does not have time to be rejected from the ferrite plates that form and precipitates within the plates themselves. Therefore, the carbides present in lower bainite have two distinct forms as opposed to the one type present in upper bainite.

The hardness of either type of bainite varies almost linearly with the carbon content[36] and for a fully bainitic microstructure the change in hardness is about 190HV per wt%C. In terms of strength it is the fine bainite grain size that has the more predominant effect – the small distance between plates results in a low mean free path for dislocation glide. In general, evidence for the dependence of impact toughness on microstructural parameters could not be found. However, the morphology of any carbides present is likely to have an effect on the ductility and possibly the mode of failure in an impact test.

Martensite

Martensite is a non-equilibrium phase found in low carbon steels. Its formation depends on both steel chemistry and the speed of cooling from the austenite region. The general appearance of martensite in low carbon steels is of fine laths grouped together in 'packets' with the laths all tending to have the same orientation within a single packet.

The mechanism of martensite transformation is displacive or diffusionless, as opposed to the diffusional mechanisms of the ferrite and pearlite transformations. The fraction of martensite produced after quenching to a given temperature is described by the equation[37]:

$$f = 1 - \exp -[0.01] (M_s - T_q) \qquad [2.9]$$

where f - fraction martensite transformed after quenching

T_q - temperature to which material is cooled

M_s - martensite start temperature

It can be seen that the amount of martensite formed at a given temperature is therefore only a function of M_s and not the time at that temperature. The implication for welding

schedules is that the use of pulse welding will only inhibit the formation of martensite if the current pulses slow the cooling rate prior to reaching M_s as holding the temperature, or slowing the cooling rate, after this temperature has been reached, will not change the amount of martensite formed. The actual value of M_s is a function of the alloy content of the steel, with sharp decreases in M_s observed as carbon content is increased.

Tempering of martensite is commonly carried out in order to improve the toughness of an alloy, although a reduction in steel strength also occurs. This process reduces the level of residual stress present in the microstructure as a result of the shear transformation process, and alters the carbide morphology. Autotempering occurs when the temperature after transformation is high enough for some carbon diffusion to take place, resulting in some stress reduction and carbide coarsening without requiring a separate treatment. The consequence of a low M_s is that autotempering is limited.

The properties of martensite reflect the fact that it is a supersaturated solid solution of carbon in iron. It has been shown[32] that there is a strong dependence of martensite hardness on the carbon content of the steel. The yield stress is similarly dependent although other contributors to strength are the lath and packet size of the martensite. The maximum lath size is in turn related the austenite grain size, and a Hall-Petch type relationship has been found for some steel grades[32].

It has been suggested[34] that the high hardness of lath martensite in welds should not have the poor reputation for mechanical properties that it currently holds, as the martensite observed is, in general, refined in nature resulting in acceptable mechanical performance. As previously stated, the transformation to martensite is a shear process and, when unrestrained, the change in microstructure can result in surface relief. The restriction of this dimensional change by the electrodes during spot welding may result in residual stresses high enough to have a detrimental effect on toughness. A thermal treatment may relieve some of this stress although coarsening of the lath size should be avoided. However, the expansion and contraction of the weld overall is thought likely to be of greater significance than the expansion due to martensite formation. One reason for this is the relatively low carbon content in automotive steels, typically less than 0.2wt%. This low carbon level means that the distortion of the lattice during martensite formation will be low and thus the stress induced by the transformation correspondingly low. Martensite

is common in all but very low carbon steel welds because of the fast cooling rates that the process generates. If its presence is to be tolerated or used to mechanical advantage the properties generated and the method of controlling them needs to be fully understood.

2.2.2 High Strength Steels for Automotive Applications

A greater understanding of the role of complex alloy compositions and microstructures combined with improvements in thermo-mechanical process control have yielded several important classes of high (yield strengths > 200MPa) and ultra high strength steels (yield strengths > 550MPa) that have potential within the automotive sector.

High Strength Low Alloy Steels

HSLA steels make use of potent, so called micro-alloying elements such as niobium, titanium and vanadium[38]. These elements have a dual role as ferrite grain refiners and precipitation hardeners. The increased strength afforded by both these mechanisms means that alloys with high strengths can be achieved with very low carbon levels. Properties of HSLA steels include high yield strengths and good formability. It is also stated that they have good weldability characteristics due to the low carbon equivalent values.

Carbon Manganese (CMn) Steels

This grade of steel depends on a number of different strengthening mechanisms to optimise its mechanical strength with minimum consequence in terms of formability[38]:

- A fine ferrite grain size
- Solid solution hardening from the manganese
- The relative proportions of the ferrite and pearlite in the two phase structure
- The interlamellar spacing of the pearlite.

Despite the strengthening effect of the pearlite, the carbon content is kept relatively low (~0.2%) to prevent a reduction in toughness and also in an attempt to produce satisfactory weldability characteristics.

Corus[39], in their handbook for the product 'Tenform,' consider that the two main advantages of this type of steel are that the output from each tonne of steel can be increased and that products can be made stronger, lighter and safer under load. The product range is characterised by high yield strengths (250-350MPa), low yield strength to tensile strength ratios and excellent formability.

Dual Phase Steels

Dual phase steels are so called because of their microstructure, which consists of a soft ferrite matrix containing a proportion (usually around 20%) of hard martensite islands. This combination of phases provide the steels with properties that make them highly attractive to the automotive sector, namely continuous yielding behaviour, low yield to tensile strength ratio and a high rate of work hardening. It is the high strength combined with high formability that makes this range of steels a desirable choice for use in the down-gauging of automotive components[5-7].

It is thought that the strength is increased by the presence of high dislocation densities at the interface between the ferrite and martensite phases. Further, it is generally thought that the strength is linearly proportional to the volume fraction of martensite in the structure. Work by Furukawa et al[40] illustrates this point. In their study on a 0.12%C-2.0%Mn steel, the volume fraction of martensite, developed at different quench temperatures, was measured and the plot of this data has the same shape as that of the tensile strength curve.

The formability of dual phase steels is high but they also have a high rate of work hardening, which leads to the most favourable distribution of strains during forming, particularly of complex parts. This prevents excessive localised forming which may otherwise produce failure.

The manufacture of dual phase steels is generally achieved in one of two ways[41]:

- Continuous annealing of cold-rolled strip
- Accelerated cooling during hot strip-mill rolling of steels to be used in as-rolled strip.

In the first method the steel is reheated into the two-phase $\alpha + \gamma$ region using a temperature that facilitates the formation of approximately 20% austenite. Austenite contains a high carbon content due to its atomic structure and, providing the subsequent cooling rate is high enough, will transform into martensite. Alternatively, the desired microstructure can be achieved on the run out table via stepwise cooling. Figure 2.8[42] shows an example of how a steel is cooled until there has been ~80% transformation to ferrite and then the temperature is dropped below the martensite start temperature allowing the desired 20% martensite to form.

The temperatures at which the above heat treatments are carried out affect the proportion of second phase that is developed and further, the chemistry interacts with the thermal process to provide a variety of final microstructures. Mondal and Ray[43] took three steels of different compositions and determined the relative phase proportions on heat treatment. It was found that the different alloys produced increasing amounts of martensite, which appeared to be in line with the carbon equivalent of the steels. Further, for a given composition, the volume fraction of martensite increased with increased intercritical annealing temperature. Further work in this area has been done by Hillis et al[41]. These trends emphasise that composition will be an important consideration when developing a robust welding schedule for dual phase steels.

Another development in the area of dual phase steels is that of ferrite + bainite microstructures as opposed to the more common ferrite + martensite. Sudo et al[44] investigated the properties of a Niobium bearing steel containing ferrite with 10-20% bainite instead of martensite. They found that developing bainite as a second phase, through a reduction in the cooling rate used during processing, led to improved properties such as hole expansion, Charpy impact and flash butt welding characteristics.

Complex Phase Steels

There is little published work available on steels with microstructures consisting of three or more phases, or complex phase steels. The term complex phase sometimes relates to steels that have a proportion of retained austenite, in addition to ferrite and bainite[43], leading to transformation induced plasticity strengthening (TRIP – see next section). Alternatively it is used to describe steels where bainite is formed in the structure, along with the martensite and ferrite[45, 46]. Bainite is not as hard or brittle as martensite so its presence makes for a tougher microstructure. In the former example[45], a cooling path that allowed bainite formation was necessary to allow sufficient carbon enrichment of the austenite. This depressed the martensite start temperature below ambient and the austenite was retained without having to use expensive, high alloy chemistries. Kim et al[46] found that the substitution of martensite with bainite significantly improved the ductility of the steel without greatly affecting the strength. For example, an increase of approximately 10% in strain to failure, from TP1 to TP4, with a loss in strength of only 50 Nmm^{-2}, was found between an alloy containing 1% bainite-15% martensite compared to one containing 15% bainite-1% martensite.

Transformation Induced Plasticity (TRIP) Steels

TRIP steels make use of retained austenite in the steel microstructure that is present in a chemically unstable state. This austenite transforms to martensite on deformation leading to increased strength in the deformed steel. The result is a steel with a high final strength with improved ductility compared with other steels of a similar strength. An additional advantage is that the retained austenite can promote crack tip blunting through a localised TRIP mechanism[47]. Sakuma et al[30] found that a TRIP steel had better fatigue strength than a dual-phase steel of a given tensile strength, possibly due to this mechanism.

2.2.3 Microstructure – Property Relationships in Welded Steels

It is clear that the microstructure of advanced high strength steels, such as dual phase grades, is central to the improved properties exhibited by such grades. However, welding processes produce significantly altered microstructures compared to their unwelded counterparts. The changes vary depending on location within the weld. For example, in the centre of a spot weld the prior-welding microstructure is obliterated by the melting and solidification of the nugget material. The heat-affected zone also reaches peak temperature high enough for solid state phase transformations to take place but the peak temperature will vary with distance from the weld centre.

The range of microstructural constituents present in welded steel has been investigated extensively but the majority of work considering resistance spot welding has been carried out on high strength low alloy steels and plain carbon manganese grades and not on modern dual phase grades. Indeed, much of the work considering complex steel compositions relates to arc welding processes. It has been commented[48] that the complex microstructures developed through welding processes are difficult to quantify due to the mixture and fine nature of the microstructural constituents present. These effects are likely to be increased by resistance welding processes where cooling rates are higher.

Both Williams[49] and Chandel and Gaber[50] considered the effect of prior microstructure on the transformation constituents developed in welds. Williams[49] stated that a parent structure of ferrite and pearlite causes austenite to form in the pearlite on heating, and to spread out radially. The work also commented on the role of stress in microstructural development within welds noting that the localised heating and cooling during welding can cause local stresses that increase the chance of martensite formation even in low

carbon steel. Chandel and Gaber[50] considered the resistance spot welding of bainitic and martensitic steels. They found that softening of the heat-affected zone of spot welds was more pronounced in the bainitic and martensitic steel than for annealed or cold worked low carbon grades. This seems sensible as these microstructural constituents are susceptible to tempering at the temperatures developed in heat-affected zones and this could lead to softening compared to the parent material.

The presence of carbides in the prior-welding microstructure was considered by Savage et al[51]. They found that fine carbides dissolve on heating more rapidly than large carbides. The result of partial dissolution of carbides is a gradient of carbon concentration around the carbides that can have a detrimental effect on the final microstructure of a heat affect zone. It was found that the high carbon concentration around carbide particles can lead to a network of martensite on transformation potentially resulting in low toughness. The following equation describes the diffusion distance, d_o as:

$$d_o = 4\sqrt{Dt} \qquad [2.10]$$

Where D is the diffusivity of carbon and t is the time at temperature of an area of material. It was determined that the distance between two particles needed to be twice the value of d_o to prevent a martensite network from forming.

The range of microstructures in welds is similar to those defined for strip steel but the faster cooling rates found in welding compared to, for example, the hot mill run-out table, result in much finer constituents forming. A comprehensive review of the ferrite constituents that form during welding has been carried out by Dunne[34] and a more general review, considering the effect of all aspects of microstructure by Grong and Matlock[52]. Dunne considers the different ferrite morphologies observed in welded steel and notes that there are three prominent classification systems currently in use as well as many further systems devised by individual researchers. An attempt to standardise the classification of weld constituents has been attempted by the International Institute of Welding[53] and includes the following classifications: Polygonal Ferrite (Grain Boundary); Polygonal Ferrite (Intragranular); Ferrite with a Second Phase (Side Plates / Non-Aligned / Aligned); Acicular Ferrite; Martensite. Bainite, both upper and lower are contained within the ferrite with a second phase classification and there is no equivalent to the irregular, large ferrite phase known as quasi-polygonal ferrite[34]. Clearly, whilst a catch-all

classification system provides a reference point for researchers in the field of weld metallurgy it is likely that locally defined systems will remain helpful in describing the constituents observed in steel welds. Further, standard classification systems are based on work on low alloy welds and the constituents present in higher alloy grades may not fall within the system as it is defined.

As for strip steels, composition has an effect on the transformation products found in welds, partially through the effect of alloying elements on the transformation start temperatures. Several papers have considered the effect of manganese on weld transformations[54, 55] and it has been found that increased manganese additions decrease the transformation start temperatures as for strip steels. Other alloying elements, such as carbon, also have similar effect in weld materials. The effect of microalloying elements has also been investigated[56, 57]. Harrison et al, in both these papers, consider the effect of niobium on arc weld microstructures and found that increased niobium additions refined the weld microstructure and promoted the acicular ferrite content. A similar effect has been found for titanium additions of 30ppm[58] within arc welds. This work also considered other microalloying elements and reported that niobium in isolation provided some improvements in impact energy but, when added in conjunction with 35ppm of titanium, a significant drop in energy was observed with increased niobium additions. Clearly both solid solution alloying elements and microalloying elements have a role in the final microstructure of weld metal. The trends observed in low alloy steels need to be compared to the results in higher alloy, modern high strength steels.

The high cooling rates present during welding have been considered by many researchers[49, 54 – 57, 59] and all have reported a significant effect on microstructure with an increased cooling rate, similar to that found for strip steels. Most CCT diagrams available consider temperatures up to a few hundred degrees centigrade whilst resistance welding temperatures have been reported to be as high as $1x10^5$°C/s. Clearly it is important to establish the range of relevant cooling rates and associated microstructural response in modern ferrous alloys.

Prior austenite grain size has also been mentioned by several researchers[49, 52, 56] who noted that a large prior austenite grain size can have the effect of decreasing the transformation temperature. In addition, Harrison et al[60] reported that a reduction in the

prior austenite grain size provides more grain boundary sites for nucleation and that the result was an increased volume fraction of polygonal ferrite. Conversely, as the prior austenite grain size decreases, nucleation at grain boundaries is less likely and an acicular ferrite constituent predominates.

The effect of changes in weld microstructure on mechanical properties is, in the main, expressed as an effect on hardness, sometimes considered in conjunction with CCT diagram development. An example is Abson[48] who showed that an increase in cooling rate, for a C-Mn steel alloy, significantly increased the measured hardness. One study has considered the toughness of C-Mn arc weld material[60]. In this work, Farrar and Harrison presented the concept of an 'optimum toughness regime.' This was defined on a plot of alloy addition, for example Mn, vs. cooling rate and considered to be the cooling rate and composition combinations that resulted in weld microstructures containing acicular ferrite. Pearlite and martensite were considered detrimental to impact toughness. It was found that an increase in Mn content pushed the optimum toughness regime to lower cooling rates and correspondingly, faster cooling rates reduced the Mn range at which the acicular ferrite zone existed.

The wide range of influences present during welding clearly has a considerable effect on weld microstructure. The important influences can be summarised as: alloy content; nature and distribution of non-metallic inclusions; the prior austenite structure; the thermal cycle including peak temperature and cooling rate.

2.3 Continuous Cooling Transformations

Continuous cooling transformations (CCTs) are distinct from isothermal transformations in that the time at temperature is dictated by the cooling rate that a sample is exposed to. Welding is a typical process where an understanding of CCT behaviour is important as the practicalities of welding mean that isothermal transformations cannot be applied and weld microstructures are thus a function of their cooling rate. For arc welding the use of weld pretreatments can assist in the control of cooling rate but the practical use of similar techniques within resistance spot welding has not been exploited commercially.

This section considers the principles behind the monitoring of CCTs and their visualisation through the use of CCT curves or diagrams. The nature of continuous cooling thermal cycles and diagrams applicable to welding are considered along with attempts that have been made to quantify such transformations in practical welding situations.

2.3.1 Continuous Cooling Transformation Curves

Continuous cooling transformation (CCT) diagrams are a visual representation of the transformations that take place in a continuously cooled sample of material. Once constructed they can be used to predict the microstructure of a sample at any cooling rate covered by the diagram. For resistance welding the cooling rates are expected to be high, potentially several thousands of degrees centigrade. However, it is important to characterise the full range of a material's behaviour in order to establish any potential for modification of microstructure through the control of cooling rate.

The principles of CCT curves were laid down by Christenson et al in 1945[61]. Since then, many attempts have been made to refine the technique and provide different means of access to the CCT behaviour of a material, through the use of, for example, modelling techniques.

Farrar and Zhang[62] carried out experimental verification of CCT curves produced through a combination of dilatometry experiments and metallographic examination. Dilatometry involves making sensitive measurements of the expansion and contraction of a sample of material on heating and cooling. Arrests in the linear expansion or contraction indicate a

phase transformation and several experiments can be carried out to build up a plot covering the temperatures of transformation at a range of cooling rates.

Modelling attempts have been made to predict CCT curves[63] and some researchers have combined experimental and mathematical modelling techniques[64]. The former model[63] made use of artificial neural networks which, 'learnt' the rules for predicting the curves, based on steel chemistry (12 elements), from previously determined curves. The results were deemed "satisfactory" but a precise match was not possible. The reason given for this was the small dataset available for 'training' the network.

The work by Mesplont et al[64] used a single sample and subjected it to multiple thermal cycles. The magnitude of the thermal expansion during each cycle was related mathematically to the thermal expansion of each individual phase and the volume fraction of a given phase thus calculated. The A_3 and A_{cm} temperatures were predicted using ThermoCalc software. The model was validated by comparing the measured hardness values with those calculated using the volume fractions of microstructural constituents predicated by the model. The agreement between these two values was considered good. However, there are a number of concerns regarding the use of this model. The model has only been tested on one grade of C-Mn steel raising questions about its applicability to more complex alloy systems. In particular, validation of a model based on hardness would be questionable in an alloy, such as some dual phase grades, that combine microalloying with solid solution strengthening. The model made use of only one sample for all its experiments and this was considered favourable due to possible variations in the carbon content between samples leading to variations in the measured dilations. However, slight variations are likely in production grades and any technique used to monitor CCT behaviour in such alloys should be robust enough to establish trends in behaviour regardless of practical variations in such parameters. The austenitising treatment used for the CCT experiments was 2 minutes at 1200°C, which may, as mentioned, result in an equivalent austenite microstructure for each cycle. However, no measurements of prior austenite grain sizes were given.

Several dedicated dilatometers exist for the production of CCT curves. A common limitation with respect to a strip steel specimen is the required sample size. For example, the quench dilatometer used by Manohar[65] required 3.2mm diameter cylinders and 4mm

diameter samples are common. The use of strip steel samples of up to 2mm, typical thicknesses for high strength automotive grades, requires the use of a more versatile machine. A Gleeble thermomechanical simulator can provide this flexibility, as described in its manual[66]. It has been widely used for CCT production, two examples being Vass[67], who used it to determine CCT diagrams for rotor steels and Storer[68], who used it to simulate the CCT behaviour of arc welds in low alloy weldments.

2.3.2 Application of Continuous Cooling Transformation Curves to Welding

Continuous cooling transformation curves can be used in conjunction with a number of different heating processes including hot rolling, annealing as well as welding processes. However, the thermal cycle used to produce the CCT curve is critical to ensuring the applicability of the curve to the chosen process.

One of the most important factors to be considered is the prior austenite grain size, that is, the grain size at the time of first transformation from austenite. Many studies have considered the effect of prior austenite grain size on the transformation start temperature or AR_3 for hot rolling and annealing processes. For example, Yamamoto et al[69] found that a ten fold increase in the prior austenite grain size, from 20 to 200 microns, decreased the AR_3 temperature by around 50°C at a cooling rate of 0.5°C/s. However, this effect had reduced to a difference of only a few degrees at a cooling rate of 30°C/s. Sun et al[70] found that an increase in austenite grain size from 15 to 60 microns decreases the AR_3 by approximately 30°C at cooling rates between 2 and 15°C/s.

The austenite grain size can be controlled in two main ways: through a change in the temperatures used at part of a heat treatment or through a change in the time held a single temperature. Matsuzaki and Bhadeshia[71] subjected two C-Mn steels, one with additional Si and one with Cr additions, to a treatment consisting of: a peak temperature hold of 600 seconds; a further hold at 800°C for 600 seconds; transformation to bainite at 450 or 435°C; a cool to room temperature. The peak temperature was varied between 1000 and 1300°C and this variation was seen to increase the grain size by approximately 200 microns, from 80 microns at 1000°C to 290 microns at 1300°C.

Wilson and Howell[72] considered the grain coarsening characteristics of niobium alloyed steels and in particular used a range of austenitising temperatures from 900 to 1300°C.

Overall there was an increase in the prior austenite gain size with an increase in temperature but the increase could be split into three regions on the plots. The low temperature region lies between 900 and 1025°C, varying slightly with Nb content, during which there is a small increase of around 40 microns in the austenite grain size. In the second region some abnormal grain growth starts to take place, between around 1025 and 1100°C. In the third region abnormal grain growth continues leading to austenite grain sizes in excess of 200 microns at an austenitising temperature of 1300°C. This clearly shows the effect of both an increase in temperature and the intervention of microalloy precipitates until critical temperatures are reached.

The effect of time on an isothermal hold was investigated by Militzer et at[73]. They used temperatures of between 950 and 1150°C and measured the grain size after different hold times. They found that there was very little grain growth at 950°C regardless of the hold time. An increase to 1000°C still resulted in an increase in austenite grain size of only a few microns up to a hold time of 100 seconds after which sizes of up to 100 microns were observed. Higher temperatures of 1050 to 1150°C resulted in increasing grains sizes up to a maximum of approximately 200 microns for the 1150°C hold temperature after 400 seconds.

There are many studies considering CCT curves in conjunction with welding processes with the work predominantly being concerned with arc welding. The importance of a relevant austenite grain size on the validity of a CCT curve has been mentioned[62, 74]. In these studies the emphasis experimentally is on the peak temperature as the cause in of a change in AR_3, rather than the corresponding austenite grain sizes. One extensive early study[75] considers the effect of peak temperature without reference to austenite grain size. This work discussed the idea of a critical cooling time, C_f, that indicates the fastest 800-500°C cooling time that still resulted in a microstructure containing some proeutectoid ferrite. This parameter was found to be a reliable index of weld ductility and toughness for the steels in the study. It is difficult to derive the effect of grain size in this work as distinct from the effect of peak temperature. However, the prior austenite grain size is important as a reduction in grain size increases the volume fraction of grain boundaries available to provide nucleation sites for transformation. As discussed earlier, this can have a significant effect on the transformation products, for example, resulting in bainite rather than acicular ferrite.

Clearly the thermal cycle and austenite grain size used to produce a CCT curve for use in conjunction with welding is important. For heat-affected zones this could mean attempting to produce large prior austenite grains to simulate the grain coarsened heat affect zone in an arc weld. For resistance spot welding, obtaining a fine enough austenite grain size is likely to be the key issue.

Simulating the thermal conditions for a weld nugget where the material has melted and resolidified is more complex. The columnar grain structure typically seen in spot weld nuggets is a result of the strong, almost linear cooling effect of the water cooled electrodes. In stand alone dilatometers and the Gleeble melting of samples is difficult and the uni-directional cooling cannot be achieved.

One solution to the issue of monitoring solidification followed by solid-state transformation was suggested by Wen et al[76]. In this work, molten metal droplets were dropped onto a pair of thermocouple tips that were sealed into the base of a ceramic cup. The temperature changes could thus be measured during solidification and subsequent solid state transformation. This method provided some information about transformation start temperature but the range of cooling rates possible was low at only 10 to 40°C/s. These rates are possibly suitable for arc welding simulation but not resistance spot welding and the control in the technique is limited. Further the samples were too small to allow meaningful metallographic examination or mechanical testing to take place after cooling.

2.3.3 Monitoring Cooling Conditions during Welding

One noticeable omission from many published reports on CCT behaviour during welding is evidence of attempts to directly monitor the thermal cycle generated by the welding schedule. This view has been mentioned only once[74] with the author noting that many experimental conditions were selected on a trial and error basis. A means of monitoring temperature during welding would not only provide information for use in conjunction with CCT curves but also provide evidence of the effect of variations in weld schedule on thermal profile. This could be particularly important when considering advanced welding schedules such as pulsed welding or controlled cooling.

Some researchers of arc welding have attempted to monitor thermal profile with thermocouples inserted into weld specimens at key positions near to the weld line. For example, Winarto[77], in work on MIG welding of aluminium alloys, made use of thermocouples placed in drilled holes in the plates being welded, to accurately determine the temperatures generated. The key point was that the thermocouples used were not seen to have any adverse effect on the temperature measurement by virtue of their presence. Kerry et al[59] were more concerned with the weld pool conditions and monitored the cooling cycle by "plunging a thermocouple into the weld pool once the heat flow had reached a steady state." The temperature was then logged as the thermocouple was frozen into place and the weld cooled. A disadvantage of this technique is that no information can be gathered about the heating portion of the welding process, which could be important, as mentioned above, for understanding the effect of advanced welding schedules on thermal profile.

Many researchers have warned against the use of thermocouples, as it is believed that a foreign object would alter the temperature distribution developed during welding by virtue of its presence. Indeed the thermocouples used in arc welding trials can be several millimetres in diameter, which would be impractical for use in a spot welding trial involving only 2mm thick steel strip. However, there are some examples of thermocouple use in resistance spot welding: the work of Nishi et al[19]. In this work, 0.1mm thermocouples were used to determine the temperatures found in the heat-affected zone during the spot welding of thin gauge mild steel strip. It was suggested that heat flows more to the electrodes during the hold time of the cooling cycle but it was not thought, by the authors, that this invalidates the method.

A model developed by Han[78] used finite difference formulation of the heat equations to predict temperature distributions as a function of time and location within a spot weld. The actual temperatures were measured experimentally using carefully placed thermocouples that were attached to the top plate of the two coupons, in a machined groove and fixed with a spot weld. The slots were machined to end in the heat-affected zone and the position of this was determined by metallography on some trial samples. Overall "acceptable" agreement was found between the practical results and those predicted by the model in terms of nugget size.

An attempt at calculating the thermal cycle during laser welding of dual phase steels was carried out by researchers at Corus[79] in which the peak temperatures in the heat-affected zone were found to be very sensitive to the distance from the nugget centre. At a distance of 0.75mm from the centre of a 0.50mm weld nugget the peak temperature was found to be approximately 850°C. However, no experimental validation of this prediction was available.

An alternative to thermocouple measurement is indirect temperature measurement, an in-depth review of which has been previously carried out[80]. It was considered that one of the most advanced methods available was the use of a thermal imaging camera, to detect temperature distributions at the edge of a spot weld during production, combined with metallurgical examination to infer the actual temperatures experienced. This technique has an advantage in that it is fairly simple in nature and does not require any special set up in terms of making the spot welds. However, a key disadvantage is that the information generated does not give precise temperature measurements at different points within the spot welds.

2.4 Mechanical Testing of Sub-Size Specimens

The measuring of mechanical properties is, where possible, always carried out using standard tests in order to allow comparison with other researchers' results. However, where the amount of material available for testing is not enough to produce a standard test specimen alternative tests are required. This section considers the alternatives that are available to standard tests and the material dimensions that would be required to make use of them.

2.4.1 Hardness

As discussed in section 2.1.3, hardness is a test commonly used to monitor mechnical properties in welded samples due, in the main, to its simple nature. The hardness of welds has been shown to have a relationship with other properties such as toughness[30], ductility ratio[24] and failure mode[20]. Within welding, microhardness measurements are more commonly used than bulk hardness measurements. Microhardness usually refers to measurements made with loads of less than 1kg and typically between 100g and 500g. Figure 2.3 gives an example of how microhardness measurements were used to monitor the effect of post weld heat treatments on the properties of resistance spot welds.

2.4.2Yield and Tensile Strength

The tensile properties of a material are normally assessed through the use of a uniaxial tensile test. The standard gauge length used in the tensile machines at Corus' Welsh Technology Centre is 80mm. However, some work has been carried out considering a significantly shorter gauge length of 10mm[81]. The research found that there was a good relationship between the 10mm and 80mm ultimate tensile strength results. The empirical relationship can be expressed by the equation:

$$UTS_{80mm} = 0.96\ UTS_{10mm} + 12.48 \qquad [2.11]$$

The confidence limit for this relationship was found to be 98%. The elongation determined from the 10mm gauge length test had the following relationship with the full size result (90% confidence limit):

$$elongation_{80mm} = 1.18\ .\ elongation_{10mm} + 10.21 \qquad [2.12]$$

It appears that it is possible to use the results from a miniature tensile test to compare properties with a full size test but these tests did not include any dual phase type steels and it is unclear if this would affect the relationships presented. The use of miniature tensile tests for dual phase steels is also dependent on a machine suitable for testing them

being available, that is, a machine with a small enough extensometer for monitoring elongation but a high enough load cell to cope with the high strengths involved.

An alternative to the miniature tensile test is the miniature disc bend test. Two different apparatus have been suggested for use in this type of testing[82 - 86]. Hoffman and Birringer[82] and Li et al[83] described equipment that could be used to test 3mm diameter discs of material with thicknesses between 0.2 and 0.6mm. They found from tests on NiAL samples that the disc bend tests could produce a reasonable value for the Young's Modulus. One concern with the use of this method for dual phase steels is that the small amount of material within a sample means that small areas of potentially brittle second phase could have a disproportionate effect on the results. A larger test piece would provide a more representative sampling of the dual phase microstructure. Li et al[83] determined that 0.2% proof stress could be accurately determined using 3mm disc tests. They did, however, stress that homogenous samples were necessary for reproducible results, emphasising the concern presented above. Interestingly, they did not consider the accurate centering of the discs in the test equipment to be of importance for accurate testing.

A test using larger discs has been described by Norris and Parker[84] and also used by Lewis[85] and Lewis[86]. Norris and Parker[84] used a 9.5mm disc and considered the effect of disc thickness, punch diameter and die clearance on the results produced by the test. An increase in disc thickness from 0.5 to 1mm was found to increase the ultimate tensile load (UTL) and yield loads. Increasing the punch diameter from 2 to 4mm had no effect on the yield load but a significant effect on the UTL. A decrease in the clearance between the punch and die was found to increase the UTL.

It is important that this test makes use of larger samples, which would allow a more representative sample of the dual phase microstructure to be tested. However, Norris and Parker noted that repeatability was better for pure copper and aluminium samples than for the low alloy steel. Lewis[85] successfully carried out disc tests on IF steels that have a very low solid solution alloy content and rely instead on microalloying. Lewis[86] found that experiments in line-pipe grades were more accurate in the thicker 1mm discs tested compared to the 0.5mm discs that were tested. For example, the UTS predicted from the tests was found to be accurate to ±1.5% in the 1mm discs compared to ±4.5% for the

0.5mm tests. There is potential for the use of this test. However, the suitability of disc tests for use with advanced steel alloys with complex alloy compositions and microstructures needs to be established.

2.4.3 Impact Energy

Microstructure has been shown to have a significant effect on both impact energy[35] and in fracture toughness[87]. A standardised test for measuring impact energy is the Charpy V-notch test. The European standard EN 10045[88] defines the standard test specimen as 10mmx10mmx55mm. As the impact properties of rolled thin gauge strip steel need to be determined, a standard specimen, as laid out in EN 10045, will not be possible. Sub-size specimen dimensions have received some attention from researchers. For example there were three papers covering the issue at the Charpy Centenary Conference[89]. It is clear that a variety of subsized specimens are possible but that relating the results to standard size specimens is more complex for very small samples. Indeed samples with a cross section of 0.7mm square were called into question at the conference mentioned. For reasons of representative sampling, as described above, very small samples are not desirable when testing dual phase steel. The final dimensions selected will be dependent on the material availability.

3. PROGRAMME OBJECTIVES

The review of literature indicates the sensitivity of steel alloys to the thermal cycles generated during resistance welding, including such parameters such as peak temperature, time at temperature as well as the high heating and cooling rates typical of this process. The production of dual phase steels, in terms of their chemistry and processing route is well established but the subsequent effect of welding processes on the microstructures generated, and the associated effect on properties has not been covered to any significant degree. Further a detailed, systematic evaluation of resistance spot welding conditions and their influence on thermal cycle has not been carried out. These knowledge gaps may limit the widespread application of dual phase steels. Clarification of these issues will afford manufacturers greater confidence in the selection and use of these advanced steel grades, which not only assists in meeting the demands of their customers, but also offers potential savings in overall material costs. In addition, information regarding the potential benefits of desirable thermal cycles can be incorporated into the design of procedures for other welding processes, such as laser welding, as they become more prevalent in manufacturing operations.

Considering these issues, and based on the review of literature, the specific objectives of this research programme were defined as:

1) Establish the nature of resistance spot weld microstructures in dual phase steels compared with those in mild steel grades, made using single pulse weld schedules. In particular, determination of the influence of alloy chemistry on the transformation products present in resistance spot weld microstructures.

2) Investigate the continuous cooling transformation behaviour of selected dual phase steels under conditions that represent potential thermal cycles experienced by welded material. This should include:
   a) Development of a technique to be used in conjunction with a Gleeble 1500 and 3500 that allows the production of continuous cooling transformation curves from strip steel samples.
   b) Determination of suitable conditions for the production of continuous cooling transformation curves.

c) Assessment of the influence of cooling rate and alloy composition on the microstructure of dual phase grades and a mild steel grade for comparison.

3) Measurement of the relationship between the range of continuously cooled microstructures possible in dual phase grades and the mechanical properties. This should cover:
   a) Hardness
   b) Impact energy
   c) Tensile properties

   As a result of the Gleeble technique the amount of material available for testing will be small and suitable techniques for measuring the impact and tensile properties of sub-size specimens will need to be developed.

4) Investigation into the influence of weld schedule on the thermal profile of the resistance spot welding process. This will require the development of a technique to measure temperature accurately during spot welding in both the weld nugget and heat-affected zone areas. As well as conventional, single pulse welding, advanced welding schedules to be considered should include:
   a) Pulsed welding
   b) Controlled weld cooling
   c) Post weld heat treatments (tempering)

5) Relate the findings of the laboratory based research programme to the likely performance of resistance spot welds in body-in-white applications.

Overall, this programme is designed to highlight some of the important relationships between the two fields of ferrous metallurgy and practical resistance spot welding, in order that the route to optimisation of spot welds, in advanced high strength steel alloys, can be established.

4. EXPERIMENTAL PROCEDURE

A wide range of experimental techniques was employed during this research programme including:

(a) A technique allowing the superior thermal control, offered by the Gleeble series of thermomechanical simulators, to be used with strip steel samples. In conjunction with detailed metallographic examination, this was used to generate continuous cooling transformation curves.

(b) Mechanical tests to determine the effect of different continuously cooled microstructures on mechanical properties, using smaller than standard size test pieces.

(c) A novel method of monitoring the thermal profiles developed during resistance spot welding, which allowed the effect of varying weld schedules, on the temperatures and cooling rates generated, to be evaluated.

The welding, both the benchmarking work and the temperature datalogging was carried out using a pedestal resistance spot welder that is typical of that found on an automotive sub-assembly manufacturing line. The following section describes the materials selected for the investigation and gives details of the experimental techniques used.

4.1 Materials

Six steels were selected for this investigation. Two were Corus products (LC and LCNb) and the other four (DP600 – DP1400) were commercially available dual phase steels. The dual phase designations are industry standard terminology with 'DP' indicating a dual phase grade and the following number the nominal tensile strength. LC refers to a low carbon, mild steel grade and LCNb to a low carbon grade with a level of niobium microalloying comparable to that of the higher alloy dual phase grades (0.016wt%). The overall aim was to characterise behaviour for dual phase materials. However, the primary means of selection within the range of steels available involved choosing grades with different carbon equivalent values. As discussed in the literature review, carbon equivalent (CE) has often been used as an indicator of weldability. The CE of the six materials selected, calculated using the Ito-Bessyo equation[33], ranged from 0.04 to 0.27. The chemical composition and the CE of each grade are detailed in Table 4.1. The chemical composition analysis was carried out by the Basic Oxygen Steelmaking laboratory, at Corus, Port Talbot, using a combination of optical emission and combustion analysis.

Two of the materials, LC and LCNb, were included in the study as references. LC is a plain carbon steel with 0.04wt%C. LCNb is a low alloy grade, with 0.05wt%C and 0.40wt%Mn and also 0.016wt%Nb. This steel grade was used to evaluate the effect of microalloying on the continuous cooling transformation experiments performed. The dual phase steels have increasing carbon contents (0.103 to 0.163wt%) with increasing grade number. The DP600 also contains Mn (0.5wt%) and Si (0.32wt%) but no microalloying whereas the other three (DP800 to DP1400) have Mn levels around 1.5wt%, Si levels around 0.5wt% and Nb levels around 0.02wt%, in addition to the increasing carbon content. This combination of compositions allowed the effect of increasing carbon, manganese, silicon and niobium on the continuous cooling transformation (CCT) behaviour and weld microstructures to be examined.

The materials used for this programme are production grades and were received in one of the thicknesses typically used for automotive applications. The thicknesses were 1.6mm, 2.0mm, 1.8mm, 2.0mm, 1.2mm and 1.0mm for the materials LC through to DP1400 in increasing carbon content respectively.

The mechanical properties are summarised in Table 4.2. The properties were measured using samples with an 80mm gauge length and overall dimensions of 20mm x 120mm. The tests were carried out according to BSEN 10002: Part 1(1990) using a Zwick 1474 test machine. The load cell used was 100kN and the machine was calibrated to UKAS standards. The speed used up to the 0.2% proof stress was 2.5mm/min and after this point 50mm/min. Four samples were tested, two taken from the rolling direction of the supplied sheet and two perpendicular to the rolling direction. The average of the four tests is presented in Table 4.2. The tensile strengths ranged from 195MPa to 1463MPa and the 0.2% proof stresses from 166MPa to 1335MPa. This represents a wide range of properties that could potentially be used in body-in-white applications.

4.2 Manufacture of welded coupons

4.2.1 Weld Equipment

An IIW investigation[90] reported that the measured weld lobe for a given material can be affected by the equipment used. Therefore, full details of the welding equipment and schedules will be given.

All the welding was carried out using a 75kVA Sciaky pedestal resistance welder, Figure 4.1. This is an automatic, foot operated welding machine with electrodes mounted vertically and the electrode force generated by an air cylinder mounted on the top arm. The machine has six transformer tappings and for this work tap five was used. This represents an available voltage of 6.5V and a maximum current availability of 33kA. Portions of this available current can be used by actually applying current to the electrodes for only a given proportion of the time for which it is available. This is achieved by programming in the number of cycles, out of a maximum of 100 that the current should be applied for, with one cycle actually representing 0.02s in time. The electrodes were cooled using a forced water circuit with the water flow rate set a 5 litres/min. The electrodes used were truncated cone, Cu-Cr-Zr with a 120° included angle and the tip diameter varied depending on the thickness of the steel being welded. The stroke was set at 22mm. These parameters are summarised in Table 4.3 and the electrode tip sizes are given in Table 4.4.

The force was set at 4.2kN for these experiments. This is slightly higher than might typically be used in on-line manufacturing equipment, with typical forces being 2-3kN. However, this force was selected, based on previous experience, so that consistent welds could be produced in the full range of materials. A Maltron weld force probe gauge (98558) was used to set the force at the desired level and also to regularly check that there had been no deviation from the set level. The measurements were accurate to +/- 0.5% of the actual force and an in-built signal control negated the effect of initial shock loads when the electrodes closed.

The welding schedule was programmed using a British Federal Digital Weld Control Type S3HUB/2. This allowed the pre-squeeze, squeeze, weld time and hold time to be set along with a value known as the phase shift, which controls the applied current. The first four parameters are programmed in cycles where 1 cycle is 0.02 seconds. The squeeze

time is a short contact time for the electrodes before the current is applied. A pre-squeeze is slightly different in that it is a squeeze applied before a combination of pulses is used whereas a squeeze is applied to each individual pulse. The pre-squeeze is made use of during pulsed welding (see below). The phase shift is a percentage of the available alternating current and, by varying this setting between 1 and 99, the percentage of the sinusoidal current wave form, for which the current is applied, is varied. In order to measure the actual current applied at a particular setting a Miyachi Weld Tester (315A) was used. This meter had a toroid attached that sat around the lower electrode mount, which allowed it to measure the secondary root mean squared (RMS) current. The meter was accurate to +/- 2% and the reading for each weld was given via a digital display. For single pulse welding the current readings could be taken at the end of weld production. However, as there was no logging facility for this meter, for pulsed welds and post weld heat treatments the display had to be monitored throughout welding in order to capture the magnitude of each current pulse.

4.2.2. Weld schedules

The actual programmes used varied according to the desired outputs. Details of the currents used are given in Section 6.1 (results from welds). A summary of the programmes used to produce standard welds in each of the six grades is given in Table 4.4. A standard weld size of $5\sqrt{t}$ was used throughout all the welding experiments, where t is the thickness of the steel strip being welded.

Single pulse welding

In order to produce a $5\sqrt{t}$ weld that would provide the base weld that other modified programmes would be compared against a basic, single pulse programme was used. This took the form of:

Squeeze (35) – Weld Time (14) at Heat (B) – Hold Time (25) [4.1]

where the numbers in brackets are measured in cycles. 'B' is the phase shift used (termed 'Heat' on the controller) and, as described above, is programmed as a percentage. The initial weld lobes were produced using a weld time of 14 cycles with B varied from a low setting (given by BS1140 and depending on the steel thickness) to splash, which is where

molten metal is expelled from the weld. The weld size was measured by chiselling open the welds and measuring the visible weld using Vernier callipers. The conditions for the production of a $5\sqrt{t}$ weld were determined from these weld curves and welds made using these conditions were sectioned and prepared using the techniques given in Section 4.4 for metallographic examination. The final weld conditions used for the $5\sqrt{t}$ welds in each of the six materials can be found in Table 4.4. Two variations on this basic programme, using 25 and 50 cycles of weld time were also used to assess the effect on the cooling rate of extending the time of the weld and reducing the applied current. The results of this can be found in Section 6.4.

Multi-pulse welding

Previous experience suggests that by varying the number of pulses used to produce a given weld size the thermal profile across a weld could be modified with a potential effect on the microstructure and properties. To this end, a series of multi-pulse weld lobes were produced for the DP800 grade using the following programme:

Pre-squeeze (35) – Squeeze (0) – Weld Time (X) at Heat (B) – Cool (1) – No. Pulses (Y) – Hold time (20) [4.2]

The parameters X and Y are programmed in cycles and, as before, B is a percentage of the total current waveform actually used. The Cool setting was a short time when the electrodes stayed together but there was no current flowing. For these welds this was set to the minimum possible, 1 cycle. X was set at 7, 2 or 1 and Y was set at 2, 7 or 14 respectively. These programmes of pulses all combined to give a total of 14 cycles of weld time, that is, 2 x 7 cycles, 7 x 2 cycles and 14 x 1 cycles. Combined with the 1 x 14 cycles (single pulse welding) this gave four pulsed welding options to compare. B was increased from a low setting, predicted from the single pulse welding lobes, to the setting that resulted in splash.

The weld size was measured from sectioned, metallographically mounted welds using the techniques given in Section 4.4. The $5\sqrt{t}$ welds were examined in detail and the appropriate settings recorded for use in conjunction with thermal profile measurements (see Section 6.1).

Controlled Cooling and Post Weld Heat Treatments

Further advanced welding schedules that were produced for the DP800 dual phase grade are detailed in this subsection. The cooling rate of resistance spot welds can be modified by the application of small, low current pulses, shortly after the main welding pulse. The additional current is passed before the weld has fully cooled down. The following programme was used to introduce these post weld pulses:

Pre-squeeze (35) – Squeeze (0) – Weld Time 1 (X_1) at Heat 1 (B_1) – Cool (Z_1) – Weld Time 2 (X_2) at Heat 2 (B_2) – Hold time (20) [4.3]

As before, the weld times are measured in cycles and the heat settings are given as a percentage. The parameters X_1 and B_1 are the settings used to create the initial weld pool. Controller limitations meant that it was not possible to use pulsed welding for this initial weld so X1 was set at 25 or 50 cycles and B_1 at 26 or 22. X_2 and B_2 represent the settings for the post weld pulse and the correct values for these parameters, along with the cool time (Z_1) were determined from the thermal profile measurements (see Section 6.4).

A pulsed programme was used, which included two small post weld pulses. It was thought that this might offer greater control of the weld cooling. The programme was:

Pre-squeeze (35) – Squeeze (0) – Weld Time 1 (X_1) at Heat 1 (B_1) – Cool 1 (Z_1) – Weld Time 2 (X_2) at Heat 2 (B_2) – Cool 2 (Z_2) – Weld Time 3 (X_3) at Heat 3 (B_3) – Hold time (20) [4.4]

As before the parameters X_1 and B_1 were set to produce a spot weld and the parameters $X_{2\,\&\,3}$ and $B_{2\,\&\,3}$ were the post weld pulses. For these experiments two separate cool times were required: the time after the weld had been made before the post weld pulses are initiated (Z_1) and the time between post weld pulses (Z_2). See Section 6.4 for details of how these parameters were set.

A further step in the use of advanced welding programmes was the development of a post weld heat treatment that can be applied by the pedestal welder without moving the sample. This differs from the controlled cooling experiments in that the objective was to temper the welds using small pulses applied after the original weld pool had completely cooled as opposed to during cooling. The programmes used were the same as for the

controlled cooling but the values for $X_{2,3}$ $B_{2,3}$ and $Z_{1,2}$ were modified. The values chosen were again a result of the thermal profile work (Section 6.4). An important difference was that the first cool time was set at the maximum of 99 cycles. This was to give the weld the maximum possible time to cool before tempering occurred. The appropriate settings determined and the resulting thermal profiles and weld analysis are given in Section 6.4.

4.3 Control of Thermal Cycle

It was considered necessary to investigate the influence of controlled thermal cycles, on the properties of each steel, for two reasons:

(a) to produce continuous cooling transformation curves

(b) to produce samples, with modified microstructures, suitable for mechanical testing.

4.3.1 Gleeble Operation

For both purposes, Gleeble thermo-mechanical simulators were used. These machines are produced by Dynamic Systems, previously named Duffers Scientific. Two models were employed – the 1500 (Figure 4.2) and the 3500 (Figure 4.3). The basic principles of operation were common to both types and are explained below.

Control of heating and cooling rate

Heating is achieved by passing a controlled current along samples, which are subsequently heated due to the bulk resistance of the material. Heating rates can be varied between 0.002 and 10,000°C/s, depending on sample size, with faster heating rates possible in smaller samples. Careful control of the thermal profile is achieved via a feedback reading from a pair of thermocouple wires spot welded to the centre of the sample. These thermocouples can be type K (Cr-Al) or type R (Pt – Pt/Rh). In all experiments carried out in this programme, type K thermocouples were used which have a temperature limit of 1200°C for long term use or 1300°C for short term use.

The Gleeble 1500 has two pairs of terminals allowing for a control thermocouple and one extra reference pair to be used per test. The Gleeble 3500 has four pairs of terminals allowing for three extra pairs of thermocouples to be used per test.

Vacuum chamber

Samples are contained within a vacuum tank during experimentation. This allows heating to be carried out either under vacuum or a controlled atmosphere such as argon. The vacuum was used where possible. However, during air and water quenching this was not possible (see below). The benefits of working under a vacuum are minimisation of surface oxidation and a reduction in the heat lost via surface radiation.

The chamber for the Gleeble 1500 is open at the top (Figure 4.4) and is sealed with a separate 25m Pyrex glass lid. The Gleeble 3500 chamber is set on its side (see Figure 4.3)

and the lid is attached by hinges at the top of the chamber. For both machines a roughing pump proved sufficient to prevent oxidation and the diffusion pump was not used.

Programming thermal cycle

A computer attached to the Gleeble instrumentation of either model is used to control the applied thermal cycle. The basic language is known as Gleeble Programming Language (GPL) and it allows the required temperature at a series of steps in time to be defined. Further definitions are possible, such as the position of jaws to effect tensile or compressive strains during the heating or cooling cycle, but this was not required for the purely thermal programmes used for these experiments.

In addition to programming the time steps, it was necessary to instruct the Gleeble to turn on the desired systems at the correct times. These were: the general system, heat, mechanical, acquisition and for some tests the two quench chambers. The overall data acquisition rate could be defined for each programme and this divided by the number of channels, which were being acquired. The maximum number of channels that can be acquired is eight. For these experiments the programmed and actual temperatures were logged along with the change in sample size for the continuous cooling transformation experiments. The maximum number of sample points per channel was 32,767 but the rate was varied so that the number of samples for the cooling portion of each test was sufficient to determine the turning points in the dilation curves. This ranged from 0.5Hz for the slowest cooling rate up to 100Hz for the fastest cooling rates.

The Gleeble 1500 computer interface is DOS based and runs on a 386 PC. For this version of the software, a programme was written with each line of a table based programme referring to the desired components, for example, the heating module or the quench tanks, by their numbers in the manual. The updated Gleeble 3500 software has a windows interface and is run on a Pentium III PC. In this software, drop down menus allow components of the machine to be selected.

The output of an experiment is a table of data giving the time, programmed temperature, measured temperature and dilation (where applicable) for a given sample. This data can be manipulated as required by Dynamic System's own software but can also be exported as an ASCII file in order to be used in a spreadsheet package. For these experiments

Excel was used for data presentation and analysis.

Sample set-up

The geometry of the steel samples used for determining the continuous cooling transformation curves was different to that used for the mechanical test specimens. However, the means of fixing the specimen within the Gleeble chamber was the same (see Figure 4.5).

The samples were held between machined copper blocks known as a wedge set. The taper on the outside surface was 10°. This arrangement provided good electrical and thermal contact between the samples and the blocks. The blocks and specimen were then placed in the main jaws of the Gleeble within the vacuum chamber. A U shaped jack was inserted either side of the copper grips and tightened. This produced good contact between the wedges and the main jaws and also maintained the good contact between the sample and the wedges.

Refining the set-up

The Gleeble (1500 or 3500) is designed to follow closely the thermal programmes complied using GPL but sometimes the system needs minor corrections to make sure that this is achieved. A common reason for this can be a significant change in the sample dimensions or jaw spacing between tests. The jaw spacing was therefore set at 35mm. However, due to the variation in steel thickness some changes to the temperature trim were necessary. Before each run of tests of a particular steel grade, a trial sample was heated up to 1000°C and the difference between the programmed temperature and the actual read temperature reduced to zero using the temperature trim control dial.

4.3.2 Continuous cooling transformation curves

As described in the review of literature, a continuous cooling transformation (CCT) curve is a visual means of representing the microstructural constituents that will be present in a given material after cooling at a series of different rates. Developing CCT curves, that cover cooling rates relevant to welding processes, assists in the identification of materials that may be improved, in the welded condition, by changes to the process and subsequent cooling rates.

CCT curves were produced using a Gleeble 1500 or 3500 through the use of a dilatometer attachment. A programme, written in the form described above, was modified to produce a range of cooling rates and changes in the sample size, through expansion and contraction, were followed using a clip-on dilatometer. The following sections give details of the sample geometry, dilatometer design, employed cooling rates and the specifics of the operation of the Gleeble 1500 and Gleeble 3500 models for use in producing CCT curves.

Specimen Geometry

The standard sample size for use in CCT curves generation is a 6mm or 10mm diameter rod. However, the material for this programme was only available in thin strip form, with a thickness of between 1 and 2 mm so an alternative geometry was requested from the manufacturers. A schematic diagram of this sample is given in Figure 4.4. The length was 178mm and the width 50.8mm. The pair of 25mm long slots were machined centrally to create an isothermal plane across which the dilation could be measured.

The pair of thermocouples used to control the thermal profile of samples during experiments were positioned by marking a cross on the sample and spot welding them 0.5mm either side of the centre of the cross. This was a repeatable means of achieving the manufacturer's recommendation that the wires be attached between five and ten times their diameter apart.

Selecting Austenitising time and temperature

In order to produce CCT curves that are relevant for use in understanding weld microstructures, the austenite grain size, from which the transformations in the CCT samples take place, must be equivalent to the grain size in the regions of the weld that are

of interest. Within each spot weld, two isotherms can be identified as a result of the transformed microstructures. The boundary between the weld nugget and the heat-affected zone is the melting point of the steel alloy, which would be approximately 1530°C and the boundary between the heat-affected zone and the unaffected parent materials must be the austenite transformation temperature of the steel. This can vary but will be approximately 730°C. A position approximately half way between these two isotherms was selected as suitable for focus in terms of the grain size and thermal profile measurements. Due to the thermal profile of the heat-affected zone varying between these two points it is not possible to simulate the conditions at all points in one test but the trends in transformation behaviour for the six steels used in this investigation were considered to be representative.

Three sets of experiments were carried out to establish suitable settings for use in the generation of CCT curves, using samples of DP800. Following each test, the prior austenite grain structure was revealed and measured using the techniques detailed in Section 4.4. The first experiment assessed the effect of heating rate on the prior austenite grain size. The programme consisted of a heating rate varied between 10 and 1000°C/s; a peak temperature of 1000°C; a 1 second soak at this temperature; followed by water quenching to room temperature. The measured prior austenite grain sizes for each of five heating rates are given in Table 4.5. It can be seen that the prior austenite grain size varies between 3.9 and 6.3 microns but no clear relationship between size and heating rate could be seen. Due to the size of the strip samples used, very fast heating rates were difficult to control accurately without some overshoot at peak temperature. In some cases the Gleeble's safety system shut the current off due to the high current draw by a sample in order to achieve a high heating rate. Therefore a heating rate was selected that allowed good control during heating – 30°C/s

The second set of experiments aimed to isolate the effect of peak temperature. For these experiments the programme used was: heating at 30°C/s; a peak temperature varied between 900 and 1300°C; a 1 second soak at this temperature; followed by water quenching to room temperature. The measured prior austenite grain sizes for each of five heating rates are given in Table 4.6. It can be seen that the prior austenite grain size varies between 3.8 and 80.0 microns. The grain size is not greatly affected by a change in peak temperature from 900 to 1000°C. However, at 1100°C/s it almost trebles, from 6.2 to 16.6

microns. The large increases continue when using higher peak temperatures: 44.2 microns at 1200°C and 80.0 microns at 1300°C. The measured prior austenite grains size in the heat-affected zones of the spot welds were found to be of the order of 10 microns (see results – Section 6.1). Therefore, a peak temperature that represents a possible true heat-affected zone condition, without causing extensive grain growth, was selected – 1000°C.

The final set of experiments considered the soak time that would produce the correct prior austenite grain size. The programme consisted of: heating at 30°C/s; a peak temperature of 1000°C; a soak time varied between 0.1 and 40 seconds; water quenching to room temperature. The measured prior austenite grain sizes for each of five heating rates are given in Table 4.7. It can be seen that the prior austenite grain size varies between 4.6 and 8.3 microns. The grain size does increase with soak time but the growth appears to stabilise between the 20 and 40 second soak. Very short soak times are difficult to accurately reproduce in the strip samples used. As mentioned previously, this is due to the relatively large specimen size, which increases the current density required to produce given heating rates and peak temperatures. Therefore, a soak time that produced stable conditions was selected – 30 seconds.

The final programme used for the CCT diagram determination was thus: heating at 30°C/s; a peak temperature of 1000°C; a hold time of 30s; cool to room temperature at the programmed rates. A sample of each of the six steels under examination was heated up using this programme and then water-quenched. The prior austenite grains sizes were measured using the techniques already described.

Determining cooling rate

The most important range of temperatures from the point of view of phase transformations is from 800 to 500°C. Therefore, where cooling rates are quoted it is the rate over this range that is given. The precise cooling rate generated during a thermal cycle was dependent on the means of cooling that was used and was calculated as follows:

$$\text{Rate} = \frac{t_a - t_b}{a\text{-}b} \ (°C/s) \qquad [4.5]$$

where t = time readout at temperature a or b

a and b are the temperatures closest to 800 and 500 respectively given in the output

ASCII file for each sample treated.

For the lower cooling rates the precise rate was controlled by the current applied to the sample and matched the programmed cooling rates exactly. However, the faster cooling rates were generated using forced air and water quenching (see below) and in these cases the cooling rate had to be calculated for each individual sample.

Controlling Cooling Rate

Rates quoted in the literature[49, 14] suggest that cooling rates of between 2000 and 100,000°C may be experienced by material welded using the resistance spot welding process. Therefore, a wide range of cooling rates was required in order to develop the most representative CCT diagram.

A series of experiments were carried out to determine the fastest controlled cooling rate that could be generated using the sample dimensions quoted by Dynamic Systems. The experiments started at 0.5°/s and the rate increased to 1°C/s, 2°C/s, 5°C/s and then by 5°C/s until the measured rate no longer matched the programmed cooling rate. This rate was found to be approximately 25°C/s. As the CCT curves were to be used to further understanding of welded material, which has been subject to a range of very fast cooling rates it was decided to reduce the length of the sample in order to reduce the amount of material being heated / cooled. The reduction in length also increases the efficiency of the conduction of heat away from the ends of the sample. The modified sample dimensions, with a reduction in the specimen length from 178 to 89mm, are given in Figure 4.7. By this means, the maximum cooling rate possible without any air or water treatment was increased to 50-75°C/s, with the faster rates being achieved in the thinner material.

It is possible, with both the Gleeble 1500 and the Gleeble 3500, to introduce a quench head into the experimental setup and to use this to force air or water onto a heated sample in order to achieve faster cooling rates. This is illustrated in a schematic diagram in Figure 4.8. Using this technique two additional cooling rates can be achieved for each steel grade, one using air quenching and one using water quenching. The quench system itself only offers the option of 'on' or 'off' in terms of control and thus the rates are slightly different for each material, due to the different grades' thicknesses and bulk resistivity. The full range of cooling rates used for each steel is given in Table 4.8. It can

be seen that controlled cooling was available between rates of 0.5 and 35°C/s, air quenching produced rates of between 70 and 400°C/s and water quenching rates of between 1950 and 9450°C/s.

In addition to decreasing the length of the samples the thickness of some samples were also modified in an attempt to increase the cooling rate. Samples of 2mm thick DP800 were ground to thicknesses of 0.5mm, 0.9mm and 1.5mm and the difference in cooling rate when using an air quench was measured. Table 4.9 gives the results of the machining and it can be seen that from a rate of 119°C/s for the 2mm thick sample, the cooling rate was increased to 465°C/s for the 0.50mm sample. The transformation temperatures from these tests were included on the appropriate continuous cooling transformation curve.

Dilatometry techniques

- **Dilatometry using a Gleeble 1500**

In order to use the Gleeble 1500 to produce CCT curves it was necessary to make very sensitive measurements of the dilation of the samples under test, as they are taken through a range of temperatures. For this purpose, the manufacturers, Dynamic Systems, produce a commercially available dilatometer, designed around a linear variable differential transducer with essentially infinite resolution. A photograph of this dilatometer, in position in the Gleeble 1500 chamber, is given in Figure 4.9. The dilatometer has a range of +/- 0.625mm and has a resolution of 0.00025mm, based on the electronic signal conditioning used. This high resolution was very important for making fine measurements of the change in sample dimensions during heating and cooling. It also made it possible to resolve the subtle changes in dimensions that take place during a phase transformation. The dilatometer reading was zeroed manually, after positioning in the test chamber, using the strain display panel of the Gleeble. A rod and spring arrangement was used to clip the dilatometer onto a sample around the position of the thermocouple wires. The rods were made of quartz glass in order to minimise the effects of thermal expansion. The dilatometer was stabilised by wrapping an elastic band around the fixed rod and then looping either end of it to two support rods attached to the Gleeble jaws themselves. This is the manufacturer's standard means of producing dilation curves with temperature.

As noted in Section 4.3.1 the output of any thermal simulation was a table of data that could be transformed as required using a spreadsheet package such as Excel. In order to

determine the start and finish temperatures of the phase transformations that occurred, the measured dilation was plotted against the measured temperature. A schematic diagram of this behaviour is given in Figure 4.10. The temperatures at which transformations are taking place can clearly be seen as points of deviation from linear expansion or contraction. The precise temperatures were determined by drawing, within Excel, a line along a portion of linear contraction and selecting, at a magnification of x200, the temperature at which the linearity ceases.

The temperatures determined are transferred to a plot of temperature verses time and, when the points measured at different cooling rates are connected, provide a map of the transformations that occur for a particular steel chemistry that has been transformed under a particular set of conditions. These results can be refined using quantitative metallographic analysis of the transformed microstructures (see Section 4.4).

A concern with this technique was that although an overall start and finish temperature for each sample could be determined, the individual start and finish temperatures for specific phases could not be resolved.

- **Dilatometry using a Gleeble 3500**

In order to obtain more detailed information about transformation temperatures using dilatometry the Gleeble 3500, which has a higher resolution data acquisition system, was used to produce a replica set of transformation curves.

A Gleeble 3500, located at The University of Wollongong was available for a limited period of experimentation. The Gleeble 3500 has an identical setup, with regards producing CCT curves, as the Gleeble 1500. The main advantage of the more modern system was the more sensitive resolution of the data acquisition system and, in addition, the updated, windows based software allowed different acquisition rates to be selected for different portions of the transformation curve. This allowed the heating and plateau portion of the dilation curves to be acquired at low rates and the cooled portion to be acquired at a higher rate. The result was high resolution where it is required without an unmanageable file size being created. This technique was used to produce CCT curves for LCNb, DP600, DP800 and DP1000. The results are given in Section 6.1.

The use of time-temperature plots to identify transformation temperatures applicable to quenched samples

A different approach to the analysis of CCT data, that is a technique other than dilatometry, has yielded some positive results regarding the identification of transformation temperatures in water-quenched samples.

The Gleeble was chosen for CCT curve determination because of the excellent control over time – temperature cycles. This is achieved by passing a current along the samples, which then heats up due to its bulk resistance. Two feedback thermocouples ensure that the current density is correct and the programmed temperature is followed precisely. This feedback system thus takes account of the heat loss through conduction at the ends of the sample as well as heat input.

However, when samples are quenched the cooling is not controlled by the feedback system but by the consistent application of the quenching media (usually air or water), with the current being turned off once the cooling cycle has commenced. In these cases the reference thermocouples, which are required to control the heating part of the program, simply monitor and record the cooling rate that is achieved within the sample. This enables advantage to be taken of the fact that the austenite decomposition reaction is exothermic in nature[91]. Figure 4.11 is a schematic diagram of the cooling part of a time - temperature curve during an air quench test. There is a clear deviation from the otherwise fairly linear cooling rate in the second part of the curve. As an example, for the DP800 the start temperature of the phase change was determined as 460°C, which is 12°C different from the temperature determined by the dilatometry technique (448°C). The time – temperature and temperature – dilation curves for the other air-quenched samples also agree well.

This correlation between the two sets of results indicates that the time - temperature plot can be used to provide an indication of at least the start temperatures of transformations taking place in water-quenched samples. This is an important result because it is only in the water-quenched samples that low transformation temperature phases (mainly martensite) start to appear in the microstructures of some of the steels. Evidence of the transformation temperature assists in the determination of phases which reveal similar morphologies using light and scanning electron microscope examination.

- **Improving the dilatometer for use with the Gleeble 1500**

The improvements noted when using the Gleeble 3500 resulted in an investigation into how the dilatometry results obtained from the Gleeble 1500 model could be improved. The dilatometer, and its stabilisation with an elastic band were thought to be one area where improvements could be made. In particular, the following improvements in the dilatometer's performance were desired:

- greater stability during forced air and water quenching
- increased resolution of transformation temperature
- improved repeatability of dilatometer positioning

Section 5.1 gives full details of the investigation and the improved design.

4.3.3 Production of samples for mechanical testing

Two samples of each steel were subjected to the same thermal cycles as used for determining the CCT curves so that test pieces for mechanical testing could be machined from them. This resulted in two sets of ten samples, for each steel grade, from which miniature Charpy impact and miniature disc samples could be taken.

Sample geometry

The basic coupon, from which the mechanical test specimens were taken is given in a schematic diagram in Figure 4.12. The external dimensions were the same as those for CCT curve generation but no slots were machined in these samples. The reference thermocouples were positioned as for the CCT samples, by marking a diagonal cross on the coupon and placing the thermocouples 0.5mm either side of the centre of the cross.

Determining the useful hot zone

The minimum width of hot zone required to provide sufficient material for the widest mechanical test specimen was 10mm. The jaw spacing used for the CCT curves was 35mm and a sample modified using this spacing was examined to establish the useful portion of treated material generated. Microhardness measurements, using a 100g load, were taken at 2mm intervals showed that the variation in hardness from the centre to the edge of the central 10mm of a sample was 8%. This variation was due to the thermal gradient along the length of the sample, created by the conduction from the sample ends. However, this variation would be present in all samples and thus any trends established, using samples from the central portion, would be valid.

4.4 Material Characterisation

Metallographic preparation and examination was required for three reasons:

(a) to document the microstructures formed following the resistance spot welding process

(b) to quantify the amount of transformation products present in continuously cooled samples, for use in CCT curve generation

(c) to examine the fracture surfaces of fractured Charpy impact samples

Sample preparation

Welds and CCT samples were sectioned using a Struers Discotom:

a) Welds were examined in cross section. In order to view the central line of a weld, parallel lines were drawn at opposite sides of the surface of the weld, the mid-point marked and a line marked 0.5mm to one side of this point (see Figure 4.13). The weld was sectioned at this point and a fine notch scored down to the previously marked mid point. Once this notch had been ground / polished away it was known that the mid-point of the weld had been reached.

b) The CCT samples were examined along the central line of the thermally cycled area. This was determined by marking parallel lines either side of the heated area (see Figure 4.14) and marking the mid-point. This point also coincided, as expected, with the location of the reference thermocouples attached to a specimen during testing. A line was marked 0.5mm to one side of the midpoint and the specimen sectioned along this line. A notch was made, as when examining welds, down to the central point previously determined, in order to act as a reference for subsequent grinding and polishing.

Mounting and Polishing

Once sectioned the samples were lightly ground to remove any burrs and mounted. CCT samples were mounted in conductive bakelite using a hot press to facilitate the use of the Scanning Electron Microscope for higher magnification examination. Welds were mounted using Struers cold mounting resin.

Mounted samples were ground using 120, 240, 600 and 1000 grit grinding discs and finished using 6 and 1μm diamond paste polishing wheels.

Etching

Three etchants were used to reveal the microstructures of the samples:

a) A 5% Nital solution was used for general etching of both welds and CCT samples. This revealed features such as grain boundaries and enabled different transformation products to be identified. Etching times of between 2 and 5 seconds were used, depending on the grade of steel being examined.

b) A Picral solution was used to reveal the prior austenite grain boundaries.

Microscopy

Two microscopes were used for examining sample microstructures:

a) A Polyvar Optical microscope was used to examine samples at magnifications between x20 and x2000. Measurements of the grain size and volume fraction of transformation constituents was also made using this system:

- Grain size measurements

  These measurements were carried out at a magnification that allowed a representative sample of grains to be clearly observed and distinguished in one field. This magnification varied from x200 to x2000 depending on the grain size of the sample. For each measurement, a rectangular frame was superimposed over the field of view and the number of grains intercepted by the four sides counted. The length of the perimeter line was measured using a calibrated graticule. Five fields were evaluated in this way for each sample on which measurements were made and the average number of grains per line was calculated using the following equation:

$$\text{Grain size (mm)} = \frac{\text{measured length of rectangle perimeter line (mm)}}{\text{Average number of intercepts}} \qquad [4.6]$$

- Volume fraction measurements

  The volume fraction of different microstructural constituents was determined using a point counting technique. As for the grain size measurements a magnification that allowed the different constituents to be clearly observed and distinguished was used and this varied from x200 to x2000 depending on the nature of the microstructure. The graticule, present in one eyepiece of the optical microscope, was used to carry out the point counting. It had 11 points marked, from 0 to 10 inclusive and for a single location the nature of the constituent

present at the tip of each marked point was recorded. The stage was moved by regular intervals to allow a series of measurements to be made on a grid of 11 x 11 points without any operator bias. Five fields were examined in this way resulting in a total of 550 measurements. From these measurements the percentage of each constituent observed could be established. By ensuring that a representative number of points were observed, these measurements could be approximated to volume fraction measurements.

b) A Jeol JSM-840A Scanning Electron Microscope (SEM) was used at magnifications between x200 and x20,000. It was used to examine etched welds, CCT samples and the fracture surfaces of failed impact specimens. A working distance of 15mm was used for all imaging. The accelerating voltage was set at between 20k and 30k. An attached Link ISIS EDX system, with a resolution of 62eV, was used. Point chemical analysis, of the precipitates found on the fracture surfaces of the impact test specimens, was carried out at a magnification of x10,000.

Microhardness Testing

A Leco Microhardness machine was used to carry out microhardness measurements on both welds and CCT samples. A 500g load was used to determine the weld microhardness profiles. These profiles were used to establish different regions of the heat-affected zones (HAZs) in welds with indents being made at 1mm spacings. They also allowed the effect of different welding schedules to be monitored. Individual measurements were made using a 10g load to assist in the identification of different transformation products in CCT specimens. The low load was required to ensure that the indent was only made on one type of constituent, particularly in the finer microstructures observed at higher cooling rates.

4.5 Mechanical Testing

Three types of mechanical tests were used to establish the effect of different continuously cooled microstructures on the properties of the six steels used in this programme: bulk hardness tests; miniature Charpy impact tests; and miniature disc bend to determine the yield and tensile strengths.

4.5.1 Bulk Hardness

A Mitutoyo AVK-C1 hardness tester was used to measure the bulk Vickers hardness of the CCT samples. A 10kg load was used and five indents per sample were made. Indents were made at regular intervals using the micrometer attached to the stage of the microscope so as to avoid any operator bias. The hardness of the unwelded material was measured for each of the six steel grades used and this was compared with the microhardness profiles of the welded material. In addition the Vickers hardness of the six alloys after each of ten CCT cycles was monitored.

4.5.2 Miniature Charpy Impact Tests

Good impact performance is an important property in automotive steels. Therefore, it was decided to carry out tests to determine the effect of changing microstructure, through different continuous cooling cycles, on the impact energy subsequently absorbed.

Specifications for sub-size Charpy specimens were considered but none of the previously defined sub-size dimensions made maximum use of the material that was available. A larger sample was considered desirable, as it would allow a more representative portion of material to be tested. A standard Charpy specimen is 10x10x55mm. The dimensions used for these tests were: 10mm x [as supplied steel thickness (mm)] x 50mm. The reduction in length from 55mm to 50mm was necessarydue to the maximum length of material available from a Gleeble modified sample. The thickness available was limited to the thickness of the material that was available. A schematic diagram of the chosen sample dimensions is given in Figure 4.15. Choosing non-standard specimens means that the results are can only be compared for the six steels used for this programme. This procedure was necessary because of the dimensions of the material available for this investigation.

A Manlabs Charpy impact machine with a range of up to 41J was used to carry out the impact tests. All tests were carried out at room temperature. In order to check the repeatability of the results, ten samples of the DP800 material, in an unmodified state, were first tested. The average result obtained was 10.55J/mm^2 with a standard deviation of 0.34J/mm^2 or 3.2%. This was considered a reasonable variation and therefore the machine was used for the remainder of the impact tests. The results of the impact tests can be found in Section 6.2.

As fracture surfaces are known to vary in appearance according to the nature of the fracture, that is, brittle or ductile, an SEM examination of selected fracture surfaces was carried out. The failed samples were mounted on an SEM holder using graphite discs and positioned so that the fracture surface was parallel with the base of the holder.

4.5.3 Miniature Disc Bend Tests

The yield and tensile strengths associated with the different microstructures produced by the different CCT thermal cycles were measured using the miniature disc bend test.

Miniature disc bend tests have, as described in the review of literature, been successfully used for determining yield and tensile strength from 9.5mm discs in pure, non-ferrous materials and ultra low carbon steels[84]. However, there were concerns that the results from disc tests would be unreliable for multiphase alloys, where the influence of precipitates or small regions of less ductile phases, such as martensite or pearlite, would have a disproportionate effect. This effect can clearly be minimised by taking as large a sample of the microstructure, in terms of thickness, as possible. Previous experiments used 0.5mm thick discs so it was necessary to establish the accuracy and repeatability of the disc test for the multiphase steels. Full details of the experimental configuration used and the series of experiments carried out in order to determine the validity of the miniature disc bend test for this application, are presented in Section 5.2.

4.6 Weld Thermal Analysis

In order to link the CCT curves, generated using the Gleeble thermomechanical simulators, with the practical process of resistance spot welding it was necessary to establish the thermal cycles generated during welding itself. Previous experiments in this area have made use of a thermal imaging camera but this technique was not suitable for this application because the desired results were thermal profiles linked to specific locations within the weld. The thermal imaging camera could only image the edge of a weld and therefore would not be suitable for providing information about a specific point between two sheets of steel.

Direct measurement of the temperature at a certain point was only possible through the use of an innovative thermocouple technique. Section 5.3 provides details of the series of experiments carried out to determine the experimental set-up that provides the optimum results whilst also considering the trade-off with the cost of the equipment.

5. RESULTS AND DISCUSSION – EXPERIMENTAL TECHNIQUES

This section details important development in three key areas of experimental investigation: dilatometry, miniature disc bend testing and thermal monitoring during resistance spot welding. These techniques were developed and then used to produce some of the results given in Section 6. Therefore, the results and discussion associated with each area are included in this chapter so as to justify the use of these techniques for the further work contained in Section 6.

5.1 Improved dilatometer for a Gleeble 1500

5.1.1 Investigations

As discussed in Section 4.3.2, the original experiments carried out on the Gleeble 1500 located at Swansea University highlighted difficulties in reproducibility of the setup, using the dilatometer as shown in Figure 4.7. It can be seen that the dilatometer is stabilised only by a taut elastic band, which is the manufacturer's recommended technique. This introduces a number of difficulties:

- Accurate setting of the dilatometer in the vertical plane is difficult, as positioning is only achieved by varying the height of the rubber band on two support rods. This cannot be measured particularly accurately and although this is not of great concern when using rod or cylinder samples, which have the same dimension regardless of the angle of the dilatometer to the vertical. However, for strip samples the angle of the dilatometer is more critical because there is a small difference in the dimension measured if the dilatometer is located in a different position. The dilatometer remains accurate provided it remains at the same angle throughout the test but slippage during a test could lead to small changes in the displacement of the rod within the transducer making for difficulties in interpreting results.
- Positioning of the transducer at precisely the centre of the sample also relies on the accurate positioning of the rubber band. As above, this is possible but accurately repeating the same set-up for several samples is subject to the skill of the operator making the procedure less robust than is ideal.
- The resolution of the transformation temperatures can be reduced by movement in the dilatometer during a test. Typical dimension – temperature curves for a sample tested using the Gleeble 1500 are given in Figures 5.1 and 5.2. It can be seen that under the stable cooling conditions (Figure 5.1) the dilatometer performs as desired, following

the transformations clearly. However, in the water quenched result (Figure 5.2) the oscillations in the readings increase and mask any transformations that may be occurring.

5.1.2 Results from the Gleeble 3500

It was hoped that some insight into the causes of the difficulties noted on quenching could be gained from the experiments carried out on the Gleeble 3500 model based in Wollongong. This model has improved electronic control systems and whilst the dilatometer setup was essentially similar as for the Gleeble 1500 there were a few small differences.

- The chamber was tilted forward meaning the grips were now at 90° to their position on the Gleeble 1500.
- As a consequence of the above, the dilatometer was supported in the horizontal position.
- The quench head had a different arrangement of spray holes. The Gleeble 1500 arrangement is two rows approximately 8mm apart on either side of the fixed C-shaped head whereas the Gleeble 3500 arrangement was a single row in the centre of each side, again of a C-shaped head but in this case the individual prongs on the head could be rotated to direct the single jet of water in a particular direction on either side.

With these differences in mind a number of water quench tests were carried out. An example of the dilation curve obtained using the Gleeble 3500 is given in Figure 5.3. It can be seen that although oscillations in the dilatometer readings are significantly reduced, no clear transformation points can be detected. However, general vibration within the jaw setup was greatly reduced compared with the Gleeble 1500 system. Further analysis of the data collected for each test revealed an alternative method of determining transformation temperatures (see Section 4.3.2). However, the problem of the dilatometry evidence not providing accurate transformation temperatures was not solved.

Additionally, it was noted, that for non-quench tests, using the Gleeble 3500, that is those using controlled cooling, many plots revealed the transformation temperatures of the second constituents. This detail was not observed in the original Gleeble 1500 results and it was felt that improvements to the system setup would improve this measurement. In

particular, the transducer available with the Gleeble 1500 was more sensitive than that available with the Gleeble 3500 and should have produced more sensitive measurements of the sample expansion and contraction than the 3500. However, this was not observed in practice and it was therefore considered that the procedure for carrying out dilatometry using the Gleeble 1500 had not been optimised.

5.1.3 Requirements of the new Gleeble 1500 setup

There were several drawbacks to the original system of measuring dilation in continuously cooled samples tested using a Gleeble 1500, as described above. The key features of any new system needed to be:

- Amenable for use on any shaped / sized sample without modification in order to cope with the range of samples used in the Gleeble, that is, it should have the flexibility that the clip-on original design bestowed.
- The position of the dilatometer must be movable in three directions to allow for precise positioning.
- The position should be readily altered, i.e. not require parts to be changed, to allow for rapid, accurate changes to be made during a series of experiments.
- Ideally the positioning should have some lockable positions, for example a 'test' position and a 'change sample' position to allow for rapid and repeatable changes of sample during a series of tests.

The new design should provide greater stability to the high water pressure used during water quenching.

5.1.4 Design and production of the stand

An attachment, to be used within the test chamber of the Gleeble 1500 was designed and manufactured. The designs of this attachment are presented in Figures 5.4 and 5.5. Figure 5.4 illustrates the arrangement for support of the transducer. The transducer itself is held in a solid aluminium casing and the quartz rods aligned as in the original device but with a solid ceramic block, as well as a further aluminium block, providing support and ensuring true alignment. The ceramic block also helps to shield the transducer from the heat given off by the sample. The support clamp shown in Figure 5.4 is the means of attaching the dilatometer to the main support stand inside the chamber. This is illustrated further in Figure 5.5. In Figure 5.5(a) the dilatometer is in the raised position allowing

easy insertion of samples and cleaning of the chamber after water quenching. Figure 5.5(b) illustrates the test position of the set up. The attachment was manufactured from an aluminium alloy to reduce the chance of corrosion affecting the operation of the setup on exposure to high temperature environments and water spraying.

Photographs of the completed attachment taken offline are given in Figures 5.6(a) to (c). Figure 5.6(a) indicates the three directions in which the position of the dilatometer can be adjusted and the detail of how the transducer and quartz rods are incorporated into the design can clearly be seen. Figure 5.6(b) illustrates the full setup, including the two aluminium blocks, which provide the basis for attachment to the jaws within the chamber and the runners (two rods). These rods not only allow the adjustment of the dilatometer sideways in the chamber but also enable the relative position of the two large aluminium blocks to be changed, when the left hand jaw in the chamber is adjusted, without having to remove any part of the stand. The attachment is therefore, fully integrated with the Gleeble chamber. This can be seen clearly in Figure 5.7(a) and (b).

One modification carried out before final testing was the removal of the back quartz rod from the dilatometer. In the new design the front rod (the shorter of the two in the figures) works independently from the back rod and is not required for stability as in the old setup where the dilatometer was 'clipped' round the samples. Due to the longer rods position in front of the holes in the quench head it was thought possible that it could still be a source of instability in the setup and was therefore disconnected before insertion of the attachment into the chamber.

5.1.5 Testing of the attachment

- **Room temperature tests**

The initial tests carried out were to ensure that there was no movement of the dilatometer on application of the quench media. This was tried for both air and water quenches and the dilatometer showed no movement. It was noted, however, that a small amount of vibration was picked up by the dilatometer although this was not sufficient to affect the readings.

- **Water quench tests**

In order to determine the effectiveness of the modified method of attachment in stabilising the dilatometer, three water quench tests were carried out. The standard heating cycle was used (30°C/s heating rate to 1000°C, 30s hold, followed by the quench) and time, temperature and dilatometry readings collected. Following success with determining transformations from the time – temperature plots on the Gleeble 3500, the transformation temperatures were determined from both the dilatometer and thermocouple outputs using the method previously described. The results are given in Table 5.1 and a typical time-temperature output from a water quench test using the modified dilatometer is shown in Figure 5.8.

It can clearly be seen that there is no consistency with regards the first transformation temperature. However, the Gleeble 3500 result, taken from the thermal output did not show any transformation at these temperatures. The second transformation temperature was measured more consistently. The dilatometer readings, however, still showed a variation of 76°C, which is not sufficient to give any confidence to be given to a single result. The thermocouple readings showed a maximum of 8°C difference.

These results indicate that more work is required to determine the source of the large scatter in dilatometer readings produced on water quenching of samples. The readings from the thermocouples, however, showed good consistency suggesting that this is a suitable method for reliable generation of transformation temperature data in the absence of any dilatometry readings.

It should be noted, that no finish temperatures could be detected in the time temperature plots so it is still of importance to determine the sources of error in the Gleeble 1500 dilatometer output. Further, although variations in the measured temperatures were still substantial for the dilatometer, a general reduction in the amount of scatter in the readings collected was observed. This suggests that an improvement in the operation of the dilatometer has been achieved but further fine-tuning is required to improve the results obtained when using water quenches.

- **Repeatability and sensitivity tests**

In order to determine any improvement in repeatability afforded by the use of the attachment three air quench tests and four controlled cooling tests, at a 10°C/s cooling rate, were carried out.

The results from the air quench tests are given in Table 5.2 along with those from the original series of tests carried out on the Gleeble 1500. It can be seen that the average transformation temperatures determined are similar for both methods. However, a small improvement in the variation is associated with the results obtained whilst using the attachment.

The results from the controlled cooling experiments are given in Table 5.3. There are three points of interest in the readings.

- The results using the new dilatometer attachment indicate a slight improvement in variation compared to the original readings, as measured in terms of the standard deviation.
- The results obtained using the new attachment included the start and finish temperatures of more than one transformation. See Figure 5.8 for an example of the results obtained from the original setup and Figure 5.9 for the results obtained with the new attachment. This was not seen in any of the original Gleeble 1500 work and indicates that the dilatometer is more sensitive to such small changes in sample expansion and contraction that whilst setup using the rubber band. This improvement in the sensitivity was seen to be consistent through the four tests with two samples showing the four start and finish temperatures and the other two tests agreeing well with two of the four temperatures determined in the other tests.
- The results achieved in these tests were within 1% of the results obtained on the Gleeble 3500.

5.2 Optimised Miniature Disc Bend Tests

Miniature disc bend tests have been shown to be a reliable means of determining the yield and ultimate tensile stress from small amounts of sample material. However, the test has never been used for dual or multiphase steels and the test and sample selection required optimisation before the test could be used for determining the properties of the continuously cooled material. The parameters requiring investigation were: experimental setup – particularly die clearance; disc thickness; test speed; and the most reliable means of converting the measured loads into calculated stresses.

5.2.1 Sample preparation

Discs of material, 9.5mm in diameter, were punched from coupons of steel that had been heat treated using the Gleeble 1500 (Figure 5.10). A jig was manufactured to ensure that discs were taken from within the central area of the coupon, which had been confirmed as suitable for testing by means of metallographic examination. Discs 2 and 3 were used and discs 1 and 4 punched to provide reserves if any difficulties were encountered when testing the first two samples. They also provided further material if pairs of samples produced significantly different results.

Punched discs had a slight burr in the softer material and in addition, the discs had to be ground to the desired thickness for testing whilst still producing a suitable surface finish. Norris and Parker[84] indicated in their work that a fine surface finish was desirable, and thus the final grinding was carried out using 800 grit wet grinding paper. For steels that required rough grinding prior to finishing, a 100 grit paper was used to take the disc to within 0.1mm of the desired thickness.

5.2.2 Basic experimental setup

Figure 5.11 is a schematic diagram of the miniature disc test setup. The disc of material was placed in the die as indicated and the upper die screwed in place. A mark was made on the top of the upper die and the main body of the holder. When these two marks were lined up the force on the edge of the disc was the same and thus ensured a repeatable clamping force for all tests. After each disc was in place, 1g of polytetrafluoroethylene (PTFE) powder was added down the slot leading to the disc in order to minimise any potential friction between the disc and the punch. The punch was lowered into the slot, the whole assembly placed under a platen attached to the moving arm of a mechanical test

machine and the platen lowered until it just touched the top of the punch. For these experiments a Hounsfield S-series HTE test machine was used. The machine had a load cell of 50kN and was used in compression. The displacement of the paddle and the measured load were logged at a rate 0.5Hz. Figure 5.12 shows the equipment in place on the Hounsfield test machine.

5.2.3 Determining die clearance and punch diameter

The die clearance must be sufficiently large to avoid any seizure of the apparatus during testing. It is calculated as follows:

$$Cl = A - (D + 2t) \qquad [5.1]$$

Where Cl = die clearance

A = lower die diameter

D = punch diameter

t = disc thickness

The locations from which these parameters are taken are illustrated in Figure 5.13.

With regards to die clearance, Norris and Parker[84] showed that increasing die clearance from 0.5mm to 1.5mm for a 0.5mm thick disc reduced the maximum load generated by approximately 0.5kN. Further, they showed that increasing the punch diameter from 2mm to 4mm, again for a 0.5mm thick disc, more than trebled the maximum measured load to 3.8kN from 1kN.

It was considered that using a punch of 4mm diameter would be more desirable because the larger contact area with the disc would result in a more representative sample of the multiphase microstructure being subject to the test. This should reduce the chance of a single area of brittle microstructural constituent (for example an island of martensite or pearlite) resulting in failure prior to the true potential maximum load being reached.

Due to the increase in load expected when using the 4mm punch it was decided to maximise the die clearance. Two disc thicknesses were used for these experiments, 0.5mm and 1mm, (see Section 5.2.5) and in order to minimise changes in the die clearance with different thicknesses two lower dies were used. The largest available die had a diameter of 7mm and this resulted in a die clearance of 1mm for 1mm thick discs. To achieve a similar die clearance with the 0.5mm thick discs, a 6.4mm die was used

which resulted in a die clearance of 1.4mm.

5.2.4 Determining yield and ultimate load

Predicting the yield and ultimate tensile stress from the miniature disc bend tests required that values for the yield and ultimate load be determined. An example of the load-displacement curve generated by a disc bend test is shown in Figures 5.14. The curve was produced during a test on a 1mm thick disc of the low alloy LCNb grade. The yield and ultimate loads are marked on the graph illustrated in Figure 5.15. The yield load was measured as the point at which the load – displacement relationship deviated from the initial elastic portion of the curve. The ultimate load is the maximum load supported by the disc prior to necking and eventual fracture of the disc. The displacement to fracture was also determined for each disc test.

5.2.5 Optimising disc thickness

As previously mentioned, two disc thicknesses were considered for these tests: 0.5mm and 1mm. It was thought that using 1mm discs would be preferable for similar reasons to those given for the selection of the 4mm punch. That is, that a 1mm thick disc would provide a larger sample of microstructure for testing, and thus limit, the effect of any one area of a particular constituent.

Tests were carried out at both thicknesses using discs of DP800 steel. The results of three tests are presented in Table 5.4. The average ultimate load determined for the 0.5mm discs was 3048N with a standard deviation of 83.9N or 2.8%. For the 1mm thick discs, the average ultimate load was 7058N, with 64.1N or 0.9% for the standard deviation and % standard deviation respectively. This indicates that the 1mm discs produced slightly more reproducible results in terms of the measured results.

This agrees with results from Lewis[86] who found that using 1mm thick discs was slightly more beneficial than using 0.5mm thick discs for predicting ultimate tensile strength. Specifically, the work found that the actual result from a tensile test was within 1.5% of the predicated value for 1mm discs and within 4.5% of the predicated value for 0.5mm discs. In terms of predicting yield stress, Lewis found that 1mm discs could provide a predicted result within 2% of the measured yield stress after 15 tests but that no reasonable correlation could be made with results determined from 0.5mm discs.

Examination of the failure mode of DP800 0.5mm and 1mm discs, see Figures 5.15 and 5.16 respectively, indicated a possible reason for the improvement in repeatability. In Figure 5.15, it can be seen that the disc has fractured across the dome created by the pressure of the punch. This suggests a failure that is more brittle in nature possibly indicating that a small region of brittle microstructure filling most of the thickness of the disc has influenced the failure. Figure 5.16 shows a disc that has failed around the dome or cup. This indicates a more ductile failure and suggests that the results obtained are more likely to be close to the true ultimate load of the material; hence the improved repeatability compared to the 0.5mm results.

5.2.6 Establishing a suitable test speed

The machine used for the disc tests could be controlled in terms of crosshead speed, that is in $mm.min^{-1}$. Three speeds were used to test 1mm discs of LCNb, DP600, DP800 and DP1000 unmodified material: $1mm.min^{-1}$, $3mm.min^{-1}$ and $5mm.min^{-1}$. Figure 5.17 shows the correlation between the measured ultimate load and predicted UTS for the four materials. It can be seen that the results are good for all test speeds. R^2 is a measure of how well a regression line fits real data and it can take a value of between 0 and 1 with 1 indicating a perfect fit. The R^2 value for each speed is given in Table 5.5 from which it can be seen that the $1mm.min^{-1}$ results are a marginally better fit to a linear trend line compared to the other two speeds.

The slower two speeds were also used to test 0.5mm discs of DP800 and the nature of the failure of both the 0.5mm and 1mm discs was examined. Figures 5.18 and 5.19 are photos of the fracture of a 0.5mm and 1mm disc respectively, tested at $3mm.min^{-1}$. It can be seen that the 0.5mm disc in Figure 5.18 has experienced further cracking across the cup compared to the slower tested disc pictured in Figure 5.15. This suggests that the thinner disc, when subject to the increased work hardening associated with faster test speeds, becomes more sensitive to the presence of small areas of brittle microstructure, resulting in further brittle cracks on failure.

The 1mm DP800 disc tested at $3mm.min^{-1}$, pictured in Figure 5.19, shows a similar failure to the slower tested disc as shown in Figure 5.16. This indicates that the thicker 1mm discs are not as sensitive to the increases in strain hardening with respect to changes in the effect of small areas of brittle constituents, which further supports the decision to

use 1mm discs for testing.

Although the improvement in correlation for the slowest test speed of 1mm min^{-1} was small, the change in the fracture mode of the thinner discs raised concerns about how the more brittle, faster cooled samples would respond to disc testing even if 1mm discs were used. Therefore, a test speed of 1mm.min^{-1} was chosen to minimise the possibility of brittle fractures being induced by the increases in work hardening caused by faster test speeds.

5.2.7 Analysing data from miniature disc bend tests

- **Correlating yield load and 0.2% proof stress.**

Norris and Parker[84] investigated the relationship between the yield load measured from a miniature disc test and the corresponding 0.2% proof stress. They found that the relationship was proportional and that the proportionality factor was the same regardless of the material being tested. The range of materials tested included a low alloy steel as well as copper and aluminium. Consequently, it was decided to investigate the relationship proposed for these materials applied for the untreated LCNb, DP600, DP800 and DP1000, used in the present studies.

The previously referenced research found that the yield load was dependent on disc thickness and the relationship determined was:

$$\sigma_{0.2} = \frac{L_y}{t^2(2.19)} \qquad [5.2]$$

The units of 0.2% proof stress are MPa, the yield load (L_y) is in N and the disc thickness (t) in mm.

The research by Norris and Parker found that the use of this equation produced 0.2% proof stress values of which 95% were within ± 20% of the value measured using a standard tensile test. These results spanned all three materials studied: aluminium, copper and a low alloy steel. In the present research it was found that, for the four steels tested, the calculated proof stress was within ±15% of the measured result (see Figure 5.20).

- **Ultimate Tensile Stress**

The ultimate load measured in miniature disc tests has been correlated successfully with the ultimate tensile strength measured in standard tensile tests. Norris and Parker[84] established the following relationship between the two parameters:

$$\sigma_{UTS} = \frac{L_U}{t\,(2.32D - 0.9Cl + 0.56)} \qquad [5.3]$$

where σ_{UTS} is measured in MPa, L_U (the ultimate load measured in a disc test) given in N and the thickness (t), punch diameter (D) and die clearance (Cl) all measured in mm.

This relationship resulted in 86% of the predictions made falling within ± 10% of the measured UTS. The relationship proved weaker for the steel discs tested compared with the pure aluminium and copper samples. The cited reason was that the low alloy steel contained non-metallic inclusions, which increased the variability of the results for the steel discs. However, the disc thickness used in Norris and Parker's tests was 0.5mm. The results given in Section 5.2.4 indicated that an improvement in the repeatability of the disc yield and load measurements was obtained through the use of a thicker, 1mm, disc.

The results of the measured UTS against the calculated UTS are plotted in Figure 5.21. This plot indicates that there is a strong relationship between the measured and predicted UTS with on average a correlation of ±5%. This is also the maximum deviation for any individual steel grade.

- **Critical displacement to failure**

One further aspect of Norris and Parker's investigation was the consideration of the displacement of the punch when the discs failed. The displacement of the punch affected the area of the disc that was in contact with the punch. This was defined through the contact angle, which is illustrated in Figure 5.22. It can be seen that the contact angle, α, is the "angle subtended from the last point of contact of the disc and punch to the vertical centreline of the punch." By measuring the contact angle at a range of displacements at failure it was shown[84] that there was a critical level of displacement, dependent on the punch diameter, at which the contact angle was at a maximum of $\pi/2$ or 90°. Further tests showed that this critical displacement was in fact almost equal to the punch diameter. For materials that failed below this critical displacement the ultimate load was found to be

dependent on the displacement, as well as the previously mentioned factors. The alternative relationship was given as:

$$\sigma_{UTS} = \frac{L_U}{t\,(0.14D - 0.82Cl + 2.17d_f + 0.56)} \qquad [5.4]$$

where d_f, the displacement to failure, is given in mm and all other variables are as previously defined.

Equation [5.4] was used to calculate the ultimate load for any of the discs that failed with a displacement below the punch diameter of 4mm. A greater number of discs fell into this category in the higher strength steels: DP800, DP1000 and DP1400. The correlation was significantly better when this relationship was applied. For example, for the DP1400 discs the correlation doubled when the alternative equation was used for the faster cooled, more brittle discs.

5.3 An Innovative Direct Temperature Measuring Technique

As indicated in the review of literature there is no published work considering in depth the use of thermocouples to pinpoint the thermal profile associated with specific microstructural features or areas of a resistance spot weld, such as the heat-affected zone. This section details the investigation carried out to establish the possibility of using thermocouples for this purpose.

5.3.1 Attaching thermocouples to a spot weld coupon

BS1140[26] specifies the standard size of steel coupon, for use in weldability tests, as 50mm x 50mm. Coupons of this size were thus manufactured from DP800 steel. Due to the potential cost of sheathed thermocouples that are capable of withstanding the likely temperatures experienced during welding (>1500°C) the possibility of using plain wire thermocouples was investigated.

This technique makes use of a pair of thermocouple wires that, when spot welded to the surface of a steel coupon produce a thermocouple junction. The thinnest, economical K- and R-type plain thermocouple wire were sourced and found to be 0.2mm in diameter. K-type thermocouples can be used up to approximately 1350°C and were therefore considered to be suitable for use in the heat-affected zone areas of welds. R-type thermocouples can measure up to approximately 1700°C, which was considered suitable for monitoring the thermal profile within the weld nugget. The K-type thermocouples were made of nickel-chromium and aluminium-chromium and the R-type from platinum and platinum - 10% rhodium. When referring to individual thermocouples in the rest of this section, a name of the form 'thermocouple type + thermocouple number' will be used. For example, R1 refers to an R-type thermocouple in position 1 etc.

In order to prevent the bare wires from touching the surface of the coupons and creating unwanted junctions away from the point of interest an insulating coating was required. Teflon coatings are widely available but, in general, will only protect the wires up to approximately 850°C. This temperature will easily be surpassed, at least in the weld nugget and inner parts of the heat-affected zone. Thus, the Teflon coatings are unlikely to survive through to the cooling part of the thermal cycle. As the most important part of this investigation related to this cooling period Teflon coatings were deemed unsuitable and a ceramic sheath was identified as the optimum solution. A double bore ceramic sheath was

used which had an internal bore diameter of 0.25 mm and an external diameter of 1.2mm. The total thickness of the steel was 4mm so this external diameter was considered acceptable in terms of leaving sufficient material surrounding the sheath that the thermal patterns would not be significantly disturbed.

The issue of accommodating a solid rod of ceramic material within the weld coupon was addressed by machining grooves into the samples to remove sufficient material to enable the rods, and thus the thermocouples to sit in the coupon without disturbing the setting of two coupons into a test piece. Further, the ceramic coating was inherently brittle and unless material was removed the sheaths would crack and leave the thermocouples exposed to the steel coupon.

To facilitate the drilling of accurate slots into which the rods could be placed two coupons were clamped together and the desired location of the thermocouple junction marked onto the outside of one sample. Holes were then drilled into the side of a pair of coupons with a limiter ensuring that the hole was only drilled to the centre of the sample (25mm depth). One difficulty encountered was that the drill bits tended to wander as they penetrated past approximately 15mm into the sample. This caused two problems: (1) The tips of the slots were not in the marked location with reference to the outside of the test piece and (2) the ceramic rods, being very brittle, could not withstand any bending without breaking. High strength drill bits could not remedy this problem and so the coupon dimensions were modified to 50mm x 30mm. This required only a slot depth of 15mm, which was reproducible. Plain, undrilled samples of these dimensions were welded under typical welding conditions to produce a weld with a size equal to $5\sqrt{t}$ (where t is the steel thickness) to establish any effect that a smaller test piece might have on the required weld schedule. No difference in terms of splash conditions or weld size was found.

Figure 5.23(a) shows a single coupon (from a pair) drilled with four slots. The central slot was reserved for an R-type thermocouple. The other three slots accommodated K-type configurations. Small burrs, that were present on the edge of the slots after welding were smoothed using fine emery paper.

In order to obtain a reliable reading from a thermocouple pair, the wires should be

attached to the surface providing the junction approximately 5-10 wire diameters apart. The accurate positioning of wires on the test coupons was achieved by using the miniature resistance spot welder that is supplied with a Gleeble (1500 or 3500) for use in attaching thermocouples to Gleeble test samples. In particular, the precisely controlled stage allowed good repeatability in attaching the wires in the desired locations. The point of attachment was just outside the inner tip of the drilled slots since early experiments with the wires attached inside the slot produced much lower readings than known to be the case.

Figure 5.23(b) is a photograph of one half of a test specimen with three pairs of wires attached. The fourth, and outmost K-type position was used during a few early trials but, due to the low level of information provided, it was decided to boost the datalogging capacity for the other thermocouples and discontinue the use of this slot.

The wires were attached perpendicular to the surface of the weld coupons due to the configuration of the miniature resistance spot welder and following the welding they were carefully bent over the tip of a sheath to force them to lie flat in the machined slots. The ceramic sheaths were fitted by carefully sliding the two thermocouple wires, simultaneously, into an approximately 15mm length of the sheath. This procedure minimised any damage to thermocouple wires ensuring that a good bond was maintained with the surface that would not be damaged by welding.

Additional polymer sheaths were individually added to wires outside the steel sample to provide further shielding from the metal coupons and also the metal surfaces around the electrodes. These polymer coatings did not have to withstand the same high temperatures as those sheaths located within the test piece and in addition the polymer sheaths were more flexible to assist with positioning of the external wires during experimental setup.

Two halves of a fully prepared test specimen can be seen in Figure 5.23(c).

5.3.2 Positioning of test coupon and wires

In order to ensure that the thermocouples measured the thermal profile in the desired location within a weld, it was necessary to position the test specimen accurately onto the centre of the copper electrodes. To ensure that the centre of the sample, and thus the tip of the R-type thermocouples, was in the correct position, the centre of the sample was marked on the outside of one of the coupons. The thermocouples were attached to the appropriate compensating cables (see below) and their reference numbers clearly marked onto the sample to ensure the correct matching of thermocouple reading with physical location at later stages of analysis. Once all the stages that could disturb the position of the sample had been completed two portable markers, at 90° to each other were positioned to mark the centre of the lower electrode. The sample was slid into position beneath these markers and positioned so that the centre of the sample matched the central point indicated by the markers. Due to the careful positioning of the sample no further support was required to hold the sample in position before welding. Figure 2.24(a) shows a test sample in position on the lower of the two electrodes and 2.24(b) with the upper electrode lowered. Five trial welds were produced using this technique to ensure that the weld produced was central to the sample and in all five cases this was true. Thus, the technique was proven to be repeatable enough for use in extended sample runs.

Due to the expense of the thermocouple wires, compensating cables were used to connect the thermocouples to the datalogging equipment. These cables can be clearly seen in Figure 5.25. Different cables have to be used with the different thermocouple types (K and R) to ensure the correct output from the thermocouples. In order to minimise the length of the cable that was within the strong magnetic field produced by the welding equipment during operation the cables were run directly out from the electrodes.

5.3.3 Logging temperature measurements during resistance spot welding

Datalogging was carried out using a stand-alone datalogger connected to a laptop computer running Windows 98 and an off-the-shelf software package from National Instruments (NI). The NI package allowed data from each thermocouple (channel) to be individually logged and automatically calibrated to the correct thermocouple type, as well as previewing the output on a real-time window. The full experimental setup can be seen in Figure 5.26. Some additional safety screens had to be removed for this photograph to be taken.

Up to five channels could be used with the datalogger but for the present research three were used: 1 R-type calibrated channel, the results of which are marked 'R1' in the Results Section 6.4; and two K-type channels, which are marked K1 and K2. In general the R-type thermocouple was located at the centre of the weld nugget and the two K-types in the heat affect zone of the welds. See Section 5.3.4 for more on the precise location of the thermocouples.

The logging rate was maintained at 500Hz (500 samples per second). This rate was chosen as a good compromise between the accuracy of the data in terms of pinpointing small fluctuations in the temperature and producing manageable data files. The results could be exported in CSV (comma separated values) format that could subsequently be read by Excel and manipulated as required for analysis.

5.3.4 Metallographic examination of thermocouple monitored welds

In order for the thermocouple readings to be associated with specific locations within the welds it was necessary to section, mount and etch individual welds, thus revealing the precise locations of the thermocouples. A standard procedure was developed and applied to all welds in order that the correct thermocouples would be matched up with the correct readings:

- Macro photographs were taken of the top surface of the welds to record the position of all the thermocouples and the channels that they were connected to.
- Sketches were also taken of the coupons and any notes regarding the welding made alongside them.
- Welds were sectioned, according to the procedure described in Section 4.4, lengthwise along the centreline of the sample to ensure that the position of thermocouples entering the sample from either side would be revealed.
- The two halves of each weld were then cold mounted with the upper most surface (the surface with writing on) facing outwards from the mount.
- Metallographic grinding and polishing were carried out.
- Welds were etched with 5% Nital to reveal the microstructure within key regions: the nugget and the heat-affected zone, and to establish precisely which of these regions each thermocouple fell within.

- Microhardness profiles were taken across the welds to establish any effect of weld schedule on the localised hardness of specific regions.

Micrographs and hardness profiles can be seen in conjunction with the associated thermocouple readings in Section 6.4.

5.3.5 A comparison of sheathed and plain wire thermocouples

Characteristics of plain wire thermocouple readings

Several important findings were made during early trials with plain wire thermocouples. It was found that there were mild to severe fluctuations in many of the temperature readings and that the peak temperatures measured did not match the peak temperatures expected, in some cases by several hundred degrees centigrade.

Figure 5.27 provides a typical example of these fluctuations. This plot is the output from an R-type thermocouple that was located in the weld pool / nugget region of a spot weld produced using 25 cycles of current. A drop from 440°C to 408°C over 10 samples (0.02 seconds) is highlighted. Overall this plot suggests that during the weld, drops of approximately 35°C occur in between the application of one cycle of current and a subsequent application. Such a drop would require that a big heat sink effect was present around the weld to draw the heat out fast enough to see this effect. Although the electrodes, which are in close proximity to the weld pool, are water cooled it was unclear if there would be sufficient a thermal gradient to produce this effect from the current cycling alone. It was also of concern that the maximum reading, in this example, was only 800°C. This suggests that the metal had not actually melted and yet a full weld, of the expected size was found on sectioning of the coupon.

It was considered possible that interference from the magnetic field associated with the spot welding machine was causing the distortion of the readings. To establish if the effect was solely due to the magnetic field, a thermocouple was attached to a plain steel coupon and laid parallel to the thermocouples attached to a test coupon. Thus, any magnetic effects, inducing currents in the wires would affect the non-weld thermocouple as much as those attached to the test coupon.

Figure 5.28 is a plot of the results obtained from the cold sample thermocouple. It can be seen that the fluctuations are consistent in magnitude at around 1°C, centred around a temperature of approximately 20.8°C. It is also clear that one fluctuation takes approximately 1 cycle or 0.02 seconds. Therefore, it seemed that these fluctuations of less that 1°C were related to the magnetic field fluctuations caused by the cycling current application. However, the larger distortions seen in Figure 5.27 could not be attributed to the magnetic field variations during welding.

In some samples a large dip in the measured temperature occurred at the start of welding (current application). An example of this can be seen in Figure 5.29. Clearly a temperature of -450°C is not the true temperature of the weld sample and other samples showed similar and larger drops on initial application of current.

A further possibility was that an electrical effect, due to the direct contact between the thermocouple and the weld coupons could be responsible for the fluctuations in the temperature readings. Figure 5.30 provides a typical plot for the three thermocouple outputs from a weld produced using 15 cycles of current.

The output from R1 climbs fairly steadily to approximately 1050°C. It then experiences fluctuations of up to 100°C. Nine clear, smaller peaks can be seen and after the last 'sharp' peak there is a drop of 200°C followed by a small rounded peak. K1 shows a similar trend with a smaller initial rise of 200°C followed by 14 small, sharp peaks. After the last 'sharp' peak a more pronounced, wider, more rounded peak exists of approximately 650°C followed by gradual decrease in temperature. K2 shows a few small peaks after an initial peak of 500°C, the first half of which are more pronounced that the second half. After the last 'sharp' peak there is a gradual rise of 50°C over the next 100 cycles (0.2 seconds) followed by a slow cool.

Considering the K2 readings, as there are 14 peaks (15 troughs) it seemed likely that these patterns were in some way related to the cycles of current being applied. The smooth, rounded peak at the end of the 15 cycles does not appear to be distorted in the same way as the measurements taken during the weld cycles. It is postulated that electrical interference could be causing the cycling of the thermocouple readings by 'pulling down' the readings from the true temperatures during current application. This effect is removed

at the end of the heating cycles.

Again using K2 as an example, in a 15 cycle weld, the first cycle causes a temperature rise. At the first peak the alternating current changes direction and, due to electrical interference, a drop in the temperature reading is seen. This pattern persists until the end of the last peak. The final peak is actually the point at which the current is switched off and the temperature reading initially drops due to the decay of the interference. The subsequent large increase in the measured temperature suggests that the true temperature experienced by K2 was far higher than measured and that thermocouple K2 was only 'free' to read the accurate temperature after the current had been switched off. A similar theory could be applied to the readings from R1.

Many readings from plain wire thermocouples displayed similar patterns to those described above. This suggests that wire thermocouples may be suitable for determining cooling rates but not necessarily peak temperatures.

An example of the location of a wire thermocouple in a spot weld is given in Figure 5.31. This micrograph indicates that the thermocouple in this example was successfully located in a position that allowed the heat-affected zone's thermal profile to be measured. This result validates the technique used to position the wire thermocouples prior to welding.

Practical aspects of using sheathed thermocouples

Due to the limitations of the plain wire thermocouples, K-type sheathed thermocouples were used with two trial welds. Figure 5.32 shows a sample with sheathed thermocouples in place. The external diameter of the sheathed assemblies was 1.5mm. The nickel - aluminium and chromium wires that actually make up the thermocouple are insulated by a mineral powder filling inside a metallic alloy shell. The thermocouples were 50mm in length and connected to matched compensating cables at the thick metal connection seen in Figure 5.32.

There is no electrical connection between a sheathed thermocouple and a weld coupon due to the containment of the actual thermocouple wires within the sheath. Thus, if the passage of electrons from the sample to the plain wire samples, or vice versa, is responsible for the fluctuations in temperature previously shown, sheathed thermocouples

should eliminate the effect. Due to the heavier nature of the sheathed thermocouples the two halves of the weld coupon had to be lightly taped together to prevent them coming apart prior to welding.

Characteristics of sheathed wire thermocouple readings

Two trials were made with the K-type sheathed thermocouples in place. One had the thermocouple in a heat-affected zone 'slot' and the other in the weld nugget / weld pool 'slot.' The second test was designed to verify the peak temperature as being greater than, for example, the 800-1000°C previously measured. However, due to the maximum operating temperature of 1350°C for K-type thermocouples it was expected that the sheathed thermocouple in the weld pool would not survive to measure the cooling rate of the weld nugget.

Figure 5.33 is the output from the sheathed thermocouple positioned in the heat-affected zone 'slot' of a weld coupon. A smooth increase in temperature from room temperature to approximately 450°C can be seen followed by a smooth cooling section. The increase to the peak temperature takes 1 second, which is equivalent to 50 cycles. This result suggests that the temperature of the heat-affected zone continues to increase for some time after the application of the current ceases.

Confirmation of this suggestion can be found in Figure 5.34. In this figure the rate of change of temperature can be seen. Many clear peaks in the graph can be seen but they are not as sharp as those in, for example, Figure 5.30.

A total of 15 peaks can be seen, each peak preceded by a deep trough followed by some smaller intermediate, closely spaced peaks. In the earlier part of the welding cycle the smaller peaks are not as easily distinguished but so still appear to separate larger peaks. In the latter part of the welding cycle the intermediate peaks are clearly visible and regular. As this graph shows the rate of change of temperature each positive peak represents a peak in the rate of increase of the heat-affected zone temperature. Thus the 15 peaks indicate 15 cycles of current. On application of a current, the rate of increase of temperature increases to a maximum, then the 'off' part of the current cycle occurs, that is the time for which the current is not actually flowing as a result of the chopped waveform used, and the rate of increase drops. However, even during these drops the temperature is

still increasing because the rate of change of temperature is still positive. On application of another cycle of current, the rate of increase of temperature again increases and then falls.

After the first cycle is applied it is interesting to note that the rate of change of temperature in fact becomes negative, indicating a decrease in the temperature of the sample. This is likely to be because the weld coupon provides sufficient a heat sink to cool the heat-affected zone by drawing out the small amount of heat generated by one cycle of current. Over the three subsequent cycles of current application the rate of change increases but after the fourth cycle the rate drops off indicating that the temperature is still increasing but at a slower rate. The final eight cycles maintain a fairly constant rate of increase at 500°C/s.

After the 15^{th} cycle the rate of change of temperature remains positive for a further 240 samples (24 cycles) which agrees with the result seen in Figure 5.31. That is, the temperature of the heat-affected zone continues to increase for 0.5 seconds after the end of the heating cycle. This is thought to be because the heat is generated in the weld pool / nugget itself and due to conduction of heat energy taking a finite time there will be heat in the weld nugget to be drawn down the thermal gradient after the flow of welding current has ceased. After this period the rate of change becomes negative indicating the cooling of the heat-affected zone.

The particularly important aspect of these results is that the sheathed thermocouple readings did not experience the same distortions as the plain wire thermocouples. Thus they allowed detailed information about the rate of change of temperature during welding to be determined.

One further weld was made using a sheathed thermocouple, this time in a weld pool / nugget location. Figure 5.35 provides the output from the three K-type thermocouples used. K3 is the output from the sheathed thermocouple and K1 and K2 are plain wire thermocouples.

There are several clear features of this graph:

- The sheathed thermocouple output (K3) is smooth and not subject to the fluctuations

seen in K1 and K2.

- The temperature readings for K3 ceased abruptly at approximately 1250°C after just over 10 cycles of heating.
- The sheathed thermocouple does not start to show an increase in temperature until 3.5 cycles into the weld.
- The K-type thermocouples in the heat-affected zone locations do not appear to be as severely distorted as previously seen.

The smooth output of the sheathed thermocouple was expected but the smoother outputs from K1 and K2, with realistic peak temperatures indicates that plain wire thermocouples are not always severely affected by the electrical interference previously identified. The cut-off of the temperature readings of K3 at 1250°C was also expected due to the normal operating range of K-type thermocouples.

The critical result from this plot is that there is a lag of approximately 0.07seconds in the output of the sheathed thermocouple. This indicates that it would not be possible to combine sheathed and plain wire thermocouples in one test specimen and accurately compare the output from the two types. It also raises doubts about the accuracy of the output of sheathed thermocouples with regard to time in general, suggesting that cooling rates determined from these thermocouples may not be accurate.

One point of concern is that the sheath material itself appears to have become incorporated into the weld nugget as a result of the welding process. Figure 5.36 indicates that the nugget itself is brighter in appearance that the surrounding heat-affected zone. EDX analysis of the nugget area indicated the presence of small amounts of platinum. The effect of this alloying on the weld pool temperature and microstructure could not be clearly assessed with the two samples available. However, it is clear that the introduction of an external alloying element into the weld pool is undesirable – a robust measuring technique should ideally have no effect on the object being monitored.

In summary, the plain wire thermocouples provided a true result with time and no chemical interference with the weld pool itself, but the readings were affected by electrical interference from the strong weld currents due to the electrical contact between

the wires and the weld coupon. The sheathed thermocouples provided readings free from electrical distortion allowing greater detail to be drawn from the output. However, chemical interaction with the weld pool and a difficulty in the precise location of the thicker thermocouples inhibits the association of output with the microstructure and a significant delay in the initial output raises concerns about the accuracy of the time – temperature relationships produced by this thermocouple type.

Overall it was decided to use plain wire thermocouples to carry out the main investigation into the change of thermal profile during welding with weld schedule. The results can be found in Section 6.4.

6. RESULTS AND DISCUSSION – EXPERIMENTAL FINDINGS

6.1 Resistance Spot Weld Microstructures and Advanced Processing Techniques

This section is concerned with the results from basic and advanced welding trials. The microstructural features of $5\sqrt{t}$ welds made in each of the six steel grades are presented as well as an analysis of the relationship between the measured microhardness and the carbon equivalent value for each steel. The weld settings established for use in advanced extended weld time and multi-pulse welding schedules are identified and the change in microhardness profile associated with the use of such schedules is investigated.

6.1.1 Properties of simple schedule resistance spot welds

In order to establish the significance of carbon equivalent (CE) on weldability welds of diameter $5\sqrt{t}$ were produced in the six steel grades using the settings detailed in Section 4.2. A detailed examination of the microstructural constituents in both the weld nugget and heat-affected zone was carried out and example micrographs can be found in Figures 6.1-6.6.

LC was the lowest CE grade (0.04) and had a thickness of 1.6mm. A standard mild steel grade, it was selected to act as a reference for the other materials. Figure 6.1(a) is the unwelded or base microstructure, which is predominantly ferrite with an average grain size of 21 microns and less than 1% pearlite. The overall shape of the weld made in this material can be seen in Figure 6.1(b). The weld nugget in this steel extends to just before the notch between the two sheets. The heat-affected zone varies from 0.3 to 0.5mm at the edge of the weld nugget but is much thinner, 0.1mm around the top and bottom of the weld nugget. Figure 6.1(c) is a detailed micrograph of the weld nugget structure. Two features can be clearly distinguished: the overall columnar structure and an internal structure of fine needles which run in two direction, across the prior austenite columnar grains or parallel to their grain boundaries. The progression from the weld nugget through to the base structure can be seen more clearly in Figure 6.1(d). It is obvious that the grain size decreases as the distance from the weld nugget increases. Figure 6.1(e) is a detailed micrograph of a point half way between the two isotherms represented by the fusion line and parent material boundaries. Three features appear in this figure: there are regions of equiaxed ferrite grains of an average of 8 microns; at some of the grain boundaries there

are groups of between ten and twenty very small ferrite grains, less than 5 microns on average; and also at grain boundaries there are darker regions of carbide.

The weld in the LCNb (CE – 0.07) steel exhibited some similar features to that observed in the mild steel weld. The micrographs for this 2.0mm thick grade can be seen in Figures 6.2(a) to (e). The parent material structure, Figure 6.2 (a), is again predominantly ferrite with 4% pearlite present. The average ferrite grain size in the LCNb steel is 25% that of the mild steel grade at 5 microns. Figure 6.2(b) is a low magnification image to illustrate the macro-weld shape. This weld nugget is squarer in appearance than the LC equivalent. The fine-grained heat-affected zone is wider and present right around the weld nugget, possibly due to the thicker gauge. It also extends out to points at the extremities of the weld nugget. The weld nugget structure, Figure 6.2 (c), is similar to that observed for the LC grade. The fine needle substructure is divided along lines relating to the prior austenite structure. Figure 6.2(d) again show the detail of the progression through from the weld nugget to the base structure and it is clear that the heat-affected zone is more consistent in width than for the previous grade at 0.5mm (500 microns). A detailed micrograph of the heat-affected zone can be seen in Figure 6.2(e) and there are similarities to the structures observed in the LC grade. There are again three important features. The average grain size is 4 microns with the smaller groups of grains gathered at grain boundaries have an average grain size of 2 microns. The carbide areas are more numerous but similar in size to those seen in the LC grade.

The DP600 grade, at 1.8mm thick, has the lowest CE for the dual phase grades in this trial at 0.14. The parent structure (Figure 6.3(a)) of this alloy is a ferrite matrix with 26% martensite second phase. The martensite was located as islands at intersections between ferrite grains. The weld nugget shape can be seen in Figure 6.3(b) and as for the LCNb grade there is no obvious notch at the interface of the two sheets. A small void was evident in the centre of the weld nugget. The overall weld nugget shape is square, extending slightly further at the centre of the weld, as seen in the cross section. The weld nugget, however, is approximately oval in shape and this leads to a variation in the heat-affected zone width around the nugget. The weld nugget structure can be seen in detail in Figure 6.3(c). As for the lower CE grades, the prior austenite columnar grain boundaries can be clearly distinguished but the nature of the transformed structure is different for the DP600. The structure is lath like but many of the laths extend across the whole width of a

single columnar prior austenite grain whereas, in the lower CE grades, the structure was more needle like than lath like and the needles were much shorter in length. The change in grain size from the weld nugget through to the unwelded material is seen clearly in Figure 6.3(d). The heat-affected zone is thicker at the 'corners' of the weld at 0.5mm but at the centre and top of the weld it narrows to 0.3mm.The details of the heat-affected zone (Figure 6.3(e)) can be seen to contain far less ferrite than previous grades. The structure is predominantly fine, darkly etched laths, which appear bainitic in nature. They are difficult to resolve using an optical microscope but a scanning electron micrograph (Figure 6.6(f)) clearly resolved the lath like nature of the darker areas.

The CE of the DP800 grade is 60% higher, at 0.22, than for the DP600 dual phase steel. The base structure is dual phase ferrite – martensite but in this grade the martensite is present as continuous networks around the ferrite grains. This can be seen in Figure 6.4(a). The percentage second phase in this material is higher at 30%. The overall weld shape can be seen in Figure 6.4(b). It is square overall with a slight bulge at the centre of the weld. The weld nugget itself is approximately oval in shape and this, as seen previously, leads to a change in the thickness of the heat-affected zone around the edge of the nugget. The heat-affected zone itself extends past the notch at the centre of the sample. The nugget structure (Figure 6.4(c)) is similar to that observed for the DP600 grade with a lath substructure partitioned by the prior austenite grain boundaries. In this weld nugget there are fewer clearly defined laths and the structure, whilst extending completely across some columnar grains, is finer in nature than observed in the lower CE steels. The detail of the change in microstructure between the unwelded material and the weld nugget can be seen in Figure 6.4(d). The heat-affected zone is widest at the 'corners' of the weld where it extends to 0.8mm. At the centre and top of the weld the average thickness is 200 microns. The microstructure of the heat-affected zone is clearly different at the outer edge, adjacent to the unwelded material and at the inner edge adjacent to the nugget. The hardness of these two regions was significantly different (see Table 6.1 and Section 6.1.2). The detail of the 'outer' heat-affected zone is shown in Figure 6.4(e) and it can be seen that the average grain size is half that of the heat-affected zone in the DP600 alloy.

The DP1000 grade has a slightly higher CE at 0.24 but is only 1.2mm in thickness compared to the 2mm of the DP800. The base microstructure (Figure 6.5(a)) is similar to

the DP800 in that it presents as a continuous network of martensite (around ferrite grains. The proportion of martensite is 44%. The overall weld shape can be seen in Figure 6.5(b) to be square with an oval nugget. The weld nugget structure is similar to that seen for the DP800 weld with a lath substructure bounded by prior austenite grains. However, the columnar grains in this grade are narrower than those observed in the other steel grades. The size of the heat-affected zone is shown in Figure 6.5(d) and it can be seen that it is wider at the 'corners' of the weld, where it is 0.5mm compared to the top and edge where it is on average 0.25mm. The detail of the heat-affected zone can be seen in Figure 6.5(e). The structure is finer than for the DP800 grade with the average grain size only 70% of the lower CE grade.

The highest CE material is the DP1400 at 0.27, with a thickness of 1mm. The base microstructure (Figure 6.6(a)) is similar to that for the DP800 and DP1000 grades with a continuous network of martensite (47%) surrounding the ferrite grains in the structure. The weld shape is shown in Figure 6.6(b) and it can be seen that the weld is fairly rounded at the ends with an oval weld nugget. The weld nugget structure, seen in Figure 6.6(c) is lath in morphology but, contrary to the other grades, the prior austenite grains cannot clearly be distinguished in the nugget. In addition, the laths themselves do not run parallel to each other for more than a few laths. Welds in the other steel grades had large areas, and sometimes whole columnar grains that had laths running predominantly in the same direction. The laths are much more disordered in this grade. The variation in the heat-affected zone can clearly be seen in Figure 6.6(d). As has been seen in the previous two grades, the heat-affected zone appears to have two distinct regions. The outer region is shown in more detail in Figure 6.6(e). The microstructure here is very similar to that for the DP1000 with a fine mix of ferrite grains and what is thought to be bainite grains.

6.1.2 Microhardness of 5√t welds

For each of the six materials detailed above, microhardness measurements were taken in the parent material, the heat-affected zone and the weld nugget. The average value for each area is given in Table 6.1. In all six steels the weld nugget microhardness increases with carbon equivalent. The heat-affected zone also increases with CE but there is a difference in the location of the point of peak hardness. The DP800 inner heat-affected

zone is harder but for the DP1000 and DP1400 the outer portion of the heat-affected zone is harder.

Overall there is a strong relationship between the CE and hardness in the welds. Figure 6.7 shows this more clearly. The regression line shown can be described by the following equation:

$$\text{Microhardness} = 1304(\text{CE}) + 132 \qquad [6.1]$$

R^2 is a measure of how well a regression line fits real data. It can take a value of between 0 and 1 with 1 indicating a perfect fit. The R^2 value for the line shown is 0.95. It should be noted that grain size also had an effect on the measured microhardness and this is considered further in the general discussion (Section 7).

Microhardness profiles, taken across 5vt welds made in each of the six steels in this investigation, can be seen in Figure 6.8. It can be seen that the hardness of the six welds increases in the same order as the CE value. It can also be seen that the LC, LCNb and DP600 grades have their peak hardness in the weld nugget. The higher CE (>0.22) DP800, DP1000 and DP1400 welds demonstrate a peak hardness in the heat-affected zone.

In addition to the actual microhardness of the areas of the welds, the percentage increase in hardness was also considered. The values for percentage increase are given in Table 6.2 and it can be seen that for all the grades the heat-affected zone and the weld nugget show some increase but the % increase is largest for the DP600 and DP800 welds. This pattern can be seen in Figure 6.9 with the weld nuggets and heat-affected zone hardness following different trends. For the heat-affected zone, the lower CE materials show increases of around 40%, the middle two materials 60-70% and the higher materials less than 40%. The DP1400 heat-affected zone increases only 10% from the base value. The nuggets show higher increase in general. The lower CE grade nuggets increase in microhardness by 60% compared to the base value, the middle grades by more than 80% and the highest CE grades by 40% or less. Again the DP1400 shows only a very small increase of 3%.

6.1.5 Summary

This section presented the first set of practical welding results. The microstructures observed in standard $5\sqrt{t}$ welds were found to vary with an increase in alloy content. The weld nugget microstructure changed from lath ferrite to martensite as the CE of the alloy increased, from 0.04 through to 0.27. Microhardness profiles for each of the six steels were presented and it was seen that the overall weld hardness increased in the same order as the CE values for the steels. However, the lower alloy grades, LC, LCNb and DP600 ($CE<0.15$) demonstrated a peak hardness in the weld nugget whereas the higher alloy grades DP800 to DP1400 ($CE>0.22$) showed a peak in the heat-affected zone.

6.2 Continuous Cooling Transformation Behaviour

This section presents the continuous cooling transformation (CCT) behaviour observed in each of the six steels included in this investigation. This behaviour was characterised in terms of the transformation start and finish temperatures measured during continuous cooling transformation experiments using a Gleeble thermo-mechanical simulator, and the transformation products observed. The transformation temperatures are presented in the standard format of a CCT curve and an 'atlas' of the microstructures has been created to allow the gradual changes through a progression of cooling rate to be followed. In addition, information concerning the relationships between carbon equivalent, cooling rate and transformation products have been extracted and presented separately to clarify the interactions.

6.2.1 Continuous Cooling Transformation Curves

The procedure for production of the CCT curves presented in this section can be found in Section 4.3. The transformation temperatures extracted from the raw dilation curves for each sample are described and the trends with cooling rate for each individual material considered.

Steel LC (CE – 0.04)

The CCT curve for the LC mild steel grade can be seen in Figure 6.10. The prior austenite grain size measured in a water quenched sample of this material, after following the standard programme, was slightly larger than for the other samples at 9.9μm. The transformation start temperature (AR_3) for the slowest cooled sample (0.5°C/s) was measured as 875°C. This transformation start temperature dropped to 862°C for the sample cooled twice as fast, at 1°C/s and then decreased gradually across the following six samples to 839°C. For four of the first seven samples a second transformation could be distinguished on the dilation curves produced. The samples of LC that were air and water-quenched had cooling rates that were measured as 392 and 3058°C/s respectively. These two samples demonstrated transformations at significantly lower transformation temperatures than the slower cooled samples of around 690°C. The AR_3 for the water-quenched sample was determined from the thermocouple readings used during the thermal cycle and it is interesting that it agrees with the temperature determined from the dilatometry for the air-quenched sample.

Steel LCNb (CE – 0.07)

Figure 6.11 shows the CCT curve for the LCNb steel alloy. The prior austenite grain size for these samples was 8.3μm. The transformation start temperatures for the samples cooled up to 35°C/s was consistently between 810°C and 840°C. The slowest cooled samples (0.5 and 1°C/s) demonstrated the highest transformation temperatures at approximately 840°C. The AR_3 dropped to just under 830°C for the 5 and 10°C/s samples and finally to approximately 815°C for the fastest cooled samples (20 to 35°C/s). For some of the faster cooled samples, a second transformation could be distinguished from the dilation curves. The air-quenched sample achieved a cooling rate of 73°C/s and had a slightly reduced AR_3 of 764°C. The water-quenched sample showed a further reduction in the AR_3 to 664°C as determined from the thermocouple measurements for that experiment. The cooling rate for this sample was 2575°C/s.

Steel DP600 (CE – 0.14)

The CCT curve for the DP600 grade is more complex than for the previous two grades and can be seen in Figure 6.12. The prior austenite grain size in these samples was measured at 9.4μm. The transformation start temperatures measured for this grade were, for all but one sample, below 800°C. The sample cooled at 0.5°C/s had an AR_3 of 817°C. The AR_3 then decreased steadily for the samples cooled between 1 and 35°C/s. At cooling rates of 1 to 2°C/s the AR_3 is approximately 800°C. The increase in cooling rate to between 5 and 35°C/s produces AR_3 measurements from 783 to 776°C. All but the two slowest cooled samples produced visible second transformations on their dilation curves as indicated in Figure 6.12. The air-quenched sample, which cooled at 73°C/s showed a significant reduction in the AR3 to 690°C. The water-quenched sample achieved a cooling rate of 2206°C/s and an AR_3 of 455°C was determined from the thermocouple output.

Steel DP800 (CE – 0.22)

The CCT curve for the DP800 grade can be seen in Figure 6.13. It was produced from a prior austenite grain size of 8.3μm. It can be seen that the AR_3 transformation temperatures for this grade are all below 800°C and also that they are clearly sensitive to the cooling rate, with significant drops between each subsequently faster cooled pair of samples. The highest measured AR_3, for the sample cooled at 0.5°C/s, was 767°C/s. This

decreased to just over 700°C for the samples cooled between 1 and 10°C/s. The faster cooled samples, with cooling rates of 20 to 30°C/s, showed an AR_3 of between 695 and 685°C. All but two of the controlled cooling curves revealed second constituent transformations on the dilation curves. Five air cooled samples were available for this CCT curve due to the use of prior grinding to reduce the thickness of samples of this steel grade (see Section 4.3). These samples all demonstrated a significant reduction in the AR_3 to less than 500°C. The cooling rates achieved by air quenching were between 126 and 465°C. Water quenching produced a cooling rate of 1978°C/s in the DP800 and the AR_3, determined from thermocouple measurements, was 410°C.

Steel DP1000 (CE – 0.24)

Figure 6.14 provides the CCT curve for the DP1000 steel grade. The prior austenite grain size in the samples used to produce this CCT curve was 7.8μm. The AR_3 transformation temperatures in this Figure can be seen to be strongly dependent on the cooling rate. At 0.5°C/s the AR_3 is at it highest at 785°C. This decreases to around 770°C for the samples cooled at between 1 and 5°C/s. The AR_3 then drops significantly to 731°C for the sample cooled at 10°C/s. Further steady decreases in the AR_3 are seen for the next three samples with a drop to 689°C for the fastest controlled cooling sample. Air quenching in this alloy produced a cooling rate of 133°C and a corresponding AR_3 of 560°C. The samples cooled at between 5 and 133°C/s had second constituent transformations visible on their dilation curves. The water-quenched sample had a measured cooling rate of 1950°C/s, the AR_3 in this sample being 431°C. This lies close to the second transformation temperature for the samples, cooled at 33°C/s and 133°C/s that had second constituent transformation temperatures of 407°C and 396°C. The water quench sample AR_3 was determined using the thermocouple readings whereas the second constituent temperatures were taken from the appropriate dilation curves.

Steel DP1400 (CE – 0.27)

The CCT for the DP400 alloy can be seen in Figure 6.15. The prior austenite grain size for this sample was 7.5μm. The AR_3 transformation temperatures fall steadily with cooling rate for the first eight samples. The maximum AR_3, for the sample cooled at 0.5°C/s, was 737°C. This decreases for the following seven samples with second constituent transformations seen for the two slowest cooled samples. For the samples

cooled at 5 to 10°C/s the transformations started at approximately 760°C and for the fastest controlled cooling samples the AR_3 is around 640°C. The air-quenched sample produced a relatively high cooling rate of 323°C/s and the AR_3 for this sample was 578°C. Water quenching resulted in a very high cooling rate of 9450°C/s. The transformation temperature of this sample was determined from the thermocouple readings taken during the experiment and found to be 405°C.

6.2.2 Continuous Cooling Transformation Microstructures

A detailed examination of the continuous cooling transformation microstructures was made using both optical and scanning electron microscopy. An 'atlas' of the microstructures that were found in the six steels examined are presented in Figure 6.16 through to 6.21. The main series of micrographs were taken at a magnification of x500 to facilitate the comparison of microstructures between different steels and cooling rates. Additional, higher magnification optical and scanning electron micrographs have been included where they can provide clearer detail of fine microstructure constituents. Each micrograph in the main series has been appended with the percentage of different transformation products that was measured using a point counting technique. The definition of the phases has been confined to proeutectoid (primary) ferrite, coarse acicular ferrite, lath ferrite, pearlite, bainite and martensite with each term relating to constituents as described in the review of literature, Section 2.

Steel LC (CE – 0.04)

Figures 6.16(a) to (j) is the series of micrographs illustrating the range of continuously cooled microstructures found in the LC alloy. The microstructures seen are predominantly ferrite – pearlite in nature, with the proportion of pearlite varying little with cooling rates up to 26.6°C/s (Figures 6.16(a) to (h)). The ferrite grain size decreases steadily as the cooling rate increases with an average size of 22.9μm at 0.5°C/s, down to an average of 15.8μm at a cooling rate of 35°C/s. It can be seen from Figures 6.16 (i) and (j) that following either air or water quenching the microstructure is significantly different to those produced through continuous cooling. Figure 6.16(i) shows, in the case of the air-quenched sample, more unevenly shaped grains with some lath shaped grains in between having replaced the clear equiaxed grains seen at the lower cooling rates. These structures are also seen in Figure 6.16(j), the water-quenched microstructure. In this sample the lath

ferrite has etched much darker than the ferrite. The ferrite can still be seen to have predominantly uneven boundaries in this fastest cooled sample.

Steel LCNb (CE – 0.07)

The micrographs for the LCNb grade are given in Figures 6.17(a) to (l). Figures 6.17(a) to (d) show the samples cooled at between 0.5 and 5°C/s. The microstructures in these samples is ferrite - pearlite. The ferrite grain size decreases with cooling rate across these four images going from 19.4μm at the slowest cooling rate to 14.8μm when cooled at 5°C/s. The fraction of pearlite varies between 3.3 and 4.5% in these samples.

At a cooling rate of 10°C/s a ferrite constituent with a different morphology is seen. An example of this can be seen in Figure 6.17(e). More detailed micrographs of the two variations seen for this constituent are given in Figures 6.17(k) and (l). The constituent has a needle like shape. This can be clearly seen in Figure 6.17(k), in which the needles are lying parallel to each other. The needles were also often observed to be interlocking in nature as seen in Figure 6.17(l). The presence of these needles was generally associated with fine areas of pearlite. Occasionally, only one or two needles would be seen intersecting an area of pearlite whereas in other areas the number of needles was much higher. The features seen are consistent with the coarse acicular ferrite (CAF) constituent previously reported by Harrison[56, 57]. In the sample demonstrating this feature, a general refinement in the ferrite grain size can be seen.

As the cooling rate increases, the ferrite grains become more irregular in shape and the proportion of CAF increases, as shown in Figures 6.17(g) to (i). In the samples cooled at 35 and 73°C/s no pearlite was detected indicating that the excess carbon, previously accommodated by the pearlite, is now incorporated into the non-equilibrium structures observed.

The large increase in the cooling rate to 2575°C/s, on water quenching, results in a significantly different microstructure to those already seen in this grade. In this sample approximately one third fine grained, proeutectoid ferrite was present. The remainder of the structure is lath ferrite, different from the CAF in that the grains are not associated

with fine regions of pearlite and they are less clearly defined in shape than the CAF needles.

Steel DP600 (CE – 0.14)

Examination of the DP600 continuously cooled samples revealed a range of microstructures. Figures 6.18(a) to (m) provide the series of micrographs illustrating them. The slowest cooled sample (0.5°C/s) reveals a ferrite – pearlite microstructure with 6.2% pearlite measured. Using an optical microscope indicated that the pearlite islands appeared similar to the martensite islands previously seen in the base structure. However, the scanning electron micrograph shown in Figure 6.18(k) indicates that the dark islands have the lamellar structure that is characteristic of pearlite. This dual phase structure persists to a cooling rate of 5°C/s with a refinement in both the ferrite and pearlite grain sizes seen in Figures 6.18(a) through to 6.18(d).

The sample cooled at 10°C/s revealed an additional microstructural constituent. A small area of this can be seen in Figure 6.18(e) and an enlargement of a different area can be seen in Figure 6.18(l). The constituent consisted of ferrite needles associated with fine areas of carbide, which indicates the presence of coarse acicular ferrite (CAF). This feature increases in volume fraction as the cooling rate increases through 20, 25, 35 to 72°C/s and the increase in cooling rate was also associated with a further refinement in the ferrite grain size.

At a cooling rate of 24.9°C/s, the areas of CAF become associated with larger, darker etching areas that have some needle like features present surrounded by areas of carbide. This is different to the areas of CAF that were associated with small particles of pearlite in previous samples. A detailed micrograph of an example area is shown in Figure 6.18(m). To assist with identification of the darker etching constituent, microhardness measurements were taken of the two areas using a 10g load. The low load was necessary to ensure that the diamond indent was small enough not to impinge on more than one constituent. The measured microhardness of the CAF was 72Hv, consistent with that measured in samples that displayed no darker etching carbide areas. The carbide areas themselves measured 248Hv in microhardness. These measurements, coupled with the change in two-dimensional morphology resulted in the darker etching phase being defined as bainite.

The microstructure of the fastest cooled sample, shown in Figure 6.18(j) exhibited a different overall structure to the slower cooled samples. Individual proeutectoid ferrite grains could not be distinguished. Microhardness measurements of the lighter and darker etching areas revealed no significant difference (the light areas were measured at 408Hv and the darker areas at 414Hv). The structure was thus considered to be predominantly martensitic with some areas of fine bainite.

Steel DP800 (CE – 0.22)

The series of micrographs for the DP800 alloy are given in Figures 6.19(a) to (l). At slower cooling rates of up to 2°C/s (Figures 6.19(a) to (c)) the microstructure was ferrite pearlite in nature. Using the scanning electron microscope also confirmed the presence of the pearlite. An example of one area of pearlite can be seen in Figure 6.19(k) where the lamellar structure of the constituent can clearly be seen. The lamellae are often broken up as opposed to being totally regular and this variation on a regular lamellar structure is often called 'degenerate.' The volume fraction of pearlite decreases from 25.5% at a cooling rate of 0.5°C/s to 18.9% in the sample cooled at 2°C/s. The grain size of both the ferrite and the pearlite decreases, as the cooling rate increased within this range, Figures 6.19(a) to (c).

From Figure 6.19(d), relating to a cooling rate of 5°C/s, the CAF, seen in lower carbon equivalent materials emerges in the microstructures. In the case of the DP800 steel this constituent was finer in nature than previously seen. Increasing the cooling rate to 5 and 10°C/s also lead to a further reduction in the ferrite and pearlite average grain size.

From a cooling rate of 20 to 119°C/s, Figures 6.19(f) to (i), a bainite constituent was seen in the microstructures. This constituent is clear in Figure 6.19(g). It etches darker than the CAF and had a less clearly defined needle like structure that could be resolved through the different relief of the separate needles. The scanning electron microscope provided more detail of these darker areas and an example can be seen in Figure 6.19(l).

Martensite was detected in the microstructure of the continuously cooled samples from a cooling rate of 35°C/s onwards. The appearance of the martensite was different to the bainite observed in the structure, in that it was more lath like and no clear carbides could be distinguished in between laths. Further, microhardness measurements distinguished

two clear constituents. For example, the areas described as bainite had a microhardness of 364Hv in the sample cooled at 119°C/s whereas the martensite had a microhardness of 409Hv. All the readings were taken using a 10g indenting load. In the water-quenched sample (seen in Figure 6.19(j)) no difference in the microhardness was measured for different areas of the microstructure and this sample was considered to be fully martensitic.

Steel DP1000 (CE – 0.24)

Figures 6.20(a) through (k) provide the series of micrographs showing the continuously cooled microstructures obtained with the DP1000 grade. The two slowest cooled samples (0.5 and 1°C/s) seen in Figures 6.20(a) and (b) showed microstructures considered to be ferrite pearlite in nature. The ferrite grain size halves between (a) and (b) due to the doubling of the cooling rate and the pearlite grain size is similarly refined. The volume fraction of pearlite was around 36% for both these samples.

At cooling rates of 2°C/s and greater, the CAF constituent previously described appeared in the microstructures. At a cooling rate of 5 to 20°C/s, bainite was also evident. In the sample cooled at 20°C/s, the volume fraction of proeutectoid ferrite decreased by more than 50% to 25.9% from the 63.8% seen in Figure 6.20(a) that shows the sample cooled at 0.5°C/s.

At a cooling rate of 24.9°C/s (Figure 6.20(g)), a proportion of martensite was observed in the final microstructure. The complex mix of ferrite, CAF, bainite and martensite is shown in Figure 6.20(h), which represents the samples cooled at 33.8°C/s. A higher magnification image of this sample can be seen in Figure 6.20(k). The well defined needles of the CAF can be clearly seen as well as the more lath like areas of bainite and martensite. Additional evidence for the existence of martensite was the microhardness measurements taken of the different constituents. For example, in the sample cooled at 33.8°C/s, the areas considered to be bainite had a microhardness average of 308Hv determined using a 10g load but the small areas thought to be martensite produced microhardness measurements of 439Hv. The overall microstructure of the samples cooled at 25 and 35°C/s was more refined than the slower cooled samples.

The air and water-quenched samples both revealed microstructures that did not contain any proeutectoid ferrite. In these samples it was particularly challenging to identify areas of different constituents. Microhardness measurements taken using a 10g load identified two constituents, one with a microhardness of 455Hv and the other with a reading 533Hv. Although the measurement of 439Hv was thought to indicate martensite in the sample cooled at 35°C/s, it was considered that in the water-quenched sample this reading could indicate a refined bainite constituent. The areas measured at 533Hv were thought to be martensite.

Steel DP1400 (CE – 0.27)

The 'atlas' of continuously cooled microstructures for the DP400 can be seen in Figures 6.21(a) through (k). The two slowest cooled samples, 0.5 and 1°C/s (Figures 6.21(a) and (b)) are distinct from the faster cooled samples in that they contain only ferrite and pearlite constituents. The grain size of these two phases refines slightly as the cooling rate increases from 0.5 to 1°C/s but the proportion of pearlite remains at just above 42% for both samples.

At a cooling rate of 2°C/s, CAF was observed in the microstructure and from cooling rates of 5°C/s bainite was also observed to be present. A cooling rate of 10°C/s resulted in a complex mix of ferrite, CAF, bainite and martensite as shown in Figure 6.21(e) and also more clearly in the higher magnification image, see Figure 6.21(k). The proportions of bainite and martensite quickly increased with cooling rate, from 0% at 5°C/s to approximately 96% in the samples cooled at around 24°C/s.

The air and water quenching resulted in microstructures in which no proeutectoid ferrite could be seen. These structures were considered to be fine mixtures of bainite and martensite.

6.2.3 Comparing the continuous cooling transformation behaviour of all six steels

The previous two sections considered the individual behaviour of a particular steel grade as the cooling rate in a CCT experiment increased. This section presents data that has been extracted from the CCT curves and microstructure 'atlases' in order to reveal the trends in transformation temperatures and microstructures that exist related to carbon equivalent (CE). Mathematical regression is used to develop equations that describe the trends found between parameters. Whilst regression techniques do not provide absolute measures of relationships, these equations enable the magnitude of the difference in behaviour, as the alloy content of dual phase steels increases, to be understood.

Transformation Start Temperature

Figure 6.22 shows the AR_3 transformation temperatures for the six steels plotted against cooling rate. The AR_3 is the temperature at which transformation from austenite first starts to take place. It is clear that for each individual steel, the AR_3 temperature decreased with an increase in cooling rate. In attempting to quantify the relationship between AR_3 and cooling rate, it was necessary to consider the results for the controlled cooling samples and the quenched samples separately. For the samples cooled at rates up to 35°C/s an equation was found, using regression analysis, to describe the decrease in the AR_3. This equation took the general form:

$$AR_3 = - k_{AR3} \ln (CR) + C_{AR3} \qquad [6.2]$$

where k_{AR3} and C_{AR3} are material dependent constants and CR is the cooling rate used in the continuous cooling experiment.

For each of the six steels, a value for k_{AR3}, C_{AR3} and R^2 for the regression line are given in Table 6.3. R^2, as previously defined, is a measure of how well data fits a trend line. It can be seen that overall k_{AR3} increases with carbon equivalent with the exception of the LC grade. It should be noted that the R^2 values are lower for the two low carbon grades that for the dual phase steels due to greater scatter in the results. An equation of the same form as equation [6.2] was found to describe the results for the quenched samples.

In addition to revealing the trends in AR_3 with cooling rate, Figure 6.22 highlights a clear trend with carbon equivalent. In general it can be seen that the higher the CE of an alloy the lower the measured AR_3 temperature at a given cooling rate. The exception to this

trend was the results obtained for the DP1000 grade, which were found to be generally higher than those for the DP800 at the same cooling rate.

Figure 6.23 illustrates, as an example, the AR_3 results for the samples cooled at 10°C/s. A strong linear relationship between the AR_3 and the carbon equivalent can be seen and the regression line equation for these results is:

$$AR_3 = - K_{AR3} (CE) + 874 \qquad [6.3]$$

This equation can be used to describe the AR_3 temperatures at any controlled cooling rate with the value of K_{AR3} varying with cooling rate. For 10°C/s K_{AR3} was 693. This value was lower for lower cooling rates and higher for higher cooling rates indicating that as the cooling rate increases there is a general increase in the sensitivity of the AR_3 temperature to carbon equivalent. Equation [6.3] can also be used to describe the behaviour of quenched samples but in these cases the R^2 value for the regression lines was lower at around 0.60 compared to over 0.90 for the controlled cooling samples.

Volume Fraction of Second Phase

A different extraction of data from the CCT curves and the microstructural 'atlases' can be seen in Figure 6.24. This plot shows how the volume fraction of second phase, that is, any non-proeutectoid ferrite constituents, varies with cooling rate for each of the six steels. It is clear that overall the proportion of second phase increases with cooling rate and also that the rate of increase in the proportion of second phase is greater for the higher CE materials. Using regression analysis the equation relating the volume fraction second phase with cooling rate was found to be:

$$\% \text{ Second Phase} = K_{\%2P} \ln (CR) + C_{\%2P} \qquad [6.4]$$

where $K_{\%2P}$ and $C_{\%2P}$ are alloy specific constants and CR is the cooling rate. This equation applies only to the samples where the volume fraction of second phase is less than 100%. Table 6.4 provides the values of $K_{\%2P}$ and $C_{\%2P}$ for the six steels investigated in this programme. The factor $K_{\%2P}$ can be considered an indication of how sensitive the alloy is to cooling rate and the factor $C_{\%2P}$ an indication of the proportion of second phase that would be present under equilibrium conditions, as the cooling rate tends to zero.

An alternative way of framing the change in the volume fraction of second phase is to consider the changes in the proportion of second phase in conjunction with the transformation start temperatures. That is, directly comparing the two cooling rate

dependent parameters described in Figures 6.22 and 6.24. Figure 6.25 shows the change in microstructure with transformation start temperature. Overall the expected trend of an increase in the proportion of second phase with a decrease in the transformation start temperature was seen. There is significant overlap in the results between the different steels and specific trends could not be drawn from this result.

Critical Cooling Time – C_f

Figure 6.24 further facilitates an investigation into the value of a parameter called the critical cooling time for proeutectoid ferrite, C_f. This parameter was described by Inagaki and Sekiguchi[75] and discussed in the review of literature. C_f is the 800-500°C cooling time at which proeutectoid ferrite can be observed in the final microstructure, and it was thought to be a reliable indication of the ductility and toughness of the heat-affected zone of a welded joint produced using arc welding. For the two low carbon alloys, LC and LCNb the value of C_f is greater than any of the cooling rates that were used in this programme of work allowed, with proeutectoid ferrite observed in all the continuously cooled samples. For the four dual phase steels the value of C_f decreases overall as the carbon equivalent increases suggesting that the ductility and toughness of the heat-affected zones in these materials will decrease with increasing alloy content.

Continuous Cooling Transformation Curve Regions

The trends described above consider elements of the information from the metallographic and dilatometry studies. It is also possible to examine the CCT curves themselves to establish patterns. Across the six CCT curves given in Figures 6.10 to 6.15 the position of the different transformation regions can provide information about the expected microstructural constituents in a sample.

Overall the trend across the six CCT curves is for the transformation region to shift down and towards the right. The decrease in the transformation start temperatures can be clearly seen if the CCT curves are compared. The regions representing the transformation to different microstructural constituents can also be seen to move. The proeutectoid ferrite region persists to cooling rates of over 70°C/s in the lower CE samples. On the other hand, in the higher CE steels, the ferrite region generally shifts to the right with only lower cooling rates producing some ferrite in the final microstructures.

The CAF region also makes a clear move to the right of the CCT diagram for the higher alloy compositions. In the lower CE grades, the CAF region was only present at temperatures above 10°C/s but in the higher alloy DP1000 and DP1400 the CAF reaches as far right as 2°C/s. The bainite region moves steadily from greater than 20°C/s in the DP600 material to low cooling rates of 5°C/s in the higher CE grades.

The lath constituent region, representing lath ferrite in the mild steel and low alloy grade, and martensite in the dual phase steel, is pushed to lower temperatures as the alloy content increases. It moves from just under 700°C in the low carbon grades to just over 400°C in the DP1400 samples.

6.2.4 Summary

This section has presented the continuous cooling transformation behaviour of the six steels used for this investigation. The transformation start temperature was seen to decrease with an increase in alloy content. Further, the regions of the continuous cooling transformation curves, that represent specific microstructural constituents, move to lower cooling rates as the alloy content increases. A parameter known as C_f, the critical cooling time for proeutectoid ferrite was identified for each steel as this has previously been considered a reliable index of weld ductility. It was found that the rate associated with this time was not exceeded for the two low CE grades (LC and LCNb). However, for the dual phase grades it was found that the critical cooling time increased with an increase in alloy content.

6.3 Mechanical Properties

This section presents the results from three mechanical tests carried out on samples of the six steels of interest in this programme. The change in properties is related to both the continuous cooling rate and the associated change in the microstructure.

6.3.1 Bulk Hardness Tests

The overall relationship between bulk hardness, measured at the centre of a sectioned CCT sample, and cooling rate for all six steels can be seen in Figure 6.26. This plot demonstrates that the results fall into two basic groups. The measurements for the LC, LCNb and DP600 grades increase slowly across the full range of cooling rates used from initial values of between 88 and 115Hv to final values of 210 to 163Hv. There is an exception for the fastest cooled DP600 sample, which had a measured hardness that did not follow the linear trend present for the slower cooled samples (379Hv). On the other hand, the DP800, DP1000 and DP1400 results fall higher up the plot, starting at approximately 160Hv, and the hardness increases at a greater rate with an increase in cooling rate. The higher cooling rates produced more scatter in the higher carbon equivalent (CE) alloys (group 2) than the lower CE grades.

There is a strong relationship between the CE and the hardness at a given cooling rate for the controlled cooling samples. This relationship can be expressed through the following equation:

$$Hv = k_{Hv}\,(CE) + C_{Hv} \qquad [6.6]$$

The values of k_{Hv} and C_{Hv} can be seen in Table 6.5. It can be seen that there is an increase in k_{Hv} with cooling rate but C_{Hv} did not vary much over the same range. For example at 0.5°C/s k_{Hv} has a value of 427 and this has increased to 1317 at a cooling rate of 25°C/s. This increase in the value of k_{Hv} with cooling rate indicates that increases in cooling rate increase the degree to which the alloy content influences the hardness.

An alterative way of considering the change in hardness with cooling rate is to consider the changes in hardness with the volume fraction of second phase in the microstructure of a given sample. This relationship is shown in Figure 6.27. It can be seen that there is significant overlap between the hardness results for the different alloys. In general, for a given volume fraction of second transformation product, the hardness increases as the CE increases. However, this is not true for all cooling rates and in general the DP800, with

only the third highest CE is hardest at all cooling rates. Overall, for all the steels investigated, the bulk Vickers hardness increased as the volume fraction of second transformation product increased.

6.3.2 Miniature Disc Bend Tests

The miniature disc bend tests enabled two properties of the samples modified through continuous cooling treatments to be predicted: the 0.2% proof stress and the ultimate tensile strength.

Predicted 0.2% Proof Stress

The values of the 0.2% proof stress predicted by the miniature disc bend tests were considered from two perspectives: that of a change in cooling rate and, with a change in the volume fraction of second transformation product. The relationship between the 0.2% proof stress and the cooling rate can be seen in Figure 6.28. There is a large amount of scatter in the results and the results for the six steels do not fall in an order relating to their CE, although the two lowest CE alloys, LC and LCNb, do fall lower than the dual phase grades. An attempt to perform regression analysis failed due to the large amount of scatter. Whilst relationships could be derived, low R^2 values indicate the limited usefulness of such relationships. For example, for the 0.2% proof stress results for the dual phase grades R^2 was approximately 0.25 with the exception of the DP1400 alloy that produced a relationship with an R^2 value of 0.75.

An attempt to relate the 0.2% proof stress values to the volume fraction of second transformation product also resulted in low correlation. Figure 6.29 shows the relationship between these two factors. The LC results can be seen to cluster along the y axis with a range in the 0.2% proof stress of almost 100MPa being seen for little change in the volume fraction of second phase. The LCNb samples produced 0.2% proof stresss ranging from 240 to 380MPa as the proportion of second transformation product increased from 5 to 65%. The DP600, DP800 and DP1000 dual phase results overlap and fall between approximately 20 and 100% in terms of volume fraction second phase and between 200 and 400MPa in terms of the 0.2% proof stress. The DP1400 results lie predominantly at the bottom of the plot and an increase of approximately 100MPa in the 0.2% proof stress can be seen as the volume fraction second phase increases from 40 to 100%. The considerable amount of scatter in the results suggests that there are other

factors influencing the 0.2% proof stress as well as the transformation products present in the microstructure. Such factors are likely to be the nature of the second phase and the average grain size and are discussed further in Section 7.

Predicted Ultimate Tensile Strength

The predicted ultimate tensile strength (UTS) results are plotted against cooling rate in Figure 6.30. An overall increase in the ultimate tensile strength with cooling rate is evident. The grouping of results seen in this plot is similar to that seen in Figure 6.26 for the bulk hardness results. The increase in UTS for the three lower CE materials has a lower gradient than that for the higher CE materials.

As for the bulk hardness measurements there is a relationship between the predicated UTS values and the carbon equivalent of the six steel grades. This relationship can be described by the equation:

$$UTS = k_{UTS}\,(CE) + C_{UTS} \qquad [6.7]$$

Table 6.6 provides the values of k_{UTS} and C_{UTS} that were determined for this relationship at four cooling rates. It is clear from this table that as the cooling rate increases, the value of k_{UTS} also increases. For example, at 0.5°Cs the value is 1156 and this has almost doubled to 2066 when the cooling rate is increased to 10°C/s. The constant k_{UTS} indicates how sensitive the alloy is to a change in the carbon equivalent. The change in this constant with cooling rate, as shown in Table 6.6, shows that as the cooling rate increases, the effect of the higher CE is magnified in terms of the resultant predicted UTS. For example at a cooling rate of 2°C/s the CE is multiplied by 1648 to obtain the first term of the equation but at an increased cooling rate of 25°C/s the factor by which CE must be multiplied has increased to 2727.

Figure 6.31 provides an alternative perspective on the change in UTS with cooling rate. In this plot it can be seen that as the proportion of second transformation product increases there is an overall increase in the predicted UTS. There is, as for the hardness results, considerable overlap between the predicted results for the different alloys. In general the DP1000 and DP800 samples produced the highest predictions and the DP1400 results tended to fall in the centre of the results. A range of predicted UTS results from 800MPa up to 1530MPa was produced by samples that had microstructures consisting entirely of transformation products other than proeutectoid ferrite.

6.3.3 Impact Tests

The miniature impact tests carried out produced impact energy results measured in J/mm^2 for the sub-sized specimens tested. The relationship between the impact energy and the cooling rate for samples of the six steels is shown in Figure 6.32. It is clear that the steels do not all respond to changes in the cooling rate the same way. The LCNb samples demonstrate an increase in impact energy of approximately 10% as the cooling rate increased from 0.5°C/s to around 2000°C/s (water quenching). The measured impact energy for the LC samples decreased from 0.95 J/mm^2 at low cooling rates to 0.70 J/mm^2 and for the water-quenched sample, a decrease of 15%. The DP600 samples showed changes between 0.99 and 1.03 J/mm^2 up to a cooling rate of 73°C/s. However, at the fastest cooling rate of 2206°C/s the impact energy dropped to almost 50% of the maximum at $0.48J/mm^2$. The three higher CE grades showed larger decreases in impact energy with the DP800, DP1000 and DP1400 all dropping from approximately 0.95 J/mm^2 at the lowest cooling rate to less than 0.50 J/mm^2 when water-quenched. The DP800 alloy showed the largest drop from 0.95 to 0.37 J/mm^2. Linear regression was unsuccessful at characterising the response of the different grades to changes in cooling rate with some R^2 values as low as 0.06.

The relationship between impact energy and volume fraction second transformation product showed a similar variation with CE as seen for the relationship with cooling rate. Figure 6.33 shows a plot of these two factors. The impact energy results for the LC samples are clustered to the left of the plot at low proportions of second phase, with a range of $0.2J/mm^2$ between the highest and lowest result. The LCNb results are the highest on this plot with a small overall increase in impact energy seen as the proportion of second phase increases. However, the impact energy for the water-cooled sample, seen on this plot as the one with the largest percentage second phase, was lower than the other samples at $1.34J/mm^2$. The impact energy for the DP600 remained constant throughout most of the variations in the microstructure shown in Figure 6.33. At a cooling rate of 0.5°C/s the impact energy was $1.03J/mm^2$ and this only varied by 4%, up and down, regardless of the microstructural constituents present. However, in the sample that had a bainite and martensite microstructure, the impact energy was greatly reduced to $0.48K/mm^2$. The three higher CE grade, DP800, DP1000 and DP1400 all showed significant decreases in the impact energy as the proportion of second phase increased. For a given percentage of non-proeutectoid ferrite, there were differences between the

DP800 and DP1400 for the lowest impact energy results, with the DP800 producing the lowest energy values at lower volumes fractions of second phase (up to approximately 60%), and the DP1400 producing the lowest results at higher proportions of second phase.

Scanning Electron Micrographs of Impact Fracture Surfaces

In order to obtain further information about the nature of the fracture that led to the results seen in Figures 6.32 and 6.33 a scanning electron microscope (SEM) was used to examine the fracture surfaces of the slowest and fastest cooled samples in each of the six steels. Figures 6.34 to 6.39 present SEM micrographs of the fracture surfaces observed.

The micrographs for the LC grade impact samples can be seen in Figures 6.34(a) to (c). The first image, Figure 6.34(a), shows the general appearance of the fracture surface of an impact sample produced from a sample that had been cooled at 0.5°C/s. This micrograph reveals dimples ranging from only a few microns to 40 or 50 microns in size. A close up of this surface can be seen in Figure 6.34(b) and it is clear from this image that the dimples are elongated prior to fracture and that the final fracture appears to be the result of a shear process. The surface shown in Figure 6.34(c) is also composed of dimples. This image is of the surface created by an impact test on a water-quenched sample. The dimples in this surface are much smaller than for the slow cooled sample with an average of 5 microns in the most heavily dimpled areas although some larger dimples, of more than 20 microns can still be seen at the bottom of this image.

Two micrographs of the LCNb impact sample fracture surfaces are shown in Figures 6.35(a) and (b). The first, 6.35(a), shows the appearance of the slowest cooled sample's fracture surface. This image is similar to that seen in Figure 6.34(a) for the LC slow cooled sample. However, in the LCNb sample there are more of the larger dimples and fewer areas of small dimples in between them. On water quenching, the fracture surface seen in Figure 6.35(b) was produced and it is clear that the number of dimples has increased and the average size decreased compared to the slow cooled sample. The dimples in this image appear more elongated than those seen in the LC sample that had been water-quenched.

The fracture surfaces for the two DP600 samples can be seen in Figures 6.36(a) to (c). The slow cooled sample can be seen in Figure 6.36(a). In this image the dimples can be seen to be smaller in size to those seen for the LCNb grade, but their shape is less regular than previously seen. There are also small areas that are 'rippled' in nature as opposed to dimpled. These ripples appear to be dimple walls that did not deform significantly and fractured whilst the dimple was still relatively shallow. The water-quenched sample can be seen in Figure 6.36(b) and a clear reduction in the dimple size is evident in this image. The dimples are more regular in shape and of an average size of 9 microns. There are further areas of 'ripples' in this sample and a close up can be seen in Figure 6.36(c). This image reveals that in a rippled area, thought to be composed of several undeveloped dimples, each dimple has a precipitate associated with it. This dimples are usually less than 1 micron in size although occasionally an elongated precipitate, of up to 2 microns in length was found, as seen in the right of Figure 6.36(c). EDX analysis of these precipitates revealed them to be composed of Sulphur, Manganese and Iron.

The DP800 impact samples revealed fracture surfaces of a different nature to those seen in the lower CE grades. Figures 6.37(a) to (e) provide the relevant micrographs. Figure 6.37(a) shows the fracture appearance of the sample cooled at 0.5°C/s. The surface can be seen to be composed of alternating strips of fine dimpled and long flatter areas. In this sample the surface is approximately 50% dimpled. The strips run parallel to the long edge of the sample, that is across the width of the original impact sample. A close up of this surface can be seen in Figure 6.37(b) and the flat areas are revealed as rippled, as seen previously in the DP600 samples. The water-quenched sample has a different fracture surface appearance, as revealed in Figures 6.37(c) to (e). The overall appearance of this surface can be seen in Figure 6.37(c) and two components can clearly be seen. There are areas of dimples, of on average, 6 microns in size and also large flat areas. These flat areas can themselves be split into two types: there are long narrow flat areas, parallel to the long edge of the impact sample, as seen in the slow cooled sample. There are also rounder areas with ripples appearing to originate from the centre of the area. Figure 6.37(d) provides a close up of an area of dimples. It can be seen that the dimples are fairly regular in shape and do not show any elongation as has been seen in lower CE grades. A close up of one of the flat, round areas can be seen in Figure 6.37(e). This close up reveals a surface different to that seen previously in flat areas. The earlier rippled areas appeared to be the result of dimples that fracture early in their development. This area

does not appear to have any dimples present, indicating that fracture took place too fast for them to form. The 'wavy' nature of the contours in this image is consistent with the idea of the fracture occurring via a brittle mechanism.

The micrographs for the DP1000 impact samples can be seen in Figures 6.38(a) to (d). The slow cooled fracture surface, seen in Figure 6.38(a), has both dimpled and flat areas. A close up, shown in Figure 6.38(b), reveals these areas to be rippled in nature. An important difference between this surface and that seen for the slow cooled DP800 sample is that the flat areas are shorter, up to 50 microns in length, rather than the several hundred microns in length previously seen. The surface of the water-quenched sample can be seen in Figure 6.38(c). As for the slower cooled sample the surface consists of flat and dimpled areas. The dimples in this sample are smaller than those seen in Figure 6.28(a). The close up of the flat areas, seen in Figure 6.38(d) reveal that there is little evidence of dimples in these areas. The close up also shows that the dimples are shallow in nature.

The DP1400 fracture surfaces reveal finer structures, as seen in Figure 6.39. The sample cooled at 0.5°C/s is shown in Figure 6.39(a) and no large flat areas, as seen previously, were detected in this sample. The dimples in this specimen were smaller than previously seen with few dimples larger than 20 microns in diameter seen. The shape of the dimples is fairly regular and there is some evidence of elongation prior to fracture. The water-quenched sample reveals a refined surface as seen in Figure 6.39(b). There are many round areas that appear to indicate brittle fracture in this sample, interspersed with areas of fine, shallow dimples.

6.3.4 Links between the Measured Mechanical Properties

In order to reveal the relationships between the different mechanical properties considered in this section, three comparisons were made: between the Vickers hardness and predicted UTS; between the impact energy and the UTS; and between the impact energy and the Vickers hardness. Each comparison is discussed separately below.

The relationship between the Vickers hardness and the predicted UTS can be seen in Figure 6.40. There is clearly a strong relationship between these two properties, as has

been previously reported in the literature. An equation, determined by regression, relating the two properties was found to be:

$$UTS_P = 3.21\ Hv \quad [6.8]$$

This is close to the relationship seen in standard conversion tables, that is:

$$UTS = 3.15\ Hv \quad [6.9]$$

The impact energy and predicted ultimate tensile strength are compared in Figure 6.41. Overall, a decrease in the measured impact energy is observed as the predicted tensile strength increases. At a given tensile strength the impact energy is different for different steels. For example, there are three steels with sample showing a predicted UTS of approximately 450Mpa: LC, LCNb and DP600. The impact energy for the LCNb samples is the highest at 1.51 J/mm^2, which is 0.57 J/mm^2 higher than the DP600 samples that have an impact energy of 0.94 J/mm^2. The LC samples have the lowest impact energy of these three samples at 0.81 J/mm^2.

With each of these three lower CE alloys the impact energy response, as the predicated UTS increases, is different. For the LC grade, there is a slight decrease, from 0.96 to 0.77 J/mm^2 as the predicted UTS increases from 360 to 670MPa. For the DP600 samples there is little variation in the impact energy as the predicted UTS increases from 438 to 569MPa. The variation in impact energy is only 4%. However, the highest UTS sample (1208MPa) has a much lower impact energy of 0.48J/mm^2. The LCNb demonstrates an increase from 438 to 569MPa in predicted UTS and at the same time the impact energy also shows an increase of 12% from 1.36 to 1.54 J/mm^2. However, for this grade the impact energy falls back to a value of 1.34J/mm^2 for the highest strength sample that has a predicted UTS of 1142MPa.

The results for the three higher CE dual phase grades overlap somewhat in terms of impact energy and predicted UTS. Of the three alloys: DP800, DP1000 and DP1400 the DP1000 demonstrates, in general, the highest impact energy for a given tensile strength prediction. The lowest impact energy for a given predicted UTS is split between the DP800 and DP1400 samples. For example, at approximately 800MPa predicted UTS, the impact energy for the DP1000, DP800 and DP1400 is 0.66, 0.61 and 0.55 J/mm^2 respectively, a range of 16%. At a higher predicted UTS of approximately 1300MPa the results for the three higher CE grades are 0.61, 0.37 and 0.47 J/mm^2 for the DP1000, DP800 and DP1400 respectively.

Figure 6.42 presents the relationship between the impact energy and the bulk Vickers hardness. The correlation between the hardness and the predicted UTS meant that a similar trend to that seen in Figure 6.41 was expected but this figure enables the impact energy to be compared to a property that is easy to measure, and often considered the first indicator of weldability. For each individual alloy the change in impact energy with an increase in hardness was similar to that observed for an increase in the predicted UTS. For example, as the hardness of the LCNb samples increases from 95 to 120Hv the impact energy increases from1.36 to 1.54 J/mm^2.

Decreasing the hardness of a sample, through a reduction in cooling had a bigger effect on the impact energy when the hardness range was less than 300Hv. For example, a reduction in the hardness of the DP800 samples from 206 to 154Hv had a corresponding increase in the impact energy of 65% or 0.33 J/mm^2. A similar decrease in hardness from 318 to 221Hv had no effect on the impact energy of the DP1000 alloy.

The DP800 overall showed two regions of clear change: from 150 to 200Hv and from 310 to 405Hv. In between 200 and 310 Hv there was no overall change in the impact energy. For the two higher CE grades, DP1000 and DP1400 there was no significant overall change in the impact energy as the hardness varied between approximately 200 and 450Hv.

6.3.5 Summary

This section has considered the effect that changes in cooling rate have on three important mechanical properties for the six steels that form the basis of this investigation. The results have been considered in terms of the cooling rates applied to the samples as well as the proportion of non-proeutectoid ferrite transformation products present in the microstructure. As the cooling rate, and CE of the alloys, increased, the hardness, and predicted UTS were found to increase. In terms of impact energy, the response to these changes varied, depending on the strengthening mechanisms employed in the individual grades. For example, in the microalloyed grade, LCNb (CE 0.07), the impact energy increased with an increase in the cooling rate. However, for the higher CE (>0.22) grades the impact decreased considerably with an increase in cooling rate. Considerable scatter in the predicted 0.2% proof stress results resulted in no clear relationships being found between the cooling rate and 0.2% proof stress.

6.4 Monitoring Thermal Profile during Resistance Spot Welding

This section presents the findings from the investigation into thermal profile associated with different welding schedules. A simple, single pulse weld is considered as well as the profiles associated with the two advanced schedules presented in Section 6.1, namely extended weld time and pulsed welding schedules. In addition, two further advanced programmes were developed: controlled post weld cooling and post weld tempering. In all the experiments described the alloy used was DP800 with a sheet thickness of 2mm. When referring to individual thermocouples in the rest of this section, a name of the form 'thermocouple type + thermocouple number' will be used. For example, R1 refers to the first R-type thermocouple.

6.4.1 Single Pulse Welding Schedules

The thermal profile generated during single pulse welding was monitored using both plain wire and sheathed thermocouples. The results from the plain wire thermocouples can be seen in Figure 6.43. The temperature plot, Figure 6.43(a), shows how the temperature generated at each of the three thermocouple junctions, varies with time. It can be seen that the R-type thermocouple, R1, that was located at the weld nugget centre experienced the highest temperature as would be expected. The two K-type thermocouples experienced lower temperatures with K1 recording lower temperatures than K2. Figure 6.43(b) is a macro image of the weld once it has been sectioned and etched. It can be seen that K1 lies closer to the weld than K2. The close up of the weld given in Figure 6.43(c) shows how the heat-affected zone has been slightly extended around the K1 thermocouple. The 800-500°C cooling rate was 1614°C/s for the weld nugget and although neither K-type thermocouple produced a temperature reading above 600 the cooling rate for 600-500°C was 684°C/s. A microhardness profile of a simple, single pulse spot weld in DP800 was given in Figure 6.8.

6.4.2 Extended Weld Time Schedules

The first attempt at modification to the basic welding schedule involved extending the weld time and reducing the weld current appropriately. Two weld times were trialled: 25 cycles and 50 cycles, and the appropriate weld times and weld currents, determined from weld lobes, are given in Table 6.7. It can be seen that on increasing the weld time from 14 to 25 cycles the current required to produce a $5\sqrt{t}$ weld decreased by 18% to 7.2kA. A

further 10% reduction, to 7kA, was noted when the weld time was increased to 50 cycles. The thermal profiles generated by this change to the weld schedule, in DP800 welds, can be seen in Figures 6.44 and 6.45. The cooling rates measured are summarised in Table 6.8.

The first extended weld time selected was 25 cycles compared to the standard 14 cycles. An example of the time – temperature plot for a 25 cycle weld is given in Figure 6.44(a). The readings taken during the production of this weld experienced a strong 'pull down' effect as described in Section 5.3. This effect appeared to be present for all three thermocouples. The image given in Figure 6.44(b) shows that K2 falls inside the weld nugget as weld as R1 and that K1 falls just outside the heat-affected zone. The interference with the R1 signal meant that no cooling rate could be determined for this weld, however another weld made using these conditions experienced a nugget cooling rate of 1637°C/s, which is slightly higher than that measured for the 14 cycle weld.

A further extension of the weld time, to 50 cycles, was also trialled. The time – temperature plot for this extended weld time, as determined with plain wire thermocouples, is shown in Figure 6.45(a). The cyclic interference with the thermocouple readings is clearly evident from this plot. The interference in the R1 readings initially pulls the measured temperature down below 0°C. After 26 cycles of weld current the interference stabilises and the measured temperature cycles between 500 and 700°C. Once the weld current is switched off the temperature climbs to over 800°C and then falls as the sample cools. The R1 cooling rate was 1878°C/s, 241°C/s or 14% higher than for the 25 cycle weld. The K-type measured cooling rate was 480°C/s for the K2 following a peak temperature of over 800°C and 593°C/s for K1 that reached a peak temperature of 600°C. The image in Figure 6.45(b) shows that K2 was located precisely in the heat-affected zone and but K1 was situated outside this area.

The increase in weld time was associated with a change in the ratio of the width of the heat-affected zone (HAZ) to the size of the weld nugget. These data are given in Table 6.9. The increase from a 14 to 25 cycle weld time produced little change in the ratio heat affected zone : weld nugget with an increase of only 0.001 from an initial value of 0.048. However, a further increase in weld time to 50 cycles produced a marked increase in the

ratio to 0.115 indicating a heat-affected zone that was 11.5% of the total width of the weld.

In order to establish the effect of the variation in weld time on the strength or hardness of the spot weld, microhardness profiles were taken. The profile taken from a weld made using a standard 14 cycle weld time is given in Figure 6.8. This figure shows a significant increase in hardness from the unwelded hardness to a peak of approximately 420 in the heat-affected zone followed by an average weld nugget microhardness of 418. The microhardness profiles for the welds made with 25 and 50 cycle weld times can be compared in Figure 6.46. Both welds made at the longer weld times can be seen to demonstrate a decrease in microhardness compared to the standard weld. The heat-affected zones in particular showed a reduction in hardness of up to 15%. The average reduction was 3% for the 25 cycle weld and 6.5% for the 50 cycle weld. However, the weld nuggets did not demonstrate any marked effect from a change in weld time.

6.4.3 Pulsed Welding Schedules

A further investigation in the area of advanced welding schedules involved the use of short pulses of current instead of the standard single pulse with a longer weld time. The alloy selected was again DP800. The weld time and current settings for this series of welds are given in Table 6.10. It can be seen that four combinations of (number of pulses x pulse length) were used, three in addition to the standard single pulse schedule. The variations tried were 2 pulses of 7 cycles (2x7), 7 pulses of 2 cycles (7x2) and 14 pulses of 1 cycle (14x1). A hold time of 25 cycles, and a cool time of 1 cycle, was used as detailed in Section 4.3. Logging the applied current during welding was not possible with the available equipment but measurements of the last pulse of current applied could be taken and this is the value that appears in the 'Weld Current' column of Table 6.10. It can be seen that this current was increased from 8.5kA for a standard single pulse schedule to 15.5kA for the 2x7 schedule and 16.4kA for the 7x2 and 14x1 schedules. Figures 6.47 to 6.49 provide the thermal profiles measured for the pulsed welds and Table 6.11 summarises the cooling rates measured.

Figure 6.47 provides the results for the [2 x 7] pulsed welding schedule. Some electrical interference is evident in Figure 6.50(a) that provides the time – temperature plot for this weld schedule. However, all three thermocouple outputs provide sufficient information to

determine the relevant cooling rates. For R1 the cooling rate was 1244°C, K1 1153°C/s and K2 705°C/s. Figure 6.49(b) shows the location of K1 and K2 but R1 cannot be seen at this magnification. The weld itself is quite heavily indented by approximately 40%, which is more than the 30% recommended as a maximum by Karagoulis[9]. This indicates that a reduction in force may be appropriate if pulsed schedules are to be employed. This, however, could be a benefit because most industrial welding robots have a limited force range.

The thermal profile for the second pulsed weld combination, [7 x 2], is shown in Figure 6.48 (a). In this plot R1 and K1 provide sufficient data to calculate the cooling rates. The cooling rate for R1 was 1237°C/s and for K1, 1123°C/s. The photograph provided in Figure 6.48(b) shows that K1, the K-type thermocouple that measured the highest temperature, of the J, was located at the edge of the weld nugget and that K2 was just outside the heat-affected zone. It can be seen that the ceramic sheath around K1 has cracked in this weld and molten metal has penetrated the bore and this is likely to be the reason for the similar cooling rates for the R1 and the K1 thermocouples.

Figure 6.49(a) shows the plain wire thermocouple response to a [14 x 1] pulsed welding schedule. All three of the thermocouples produced suitable data to determine the 800-500°C cooling rates. The nugget cooling rate, measured by R1 was 668°C/s, for K1: 670°C/s and for K2: 853°C/s. The image in Figure 6.49(b) shows the location of the three thermocouples. It can be seen that K1 and K2 fall on the edge of the nugget rather than in the heat-affected zones with K1 falling further out than K2.

The heat affected zone : weld nugget ratios for the welds made used pulsed welding schedules can be found in Table 6.12. All three pulsed welding schedules resulted in an increase in this ratio from the standard weld ratio of 0.048 to 0.069, 0.067 and 0.074 for the 2x7, 7x2 and 14x1 schedules respectively.

The microhardness profiles for the three pulsed schedule welds are compared to the single pulse weld in Figure 6.50. The 2x7 schedule weld showed a significant decrease in hardness, particularly in the weld nugget where there was an average drop of 14% in the microhardness reading. Overall the reduction was 11.5%. The 7x2 schedule also resulted in a weld with a reduced weld hardness. In this weld the heat-affected zone demonstrated

the biggest reduction that, on average, was 21%. The reduction in the nugget hardness for this weld was between 3 and 10% resulting in an overall average reduction of 9%. The 14x1 weld schedule produced the only weld with some points within the weld being measured as harder than the corresponding points in the standard spot weld. The nugget was, on average, no harder than the standard weld but some points can be seen, in Figure 6.11 to fall above those indicating the hardness for a 1x14 weld. The heat-affected zone for this weld showed a reduction of 16.5%.

Overall the three pulsed schedule welds showed some reduction in weld microhardness compared to the weld made using the standard technique. The 2x7 schedule weld demonstrated the largest reduction in nugget hardness whereas the greatest reduction in the heat-affected zone hardness came from the 7x2 schedule welding.

6.4.4 Controlling Cooling Schedules

An attempt to modify the microstructure and properties of a resistance spot weld was made through the use of small pulses, applied shortly after the main welding pulse, to slow the cooling rate of the weld nugget and heat-affected zones. Figures 6.51 to 6.55 demonstrate the series of steps that were taken to determine experimental settings for this process.

Figure 6.51(a) shows the time – temperature plot produced by a standard, single pulse welding schedule using 25 cycles of current. The plot shows the high temperature experienced by R1 and also the electrical interference with the signal. The cooling rate measured for R1 was 1637°C/s. The two K-type thermocouples, K1 and K2, also show fluctuating readings and an 800-500°C cooling rate of 1602°C/s could be established for K2.

Figure 6.51(b) shows the two points of interest in determining a suitable time after the main welding pulse to apply a secondary pulse to attempt to control the cooling rate. The first line marks the point at which the weld current is switched off. K2 provides the information to assist with identifying this point in that the temperature starts to rise after the current is switched off and the electrical interference has stopped. This point can also be determined from the first point at which the temperature changes from room temperature, that is, the beginning of the welding process. The second line indicates the

time at which the R1 temperature has fallen to 800°C. The time between these two points is 4.5 cycles. The temperature drop in that time was 140°C. It was therefore decided to apply a cooling pulse after 9 cycles, to arrest the cooling in the middle of the 800-500°C critical temperature range. The settings used are given in Table 6.13 and the overall schedule sequence is that defined in Section 4, that is:

Pre-squeeze (35) – Squeeze (0) – Weld Time 1 (25) at Heat 1 (28) – Cool 1 (Z_1) – Weld Time 2 (X_2) at Heat 2 (B_2) – Cool 2 (Z_2) – Weld Time 3 (X_3) at Heat 3 (B_3) – Hold time (20) **[4.4]**

Figure 6.52(a) shows the thermal profile for a weld produced using the schedule labelled 6.52(a) in Table 6.13. The second pulse can be clearly seen in both the R1 and K2 plots but K1 did not show a response. The cooling rate measured by R1 was 1263°C/s. Figure 6.52(b) shows the location of the thermocouples in relation to the weld produced.

The process carried out to determine welding parameters for a single post weld pulse schedule was repeated using the data from the plot shown in Figure 6.52(a). Figure 6.53 includes lines that show the relative position of the end of the post weld pulse and the time at which the temperature has fallen to 800°C. In this case the time was longer at approximately 9 cycles. The second post weld pulse was thus set at the level shown in Table 6.13 (marked Figure 6.54).

Figure 6.54(a) shows the combined effect of the two post weld pulses on the thermal profile. All the thermocouples respond to the series of pulses. The cooling rate has decreased compared to the previous welds and across all three peaks for the R1 readings is 650°C/s, however the R1 peak temperatures were not as high as for previous experiments. Figure 6.54(b) shows the location of the thermocouples in this weld and it can be seen that K2 is set within the heat-affected zone but that K1 is positioned on the very edge of this area.

The microhardness profiles of the three welds described in this section are shown in Figure 6.55. All three treated with post weld pulses to control the cooling were successful at reducing the hardness to a degree. The weld produced with one post-weld pulse had a microhardness profile on average 5% lower with the exception of one side of the heat-

affected zone. The hardness of the weld manufactured using two post weld pulses varied with some points falling above, an some below the hardness profile for a basic weld indicating that further work is required to identify suitable second pulse parameters.

6.4.5 Post Weld Heat Treatments

Another heat treatment that was considered to have potential in terms of modifying spot weld properties was online tempering. In principle, this would involve small pulses of current being applied to the weld after the majority of cooling to room temperature has taken place.

The first experiment considered the effect of a single pulse on the temperature generated. Figure 6.56(a) shows the temperature measured for a single pulse of 1 cycle at a maximum heat setting (99) as indicated in Table 6.15. Despite the thermocouple type being plain wire very little effect of electrical interference can be seen. The peak temperatures measured by R1, K1 and K2 were 1065, 819 and 440°C. This experiment was carried out using an unwelded sample and the temperature generated in a weld, where the bulk resistance is lower is likely to be lower. Figure 6.56(b) shows the thermocouple location and the heat pattern generated. No melting has occurred but microstructural changes have occurred in places indicating the positions of initial heating. The cooling rate for R1 in this sample was 2950°C/s and for K1 3571°C/s.

To demonstrate the principle of controlling the time at temperature a second experiment was carried out using a single pulse, this time of 5 cycles, as can be seen in Table 6.15. Figure 6.57(a) shows the thermal profile and although there is some interference in the signals it can be seen that the length of time at temperature is extended with only a small increase in the peak temperature generated, compared to the single cycle pulse. The cooling rate in this case for R1 was 2091°C/s. Figure 6.57(b) shows the location of the thermocouples and it can be seen that K2 is close to the heat-affected zone but K1 is further out. A 'swirly' pattern was observed in the 'nugget' region of this weld.

Using these two trials as a basis, three tempering treatments were devised as detailed in Table 6.16. The first used only one tempering pulse and the thermocouple output can be seen in Figure 6.58(a). The cool time of 99 cycles was the maximum setting possible but proved sufficient for the R1 temperature to drop to 150°C. The peak temperature of the

tempering pulse was 305°C and the temperature was above 290°C for 2 cycles. The micrograph in Figure 6.58(b) shows the same heat patterns seen for the 1 cycle pulse, overlaid on the structure of the initial weld.

The second tempering treatment used two pulses with half the setting used for the single pulse treatment used for the second pulse in this programme. The thermal effects of this programme can be seen in Figure 6.59(a). The peak temperature of the tempering section was significantly higher than for the first programme at 570°C and the temperature was between 550 and 570°C for 4 cycles. Figure 6.59(b) shows more extensive heat patterns present at the edge of the weld. In this case the patterns are starting to change the shape of the heat-affected zone.

The final tempering setup used half the magnitude of the previous two pulse treatment as seen in Table 6.16. The thermocouple readings are shown in Figure 6.60(a) and (b), the R and K-type thermocouple results being split up to simplify analysis. In this weld the R1 temperature during tempering is greatly increased compared to previous results, reaching over 900°C. The cooling rate following this peak was 1270°C/s. K1 and K2 also show high peaks of 700 and 550°C respectively. Figure 6.60(c) shows the same heat patterns previously seen. In this example these heat patterns have changed the shape of the overall weld.

The microhardness profiles for the tempered welds are given in Figure 6.61. Compared to the basic, single pulse weld it can be seen that the single tempering pulse is successful at decreasing hardness in the weld nugget but not in the heat-affected zones. In contrast, the two welds that had tempering treatments consisting of two pulses demonstrated a decreased microhardness in the heat-affected zones but some harder areas in the weld nuggets. The second, higher temperature tempered weld showed less variation across it microhardness plot.

6.4.6 Summary

This section evaluated the thermal profiles generated by advanced welding schedules. Changes to the cooling rates experienced by both the weld nugget and heat-affected zones were measured using the direct thermocouple technique described in Section 5.3 and it was found that pulsed welding was the most successful means of decreasing the weld nugget hardness. However, further work is required to determine if alternative weld parameter settings could improve the response, in terms of weld hardness, to controlled cooling and tempering schedules.

7. GENERAL DISCUSSION

Weight reduction in body-in-white structures is necessary to make automobiles more fuel efficient. A range of advanced, high strength steels with improved strength, but also excellent formability, has been developed to meet the needs of manufacturers who are attempting to down gauge body-in-white components. These steels will play a key role in achieving lower weights since they have the potential to achieve equivalent component strength at thinner gauges. However, the full potential of these advances can only be realised if they can be integrated into production facilities that rely on resistance spot welding as the predominant means of component joining. In particular, spot welds manufactured in these modern high strength steels will need to meet the strength and fracture resistance requirements that are based on automotive manufacturers' familiarity with low alloy steels. With over seven million spot welds a day produced on a typical manufacturing line the significance of robust processing parameters is clear.

Dual phase steels are a range of modern alloys causing considerable excitement due to their combination of high strength, high ductility and improved crashworthiness in automotive components, compared to mild steel. Their commercial production routes rely on a metallurgical understanding of how chemical composition and thermomechanical treatments interrelate to produce appropriate microstructures. Their often complex alloy compositions mean that there is potential for significant changes to take place in the microstructure on resistance welding and concern has been expressed about the potential for spot welds in these modern alloys to develop brittle microstructures and demonstrate correspondingly poor impact properties.

The present research programme has been undertaken to extend the existing understanding in the following areas:

- the metallurgical transformation behaviour of advanced dual phase steels, particularly with respect to austenitising treatment and cooling rates that are relevant to the manufacture of resistance welds in sheet steels.
- the properties of microstructures relevant to the structures present in actual resistance welds in sheet steels.

In addition, the thermal cycles involved in the manufacture of resistance spot welds have been studied using thermocouples, both for typical single pulse welds and to determine the potential for using multi-pulse programmes to control weld development, subsequent cooling rate and post weld tempering. The key aspects of the individual tasks are initially considered with respect to existing knowledge. Finally the interrelation of the information developed is discussed with particular emphasis on the practical implications of weld manufacture and performance.

It was desirable that the primary steels investigated were commercially available dual phase grades. However, to evaluate the effect of carbon equivalent on transformation behaviour two additional steels were included: LC and LCNb. The steels thus selected covered a range of compositions including:

- 0.039 to 0.163 wt% C
- Mn0.004 to 0.57 wt% Si
- 0.001 to 0.020 wt% Nb
- 0.024 to 1.59 wt%

The carbon equivalent ranged from 0.04 to 0.27, as calculated using the Ito-Bessyo[33] CE equation, thought to be the most appropriate for the range of alloy compositions selected.

7.1 Continuous Cooling Transformation Microstructures in Dual Phase steels

This section is concerned with the continuous cooling transformation (CCT) behaviour of the six steels used in this research programme. The results from the CCT investigations were presented in Section 6.1 and they provide important information about the potential for controlling the microstructure of the steels using changes in cooling rate. In addition, the response at any single cooling rate can be compared across the six grades. This provides an understanding of the consequences of using a higher strength, and thus higher alloy steel on the microstructure for processes employing different cooling rates.

The experimental thermal cycle, that was used to generate the CCT curves, produced prior austenite grains sizes that ranged from 7.5 to 9.9 microns. This is slightly larger than those observed in the heat affect zones (Section 6.1.1), which were typically less than 5 microns on average. However, the difference is small and it has been found[69] that a ten fold increase in grain size, from 20 to 200 microns decreases the AR_3 transformation start temperature by approximately 50°C. This suggests that the range of 7.5 to 9.9 microns would produce a variation in the AR_3 of less than 5°C/s. This is small compared to the overall changes in AR_3 that can be seen in Figures 10 to 15.

The experiments carried out to enable selection of appropriate austenitising conditions, detailed in Section 4.3.2 suggested that between 1000 and approximately 1100°C, abnormal grain growth starts to occur in the DP800 grade. This temperature agrees with a range quoted by Wilson and Howell[72], who found that in a niobium bearing steel, abnormal growth started to occur between 1025 and 1100°C. The DP800 grade contains 0.019wt% niobium and the LCNb, DP1000 and DP1400 grades contain similar amounts (Table 1). This suggests that the reason for the dramatic increase in prior austenite grain size in the DP800 experiment was the niobium precipitates going into solution and thus no longer being available to pin the grain boundaries. The LC and DP600 grades did not contain any niobium microalloying additions and these two grades had the largest prior austenite grain sizes, at 9.9 and 9.6 microns respectively.

7.1.1 The observed continuous cooling transformation constituents

The microstructures presented in Figures 6.16 to 6.21 are combinations of several different microstructural constituents: ferrite, pearlite, acicular ferrite, bainite and martensite. The occurrence of each individual constituent is dependent on the alloy chemistry and the cooling rate used for that sample.

In terms of alloy composition, carbon has a particularly pronounced effect. This element is more soluble in face centred cubic austenite, which has larger interstitial sites for occupation than body centred cubic ferrite. Consequently, with higher carbon additions, there is a driving force for a steel microstructure to stay as austenite on cooling. If the structure remains austenitic to a low enough temperature, the atoms will not have the energy to diffuse into the equilibrium phases of ferrite and pearlite and instead, the non-equilibrium bainite and martensite are formed. The precise combination of phases developed depends on the alloy composition of the steel. A larger amount of austenite stabilisers, such as manganese as well as carbon, in a steel results in a lower critical cooling rate for development of these non-equilibrium microstructures. It would therefore be expected that in the lower alloy LC-Nb the diffusional phases – primary ferrite, acicular ferrite and pearlite - would be present up to fairly high cooling rates. In contrast the higher alloy (higher CE) grades would demonstrate more complex mixtures of non-diffusional microstructures at lower cooling rates.

In terms of cooling rate, the effect of an increasing the cooling rate is similar in terms of the CCT curve as an increase in the alloy composition. An increase in alloy composition moves the CCT diagram to lower cooling rates whereas an increase in cooling rate falls further to the left of a fixed alloy CCT diagram. Faster cooling rates naturally equate to a faster drop in temperature from those high enough for diffusional transformation to take place to those where non-diffusional mechanisms of transformation predominate. As diffusion is a time dependent process, a shorter time at high temperatures results in less diffusional microstructures forming.

The two principles described can be used to explain the presence of the microstructural constituents seen in Figures 6.16 to 6.21. Each constituent is considered separately below.

- **Proeutectoid (Primary) Ferrite**

This phase appeared as white grains and was present at all cooling rates for the lower alloy LC and LCNb grades, up to 100°C/s in the DP600, 35°C/s in the DP800 and DP1000 and up to 25°C/s in the DP1400. These observations clearly show the effect of austenite stabilisers on the transformation products present. Less ferrite forms in the higher alloy steels because the transformation temperatures are suppressed to sufficiently low temperatures to effect displacive transformations in a portion of the microstructure.

- **Pearlite**

Under optical examination this phase appeared black and was found in between the ferrite grains, sometimes running along grain boundaries. Using a scanning electron microscope clearly delineates the lamellae within the pearlite grains – as shown in Figures 6.18(k) and 6.19(k). These alternating lamellae of cementite and ferrite grow cooperatively in the carbon enriched austenite left over after the ferrite transformation. This explains why they are seen in between the ferrite grains, that is, the pearlite forms subsequent to the primary ferrite. The microhardness of the pearlite grains is much higher than the ferrite grains that it usually accompanies (for example in the 0.5°C/s LC-Nb sample the ferrite hardness was 105Hv and the pearlite 240Hv) but the combination still tends to be fairly low in hardness. The formation of pearlite is a nucleation and growth process and occurs at temperatures high enough for long range diffusion of atoms. This means that it starts transforming at relatively high temperatures, for example around 700 – 730°C for the LC-Nb material. As the cooling rate increased, a reduction in the amount of pearlite counted in the transformed microstructure was observed. This is in agreement with the findings of Harrison and Farrar[56].

- **Acicular Ferrite and Coarse Acicular Ferrite**

This term describes blocky elongated grains of ferrite that are white in appearance and generally interwoven, as pictured in Figure 6.17(k) and (l). Normally the phase was associated with fine areas of pearlite. These observations agree with the work of Harrison et al[56, 57] who looked at the influence of niobium on the microstructures of mild steel welds. They termed this phase 'coarse acicular ferrite' and, although the needles observed in the present study are generally larger than those observed by Harrison they are morphologically similar. Dunne[34] also discusses this phase in his review of ferrite

morphology in low carbon steel, in particular noting its 'interwoven' structure and the need for some intragranular nucleation sites, such as precipitates, to allow this phase to form. This requirement would be satisfied by the niobium based precipitates that are present in four of these steels and possibly also vanadium based precipitates in the DP600. However, Bhadeshia[36] has stated that a relatively large austenite grain size is required to produce acicular ferrite instead of bainite, although no values are given. The grain sizes that were used in this study ranged from 7.8 to 9.4μm, which do not seem to be large relative to those quoted. However, it is thought likely that the concentration of precipitates compared with the grain size is more important that grain size alone. Further, whereas Harrison et al[56, 57] considered this phase to be 'pro-eutectoid in nature' Bhadeshia stated that it is a diffusionless transformation with 'carbon partitioning occurring after the transformation of acicular ferrite'. The evidence from this study is of transformation temperatures unlikely to be low enough to indicate a diffusionless transformation, although there was a range of temperatures noted. This phase has been described in all of the above studies as desirable in welds because the interwoven grains provide many barriers to crack propagation resulting in a relatively high fracture energy.

- **Bainite**

A second structure with a needle like morphology was seen in faster cooled samples. In this case, however, the needles were more closely parallel, and not interwoven, with what appeared to be films of a darker products around the edge. Harrison et al[56] also referred to this product but it was termed 'lath ferrite'. It was noted that it often formed in areas alongside the acicular ferrite, which agrees with the findings of this study. This seems sensible as acicular ferrite and bainite are essentially different morphologies of a phase that forms under similar conditions except for their nucleation sites[36]. It therefore seems likely that in a microstructure with small austenite grains (and hence a high density of grain boundary nucleation sites), and also sufficient precipitates, a mixture of the two structures could form.

The concept of low carbon bainitic ferrite is also discussed in Dunne's[34] review, with its characteristics being described as 'a lath like ferrite structure with a second constituent'. A further definition of granular bainite is also given but this was not observed in the dual phase steels considered in the present studies. However, bainitic ferrite appears to be

considered a diffusional phase with the second constituent being pearlite, martensite, austenite or a combination of these. This is in contrast with the definitions given by Bhadeshia[36] who has stated that the second phase must be carbide for it to be truly classed as bainite. The findings of this study are that the phase termed bainite started to appear in products transforming at temperatures generally too low for diffusional transformations suggesting that the product identified is more like that defined by Bhadeshia.

The appearance of bainite in some of the micrographs in Figures 6.16 to 6.21 is, as for other constituents, a consequence of a combination of the alloy composition and cooling rate. Both higher alloy content and cooling rates can suppress the transformation temperature of austenite and, as such, increase the likelihood of a non-diffusional transformation taking place. As the ferrite forms in these microstructure, carbon is rejected at the transformation interface and thus the untransformed austenite is enriched in carbon content. Mesplont et al[64], suggested that one way of revealing the level of carbon enrichment is to use bainite (or martensite) transformation temperature predictive equations, input a measured transformation temperature from CCT experiments and thus calculate the carbon content at transformation. An example of this is given below for the DP800 steel. The bainite start transformation temperature at a cooling rate of 20°C/s was measured as 548°C. The equation used by Mesplont et al was:

$$B_s\ (°C) = 830 - 270(\%C) - 90(\%Mn) - 37(\%Ni) - 70(\%Cr) - 83(\%Mo) \qquad [7.1]$$

Using this equation and solving for %C results in a carbon enrichment prediction of 0.524%. An increase in the carbon content in the austenite would have significant effect on the transformation product and the technique provides a good indication of the reason for the change in transformation product for the higher alloy steels.

- **Martensite**

The presence of martensite was distinguished in a number of ways:

- The transformation temperatures for samples containing this product were around 400 to 450°C, which is in reasonable agreement with the empirical martensite start temperatures previously calculated.
- The microhardness of areas thought to be martensite, and also the bulk hardness of samples containing it, was significantly higher than for other phases. For example, for

the DP1000 sample cooled at 35°C/s, the areas thought to be bainite were around 310Hv at 10g and the areas thought to be martensite 439Hv.

- Optically, the bainite was lighter etching than the martensite with the boundaries around the needles more clearly defined. The martensite appeared generally darker with the internal needle structure of grains distinguishable more by relief than because of boundaries etching darkly.

Although martensite is generally considered an undesirable phase in terms of weldability and weld performance, it should be noted that the high hardnesses normally associated with its presence are also related to the carbon content of the phase[26, 44]. Higher carbon contents increase the tetragonality of the body centred tetragonal structure (BCT) and hence the harder the phase and the lower the ductility. Therefore, if the carbon content is low, as in the case of DP600, the presence of a martensite phase alone is not necessarily an indicator of likely poor performance. It should be noted that the carbon content present in all six of the steels used for this programme is relatively low compared to steels that would normally be considered 'martensitic' and it is the extremely rapid cooling rates used that result in its formation in these lower alloy grades. This agrees with ideas previously presented by Williams[49].

For the lowest alloy grades used for this programme, LC and LCNb no martensite developed. However, a lath-like ferrite morphology was observed and it is thought that this was effectively martensite without the carbon enrichment.

7.1.2 Continuous cooling transformation temperatures

The transformation start temperatures (AR_3) were observed to vary with both alloy composition and cooling rate as would be expected from the mechanisms described above. The transformation products and transformation temperatures are also linked. Figures 6.22 to 6.25 illustrate these relationships. The decrease in AR_3 with both increasing cooling rate and increasing alloy content can be seen in Figure 6.22. These results can be explained in terms of the faster cool to lower temperatures resulting in insufficient time for the austenite to start transformation at higher temperatures and the austenite stabilization afforded by the increase in carbon and manganese content. The constant $k_{AR,}$ used in equation [6.2], that described the sensitivity of the transformation temperature to cooling rate, was seen to increase for higher alloy steels. This result can now be explained in terms of the mechanisms by which the alloy content stabilises the

austenite to transformation. Equation [6.2] predicts that, for a given CE value, the transformation temperature will decrease with the natural log of the cooling rate. This is the relationship that best fits the data. However, it should be noted that the natural log relationship suggests that as the cooling rate tends to 0°C/s, the transformation temperature tends to infinity, which it not correct, as the equilibrium transformation temperature is determined by the alloy composition and is a maximum for pure iron at 910°C/s. However, the values for k_{AR} highlighted the existence of two groups in the six steels used for this investigation, in terms of transformation behaviour and provide and indicator of likely hardenability.

Manohar and Chandra[65] compared the behaviour of a steel alloy with a high level of Mn+Si (1.97 wt%) with that of a low Mn+Si grade (1.17 wt%) and found that a higher Mn+Si content decreases the AR_3 transformation temperature, increases the transformed sample hardness and moves the nose of the ferrite region to lower cooling rates. Considering the two low CE grades LC (CE - 0.04) and LCNb (CE - 0.07), used in the present study, it can be seen in Table 1 that the amount of carbon in the two grades is similar (0.039 and 0.049wt%) but the Mn+Si increases from 0.042 to 0.413wt% and from Figure 6.22 it is clear that there is a decrease in the AR_3 transformation temperature between the two grades, which supports the findings of Manohar and Chandra[65].

In a separate example, it is possible to compare two grades with equivalent values of Mn+Si (DP1000 – 2.08wt% and DP1400 – 2.12wt%) and isolate the effect of carbon on the transformation temperature. It can be seen from Figure 6.22 that an increase in the carbon content from 0.142 to 0.163wt% results in a reduction in the AR_3 under controlled cooling conditions. As previously described, carbon is a strong austenite stabiliser[32] decreasing the temperatures to which austenite will persist. Forcing the transformation to take place at lower temperatures has a corresponding effect on the transformation products, as discussed in Section 7.1.3.

An exception to the trend for a decrease in transformation temperature, with increasing alloy content can be seen in Figure 6.24 for the DP1000 grade compared to the DP800 grade. Some possible reasons for this include:

(1) as indicated in Table 1, the DP1000 has small extra additions of the ferrite forming elements silicon, chromium and molybdenum. It is possible that, the effect of the ferrite formers counters the stabilisation sufficiently to allow transformation at slightly higher temperatures than would otherwise be expected. This could be considered a positive effect. The steel has a high strength but a reduced tendency, compared to the weaker DP800 to form harder microstructures, which are known to reduce ductility and toughness. However, the increases in ferrite forming elements is very small and possibly not sufficient to cause a 20°C increase in the transformation temperature.

(2) The austenite grain size is also known to have an effect on the transformation temperatures of steels. However the austenite grain size of the DP1000 was 7.8μm and the DP800 8.3μm. As previously discussed, work by Yamamoto et al[69] and Sun et al[70] indicates that much larger differences in austenite grain size have less of an effect on AR_3 than those used for this study. These results suggest that the DP1000 trend is unlikely to be significantly affected by the difference in grain size used.

7.1.3 Continuous cooling transformation microstructures

The proportion of non-ferrite microstructures present in the samples, in terms of cooling rate and transformation temperatures, was presented in Figures 6.24 and 6.25. An increase in cooling rate and a decrease in the transformation temperatures were seen to increase the proportion of non-ferrite transformation products observed. The cooling rate and transformation temperatures have been shown, in this work, to be linked and, in agreement with other work, it has been shown that the increase in cooling rate decreases the transformation temperature. This change in AR_3 has a consequence for the transformation mechanisms, that is, whether the transformation takes place via displacive or diffusional mechanism.

Both plots provide a clear indication of the change in the critical cooling time for ferrite to appear in the transformed microstructure, C_f, a characteristic observed by Inagaki and Sekuguchi[70] to provide a good indication of potential weld ductility. The faster cooling rates indicate a faster 800 – 500°C cooling time and thus from Figure 6.24 it can be seen that C_f increases for the higher alloy grades. Again this can be explained in terms of the

change in transformation temperature and mechanism associated with faster cooling rates and 800 – 500°C cooling times.

7.2 Mechanical Properties of Continuous Cooled Microstructures

The properties of steel following continuous cooling transformations is clearly affected by the transformed microstructure, which is in turn controlled by the alloy composition and the cooling rate, as discussed in Section 7.1. This section considers the hardness, tensile and impact properties measured in each steel at different cooling rates and the links between the observed microstructures and these properties. This work enables an understanding of the potential for controlling properties through thermal cycle for dual phase steels. Further, it allows the trade off between properties as the cooling rate changes to be examined.

7.2.1 Hardness

The Vickers hardness measurements shown in Figure 6.26 show the effect of an increasing cooling rate for the six different CE steels. The results can be seen to be split into two groups. The lower alloy LC, LCNb and DP600 (CE 0.04 – 0.14) showing similar behaviour and the higher CE DP800 to DP1400 (CE 0.22 – 0.27) having an increased response in comparison. The composition of the two groups provides a potential reason for this split. As seen in Table 4.1, the Mn levels in the LC, LCNb and DP600 grades are 0.024, 0.40 and 0.50wt% respectively compared with just over 1.50wt% for the three higher strength grades. Mn has a hardening effect due to its interaction with the iron lattice as a substitutional solid solution strengthener[32]. The approximately three-fold increase could explain the 50Hv difference in the hardness, at the lowest cooling rate, between the two groups. The carbon content also increases through the six steels in this study. However, this also increases for the dual phase grades individually and is likely to be responsible for the general increase in hardness through the six steels but not the significant partitioning of the results into the two groups.

The behaviour, in terms of hardness, within each of the two groups is different. The lower alloy grades' gradual increase in hardness is likely to be the result of the microstructural constituents and a reduction in the grain size (see equation [2.4]). The change in grain size can be seen in Figures 6.16 to 6.20. The higher strength grades are additionally microalloyed with approximately 0.020wt% niobium. Niobium works as a precipitation hardener to retard dislocation glide, a finer dispersion of precipitates being more effective pinners. Thus, in addition to proportion of microstructural constituents and reduction in grain size, the DP800 to DP1400 samples will also be harder as a result of microalloying. The effect of the niobium could increase with cooling rate as a faster cooling rate results

in a greater number of nuclei forming on cooling. In addition, a fast cooling rate means that there is not sufficient time for precipitation coarsening to occur that would reduce the effectiveness of the dislocation pinning. Thus, at higher cooling rates there an increase in hardness compared to the non-microalloyed samples.

Thus it can be seen that the overall relationship between cooling rate and hardness, seen in Figure 6.26, is likely to be composed of three separate relationships that have been described in the literature:

- A portion of the overall increase in hardness with cooling rate is due to the grain refinement. This is true for all six steel investigated. The relationship between strength and grain size can be described by the Hall-Petch equation:

  $\sigma_y = \sigma_o + k_y d^{-1/2}$ [2.8]

  σ_y - yield stress d - grain size

  σ_o k_y - constants

  and the relationship is the same for hardness, that is, as the grain size decreases the hardness increases.
- As the cooling rate increases the proportion of second phase increases and the increased cooling rate also affects the nature of that phase. This aspect of the cooling rate – hardness relationship has been described by several researchers. For example, Manohar and Chandra[65] described how an increase in cooling rate changed the microstructure of a C-Mn-Si steel from ferrite+pearlite to acicular ferrite, upper and eventually lower bainite. These changes in the nature of the microstructure had a pronounced effect on the measured hardness, with an increase from 194 to 316 as the cooling rate increased from 0.3 to 50°C/s. Similar results have been found by Harrison and Farrar[60, 74].

- The effect of the microalloying content of some of the steels will have a varying effect at different cooling rates as described above.

The result of a change in the proportion of proeutectoid ferrite on hardness can be seen in Figure 6.27. The results showed that, independent of composition, the hardness increased with a decrease in the volume fraction of ferrite. This agrees with the results of many

published studies[51, 52, 60] and is a result of the very low hardness of the ferrite phase due to its intrinsic low carbon content.

7.2.2 Tensile properties

The relationship between cooling rate and 0.2% proof stress can be seen in Figure 6.28 and between cooling rate and tensile strength in Figure 6.30. The increase in tensile strength with cooling rate is clear, and follows a similar trend to that seen for the bulk hardness results. However, the 0.2% proof stress results did not produce any quantifiable trends. For each steel the 0.2% proof stress increased with cooling rate. This is likely to be significantly due to the refinement of the grain size at the faster cooling rates. However, the grouping of the results is not as previously seen. In Figure 6.28 the DP600 to DP1000 0.2% proof stress results are grouped together at the top of the plot between 300 and 400MPa. The LC and LCNb results are lower, between 200 and 300MPa but, in addition, the DP1400 results fall low on the plot relative to the other dual phase grades. The 0.2% proof stress of this highest CE (0.27) grade does not surpass that of it 'weaker' counterparts until the cooling rate exceeds 1000°C/s. The results suggest caution in terms of attempting controlled cooling in welding because, although a reduction is hardness may be achieved via a reduction in cooling rate, the associated decrease in 0.2% proof stress would be undesirable and could fall below that of the parent material causing weld itself to be a source of structural weakness.

The tensile strength is controlled by similar mechanisms to the hardness and comparison of Figures 6.26 and 6.28 illustrate this. The DP600 'water quench' result on this plot falls off the linear trend set by the slower cooled samples and this is likely to be due to the critical cooling rate for martensite being reached for this steel. Further evidence of this suggestion can be seen in Figure 6.18(j), which shows the martensitic microstructure of this sample compared to the acicular ferrite and bainite microstructure of the slower cooled samples.

The effect of percentage ferrite on the two tensile properties was also different. The 0.2% proof stress showed a small increase for some steels but there was significant scatter and other factors are seen to have a more significant effect that the proportion of ferrite. For example, the 0.2% proof stress ranged from 180 to 310MPa for the LC samples with a less than 1% change in the amount of ferrite. This change is thus likely to be due to the

refinement of the grain size with faster cooling rates. The tensile strength is strongly influenced by the volume fraction of ferrite, and as for the hardness measurement, the trend is independent of composition. Figure 6.31 shows this and, further, it can be seen that a volume fraction of 'second' phase of 100% the range of tensile strengths is 820 to 1530Mpa. This wide range of values is a result of the difference in (a) the nature of the second phase, for example, lath ferrite, bainite – martensite mixtures or martensite and (b) the carbon content of that second phase that has been shown to be of particular significance for bainite and martensite constituents (see Section 7.1).

7.2.3 Impact properties

Impact properties are an important measures of crashworthiness. The impact energy, as measured through miniature impact tests, can be seen in Figures 6.32 and 6.33 to be differently influenced by cooling rate and microstructure and is further influenced by the alloy composition. In Figure 6.32 it can be seen that four of the grades decrease in impact energy with an increase in cooling rate. This decrease is a result of the increase in proportion of non-ferrite constituents in the microstructure of the samples, which are known to be detrimental to toughness as discussed in the review of literature. The samples of DP800, DP1000 and DP1400 show a significantly greater decrease with increasing cooling rate than the low alloy LC grade. This is because the high strength dual phase grades have higher alloy contents, particularly carbon, and this results in greater proportions of bainite and martensite in the transformation microstructures. The effect of this increase in proportion of second phase can be seen in the scanning electron micrographs shown in Figures 6.34 to 6.39. The slower cooled dual phase samples show more dimpling at the fracture surface compared to the water quenched samples. The rippled areas, observed on the fracture surfaces of some of the faster cooled samples, indicate a brittle as opposed to a ductile (dimpled) fracture. This undesirable effect of the change in the microstructure causes a subsequent reduction in the measured impact energy.

It is of particular interest that one of the steels demonstrates no decrease in impact energy with increases in cooling rate. The LCNb demonstrates a marked increase as the cooling rate increases from 0.5 to 75°C/s although it falls back to the original value of 1.34J/mm^2 when water quenched.

The changes in the impact properties with a change in the proportion of ferrite in the microstructure (Figure 6.33) are also significant. The LC samples show little variation in their microstructure but the measured impact energy varies from 0.8 to 1.0J/mm^2, the variation being most likely due to the variation in grain size. The LCNb samples showed an increase in the impact energy with % second phase. This can be linked to the nature of the second phase, which can be seen from Figure 6.17 to be acicular ferrite. This result agrees with those previously reported regarding the improvement of impact properties resulting from the introduction of acicular ferrite into the microstructure[26, 29, 51, 52]. The DP600 is robust to changes in the microstructure in terms of impact energy. This is an interesting result from the perspective of weldability as it implies that the impact properties of a weld would not be detrimentally affected by the rapid cooling rates associated with, for example, resistance welding processes. The DP800, DP1000 and DP1400 samples all demonstrate decreases in the impact energy with a reduction in the ferrite constituent. This reduction is, as discussed in Section 7.1, due to a combination of the volume fraction and the nature of the second phase as well as the increased alloy composition.

The most important part of Figure 6.33 from a welding perspective is the 100% 'second' transformation product line. This represents the likely impact energy response of the four dual phase steels if they are welded using existing welding schedules. The DP800 shows the poorest response of the dual phase grades and, interestingly the results of the DP1000 grade is highest at 0.60 J/mm^2.

7.2.4 Mechanical property optimisation

It is often the case that compromises, in terms of mechanical properties, need to be made in materials processing and applications. The mechanical properties of the continuously cooled microstructures individually showed some interesting trends with cooling rate. Of greater interest is how the properties interact for an individual sample or steel grade. Three comparisons are considered in this section. They are the relationships between: hardness and tensile strength; tensile strength and impact energy; and hardness and impact energy.

Hardness vs. Predicted Tensile Strength

The hardness and tensile strength results for all six steel are shown in Figure 6.40 and described in Section 6.3.4. It was shown that the following equation applied for the predicted ultimate tensile strength (UTS_p):

$$UTS_p = 3.21Hv \qquad [6.8]$$

This equation is very similar to the equation used in standard conversion tables. This agreement affords confidence in the tensile strength results predicted by the disc bend tests.

The DP800 results deviate the most from equation [6.18] with the predicted UTS (UTS_p) results being lower than expected for their measured hardness. One possible reason for this could be the discs failing in a brittle manner causing the measured ultimate load to be lower than its true value. The DP800 grade in general behaved 'worse' than its higher alloy dual phase counterparts. For example, the DP800 samples had lower AR_3 values than the DP1000 and also the highest hardness. It is therefore reasonable to consider that the microstructures present could have lead to premature failure and lower ultimate load measurements.

A further comment about Figure 6.40 is that the relationship between hardness and the UTS_p highlights the need to consider the impact energy and strength produced by any hardness reduction measures. The consequence of a significant reduction in weld hardness would also equate to an undesirable loss in weld strength.

Impact Energy vs. Predicted Tensile Strength

The trade-off between strength and impact energy is an important one to consider. Typically an increase in strength is associated with a decrease in the impact energy. However, this depend on the strengthening mechanism used and this can be seen in Figure 6.41. An increase in the strength, as a result of an increase in the alloy content or change in the microstructure can have a detrimental effect on the impact energy. However, an increase in strength due to grain refinement, as for example, the LCNb grade, actually improves the impact energy.

Figure 6.41 also provides further information about the potential for improving the impact energy of the six steels when welded. For the LC grade, as the tensile strength increases

the impact energy decreases, with a 25% reduction between the highest and lowest strength sample. In contrast, the LCNb grade responds with an increase in impact energy as the UTS_p increases. However, at the highest strength, which relates to the water quenched sample, the impact energy drops off but is still higher than for the slowest cooled sample.

The response of the dual phase steels in Figure 6.41 is of particular interest from the perspective of downgauging and welding. Taking the DP1400 results as an example, it can be seen that whilst the UTS_p ranges from 520 to 1420MPa, the impact energy is fairly constant between UTS_p values of 700 to 1420MPa. As such a decrease in the sample strength to approximately 700Mpa would be required in order to observe an increase in the impact energy. From a welding perspective this would be unacceptable because the weld would be significantly lower in strength than the parent material and a source of weakness in a component.

The range of strengths for the DP600 is wide but the majority of samples are around the 450 to 500MPa mark. The impact energy also varies little for this grade but overall is higher at a given strength than the other dual phase grades suggesting that this grade may be a better choice where impact energy is important. The DP800 and DP1400 samples behave in a similar way to the DP1400, although the DP800 shows a greater decrease in impact energy over the range 800 to 1400MPa than the DP1000.

Impact Energy vs. Hardness

Given the linear relationship between hardness and UTS_p it is not surprising that the trend in impact energy and hardness is similar to that for the UTS_p. Figure 6.42 shows this relationship and it is clear that similar conclusions can be drawn from this plot as were from Figure 6.41. By using Figure 6.42 in conjunction with 6.41 it can be seen that traditional concerns over high hardness measurements need to be considered from a much wider perspective than simply 'lower is better.'

For example, it can be seen that the hardness of the DP1400 samples reaches over 450Hv. The impact energy of the highest hardness samples (that are similar in hardness to measured weld microhardness values) is 0.50 J/mm^2. In order to increase the impact energy significantly a cooling rate that results in a hardness of <200 would be required.

However, a hardness of 200 corresponds to a UTS of <700MPa and this would be unacceptable for a weld in a 1400MPa parent material.

In addition, the cooling rate required to achieve this hardness is 10°C/s, which would require a 800-500°C cooling time of 30 seconds. This is not practical using existing welding equipment (see Section 7.3) and not acceptable in terms of the practical welding process. This is because the welding process would need to be extended in time by approximately 25 times the existing typical weld time and, thus, would be seriously detrimental to productivity.

This section has shown how the CCT microstructures discussed in Section 7.1 translate into a range of available mechanical properties for each steel. The cooling rate, by controlling the microstructure, provides a means of modifying the 0.2% proof stress and tensile strength, impact energy and hardness for a given steel.

However, these results also highlight the caution that should be exercised when considering modification of weld properties through process control. It is clear that neither cooling rate nor hardness can be considered the sole factors of importance. The cooling times required to achieve high impact energy levels are, in some cases, unacceptable for practical welding purposes and even if this barrier did not exist the UTS at the cooling rates required would be unacceptably low.

7.3 Measurement of Thermal Profile and Process Control

A technique for making localised temperature measurements during spot welding was presented in Section 5.3 and the results from a series of welds, made using a range of welding schedules, are presented in Section 6.4. This section discusses the advantages and limitations of the technique used and considers the thermal profiles generated by different welding schedules, in the context of the results reported in the literature.

7.3.1 Advantages and limitations of thermocouple techniques for monitoring spot welding

The thermocouple technique, described in Section 5.3 allowed localised temperature measurements to be made during spot welding. Two thermocouple types were used:

- bare wire; consisting of two separate thermocouple wires spot welded onto the surface of the weld coupon and protected by manually threaded ceramic sheaths
- sheathed thermocouples; manufactured with a thermocouple junction protected within an exterior sheath.

Both thermocouple types had advantages and disadvantages. The bare wire thermocouples produced readings that experienced interference, due to the high currents used during spot welding, and the electrical contact that this type of thermocouple had with the weld coupon. This meant that the bare wire thermocouples were unable to measure temperatures generated during the heating part of the operation but were able to measure the cooling rates experienced by the weld once the current had been switched off. This was due to the thermocouple reading returning to the true value after the current had been switched off. The sheathed thermocouples did not experience this interference, as the thermocouple junction did not have an electrical connection with the weld coupon. This suggests that sheathed thermocouples would be more suitable to measuring temperature during spot welding but on metallographic examination of the spot welds produced with sheathed thermocouple monitoring it was found that the sheath had melted and the sheath material had become incorporated into the weld. Clearly, neither technique provided a complete solution, but of the two, bare wires appeared to offer the method least likely to interfere with the weld formation, although the only information that could be reliably measured using this type of thermocouple was the cooling rate.

Despite the limitations of the thermocouple techniques, for measuring the precise temperatures generated during welding, the information that they did provide was considered an important tool for improving understanding of the nature of the thermal cycles generated by different welding schedules. For example, in Tables 6.7, 6.11 and 6.14 the cooling rates measured during extended weld time welding, pulsed welding and controlled cooling experiments are summarised. The measured cooling rates provide evidence of the idea, often mentioned in published work, that extending the overall weld time increases the amount of conduction to the surrounding material, thereby decreasing the thermal gradient from the nugget to the parent material, which in turn decreases the cooling rate.

A further important reason for attempting to measure the thermal profile generated by welding schedules is to assist with the design of advanced welding procedures. For example, in Section 6.4.4 the method of selecting suitable parameters to produce controlled cooling, after spot weld formation, was described. This required knowledge of time – temperature measurements made during basic single pulse welding. It can be seen that the measured thermal profiles allowed suitable times for the application of post weld pulses to be applied in order to attempt to decrease the cooling rate.

Thermocouples have been used by other investigators to monitor resistance spot welding[19, 78]. For example, Nishi et al[19] attempted to monitor the difference in cooling rate for two different hold times. Thermocouple measurements were also used to validate a model of weld growth developed by Han[78]. The analysis that thermocouple measurements can be a useful means of monitoring spot welding thus agrees with other published work.

7.3.2 Time – temperature measurements during basic, single pulse spot welding

Some aspects of the thermal cycle experienced by a resistance spot weld can be readily deduced from the transformed microstructure. For example, the boundary between the weld nugget and the heat-affected zone must, by definition, coincide with the melting point of the steel, which in low carbon grades is typically 1530°C. Further the boundary between the heat affect zone of a spot weld and the parent material must be the austenite transformation temperature, which is approximately 730°C for most low carbon steels.

The cooling rates from peak temperatures that occur in the weld nugget and the heat-affected zone were measured using plain wire thermocouples for a basic, single pulse spot welding schedule and the results are given in Figure 6.43. The peak temperatures could not be determined but the 800-500°C cooling rates were found to be 1614°C/s for the weld nugget and 684°C/s for the heat-affected zone

The cooling rates experienced by a spot weld have been quoted as being from 2000°C/s[49] to 100,000°C/s[14] although the faster cooling rates are more likely in the weld nuggets of thinner gauge steel, due to the closer proximity of the weld nugget to the water cooled electrode. In practice, cooling rates of 100,000°C/s have not been measured and these faster rates are predictions from computer models of the welding process. Table 7.1 shows the cooling rates measured during spot welding and quoted in published work. However, the means of monitoring the cooling rate, and the thickness of the strip steel used in each case highlighted, varied. It can be seen that the result, measured during simple single pulse welding in the present study, for the weld nugget, falls in the middle of the table. The work on a TRIP steel by Ellwood[93] suggests a very low cooling rate for the weld nugget. The strip thickness in this work was 2.9mm and relatively high sheet thickness could possibly have influenced the cooling rate experienced by the weld nugget. However, the measurements in this work were made using an infrared thermal imaging camera aimed at the top of the weld coupon and the peak temperature measured was only 475°C. As can be seen in Figure 6.46, the cooling rate decreases once a temperature of approximately 500°C is reached and therefore the rates measured in this work are unlikely to be indicative of the 800-500°C cooling rate. The work by Holliday[92] used a similar approach but involved 1mm thick steel. In this case, the cooling rate measured was for the electrode tip itself, at the electrode-sheet interface, and was found to be 500°C/s. This cooling rate measurement was from a peak temperature of 420°C and thus, as for the measurement by Ellwood[93], it may not be indicative of the cooling rate from higher temperatures. In addition, the electrodes were manufactured from a copper-zinc alloy and the thermal conductivity of this material is much higher than for steel (copper - 385 W/m-K; steel - 52 W/m-K), the consequence being that the cooling rate will be faster in the higher thermal conductivity material.

The range of cooling rates quoted by Williams[49] is high, from 2000 to 20,000°C/s. However, no details of possible measuring techniques are given in this review so it is not

possible to directly compare them with those measured in this research. However, the bottom end of the range quoted is of the same order of magnitude as the rate measured using thermocouples in this work.

Nishi et al[19] used 0.1mm thermocouples to measure the cooling rate during resistance spot welding. The 800-500°C cooling rate is not quoted but, from the time-temperature graph published it is estimated to be 5000°C/s, approximately 3 times that measured in the present study. The peak temperature measured for the spot weld was 980°C and the measurements were made at the boundary between the nugget and the heat-affected zone. It should be noted that the strip thickness in this work was 0.8mm thick. The DP800 grade used in the present study was 2.5 times thicker at 2mm. It is possible that the cooling rate experienced by the thinner material (5000°C/s) was faster because of the closer proximity of the thermocouple to the water cooled electrodes compared to those used in the DP800. In modelling work quoted by Gould[14] it was reported that a reduction in sheet thickness from 1.5 to 1.0mm leads to an increase from 10^3°C/sec to 10^5°C/sec. No measurements were provided to verify this prediction and a rate of 100,000°C/s is significantly higher than the others given in Table 7.1.

The cooling rate measured in the heat-affected zone of the spot weld, indicated in Figure 6.43, was 684°C/s although the peak temperature in this case was only 680°C. There are no measurements available for comparison but it is considered possible that the cooling rate in the heat-affected zone is lower than that for the weld nugget because the material in this zone is not in such close proximity to the water-cooled electrodes.

7.3.3 The effect of modified welding schedules on time – temperature measurements

Extended weld time schedules

The thermal profiles for two welds made with extended welds times (25 and 50 cycles) can be seen in Figures 6.44 and 6.45 and the cooling rates extracted from them in Table 6.8. It can be seen that the cooling rate in the weld nugget did not change significantly at a weld time of 25 cycles. The heat-affected zone:nugget ratio was also measured and found to be the same for the 14 and 25 cycle welds (Table 6.9). A further increase in the weld time to 50 cycles caused a marked increase in the cooling rate measured by thermocouple R1 in the weld nugget but a decrease in the cooling rate measured by thermocouples K1 and K2 in the heat-affected zone. It seems sensible that as the heat

input increases the cooling rate, in the heat-affected zone, decreases. The higher heat input would result in more heat being conducted into the weld coupon, lowering the temperature gradient between the weld nugget and the parent material. However, it is possible that the cooling rate in the weld nugget, being in close proximity to the water-cooled electrodes still experiences sufficient a draw on the heat energy present in the weld to maintain the high cooling rate observed.

Pulsed welding schedules

Three pulsed welding schedules were evaluated: 2x7, 7x2 and 14x1 (no. pulses x pulse length in cycles). The thermocouple readings can be seen in Figures 6.47 to 6.49 and the cooling rates extracted in Table 6.11. It can be seen from Table 6.11 that pulsed welding was successful at decreasing the cooling rate in the weld nugget although little change was seen in the heat-affected zone cooling rates. It should be noted that the pulsed welds were indented by approximately 40% and, as such, would not be acceptable to manufacturers. However, it is thought likely that the indentation could be reduced through a reduction in the welding force, which would be beneficial in practical terms, due to the low force range available to manufacturers from most typical spot welding robots.

Pulsed welding has been considered in some published work[13, 93]. Williams[13] used a combination of 5 pulses of 20 cycles and a welding current of 15.5kA to weld a high carbon, niobium alloyed steel. The weld did demonstrate a reduction in hardness but no temperature measurements were available to establish the effect of the pulsed schedule on the thermal cycle although it would appear that a cooling rate reduction is the reason for the reduction in the measured hardness.

Ellwood[93] attempted pulsed welding on a 2.9mm TRIP steel. The combination of pulses used were selected to equal a total weld time of 35 cycles and were given as: (5 10 10 10), (10 25), (15 20) and (5 10 20). No weld currents were provided and it is not known if the weld size produced using these alternative schedules were acceptable but it was stated that no reduction in hardness resulted from any of the combination of pulses tried. This work is inconclusive and cannot be compared directly with that of the present investigation because of the lack of process information. Ellwood[93] considered that a welding schedule that produced a total cooling time, from molten nugget to room temperature, of 3 minutes was likely to be required in order to facilitate a reduction in

hardness. This conflicts with the results of this study and the findings of Williams[13] that both indicate that pulsed welding can effect a decrease in cooling rate sufficient to affect hardness in a few cycles, which amounts to an extra weld time of less than 1 second.

Controlled cooling schedules

Two attempts at controlling the cooling of the weld, following solidification were made, using the welding schedules provided in Table 6.13, that is one and two post weld pulses. The time of application of the pulses was selected based on the thermocouple readings shown in Figures 6.51 and 6.53 and the resulting time-temperature profiles for the welds made using these schedules are given in Figures 6.52 and 6.54. The cooling rates measured in the weld nugget are given in Table 6.14. It can be seen that the controlled cooling experiments were successful in decreasing the cooling rate experienced by the weld nugget with one pulse decreasing the cooling rate by 21% to 1263°C/s and two pulses appearing to decrease the cooling rate by 60% to 650°C/s.

This is very promising although the hardness of the DP800 continuous cooling transformation samples, discussed in section 7.2, did not decrease significantly until the cooling rate was decreased below 100°C/s. However, the potential of small, post weld pulses to control the cooling rate appears to have potential for the future control of spot weld thermal profile. It is thought important that any future developments in this area of welding schedule design are made in conjunction with further studies, either practical or computer modelling, that assess the thermal profile generated by a set of welding parameters. The time-temperature profiles used to develop the schedules in the current programme enabled the selection of suitable times of application of post weld pulses to be made without costly 'trial and error' exercises. The thermal profile information also assists in the understanding of the reason for the success of the designed schedules, in terms of reducing the cooling rate.

Post weld tempering schedules

Three welds were subjected to post weld tempering cycles according to the parameters given in Table 6.15. The aim of these experiments was not to modify the cooling rate of the welds but rather to allow them to cool to room temperature and then modify the microstructures. It has been reported[94] that tempering a strip steel containing martensite

improves the properties by reducing the hardness and increasing the toughness. These benefits are considered desirable for welded strip steels.

The time-temperature profiles measured for the three tempered steels are given in Figures 6.58 through 6.60. Figure 6.58 shows that the short pulse applied after the spot weld had cooled was successful in producing a short low temperature treatment. However, the combination of two pulses, applied close together after the initial weld had cooled, produced higher temperature treatments rather than longer times as required. In particular the thermal profiles seen in Figures 6.60(a) and (b) indicate that weld has gone through a further solid-state transformation due to the applied heat treatment producing a temperature of over 900°C. However, the results given can facilitate further development in this area and, in particular, it can be seen that the tempering treatments can potentially be moved to shorter times after the main welding pulse.

7.4 Implication of Results for Practical Resistance Spot Welding

This research programme was concerned with the series of steps that translate a practical resistance spot welding schedule into the weld performance of a selected grade of high strength steel. The important steps are illustrated schematically in Figure 7.1. It can be seen that the first steps, the inputs, are the selection of a steel providing the desired performance, for example, formability, impact performance or corrosion resistance; and the selection of a welding schedule, including parameters such as weld current, time and force. Overall, the desired outcome from combining these two selections is acceptable component performance. The four intermediate steps: thermal profile generation; inherent continuous cooling transformation behaviour; weld microstructure and morphology; and weld properties are the means by which the inputs are translated into the desired output. Figure 7.1 further indicates the sections of this chapter that relate to each of the critical intermediate steps. In this section, the implications for practical welding will be considered.

7.4.1 Weld microstructures and properties

Section 6.1 presented a series of micrographs for $5\sqrt{t}$ welds made in the six steel alloys used for this investigation. The same amount of current flow time, measured in cycles was used to produce each of the welds but as can be seen in Table 4.4 the applied value of current decreased through the range LC to DP1400. The reason for this is two fold: the increase in alloy content, for the higher strength grades, increased the bulk resistivity of the steel grades. This increase in resistivity contributes to the total resistance of the current path and, according to Joule's law (equation [2.1]) this increases the amount of heat generated for a given amount of current application. A second reason for the reduction in the required weld current for the higher strength, higher CE grades is that the higher strength grades are thinner and thus a $5\sqrt{t}$ weld is not as large, in absolute terms, and does not require as much material melting in order to grow.

The microstructures observed in Figures 6.1 to 6.6 are sensible and follow a sensible trend that agrees with the results from the samples produced by continuous cooling transformation experiments. The LC and LCNb welds (CE – 0.04 and 0.07 respectively) both have weld nuggets consisting of lath ferrite but the LCNb grade weld has a refined heat-affected zone (Figure 6.2(e)) compared to the LC grade (Figure 6.1(e)). The dual

phase welds in general have a different appearance to the lower CE grades. The weld nuggets of all four dual phase grades contained martensite. However, the columnar prior austenite grain structure, from which the martensite transformed can be seen to be finer in the higher CE grades.

Microhardness profiles for welds made in the six steels can be seen in Figure 6.8 and show a sensible trend. The microhardness measured in both the heat-affected zone and weld nugget increase with an increase in alloy content. The location of the peak hardness, that is, in the nugget or the heat-affected zone, can be explained with reference to the microstructures seen in Figures 6.1 to 6.6. The lower CE grades, LC (0.04) and LCNb (0.07) demonstrate grain refinement in the heat-affected zones of their $5\sqrt{t}$ welds but the microstructure is still predominantly proeutectoid ferrite with some carbide transformation product. It would thus be expected that the heat-affected zone of these lower CE grades would be harder than the parent material, due to the strengthening associated with a refinement of grain size, as described by the Hall-Petch equation. However, the weld nuggets would be expected to be harder due to the lath ferrite constituent that is present. In the dual phase grades, the heat-affected zones of all the $5\sqrt{t}$ welds appear to contain bainite or martensite with martensite more prevalent as the CE increases. These are the same constituents that exist in the weld nuggets of these higher CE grades. However, the packet size in the heat-affected zone is significantly smaller than in the weld nugget and thus the heat-affected zones are harder than the weld nuggets because of the effect of packet refinement in addition to the change in the microstructural constituents from the parent material.

The overall relationship between the measured average microhardness and the CE for all four steels can be seen in Figure 6.7. The trend line indicated on the graph is described by equation [6.1]: Microhardness = 1304(CE) + 132.

This equation is practically significant in that it indicates that there is a minimum hardness that the alloys would have if there was no influence of carbon or other alloying elements that are used in the CE equation [2.7]. This value (132Hv) is higher than the typical quoted hardness value for pure iron (89Hv) and this is likely to be because of the influence of the small number of elements that are not included in the Ito-Bessyo CE

equation[33]. For example, Table 1 shows that all the steels contain small amounts of phosphorus and sulphur. In principle, however, it is sensible that as the alloy content increases the measured microhardness will increase. This equation contains several terms, as a result of the CE variable. For example, it contains the effect of carbon, which has been quoted[36] for fully bainitic structures, as seen in the DP600 weld nugget, as being 190Hv increase for each wt%C.

The average microhardness measurements for the DP600 and DP800 can be seen, from other work[95, 96] to correspond to lap shear strengths of 9.7 and 13.7kN respectively. These two values are both around 40% lower than the minimum weld strengths of 25.1 and 29.4kN that are recommended by BS1140[26]. Further work carried out as part of this series of investigations into the standard properties of dual phase grades found that the DP1000 grade also failed at lower than desirable weld strengths. The mode of failure for the DP1400 lap shear samples was plug, but due to the low weld strengths, it was considered that the failure itself was brittle, and that the plug appearance was due to brittle failure through the heat-affected zone of the weld. This published investigation demonstrates the requirement for greater understanding regarding the mechanisms of property development in advanced ferrous alloys.

Figure 6.9, which shows the relationship between the % increase in microhardness and the carbon equivalent, demonstrates that, in terms of an increase in weld hardness, the CE alone may not be a successful predictive tool. The trend seen in this figure will be influenced by the parent microstructure. In the low CE grades (LC and LCNb) the parent microstructures are ferrite with small amounts (<5%) pearlite. The increase in the hardness on welding is, as previously described, predominantly a result of grain refinement. In the middle CE grades (DP600 and DP800) the parent structure is approximately 25% martensite but, on welding, the carbon that is present in supersaturated solid solution in the martensite is released and diffuses into the area that has reached sufficient temperature. On cooling this area can transform with a modified carbon content and because the continuous cooling associated with spot welding is controllable to the same extent as a hot mill, fully bainite or martensite microstructures form that have significantly a significantly higher intrinsic hardness compared to the parent material that contains around 75% ferrite. The highest alloy grades (DP1000 and DP1400) demonstrate high hardness measurements in the unwelded state due to the high

volume fractions (around 45%) of martensite that they contain. Thus, although the carbon in the parent martensite constituent does cause fully martensitic microstructures to form on welding, the measured increase in hardness is not as significant as for the lower CE dual phase grades.

The effect of advanced welding schedules on weld microstructure and hardness

The series of advanced welding schedules, including extended weld times, pulsed welding, controlled cooling and post weld heat treatments were presented in Section 6.4. The details included microhardness profiles for the welds that have been produced using one of the weld schedules and each process, in terms of the effect on the weld hardness is considered below.

- **Extended weld time**

Two extended weld times were used – 25 and 50 cycles, compared to the basic weld time of 14 cycles, to make welds in DP800. The microhardness results seen in Figure 6.46 show that the heat-affected zones of the two welds made using longer weld times are 10-20% lower in hardness but the average hardness in the weld nuggets is not significantly changed. The decrease in the heat-affected zone hardness suggests a lower cooling rate and for the 50-cycle weld it can be seen from Table 6.8 that the cooling rate is slower at 480°C/s compared to 684°C/s for the basic weld. This is thought to be due to conduction of the heat, from the longer weld time, throughout the weld coupon. This effect would decrease the thermal gradient across the heat-affected zone and reduce the driving force for fast cooling. The cooling rate in the weld nugget increases with an increase in weld time indicating a possible reason for the high hardness measurements. It is thought that this could be due to the slight indentation of the weld nugget, which for the 50-cycle weld is approximately 10%, bringing the water cooled electrodes closer to the weld nugget and thus increasing cooling. This suggests that extended weld times could offer a potential solution, to a requirement for a reduction in cooling if the weld force were optimised.

- **Pulsed Welding**

The microhardness profiles for the welds, made in DP800, using pulsed welding schedules are shown in figure 6.50. It can be seen that all three pulsed welding schedules were successful in reducing the heat-affected zone hardness and it is thought that a similar

mechanism to that described for extended weld time is responsible for this. The nugget hardness, however, varies considerably and no clear trend with welding schedule can be seen. The thermocouple results suggest that pulsed welding is successful in terms of reducing cooling rate. The results given in Table 6.11 indicate that the cooling rate in the weld nugget is reduced by 20% for the 2x7 and 7x2 schedules and by 60% for the 14x1 schedule. This seems promising but the welds themselves, seen in Figures 6.47 to 6.49 (b) show indentation of approximately 40%, which would be unacceptable in practice. However, the potential for using pulsed welding has been established. The results of Williams[13] agree with this finding. A brief series of experiments suggested that reductions in weld hardness of approximately 21% could be achieved through the use of pulsed welding. The one result for pulsed welding was made using 5x20 cycles of weld current at a lower transformer tapping than used in this work. This weld time is longer than was considered desirable for the present work. However, the substantial reductions in thickness are seen right throughout the weld, in the work by Williams[13], and further investigation into the potential use of pulsed welding should be carried out.

- **Controlled Cooling**

The controlled cooling experiments can be seen in Figures 6.52 and 6.54. The principle of using the thermal profile measured using thermocouples to select suitable times to apply small pulses after the main weld has formed was successful in terms of reducing the cooling rate of the weld. The measured cooling rates of the controlled cooling welds were 1263°C/s and 650°C/s for one and two post weld pulses respectively suggesting that the hardness profiles should be significantly modified. Examination of the microhardness profiles in Figure 6.55, however, indicates that the single controlling pulse was more successful than two pulses.

- **Post Weld Tempering**

The principles of tempering spot welds using small pulses of current after the initial weld has cooled is demonstrated in Figures 6.58 to 6.60. The microhardness profiles can be seen in Figure 6.61. It is clear that none of the tempering schedules has a significant effect on the weld hardness. The most successful welding schedule involved one post weld tempering pulse. This is possibly because the schedules that used multiple post weld tempering pulses increased the temperature to a level where the microstructure undergoes

a phase transformation and thus the final microstructure is not tempered but undergoes a solid state transformation. This appears to be the case in Figure 6.60(a).

The selection of practical welding parameters in this section of work was made with consideration of the overall weld time. It was considered desirable that the total weld time should remain as short as possible due to the consequences of increases to productivity. In light of the findings, however, and considering the results of Williams and Lavery[13] it is considered that longer weld times may be necessary to achieve the desired modifications to the weld properties. It should be noted, however, with reference to Figures 6.41 and 6.42 that reductions in hardness correspond to reductions in strength and it is important that modifications to cooling times are not detrimental to weld strength.

7.4.2. Future development of resistance spot welding for advanced steel alloys

The advanced high strength steels studied in this research programme have complex alloy compositions and strip properties that are the result of a combination of these compositions and careful thermomechanical processing. These steels present significant challenges to welding engineers and whilst they offer desirable benefits to the automotive industry in terms of their strip properties, optimisation of welding processes is more complex than for the lower alloy grades typically in current use.

In order for manufacturers to have confidence in the welded properties of these advanced high strength steels, a deeper understanding of how practical welding processes interact with these complex alloy compositions is required. This is not a straight forward task – the thermal gradients present in a spot weld can be influenced by many practical factors such as current shunting, coating type and welding schedule. Unlike hot rolling, where soaking treatments of 30 minutes or more are available to ensure that all the necessary alloying elements are in solution, in spot welding the heating and soak times are typically fractions of a second. In the heat-affected zone, where the peak temperature varies from approximately 730°C to 1530°C, the rapid heating and cooling cycles, introduce the potential for only partial dissolution of elements. This situation is more complex and can cause localised areas of undesirable microstructural to form. Work considering this effect has been published by Savage et al[51], who found that controlling the spacing between carbide particles was critical for preventing networks of brittle transformation constituents developing in heat-affected zones. This is because partial dissolution of the

carbon, into the surrounding iron matrix could cause local concentrations that were high enough to promote martensite formation and a network of martensite was found to be detrimental to weld properties.

Further understanding in this area will be gained through a combination of practical welding experiments and more detailed laboratory based experiments. The significant challenge here is to ensure that the understanding that is drawn from practical experiments has a scientific basis and that the understanding drawn from laboratory experiments is relevant to the practical application. For example, many welding studies consider the change in a weld property, such as lap shear strength[13, 95], as a result of a change in welding parameters but the link between the selected welding schedule, thermal cycle and metallurgical condition of the resulting spot welds is not always discussed. These links will be more important to the advanced ferrous alloys as the higher alloy composition will make these modern grades more sensitive to the cooling rate. This effect has been shown in this work and agrees with the findings of Williams[13] who considered the increase in carbon in a niobium alloyed steel and Jones[15] who considered rephosphorised and dual phase steels.

In laboratory experiments, the selected thermal cycles used should be representative of practical conditions experienced. However, the thermal conditions in the heat-affected zone vary radially with distance from the weld nugget and as a result it is not possible to produce cycles that are representative of the whole heat-affected zone. Further, the weld nugget transforms from a columnar prior austenite grain size that is the result of the strong unidirectional cooling attributed to the water-cooled electrodes being in close proximity to the weld nugget. There is currently no published work on attempts to simulate the columnar grain formation and subsequent cooling. Considering the significance attributed to prior austenite grain size by researchers in welding[49, 52, 56, 60] and hot rolling[69, 70] fields it seems important that the effect of this factor be considered in future work.

Computer modelling of spot welding processes facilitates the examination of the thermal conditions through a full weld, rather than in the discreet locations afforded by thermocouple measurements. Many attempts have been made to model spot welding, ranging from simplified models[78] to more complex three-dimensional models[97] and

comparison with thermocouple measurements has yielded promising results, in terms of thermal profile prediction. However, prediction of weld microstructures from predicted thermal profiles has been limited. A recent development is a commercial modelling package called SYSWELD[98]. This package claims to use a combination of fundamental theory, regarding heat transfer, and continuous cooling transformation curves to predict weld microstructures and hardness. However, it is clear from the aim of the package that the results will be dependent on the accuracy of the continuous cooling transformation diagrams that are used, for the welding process that is being modelled, which returns emphasis to the laboratory conditions used to produce the CCT curves.

Advanced welding schedules are thought likely to offer potential in terms of spot weld property control. The work presented as part of this programme has highlighted four potential modifications to standard spot welding techniques: extended weld times, pulsed welding, controlled cooling and post weld tempering, and each of them demonstrated some changes to the thermal profile generated and weld hardness. It is considered that the optimum weld programmes may combine more than one of these options but the rationale should be based on the desired weld properties. As presented in Section 6.3 and discussed in Section 7.2 changes in any one property has consequences in terms of another and traditional, unpublished, concerns regarding weld hardness measurements above 300 or 350Hv are not relevant to modern high strength steel grades. Thus, maximising, for example, reductions in the weld cooling rate, may not be desirable as it could lead to low strength welds that provide undesirable weak points in a welded component.

A few other studies have touched on the issues presented here[13, 21, 92,] but the experiments appear to select pulsing conditions by trial and error, rather than based on prior knowledge of the desired properties and required thermal cycles. A recently initiated study into the weld quality of transformation induced plasticity steels[98] may offer some further insight into the important area of advanced welding schedules with early considerations documented as controlled cooling and post weld tempering schedules.

Extending the principles developed in this work to other welding processes is also an important consideration for future work. The Welding Institute (TWI) study already mentioned[99] considers the role of laser welding in providing greater control over weld thermal cycle. Laser welding with two beams, a primary welding beam and a secondary,

lower powered beam to effect a reduction in cooling rate, may offer the potential for greater control over cooling rate during welding. Although not mentioned in early publications from this study it is considered important that any changes in weld properties are considered in light of the relationship between thermal cycle – continuous cooling transformation behaviour, in order that information generated can be used in predictive models such as SYSWELD in future work.

As mentioned in the literature review, many automotive components, produced from modern high strength steels such as dual phase grades, will not, in practice, be welded to components made from the same grade or thickness. This introduces further variables that will influence both thermal cycle and the metallurgical properties of welds produced. Same thickness and multi-thickness stacks are known to influence weld nugget formation[99] and potentially existing work in this area could be used in conjunction with studies considering continuous cooling transformation behaviour to extend knowledge to cover more practical welding configurations.

The recent TWI study[98], in which the potential of joining transformation induced plasticity components to mild steel components is proposed, has highlighted consideration of multi-grade joints. The joining of low and high alloy steel should result in a weld nugget that has an alloy composition representative of an average of both parent compositions. This could produce desirable effects, such as a reduction in the hardness of the welds. Peterson[20] attempted to simulate this effect in same grade joints by introducing a sheet of low alloy steel between two higher alloy grades and met with some success in terms of an increase in plug failures. However, the heat-affected zones of high alloy grades will not be influenced by this dilution effect and, if demonstrated to be a source of weakness in a welded joint, will require separate consideration. This is a consideration in the case of high strength dual phase steels. Thus the continuous cooling transformation work presented in this research programme, which was produced using conditions that provided austenitising temperatures, and prior austenite grain sizes, relevant to the heat-affected zones of spot welds would be applicable even in the case of multi-grade joints.

There are clearly many threads to a complete research programme considering practical welding of modern high strength steels, that rely on composition and microstructure for

their advanced properties. The approach taken in this research considered two important areas:

- understanding of the practical welding process in terms of generated thermal cycles and the techniques for carrying out evaluation of different welding schedules;
- understanding of the continuous cooling transformation behaviour of dual phase steel alloy compositions, an important class of modern high strength steel alloys for automotive applications, under conditions that are relevant to spot welding.

A radical solution to the challenge presented by the continuous development of advanced high strength steel grades would be for welding considerations to be a key factor in alloy design. Welding engineers would be faced with the challenge of influencing alloy composition, to improve the weldability when joined using techniques appropriate to the application that the alloy is intended for, rather than simply modifying welding processes to fit the alloy compositions already in production. Further fundamental research into the effect of, for example, individual alloying elements on weld properties will be necessary for welding engineers to develop an understanding of their requirements, in order that they can contribute to alloy composition design. Expanding this research into the thermal conditions generated by a wide range of welding schedules and processes will also be an important step in preparing for the likely demands of automotive manufacturers in the future.

8. CONCLUSIONS

Weld performance is critical to the crashworthiness of the body-in-white structure. This research programme reviewed current knowledge concerning the weldability of high strength steels with complex alloy compositions and identified key areas that required further investigation. In particular, the concerns regarding the possibility of brittle microstructural constituents developing in spot welded high strength steels required investigation as well as further work considering the influence of the resistance spot welding schedule on the transformation products. Thus the aim of the present research programme was to obtain an understanding of the continuous cooling transformation behaviour of dual phase steels and to evaluate the potential for controlling the resistance spot welding process through advanced welding schedules. This programme embraced two diverse field of research: ferrous metallurgy and practical resistance spot welding. Overall, some progress has been made towards finding a clear path between the two considerations and, importantly, the next steps towards developing more robust welding schedules for modern high strength ferrous alloys have been identified. The following section highlights the main experimental techniques developed and relationships found.

8.1 Experimental Techniques

In order to achieve the aims of this project, important experimental techniques were developed. These were:

8.1.1 A novel dilatometer for use with a Gleeble 1500.

This dilatometer allowed greater accuracy and repeatability in setting up dilatometry experiments. It also provided for greater stability which was particularly important during forced air and water quench tests but also of significance during slow cooling rate / long time tests where the rubber band in previous use had sometimes sagged making results more difficult to interpret.

8.1.2 A disc compression test for measuring tensile properties.

This test had previously been used for a range of relatively pure materials, for example, copper, aluminium and ultra low carbon steel, with tests on low alloy steel being reported as less accurate due to the presence of inclusions and carbides. It has been shown that the test can be used to produce reliable results in low alloy steels provided the experimental set-up maximises the quantity of material being tested. In

this work a 4mm diameter punch was used with a 7mm die and a 1mm thick, 9.5mm diameter disc was tested. This provided for the most representative amount of material to be tested which reduced scatter in the results.

8.1.3 An innovative technique for measuring thermal profile during welding.

This method involved the use of fine thermocouple wires welded directly to the steel sample surface to measure temperature. The wires were K-type or R-type depending on their position relative to the weld and were sheathed by means of a solid ceramic two bore rod, which ran along a channel machined into each pair of samples. Wires were connected to a stand alone datalogger and a laptop recorded time-temperature data. This combined with metallographic analysis of the welds manufactured allowed measurements of temperature to be made at positions associated with specific locations within a spot weld such as the heat-affected zone.

Sheathed thermocouples were also trialled but, due to the low temperature rating of the sheaths, compared to that of the thermocouple wires, they frequently melted and contaminated the weld pool, usually resulting in a subsize weld nugget.

8.2 Experimental Findings

The conclusions of the experimental work can be split into three sections: continuous cooling transformation microstructures, microstructure – mechanical property interactions, control of resistance spot welding.

8.2.1 Continuous cooling transformation curves and microstructures

(i) The austenite start transformation temperature (AR_3) decreased with increasing Carbon Equivalent (CE) of the dual phase grades. The main elements that affected this temperature were carbon and manganese. For example, at a cooling rate of 10°C/s in the low alloy LC sample the AR_3 was 851°C but in steel DP800, that contained carbon, manganese and microalloying (Nb) the AR_3 was 705°C.

(ii) The AR_3 decreased with increasing cooling rate. This effect was more pronounced in the higher CE alloys. For example, for the LCNb grade an increase in the cooling rate from 0.5°C/s to 35°C/s resulted in an AR_3 decrease of 4%. For the DP800 the decrease in the AR_3 over the same range of cooling rates was 11%.

(iii) The transformation microstructures present in continuously cooled samples were significantly affected by both CE and cooling rate. An increasing CE, in reflecting the alloy chemistry, directly affects the transformation products at a given cooling rate by increasing the number of alloying atoms, particularly carbon, present to distort the iron lattice. Further, by decreasing the transformation temperature an increased CE further influences the transformed microstructure due to the reduced thermal energy available at these lower transformation temperatures, increasing the likelihood of non-diffusional transformation products such as bainite and martensite. As the CE was increased from 0.07 to 0.27 the microstructure at a cooling rate of 25°C/s changes from a ferrite, pearlite, and coarse acicular ferrite mixture to a predominantly martensitic microstructure.

An increasing cooling rate, by reducing the temperature of transformation, also affects the transformation products through a reduction in the energy available to the transformation. For example, for the DP1000 alloy, as the cooling rate increased from 1 to 133°C/s the microstructure changed from ferrite pearlite to fully martensitic.

8.2.2 Structure – property interactions

(i) Hardness

The bulk hardness of the continuously cooled samples was found to increase with both CE and cooling rate. The increased CEs effects were three fold. The increased alloy content had a substitutional solid solution alloying effect that increased hardness. The increased carbon content changed the proportion of transformation products as would be expected from the iron – iron carbide phase diagram, which increased the hardness. The increased CE decreased the transformation temperature, which increased the proportion of non-equilibrium transformation products as previously described. The hardness increased with a greater proportion of coarse acicular ferrite, bainite or martensite.

(ii) Tensile strength and 0.2% proof stress (disc tests)

The predicted ultimate tensile strength increased with both CE and cooling rate. The relationship with hardness was linear as expected but plotting hardness

against strength indicates that, if softening were to be undertaken via post weld heat treatments or otherwise, there are minimum hardness levels that would be desirable because if hardness drops too low the corresponding strengths would not match that of the parent material.

The failure mode of discs moves from ductile (failures round the cup) to more brittle (failure across the cup formed) indicating the influence of cooling rate and subsequent transformation microstructure on both strength and ductility. For example, in the LCNb alloy, at a cooling rate of 10°C/s the tensile strength was 402MPa but in DP800 it was 700MPa. This corresponds to a change in the microstructure from ferrite - pearlite to ferrite - bainite. An increase in the cooling rate from 1 to 330°C/s in DP1400 increased the strength by 500MPa as the microstructure changed from ferrite – pearlite to bainite - martensite but the failure mode changed from circular to transverse indicating potentially low toughness microstructures.

(iii) Impact energy

The impact energy decreased as the alloy content (CE) or cooling rate increased in the dual phase steels. This contrasts with the low carbon materials that showed a small increase in the impact energy associated with a refinement of the microstructure. For example, in LCNb at a cooling rate of 25°C/s the impact energy was 1.52J/mm^2 but in the DP1000 it was 0.68J/mm^2. In the DP800 samples an increase of the cooling rate from 1 to 73°C/s resulted in a decrease in the impact energy from 0.95 to 0.50J/mm^2 but in the LCNb there was a slight increase from 1.36 to 1.54 over the same increase in cooling rate.

The impact energy associated with high hardness materials indicated that reductions in hardness would produce only limited benefits in terms of impact energy before a hardness that related to a strength lower than the base materials strength was reached.

8.2.3 Control of resistance spot welding

(i) Standard welding schedules

Cooling rates in the weld nugget and heat-affected zones, of the order of 1650°C/s and 700°C/s respectively, were measured.

(ii) Increased weld times

Increasing the length of the weld time, with a corresponding decrease in the welding current increased the cooling rate in the weld nugget but decreased the cooling rate in the heat-affected zone.

(iii) Pulsed welding

Using a combination of pulses to produce a $5\sqrt{t}$ weld resulted in a reduction of the weld nugget cooling rate from 1650°C/s to 1250°C/s and 668°C/s for the [7 x 2] and [14 x 1] pulsed schedules respectively. A small decrease in the microhardness profile was seen for welds produced with pulsed welding schedules although this varied across the weld.

(iv) Post weld cooling treatments

Applying short time, low current pulses shortly after the main welding pulse had the effect of reducing the nugget and heat-affected zone cooling rate. For example, on application of one post weld pulses the weld nugget cooling rate decreased to 1263°C/s and there was a corresponding reduction of approximately 5% in the hardness of the weld nugget.

(v) Post weld tempering treatments

A method of using short time, low current pulses was successful in creating a post weld tempering treatment which could be varied in terms of pulse length and current level. Reductions in the microhardness profiles were seen. For example with a 2 cycle tempering pulse of 300°C an average decrease in the microhardness profile of 7% was observed.

9. RECOMMENDATIONS FOR FURTHER WORK

The results of the present research programme have highlighted a number of areas that require further investigation. In particular the following areas are considered important areas for future consideration:

1. The present research considered the continuous cooling transformation behaviour and weld quality of commercially available high strength, dual phase, steels. The chemical compositions of the dual phase steels were complex, with interstitial and substitutional solid solution strengthening mechanisms present in addition to microalloying additions. A number of the elements in the steels could be considered together through the Carbon Equivalent (CE) calculated parameter but a more in depth understanding of the effect of each element could be obtained if experimental alloys were used, that varied in only one element of interest at a time.

2. A further extension to the work in this research programme would be to consider the resistance spot welding of different steel alloys as this is most representative of the situation found in manufacturing.

3. Due to the difference in grain size between a spot weld heat-affected zone and weld nugget, the continuous cooling transformation (CCT) curves developed were only applicable to heat-affected zones of spot weld. The more recently developed Gleeble 3500 has the capability to melt and solidify samples that may allow columnar grain structures to be investigated. Finally, CCT curves produced using smaller samples would allow faster heating and cooling rates to be achieved under more stable conditions although mechanical test specimens would be more difficult to design from such specimens.

4. Further work in the area of advanced welding schedules, such as multi-pulse or controlled cooling is required and it is recommended that such work be carried out using statistical experiment design techniques to ensure that a wide range of welding conditions are considered. It would also be beneficial to establish the effect of strip thickness, in both same thickness, and multi-thickness joints. Finally, the nature of the schedules used in this programme was limited to the capabilities of the weld machine controller, thus only one type of treatment could be applied to a weld. More advanced

controllers, that enable different schedule types to be combined may increase the effectiveness of the treatments.

5. Finite element modelling of resistance spot welding schedules needs to be attempted in conjunction with further thermal profile monitoring and metallurgical analysis to enable a wide range of schedules to be evaluated.

10. REFERENCES

1. European New Car Testing Programme, Assessment Protocol and Biomechanical limits, Version 4.0, January 2003. Also see www.euroncap.com.
2. H. Hayashi, 'Forming technology and sheet materials for weight reduction of automobile', 19th IDDRG Biennial Congress, Eger, 10-14 June 1996, pp13-31.
3. J.W. Edington and F.G. Wilson 'The automobile, fuel economy and the drive for lightweight materials', Automotive Technology International, November 1994.
4. Directive 2000/53/EC of the European Parliament and of the Council of 18th September 2000 on End-of Life Vehicles.
5. P.J. Evans and D.J. Hillis, 'High strength formable steels,' British Steel Report.
6. Nippon Steel Corporation, 'Case study of energy saving contribution by applying high performance steel sheets for automobiles in Japan', Energy evaluation in the use of steel products in view of LCA, MITI: ANRE and JISF, March 1997.
7. J-O. Sperle and K. Olsson, 'High strength automotive sheet steels for weight reduction and safety applications.'
8. E. Walker and K. Lowe, 'Ultra light auto bodies constructed from steel', Automotive Materials, December 1995, pp585-587.
9. M.J. Karagoulis, 'A nuts and bolts approach to the control of resistance spot welding', Welding Journal, July 1994, pp27-31.
10. S. Ferrasse, P. Verrier, F. Meesemaecker, 'Resistance spot weldability of high strength steels for use in the automotive industry', Doc IIW-III-1076-96.
11. B.M. Brown, 'A comparison of AC and DC resistance welding automotive steels', Welding Journal, January 1987, pp18-23.
12. N.T. Williams, 'Practical considerations relating to the use of high strength steels for resistance welding applications', British Steel Technical Report, WL/FP/1226/82/C, March 1982.
13. R.C. Lavery and N.T. Williams, 'Resistance spot welding of high tensile steel in the hot rolled condition', British Steel Technical Report, No. 230/D, February 1971.
14. J.E. Gould, 'Mechanisms of hold time sensitivity behaviour in resistance spot welds on high strength steel sheet', in Proc. Conf. 'Joining High Strength Steel for Automotive Applications Seminar, Troy, Michigan, February 1999.
15. T.B. Jones, 'The weldability of rephosphorised, high strength and dual phase steels', British Steel Technical Report.

16. D.W. Dickinson and T.V. Natale, 'Observations of factors which influence the spot weldability of high strength steels', SAE Technical Paper Series, No. 810353, 1981.
17. J.W. Mitchell and U.I. Chang, 'Resistance spot welding of microalloyed steels for automotive applications', in Proc. Conf. 'Microalloying 75', Washington, D.C., October 1975, pp.599-609.
18. J.M. Sawhill, Jnr. and S.T. Furr, 'Spot weldability tests for high strength steels', SAE Technical Paper Series, No. 810352, 1981.
19. T. Nishi, T. Saito, A. Yamada, Y. Takahashi, 'Evaluation of spot weldability of high strength sheet steels for automobile use', Nippon Steel Technical Report, December 1982, (20), pp37-44.
20. W. Peterson, 'Dilution of Weld metal to eliminate interfacial fractures of spot welds in high and ultra high strength steels', in Proc. Conf. 'ICAWT '97', Columbus, Ohio, September 1997, pp331-346.
21. W.S. Simmie and A.J. Hipperson, 'Spot welding high tensile steels with automatic post heat treatment', Sheet Metal Industries, September 1944, 1609-1619.
22. K. Tanuma and T. Hashimoto, 'Static fracture appearance of spot welded joints of cold rolled carbon steel sheets', Trans. Nat. Research Inst. For Metals, 1979, **21**, (4), pp32-37.
23. H. Kitagawa, 'Report on spot welding conditions of high strength steel sheets', Doc IIW-III-808-85.
24. B. Pollard and R.H. Goodenow, 'Spot weldability of dual phase steel', SAE Technical Paper Series, No. 790006, 1979.
25. 'Recommended practices for test methods for evaluating the resistance spot welding behaviour of automotive sheet steel materials', American National Standard, ANSI/AWS/SAE/D8.9-97.
26. 'Resistance spot welding of uncoated and coated low carbon steel', British Standard, BS 1140: 1993.
27. N. Chester, 'Multi-phase high strength steels', British Steel Report, FR W418-6 972.
28. T.B. Jones, 'Impact testing of spot welds', British Steel Technical Note, August 1985.
29. J-O. Sperle, 'Fatigue strength of non-load carrying spot welds', Metal Construction, November 1984, pp678-679.
30. T. Sakuma, 'Next generation high strength sheet steel utilising transformation induced plasticity (TRIP) effect', Nippon Steel Technical Report, March 1995, (64), pp20-25.

31. R.J. Holliday and Ingo Mantei, 'Welding DP steels', Rover Technical Report, January 1999.
32. R.W.K. Honeycombe and H.K.D.H. Bhadeshia, 'Steels, Microstructures and Properties', Edward Arnold, 1995.
33. D.T. Llewellyn and R.C. Hudd, 'Steel Metallurgy and Applications,' Third Edition, Butterworth-Heinemann, 1998, p189
34. D.P. Dunne, 'Ferrite Morphology and Residual Phases in Continuously Cooled Low Carbon Steels,' Materials Forum, 1999, **23,** pp63-76.
35. H.K.D.H. Bhadeshia, 'Bainite in Steels,' The Institute of Materials, 1992, p249.
36. H.K.D.H. Bhadeshia, 'Bainite in Steels,' The Institute of Materials, 1992, pp61-68.
37. D.P. Koistinen and R.E. Marburger, A general equation prescribing the extent of the austenite-martensite transformation in pure iron-carbon alloys and plain carbon steels, Acta Metall., vol.7, 1959, p 50-60, cited in ASM handbook, vol. 9, 1995, p133.
38. G. Beranger, 'Book of Steel', 1996, p917-933.
39. 'Tenform CMn', British Steel brochure, June 1996.
40. T. Furukawa, 'Process factors for cold-rolled dual-phase sheet steels', Trans. ISIJ, 1981, **21,** (11), pp812-819.
41. D.J. Hillis et al, 'Rapid annealing of dual phase steels', Ironmaking and Steelmaking, 1998, **25**, (1), pp47-53.
42. 'Niobium Information', Information leaflet, No. 15/97, Companhia Brasileira de Metalurgia E Mineração.
43. D.K. Mondal and R.K. Ray, 'Effect of chemical composition and initial heat treatment on the structure and properties of a few dual phase steels', Materials Technology, Steel Research 60, 1989, (1), pp25-32.
44. M. Sudo, S. Hashimoto, S. Kambe, 'Niobium bearing ferrite bainite high strength hot-rolled sheet steel with improved formability', Trans. ISIJ, 1983, **23**, (4), pp303-311.
45. H. Klaar et al, 'Microstructure and properties of a C-Mn-Si dual-phase steel', Materials Technology, Steel Research 61, 1989, (2), pp85-92.
46. I.S. Kim, U. Reichel, W. Dahl, 'Effect of bainite on the mechanical properties of dual-phase steels', Materials Technology, Steel Research 58, 1987, (4), pp186-190.
47. A. Zarei-Hanzaki and S. Yue, 'Ferrite formation characteristics in Si-Mn TRIP steels', ISIJ Int., 1997, **37**, (6), pp583-589.
48. D.J. Abson and R.E. Dolby, 'Microstructural transformations in steel weld metals – a reappraisal,' The Welding Institute Research Bulletin, July 1978, pp202-207.

49. N.T. Williams, 'Metallurgical aspects of resistance spot welding of mild steel,' The Metallurgist and Materials Technologist, February 1981, pp85-89.
50. R.S. Chandel and S. Garber, 'Mechanical and metallurgical aspects of spot welded joints in heat treated low carbon mild steel sheet,' Metals Technology, September 1974, pp418-424.
51. W.F. Savage, E.F. Nippes, R.J. Hagler, 'Effect of carbide size and distribution on weldability of low carbon steels,' Welding Research Supplement, November 1978, 355s-360s.
52. O. Grong and D.K. Matlock, 'Microstructural development in mild and low alloy steel weldments,' International Metals Reviews, 1986, **31,** (1), pp27-48.
53. International Institute of Welding, IIW Doc. 835-85, 1985. Also in Welding in the world, 1986, **24**, p144.
54. P. Harrison and R. Farrar, 'Microstructural development and toughness of C-Mn and C-Mn-Ni weld metals, Part 1,' Metal Construction, July 1987, pp329R-399R.
55. R. Farrar and Z. Zhang, 'Microstructural development of C-Mn-Ni weld metals and the influence of nickel and manganese,' Conf. Proc. 6th International Conference of Joining Materials, Denmark, April 1993, pp397-404.
56. P.L. Harrison, M.N. Watson, R. Farrar, 'How niobium influences SA mild steel weld metals, Part 1,' Welding and Metal Fabrication, March 1981, pp101-108.
57. P.L. Harrison, M.N. Watson, R. Farrar, 'How niobium influences SA mild steel weld metals, Part 2,' Welding and Metal Fabrication, April 1981, pp161-169.
58. G.M. Evans, 'The effect of microalloying elements in C-Mn steel weld metal,' Welding in the world, 1993, **31**, (1), pp12-19.
59. B.G. Kenny, H.W. Kerr, R.B. Lazor, B. Graville, 'Ferrite transformation characteristics and CCT diagrams in weld metals,' Metal Construction, June 1985, pp374R-381R.
60. P. Harrison and R. Farrar, 'Microstructural development and toughness of C-Mn and C-Mn-Ni weld metals, Part 2,' Metal Construction, August 1987, pp447R-450R.
61. A.L. Christenson, E.C. Nelson, C.E. Jackson , Trans. AIME, 1945, **162**, p606.
62. R. Farrar and Z. Zhang, 'Experimental verification of the continuous cooling transformation diagram produced by the dilatometry – metallography method,' Journal of Materials Science Letters, 1993, **12**, pp1606-1611.

63. Van der Wolk et al, 'Prediction of the continuous cooling transformation diagram of vanadium containing steels using artificial neural networks', in Proc. Conf. 'Modelling of Metal Rolling Processes', December 1996, pp378-388.
64. C. Mesplont, J.Z. Zhao, S. Vandeputte, B.C. De Cooman, 'An improved method for determining the continuous cooling transformation diagram of C-Mn steels,' Materials Technology, Steel Research, 2001, **72**, (7), pp263-270.
65. P.A. Manohar and T. Chandra,' Continuous cooling transformation behaviour of high strength microalloyed steels for linepipe applications,' ISIJ International, 1998, **38**, (7), pp766-774.
66. 'Dynamic thermal / mechanical metallurgy using the Gleeble 1500', Technical Manual 2nd edition, Dynamic Systems Ltd., pp132-143.
67. A.P. Vass, 'Characterisation of rotor steels and weld metals using a Gleeble simulator', MRes thesis, University of Wales Swansea, 1998.
68. S. Storer, 'Simulation of heat-affected zone microstructures in 1/2 Cr-1/2Mo-1/4V low alloy steel weldments,' PhD Thesis, University of Wales Swansea, 1996.
69. S. Yamamoto, H. Yokoyama, K. Yamada, M. Niikura, 'Effects of austenite grain size and deformation in the unrecrystallised austenite region on bainite transformation behaviour and microstructure,' ISIJ International, 1995, **35**, (8), pp1020-1026.
70. F. Sun, H. Sun, M. Li, B. Sun, 'Effects of austenite grain size, reduction and cooling rate on AR_3 and ferrite grain refinement,' Conf. Proc. International Conference on Physical Metallurgy of Thermomechanical Processing of Steels and other metals,' THERMEC-88, June 1988, pp391-396.
71. A. Matsuzuki and H.K.D.H. Bhadeshia, 'Effect of austenite grain size and bainite morphology on overall kinetics of bainite transformation in steels,' Materials Science and Technology, May 1999, **15**, pp518-522.
72. A.L. Wilson and P.R. Howell, 'An overview of the austenite grain coarsening characteristics of Nb-microalloyed steels,' Conf. Proc. 38th MWSP, ISS, **XXXIV**, 1997, pp527-534.
73. M. Militzer, A Giumelli, E.B. Hawbolt, T.R. Meadowcroft, 'Austenite and ferrite grain size evolution in plain carbon steel,' Conf. Proc. 38th MWSP, ISS-AIME, **XXXII**, 1995, pp375-384.
74. P.L. Harrison and R.A. Farrar, 'Application of continuous cooling transformation diagrams for welding of steels,' International Materials Reviews, 1989, **34**, (1), pp35-51.

75. M. Inagaki and H. Sekuguchi, 'Continuous cooling transformation diagrams of steels for welding and their applications,' Transactions of National Research Institute for Metals, **2**, (2), 1960, pp41-63.
76. J. Wen, C.D. Lundin, B.J. Kruse, 'Phase transformations in the HAZ and weld metal,' Conf. Proc. Trends in Welding Research, Ed. S.A. David, 1982, pp259-276.
77. Winarto, 'Mechanical properties and microstructures of mechanised MIG aluminium alloy 5083 weldments', PhD first year report, University of Wales Swansea, 1997.
78. Z. Han, 'Resistance spot welding: a heat transfer study', Welding Research Supplement, September 1989, pp363-371.
79. Corus NL, 'Welding of dual phase steel,' Internal technical report, December 2001, Act-nr: 650115.
80. D.R. Attore, 'Characterisation of weld nugget formation and solidification in the resistance seam welding of uncoated and coated steel sheet, Engineering Doctorate Thesis, University of Wales Swansea, 1996.
81. L.K. Lyons, 'A comparison of mechanical properties using 10mm and 80mm tensile test pieces,' British Steel Technical Report, Report Number: WL / PD / TN / 3311 / 12 / 97 / D, August 1997.
82. M. Hoffman and R. Birringer, 'Quantitative measurements of Young's Modulus using the miniaturizes disk-bend test,' Materials Science and Engineering, 1995, **A202**, pp18-25.
83. H. Li, F.C. Chen, A.J. Ardell, 'A simple versatile miniaturized disk-bend test apparatus for quantitative yield stress measurements, Metallurgical Transactions A, September 1991, **22A**, pp2061-2068.
84. S.D. Norris and J.D. Parker, 'Deformation processes during disc bend loading,' Materials Science and Technology, February 1996, **12**, pp163-70.
85. S. Lewis, 'Cold work embrittlement in strip steels,' EngD Thesis, University of Wales Swansea, 1998.
86. J.P. Lewis, 'Miniature disc bend testing of linepipe grade steels', PhD thesis, University of Wales Swansea, 1998.
87. G.E. Pellissier, 'Effects of microstructure on the fracture toughness of ultrahigh-strength steels,' Engineering Fracture Mechanics, 1968, **1**, pp55-75.
88. European Standard EN 10045.

89. A.J.Horn, 'Charpy Centenary Conference, 2-5 October 2001, Poitiers, France' Corus Technical Report, Report Number: SL / WEM / VR / M9614 / 1 / 01 / A, October 2001.
90. M.W. Kolder and A.W.M. Bosman, 'Influence of the welding equipment on the weldability lobe of a HSLA steel', Doc IIW-III-796-84.
91. K.D. Jonnalagadda et al., J. of Intell. Mat. Sys. and Structure, 1998, **9**.
92. R. Holliday, 'Mechanisms of electrode growth during spot welding of coated steel,' EngD thesis, University of Wales, Swansea, 1996.
93. R. Ellwood, 'Resistance spot weldability of hot rolled TRIP steel,' British Steel Technical Note, WL/PE/TN/3323/6/97/D, September 1997.
94. G. Krauss, 'Steels: Heat treatment and processing principles, ASM International, 1989.
95. 'Material Evaluation of DP600 and DP800 Grades,' Corus Internal Report, Report No. WL/SMP/R?A02/7/99/R, December 1999.
96. 'Manufacturing guidelines when using ultra high strength steels in automotive applications,' ECSC sponsored research project, Technical report no. 4, December 2000.
97. P.S. Wei and C.Y.Ho, 'Axisymmetric nugget growth during resistance spot welding', J. of Heat Transfer, 1990, **112**, pp309-316.
98. 'Predictive simulation of welding and heat treatment with SYSWELD. Present Capabilities,' ESI UK Limited, 2000. Available at www.esi-group.com.
99. 'Weld quality and performance of high strength TRIP steel welds,' Minutes of launch meeting for GSP PR6090, TWI Doc, PR6090/1/02, The Welding Institute, July 2002.
100. N. Harlin, T.B. Jones, J.D. Parker' Weld growth mechanisms in two and three thickness joints,' Science and Technology of Welding & Joining, 1 February 2002, **7**, (1), pp. 35-41(7).

Table 4.1. Composition of steel alloys used for current programme.

Steel Grade	C	P	Mn	Si	S	Cr	Al (tot)	Nb	Mo	Ni	CE
LC	0.039	0.018	0.024	0.004	0.012	0.022	0.042	0.001	0.003	0.010	**0.04**
LCNb	0.049	0.013	0.40	0.005	0.006	0.014	0.040	0.016	0.004	0.011	**0.07**
DP600	0.103	0.010	0.50	0.32	0.005	0.024	0.047	0.001	0.002	0.039	**0.14**
DP800	0.126	0.013	1.52	0.45	0.004	0.028	0.043	0.019	0.004	0.039	**0.22**
DP1000	0.142	0.012	1.51	0.57	0.002	0.042	0.044	0.020	0.018	0.044	**0.24**
DP1400	0.163	0.011	1.59	0.53	0.002	0.026	0.046	0.017	0.006	0.042	**0.27**

Table 4.2. Mechanical properties of steel alloys used for current programme in the as received condition

Steel Grade	Tensile Strength ($N/mm^{2)}$	0.2% Proof Stress (N/mm^2)	Total Elongation (%)
LC	295	166	45.2
LCNb	428	285	32.8
DP600	642	402	21.2
DP800	806	513	15.4
DP1000	1060	711	8.3
DP1400	1463	1335	4.0

Table 4.3. Welding parameter settings used in this investigation.

Parameter	**Setting**
Transformer tap	5
Water flow rate	4 litres / min
Water temperature	$12.6^{o}C$
Current meter	Miyachi Weld Tester 315A
Force meter	Maltron Weld Force Probe Gauge 98558
Electrodes	Truncated Cone, Cu-Cr-Zr, tip diameter various (see table 4.4), included angle 120^{0}, 19mm diameter, 22mm stroke.

Table 4.4 Summary of conditions used to produce 5√t welds in each of the six steel grades.

Steel Grade	Electrode Tip Size (mm)	No. Weld Cycles (1 cycle = 0.02)	Weld Current (kA)
LC	7	14	10.8
LCNb	7	14	10.6
DP600	7	14	8.8
DP800	7	14	8.5
DP1000	6	14	6.6
DP1400	6	14	6.4

Table 4.5. Measured prior austenite grain size in samples subjected to a programme consisting of: heating at rates give; a peak temperature of 1000°C; a 1 second hold; water quenching to room temperature.

Heating Rate (°C/s)	Measured Prior Austenite Grain Size (microns)
10	6.3
30	5.7
50	5.4
500	3.9
1000	5.7

Table 4.6. Measured prior austenite grain size in samples subjected to a programme consisting of: heating at 30°C/s; varied peak temperature as indicated in the table; a hold of 1 second; a water quench to room temperature.

Peak Temperature (°C)	Measured Prior Austenite Grain Size (microns)
900	3.8
1000	6.2
1100	16.6
1200	44.3
1300	80.0

Table 4.6. Measured prior austenite grain size in samples subjected to a programme consisting of: heating at 33°C/s; peak temperature of 1000°C; a hold time as indicated in the table; a water quench to room temperature.

Hold Time (seconds)	Measured Prior Austenite Grain Size (microns)
0.1	4.6
1	6.21
10	7.4
20	8.5
40	8.3

Table 4.8. Cooling rates, in °C/s, used for each of the six steels included in this investigation.

	LC	LCNb	DP600	DP800	DP1000	DP1400
Controlled Rates	0.5					
	1					
	2					
	5					
	10					
	20					
	25					
	35					
Air Quench	392	73	72	119	132	323
Water Quench	3058	2575	2206	1978	1950	9450

Table 4.9. Cooling rates, in °C/s, achieved by machined DP800 samples as a result of air quenching.

Sample Number	Sample Thickness (mm)	Cooling Rate (°C/s)
1	2.00	119
2	1.60	144
3	1.06	216
4	1.04	229
5	0.50	465

Table 5.1. Transformation temperatures determined for water quenched DP600 samples using the designed dilatometer attachment.

Test number	Dilatometer Results (°C)		Thermocouple Results (°C)	
	1st transformation	2nd transformation	1st transformation	2nd transformation
1	703	432	570	424
2	629	372	679	432
3	575	356	no reading	425

Table 5.2. Transformation temperatures determined for air quenched DP600 samples using the designed dilatometer attachment.

Tests number	Results with attachment (°C)		Original 1500 results (°C)	
	Start	Finish	Start	Finish
1	710	620	720	630
2	717	631	704	634
3	715	633	716	645
Average	**714**	**628**	**713**	**636**
Std. Dev.	**3.60**	**7.00**	**8.33**	**7.77**

Table 5.3. Transformation temperatures determined for controlled cooling of DP600 samples using the designed dilatometer attachment.

Test number	Results with attachment				Original 1500 results	
	1st transformation		2nd transformation			
	Start	Finish	Start	Finish	Start	Finish
1	774	701	675	654	808	664
2	773	-	675	-	804	680
3	783	711	-	650		
4	786	718	678	648		
Average	**779**	**-**	**-**	**650**	**806**	**672**
Std. Dev.	**6.48**	**-**	**-**	**3.05**	**2.82**	**11.31**
3500 Result	781	712	685	648	-	-

Table 5.4. Results from miniature disc bend test tests carried out using 0.5mm and 1mm thick discs of unmodified DP800.

Disc Thickness (mm)	Measured Ultimate Load	Average	Standard Deviation (N)	Standard Deviation as a % of Average
0.5	3088	3048	83.9	2.8
	2952			
	3105			
1	7037	7058	64.1	0.9
	7007			
	7130			

Table 5.5. R^2 results for the three trends shown in Figure 5.16, between the measured ultimate load and ultimate tensile strength.

Speed ($mm.min^{-1}$)	R^2 value
1	0.999
3	0.998
5	0.995

Table 6.1 Average microhardness measurements taken from 5√t resistance spot welds and parent material in each of the six steel grades used in this programme.

Steel Grade	Carbon Equivalent	Microhardness HV @ 500g			
		Parent metal	HAZ close to parent metal	HAZ close to weld nugget	Weld nugget
LC	0.04	119	---165---		189
LCNb	0.07	140	---197---		231
DP600	0.14	194	---367---		398
DP800	0.22	243	395	445	418
DP1000	0.24	318	462	437	426
DP1400	0.27	452	495	464	465

Table 6.2 Percentage increase in microhardness measurements, for the heat affected zone and weld nugget relative to the parent material, taken from 5√t resistance spot welds in each of the six steel grades used in this programme.

Steel Grade	Carbon Equivalent	% increase in microhardness			
		Base metal	Outer HAZ	Inner HAZ	Weld nugget
LC	0.04	-	---39---		59
LCNb	0.07	-	---41---		65
DP600	0.14	-	---89---		105
DP800	0.22	-	63	72	72
DP1000	0.24	-	45	34	34
DP1400	0.27	-	10	3	3

Table 6.3 Constant and R^2 values derived from regression lines relating the AR_3 transformation start temperature to the cooling rate.

Steel Grade	Carbon Equivalent	k_{AR3}	C_{AR3}	R^2
LC	0.04	8.2	875	0.43
LCNb	0.07	6.1	838	0.62
DP600	0.14	9.1	804	0.92
DP800	0.22	20.1	754	0.98
DP1000	0.24	22.3	779	0.85
DP1400	0.27	26.2	724	0.96

Table 6.4 Constant and R^2 values derived from regression lines relating the proportion of second phase to the cooling rate.

Steel Grade	Carbon Equivalent	$K_{\%2P}$	$C_{\%2P}$	R^2
LC	0.04	3.7	-3.7	0.71
LCNb	0.07	7.5	-0.2	0.87
DP600	0.14	9.6	14.1	0.72
DP800	0.22	14.3	18.7	0.87
DP1000	0.24	12.1	37.6	0.88
DP1400	0.27	15.5	45.0	0.95

Table 6.5 Constant and R^2 values derived from regression lines relating the bulk Vickers hardness to the Carbon Equivalent.

Cooling Rate (°C/s)	K_{Hv}	C_{Hv}	R^2
0.5	370	70	0.98
2	460	71	0.98
10	643	67	0.97
25	903	57	0.94

Table 6.6 Constant and R^2 values derived from regression lines relating the predicated ultimate tensile strength to the Carbon Equivalent.

Cooling Rate (°C/s)	K_{Hv}	C_{Hv}	R^2
0.5	1156	284	0.99
2	1648	265	0.96
10	2066	261	0.96
25	2727	238	0.89
~2000	4194	464	0.96

Table 6.7 Heat and associated current settings used to produce a $5\sqrt{t}$ weld in DP800 using long weld times / low currents.

Schedule Type	Schedule no. pulses x no. cycles	Heat setting cycles	Weld current kA
Basic single pulse	1 x 14	34	8.5
Extended weld time	1 x 25	26	7.2
	1x 50	22	7.0

Table 6.8 Nugget and heat affect zone cooling rates measured during the production of a 5√t weld in DP800 using long weld times / low currents.

Schedule Type	**Schedule** no. pulses x no. cycles	**Nugget Cooling Rate**, °C/s	**HAZ Cooling Rate**, °C/s
Basic single pulse	1 x 14	1614	684
Extended weld time	1 x 25	1637	-
	1x 50	1878	480 / 593

Table 6.9 Heat affected zone to weld nugget diameter ratio for 5√t welds produced using extended weld time schedules in DP800.

Schedule Type	**Schedule** no. pulses x no. cycles	HAZ / nugget ratio
Basic single pulse	1 x 14	0.048
Extended weld time	1 x 25	0.049
	1x 50	0.112

Table 6.10 Heat and associated current settings used to produce a 5√t weld in DP800 using pulsed welding schedules.

Schedule Type	**Schedule** no. pulses x no. cycles	**Heat setting** cycles	**Weld current** kA
Basic single pulse	1 x 14	34	8.5
Multi-pulse	2 x 7	63	15.5
	7 x 2	70	16.4
	14 x 1	85	16.4

Table 6.11 Nugget and heat affect zone cooling rates measured during the production of a 5√t weld in DP800 using pulsed welding schedules.

Schedule Type	**Schedule** no. pulses x no. cycles	**Nugget Cooling Rate**, °C/s	**HAZ Cooling Rate**, °C/s
Basic single pulse	1 x 14	1614	684
Multi-pulse	2 x 7	1244	705
	7 x 2	1237	-
	14 x 1	668	K1 670 / K2 853

Table 6.12 Heat affected zone to weld nugget diameter ratio for 5√t welds produced using pulsed welding schedules in DP800.

Schedule Type	**Schedule** no. pulses x no. cycles	HAZ / nugget ratio
Basic single pulse	1 x 14	0.048
Multi-pulse	2 x 7	0.069
	7 x 2	0.067
	14 x 1	0.074

Table 6.13. Welding schedules used to control the cooling rate following welding

No. post weld pulses	**Parameter Settings (cycles)**					
	Cool time (Z_1)	**Weld time (X_2)**	**Heat (B_2)**	**Cool time (Z_2)**	**Weld time (X_3)**	**Heat (B_3)**
1 (Fig. 6.52)	9	1	99	-	-	-
2 (Fig. 6.54)	9	1	99	9	1	50

Table 6.14. Nugget and heat affect zone cooling rates measured during the production of a 5√t weld in DP800 using controlled cooling schedules.

Schedule Type	**No. post weld pulses**	**Nugget Cooling Rate**, °C/s	**HAZ Cooling Rate**, °C/s
Basic single pulse	0	1614	684
Controlled cooling	1	1263	-
	2	650	-

Table 6.15. Welding schedules used to establish the effect of low current, short time pulses on the generated temperatures

No. pulses	Parameter Settings (cycles)					
	Cool time (Z_1)	Weld time (X_2)	Heat (B_2)	Cool time (Z_2)	Weld time (X_3)	Heat (B_3)
1 (Fig. 6.59)	-	1	99	-	-	-
1 (Fig. 6.60)	-	5	99	-	-	-

Table 6.16. Welding schedules used to attempt to temper post welding

No. post weld pulses	Parameter Settings (cycles)					
	Cool time (Z_1)	Weld time (X_2)	Heat (B_2)	Cool time (Z_2)	Weld time (X_3)	Heat (B_3)
1 (Fig. 6.61)	99	1	99	-	-	-
2 (Fig. 6.62)	99	2	99	9	2	50
2 (Fig. 6.63)	99	5	50	4	5	25

Table 7.1 The cooling rates generated during single pulse spot welding.

Researcher and reference	Measurement type	Strip thickness (mm)	Spot weld nugget cooling rate (°C/s)
R. Ellwood[92]	Infra red camera, top surface	2.9	96
R. Holliday[93]	Infra red camera, electrode temperature	1	500
Present work	**Thermocouple, between sheets**	**2.0**	**1614**
N. Williams[49] (quote)	-	range	2000 –20,000
Nishi et al[19]	0.1mm thermocouples	0.8	~ 5000
J. Gould[14] (model prediction)	-	-	1,000 - 100,000

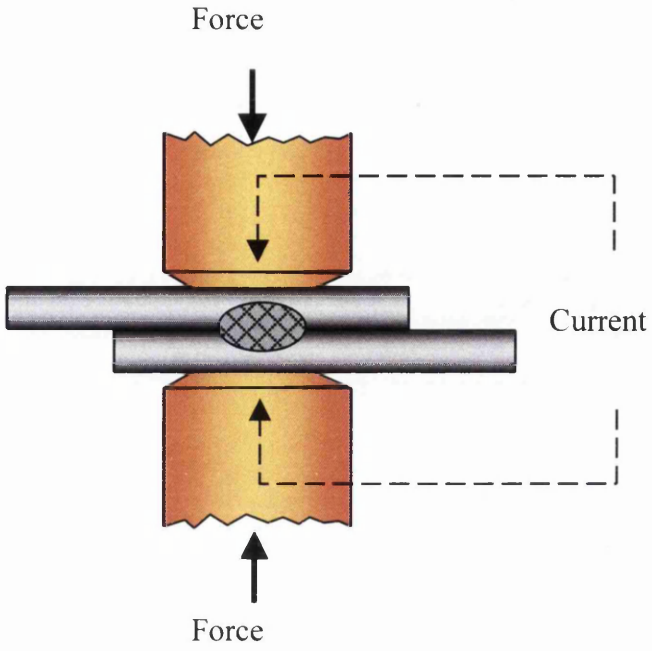

Figure 2.1. Schematic diagram illustrating the principles of the resistance spot welding process.

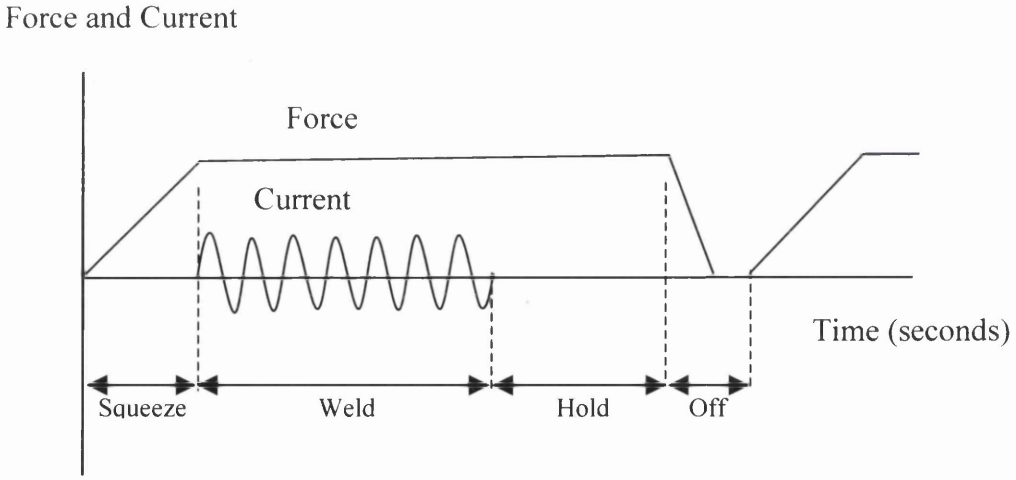

Figure 2.2. Schematic diagram of the force and current cycle applied during resistance spot welding.

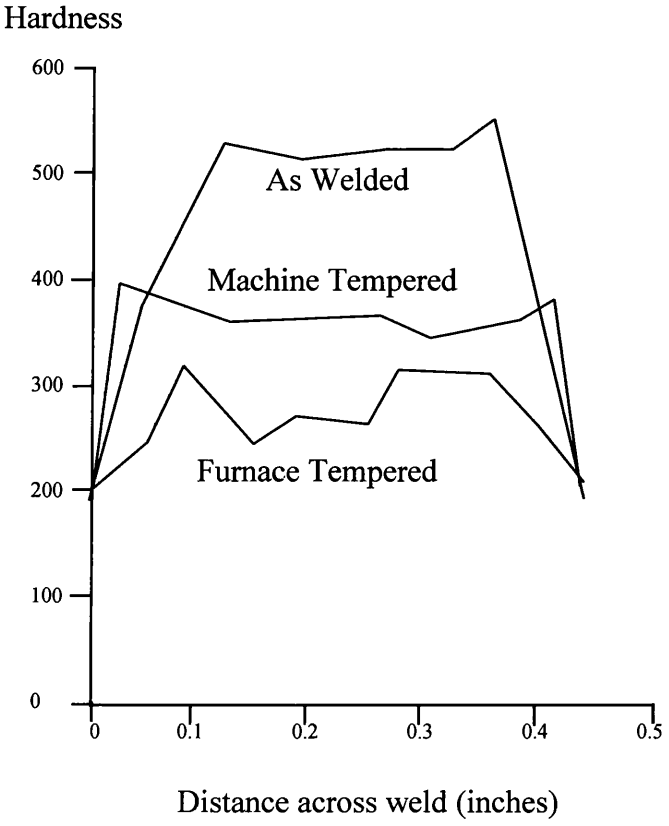

Figure 2.3. The effect of machine and furnace tempering on a spot weld in a CMn steel[21].

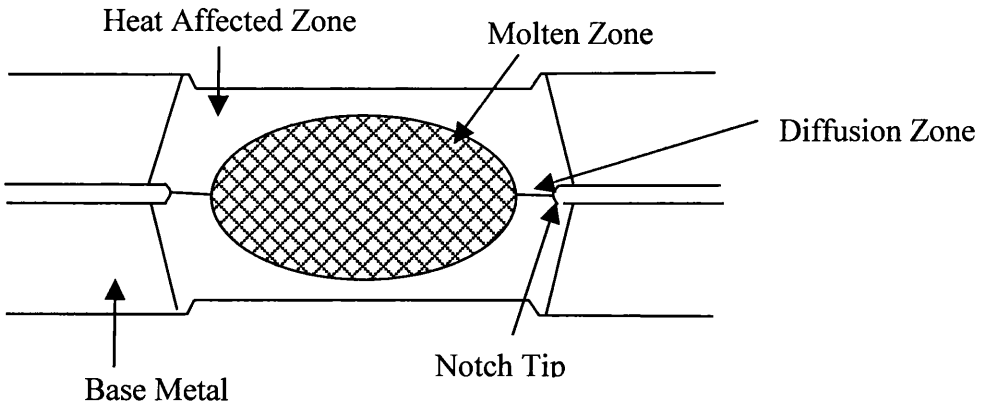

Figure 2.4. Schematic diagram of a resistance spot weld showing the 'notch' and 'diffusion zone' locations[10].

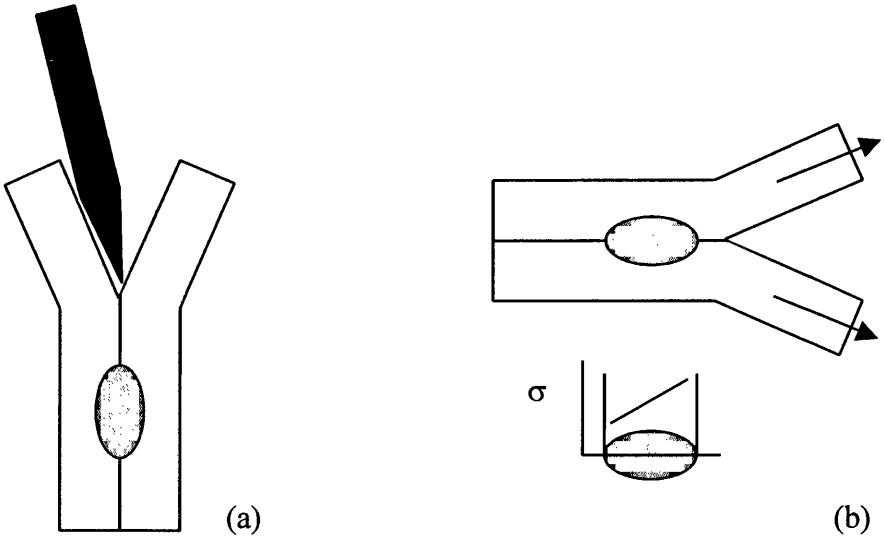

Figure 2.5. Schematic diagram of a peel or chisel test: (a) location of chisel during test; (b) stress distribution on the weld[20].

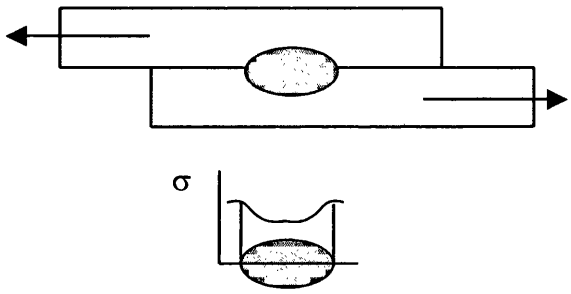

Figure 2.6. Schematic diagram of the stress distribution on a spot weld during a lap shear test[20].

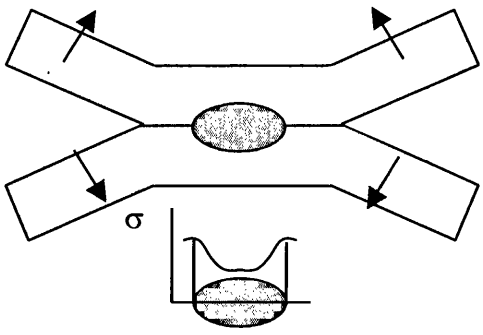

Figure 2.7. Schematic diagram of the stress distribution on a spot weld during a cross tension test[20].

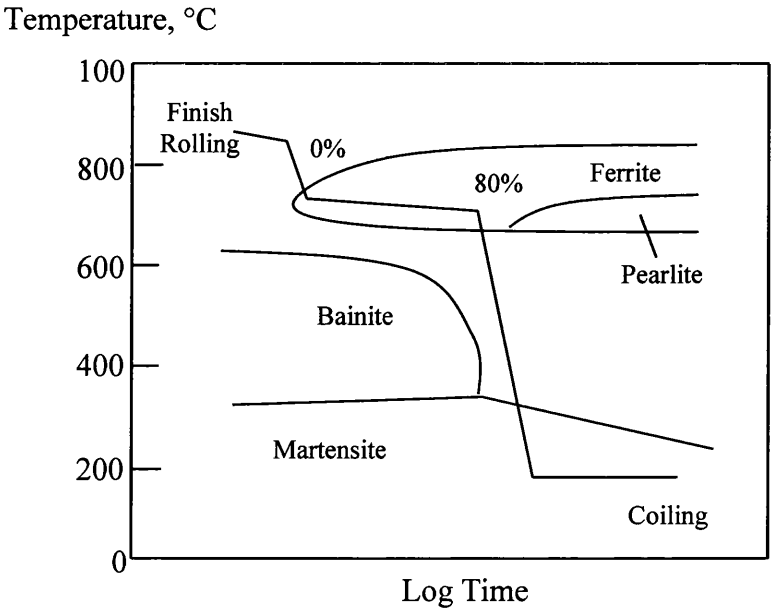

Figure 2.8. Schematic Time-Temperature-Transformation diagram for the production of a dual phase steel alloy[42].

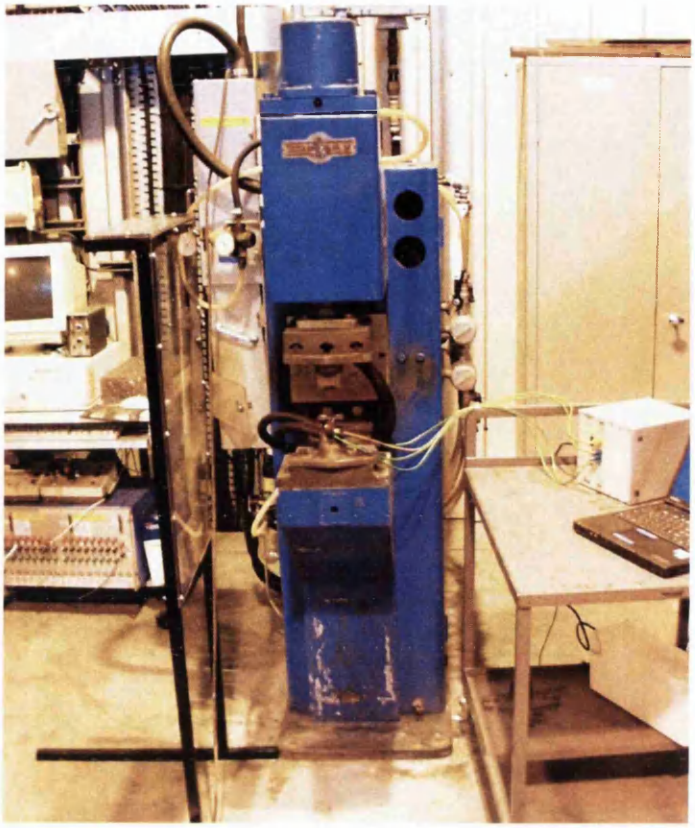

Figure 4.1 Photograph of the 75kVA Skiaky pedestal resistance welder in the Customer Technical Centre, Corus UK, Port Talbot.

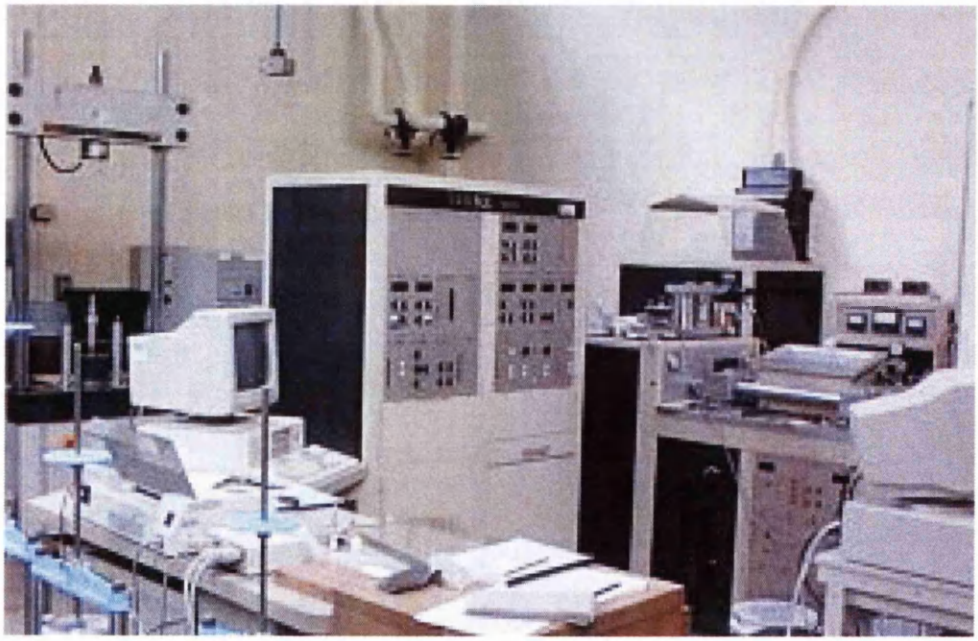

Figure 4.2. Photograph of the Gleeble 1500 thermomechanical simulator in the Marchwood laboratory, University of Wales Swansea.

Figure 4.3. General photograph of a Gleeble 3500 thermomechanical simulator.

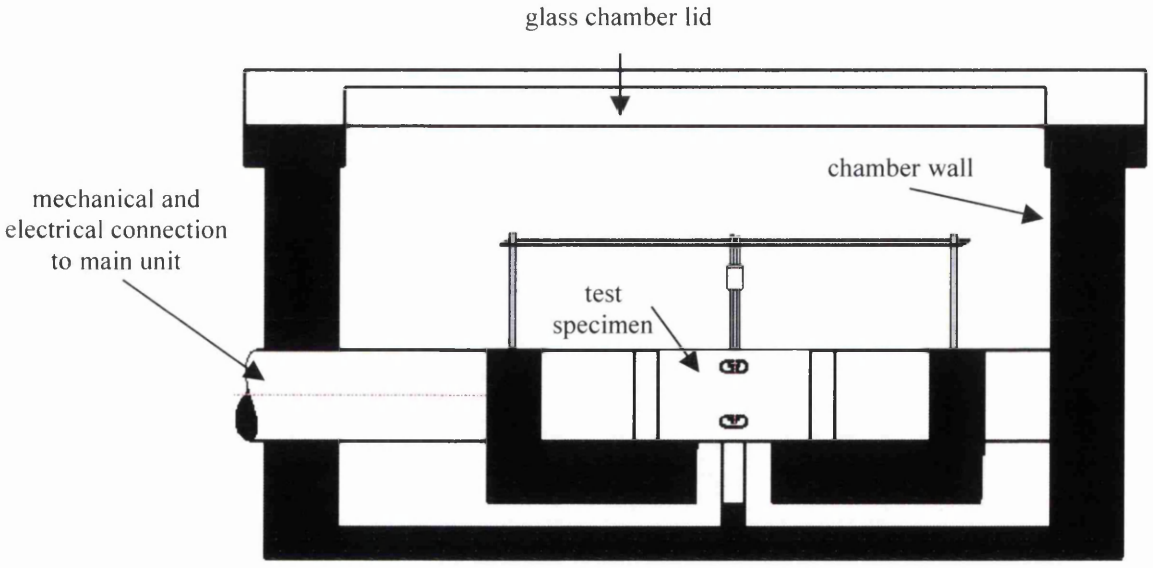

Figure 4.4. Schematic diagram of the test chamber of the Gleeble 1500.

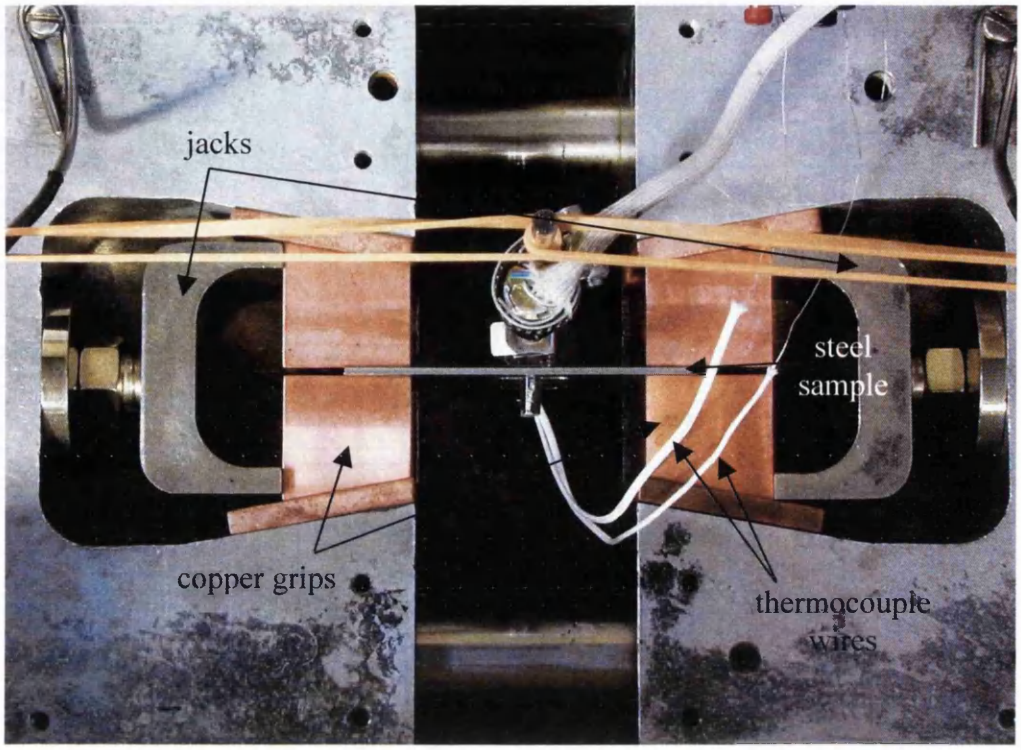

(a)

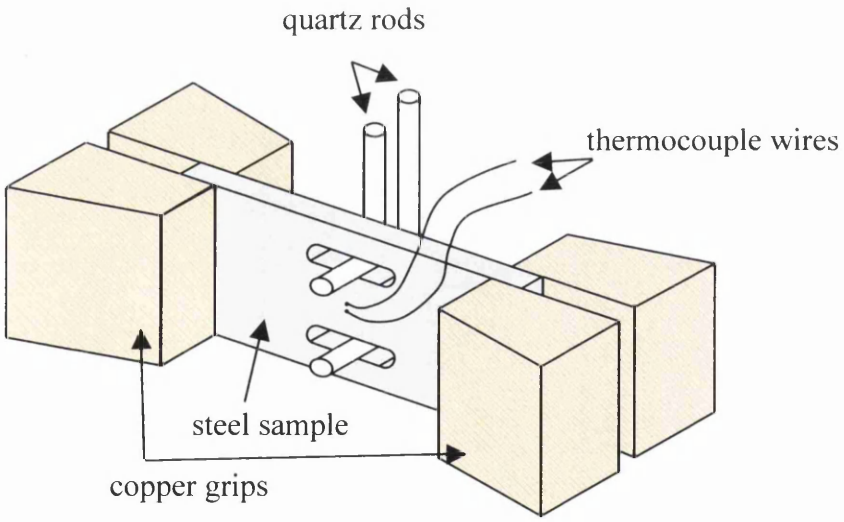

(b)

Figure 4.5 Sample and grip setup common to all tests using a Gleeble (1500 / 3500): (a) Photograph of setup in Gleeble 1500 chamber; (b) Schematic diagram of setup shown offline. Both images depict a continuous cooling transformation sample in position with the manufacturer's dilatometer in place.

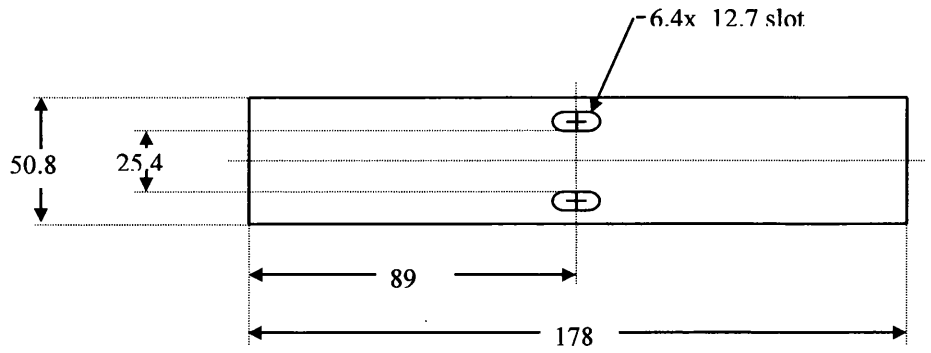

Figure 4.6. Dimensions of the manufacturer's standard dilatometry sample for use in a Gleeble thermomechanical simulator. All dimensions are in mm.

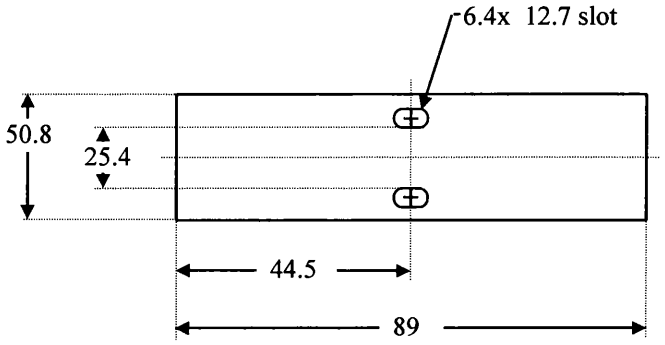

Figure 4.7. Dimensions of the modified dilatometry sample that had been shortened to increase the cooling rate in the centre section, for use in a Gleeble thermomechanical simulator. All dimensions are in mm.

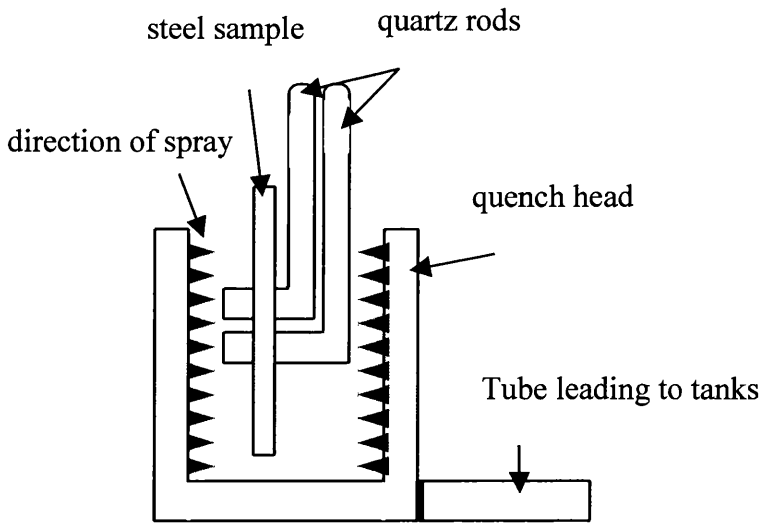

Figure 4.8. Schematic diagram of the quench head arrangement used in conjunction with the Gleeble (1500 / 3500) to increase the cooling rates available. The spray can be either air or water.

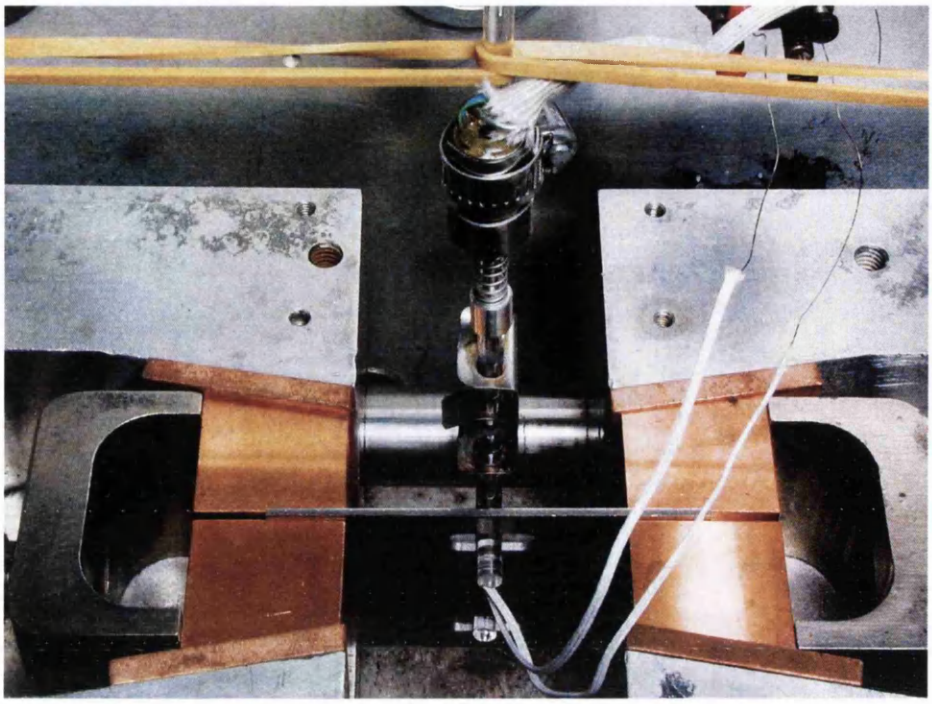

Figure 4.9. Photograph of the manufacturer's standard dilatometer arrangement in position in the Gleeble 1500 tank.

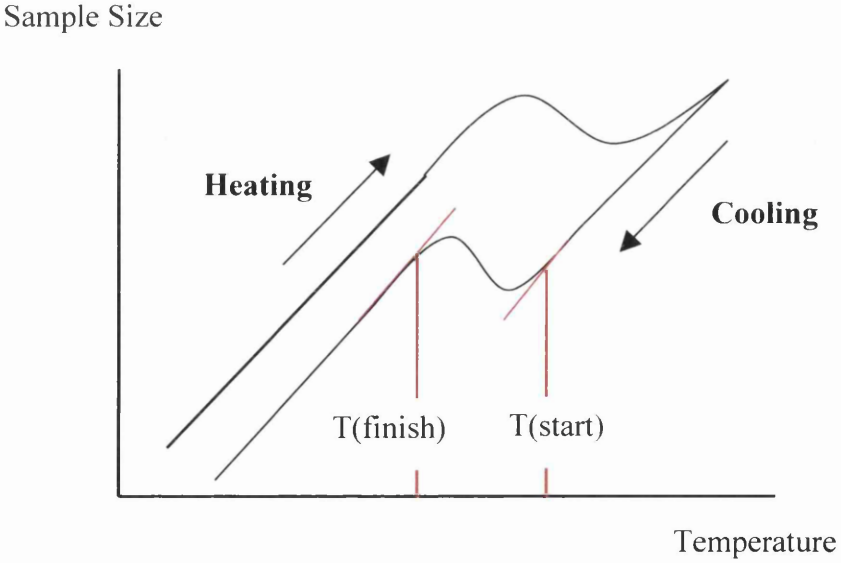

Figure 4.10. Schematic diagram of the change in specimen size measured during a continuous cooling transformation test by a dilatometer. An example of how the transformation start (T(start)) and finish (T(finish) temperatures are selected is given.

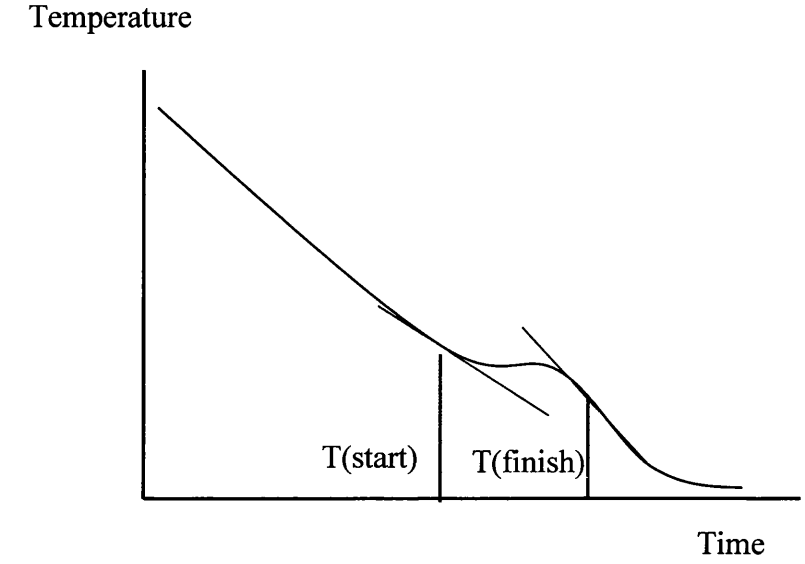

Figure 4.11. Schematic diagram of typical time – temperature measurements taken during a continuous cooling transformation experiment involving sample quenching. An example of how the transformation start (T(start)) and finish (T(finish) temperatures are selected is given.

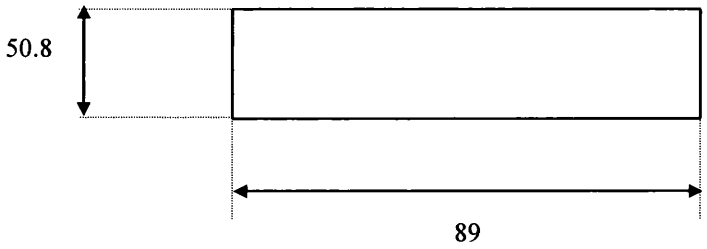

Figure 4.12. Dimensions of a Gleeble specimen, used to generate modified material under a controlled thermal cycle, to be used for mechanical tests. All dimensions are in mm.

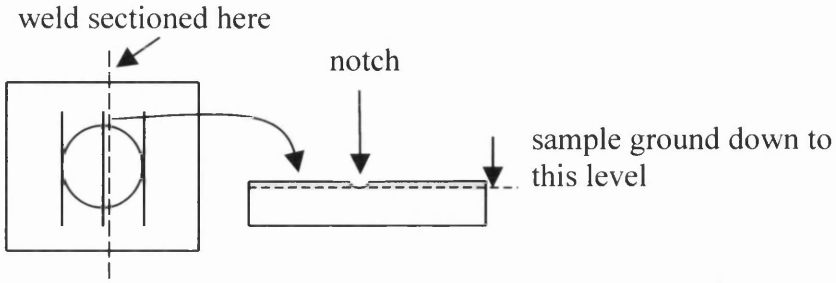

Figure 4.13. Schematic diagram of sectioning procedure used to prepare resistance spot welds for metallographic examination.

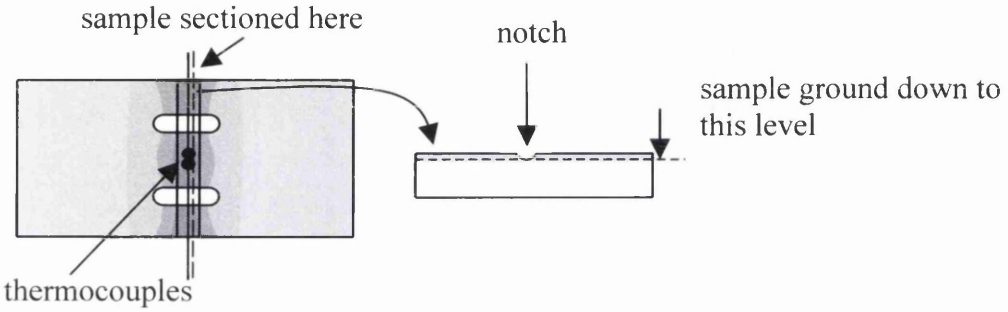

Figure 4.14. Schematic diagram of sectioning procedure used to prepare continuous cooling transformation samples for metallographic examination.

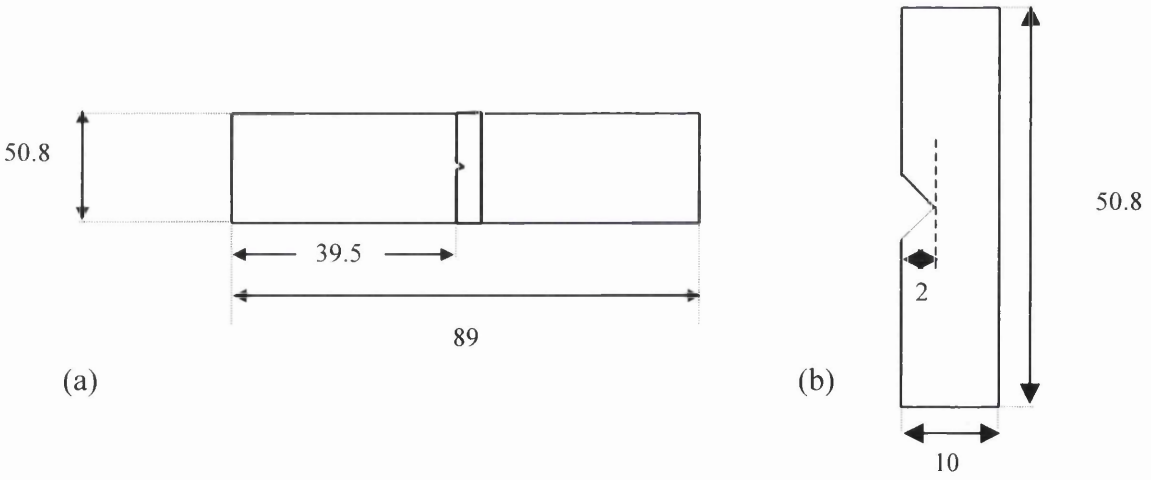

Figure 4.15. Schematic diagram of a miniature impact sample (a) location of sample with respect to Gleeble modified coupon (b) dimensions of miniature impact sample. The thickness is the as-received thickness of the individual steel grade. All dimensions are in mm.

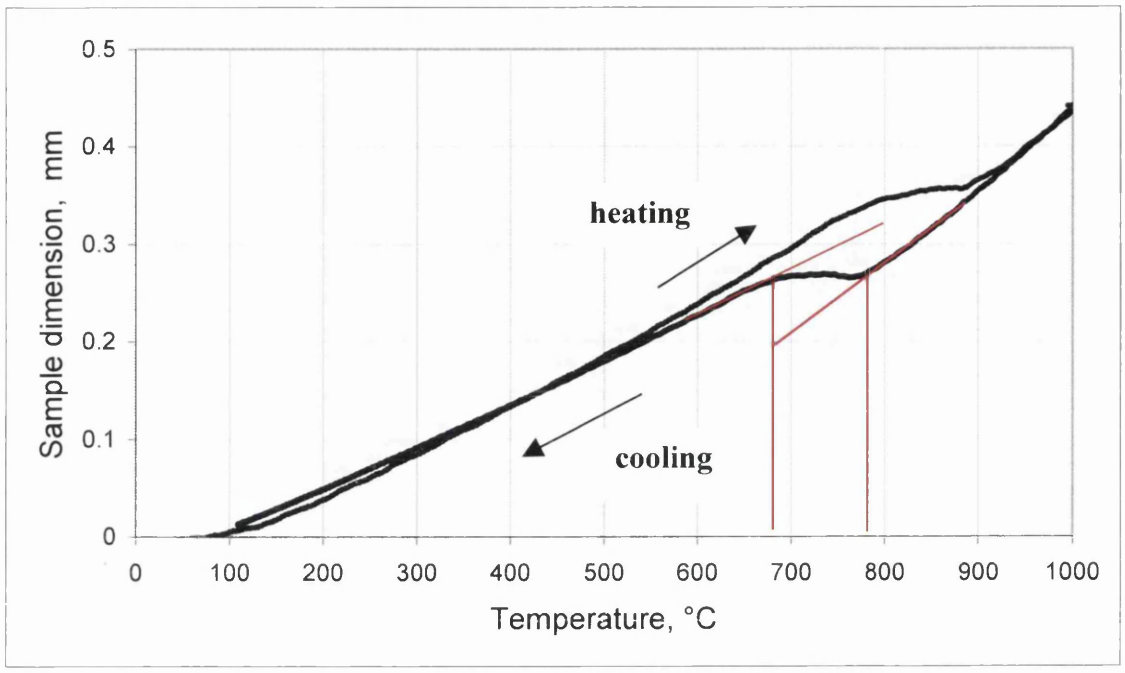

Figure 5.1. Example of a dimension – temperature curve from CCT controlled cooling experiment using the Gleeble 1500 and the manufacturer's dilatometer. The transformation temperatures selected from this curve are indicated.

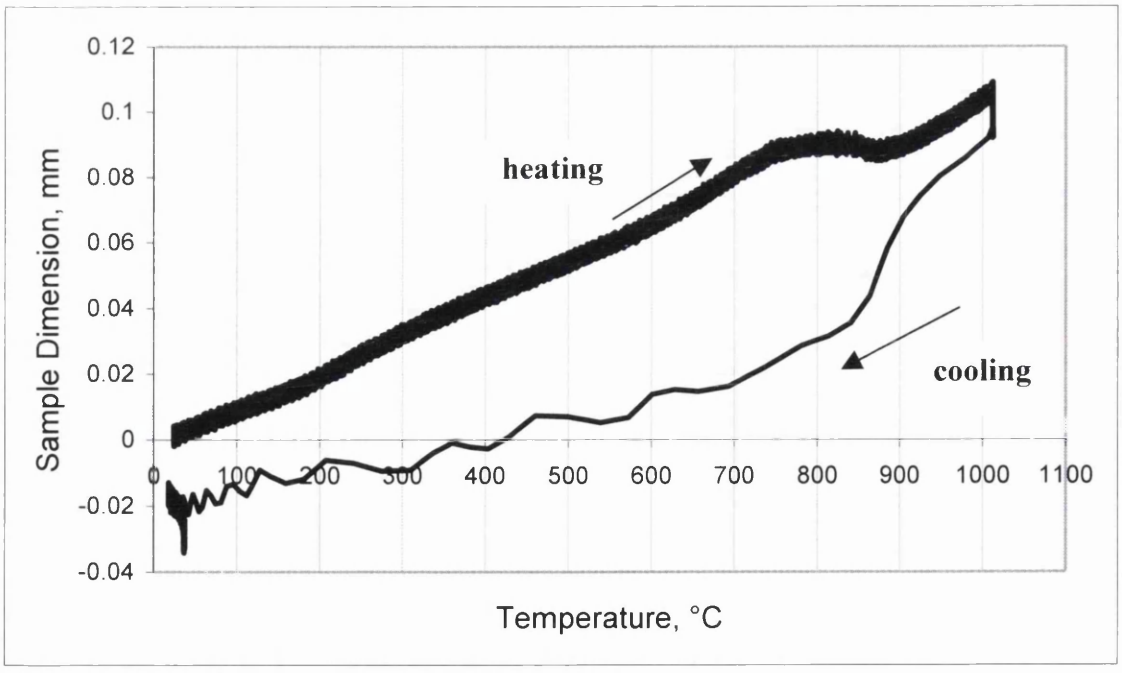

Figure 5.2. Example of a dimension – temperature curve from CCT water quench experiment, using the Gleeble 1500 and the manufacturer's dilatometer, which shows the large fluctuations in the dilatometer readings on quenching.

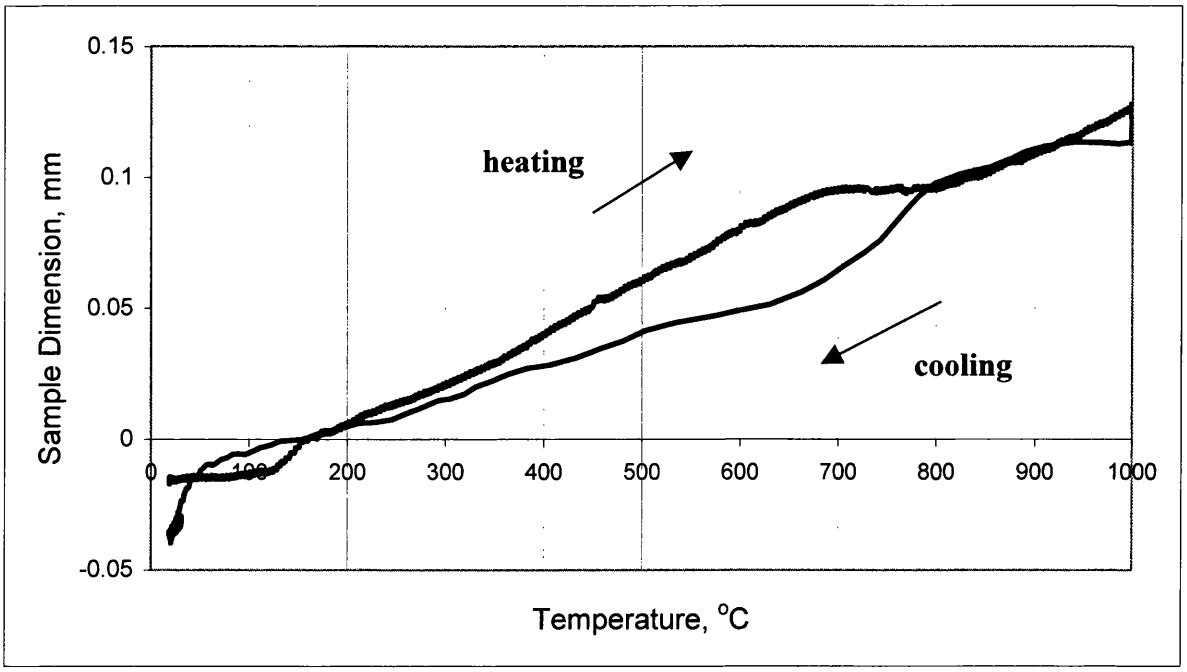

Figure 5.3. Example of a dimension – temperature curve from CCT water quench experiment using the Gleeble 3500, which shows less fluctuation in dilatometer readings on cooling than Figure 5.2

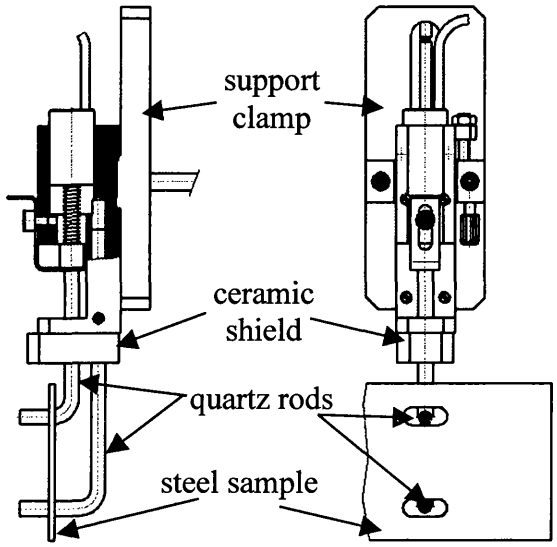

Figure 5.4. The transducer housing developed in the course of this research programme for use with the Gleeble 1500.

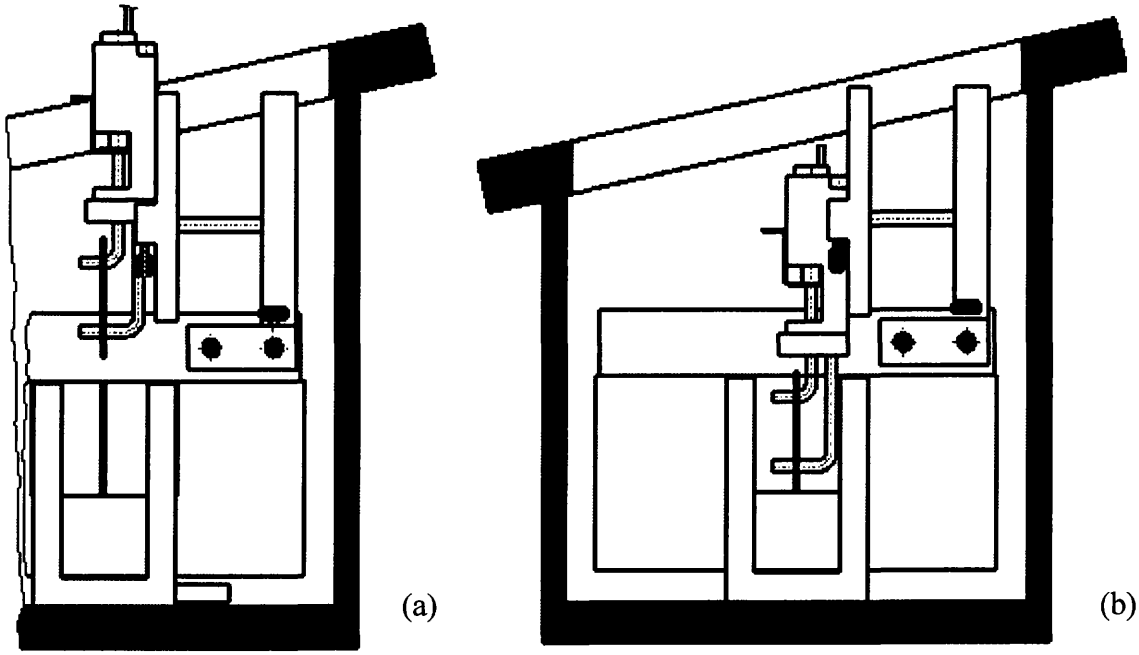

Figure 5.5. Schematic diagram of the developed attachment in place within the Gleeble 1500 chamber (a) dilatometer raised; (b) dilatometer lowered.

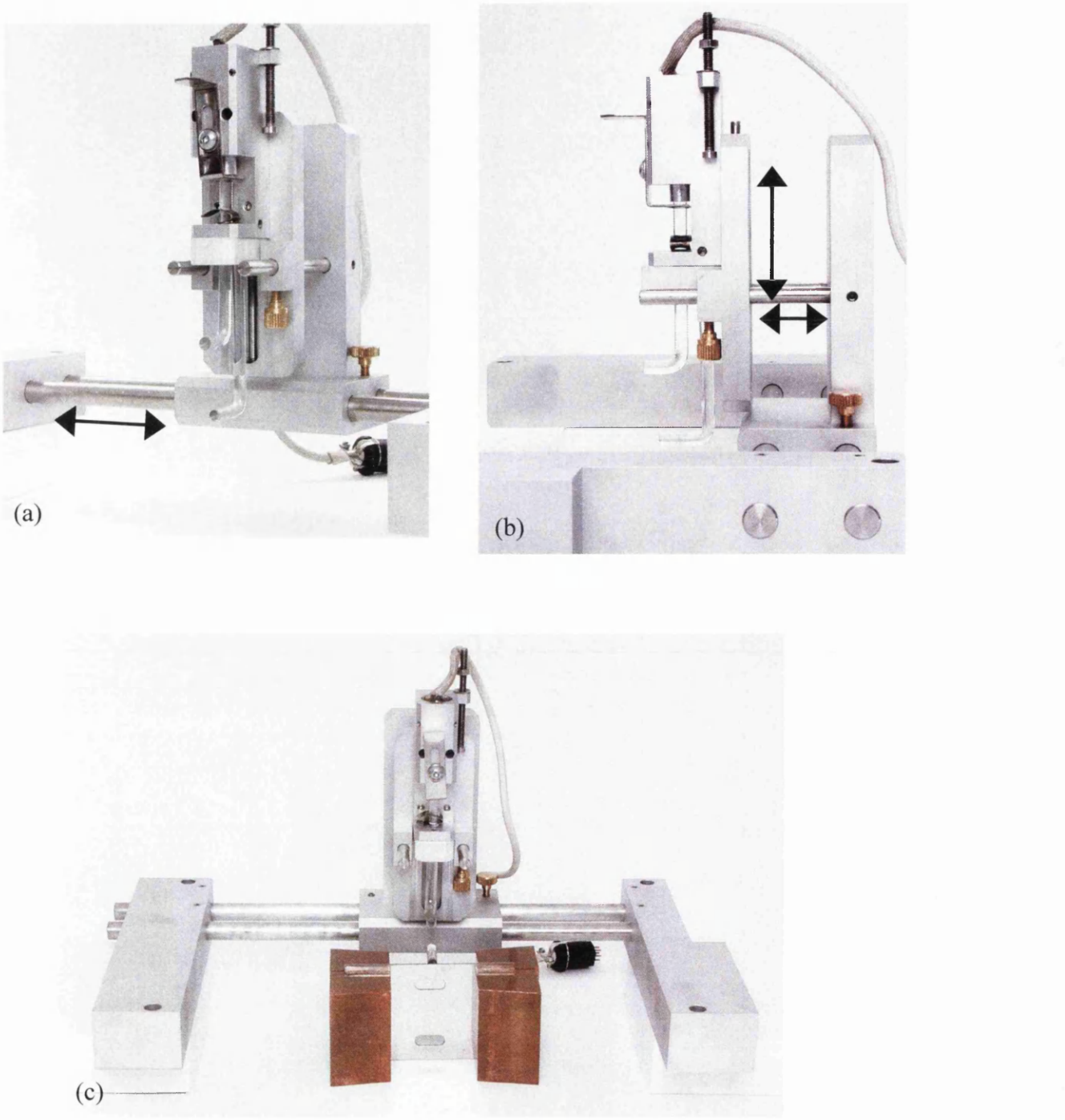

Figure 5.6. Photographs of the attachment designed for use with the Gleeble 1500: (a) front view of transducer housing; (b) side view of transducer housing; (c) the full attachment, including the transducer housing and support blocks, shown offline. The arrows in (a) and (b) indicate the adjustments, in three dimensions, that are possible in the position of the dilatometer.

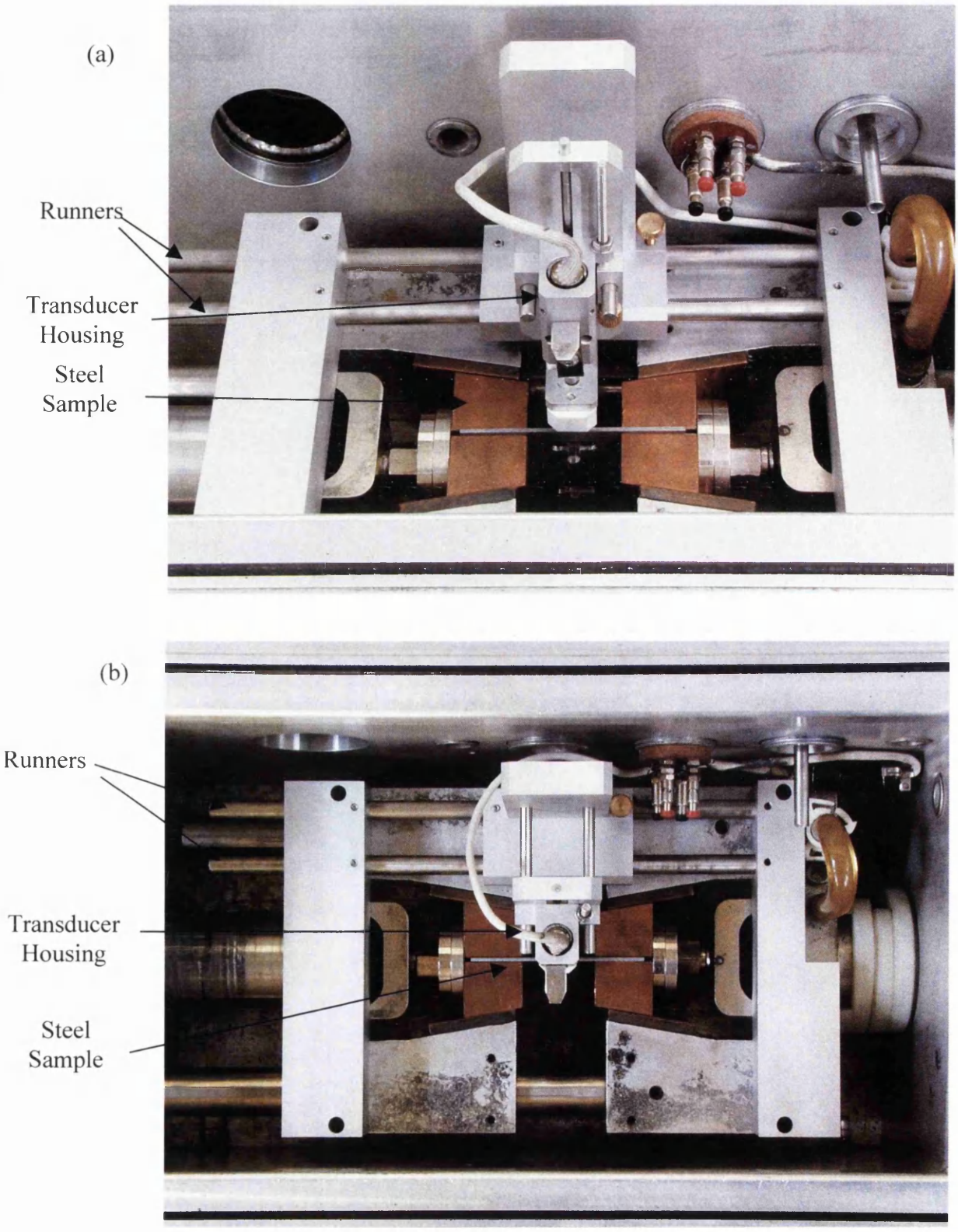

Figure 5.7. Photographs of the dilatometer attachment in position in the Gleeble 1500 vacuum chamber (glass lid not in place): (a) front view; (b) top view.

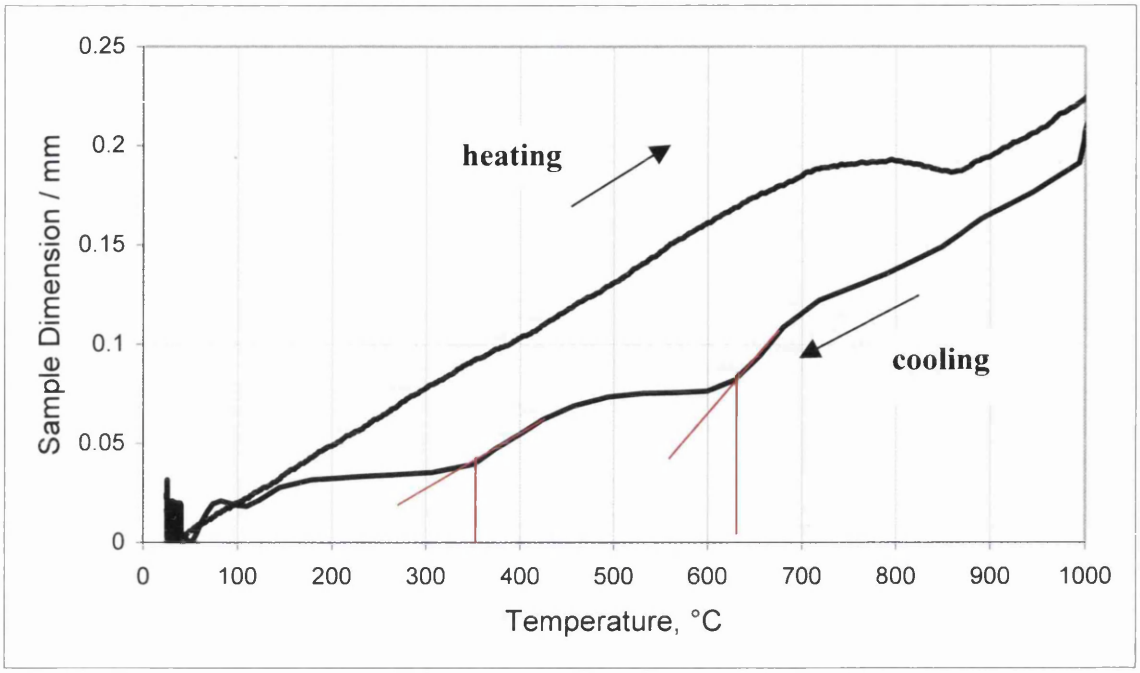

Figure 5.8. Example of a dimension – temperature curve from a CCT water quench experiment using the dilatometer designed for use with the Gleeble 1500. The transformation temperatures selected from this curve are indicated.

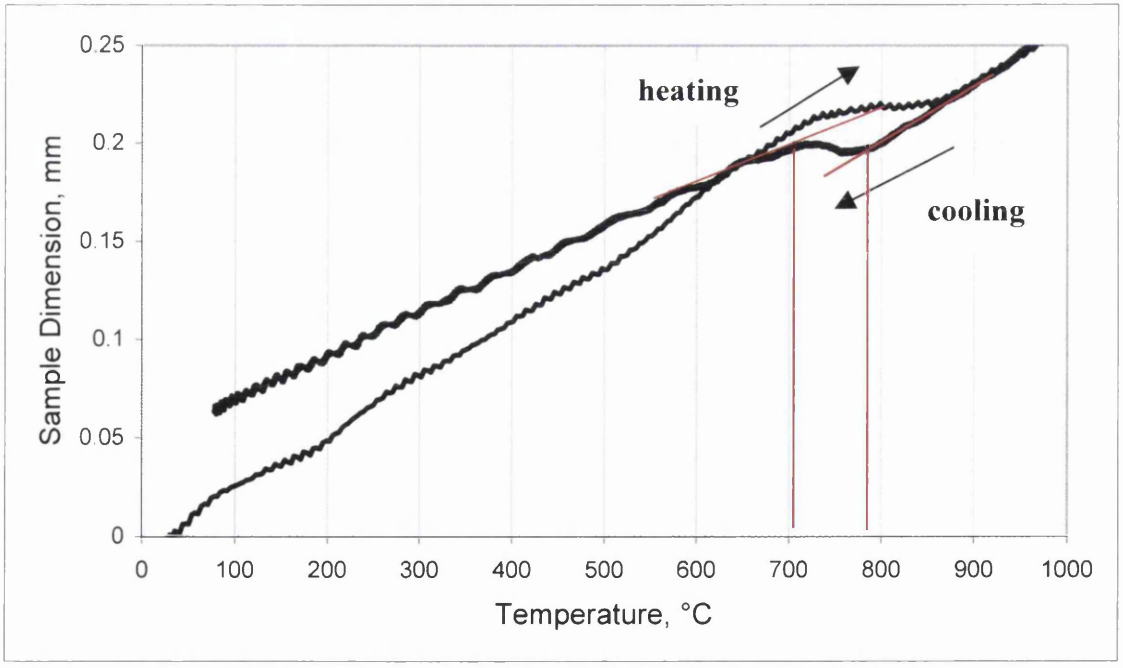

Figure 5.9. Example of a dimension – temperature curve from a CCT controlled cooling experiment using the dilatometer designed for use with the Gleeble 1500. The transformation temperatures selected from this curve are indicated.

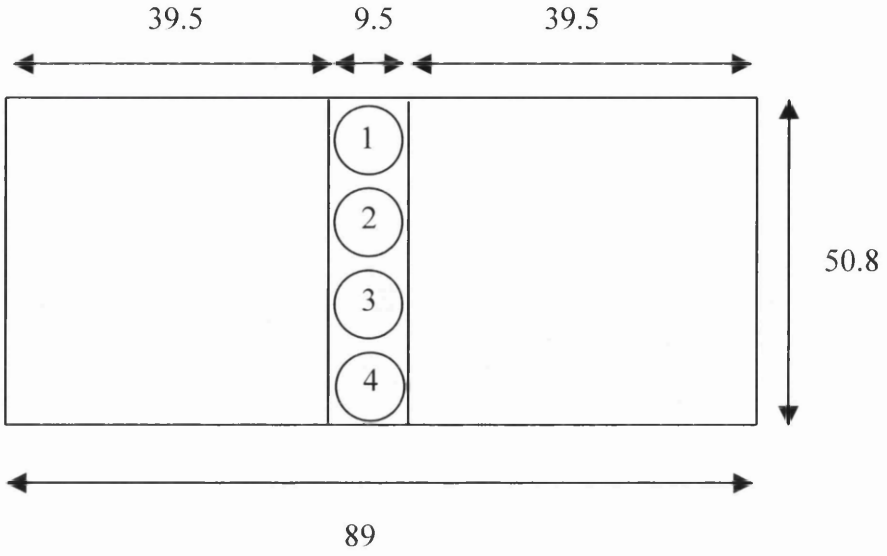

Figure 5.10. Schematic diagram of sample location for miniature discs taken from Gleeble heat treated specimens. All dimensions are in mm.

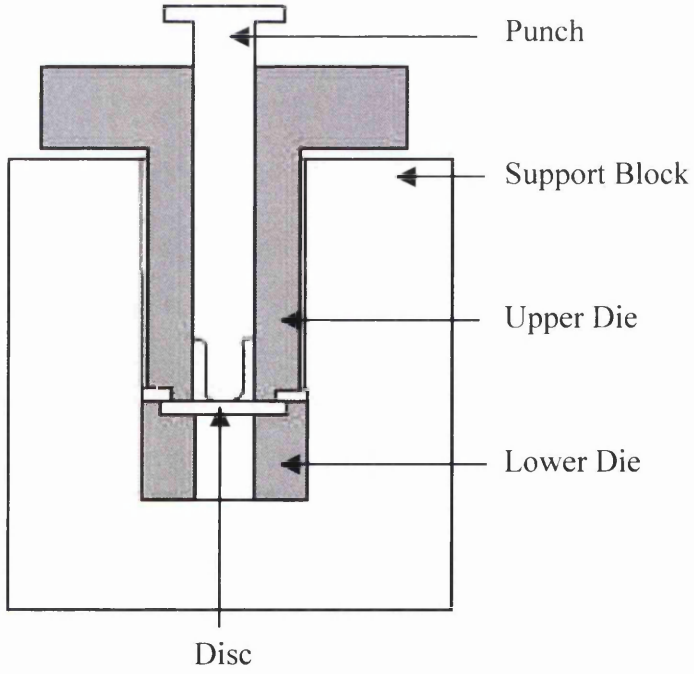

Figure 5.11. Schematic diagram of minature disc bend test experimental setup.

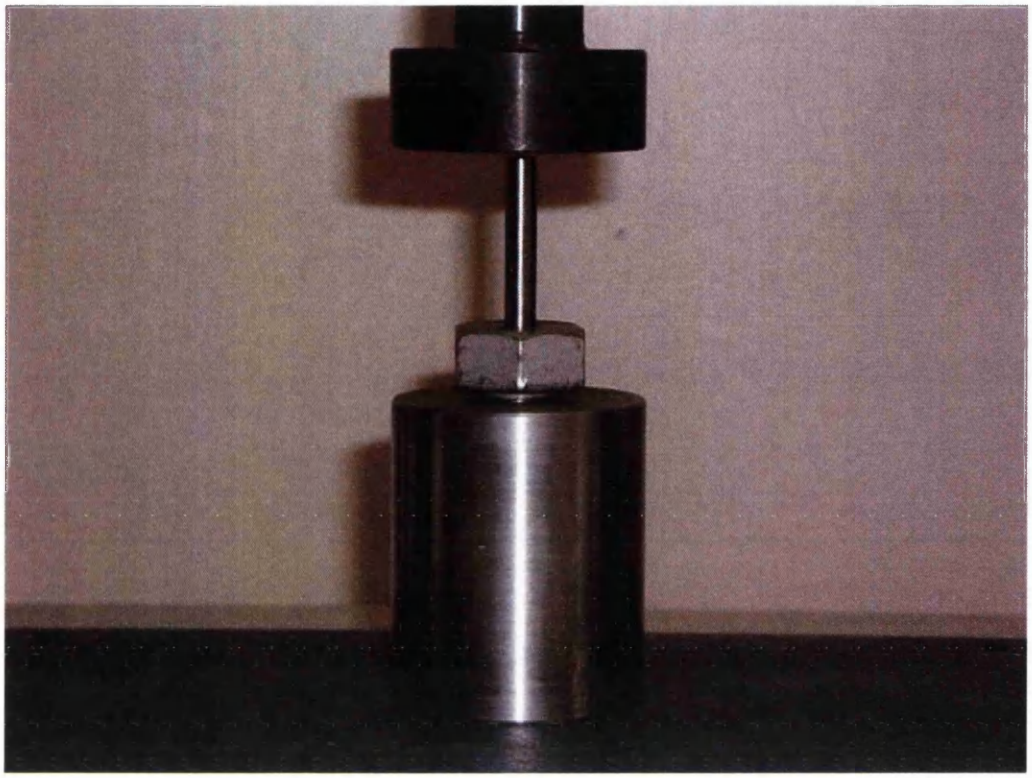

Figure 5.12. Photograph of miniature disc bend test apparatus in position under the compression platen of a Hounsfield s-series test machine.

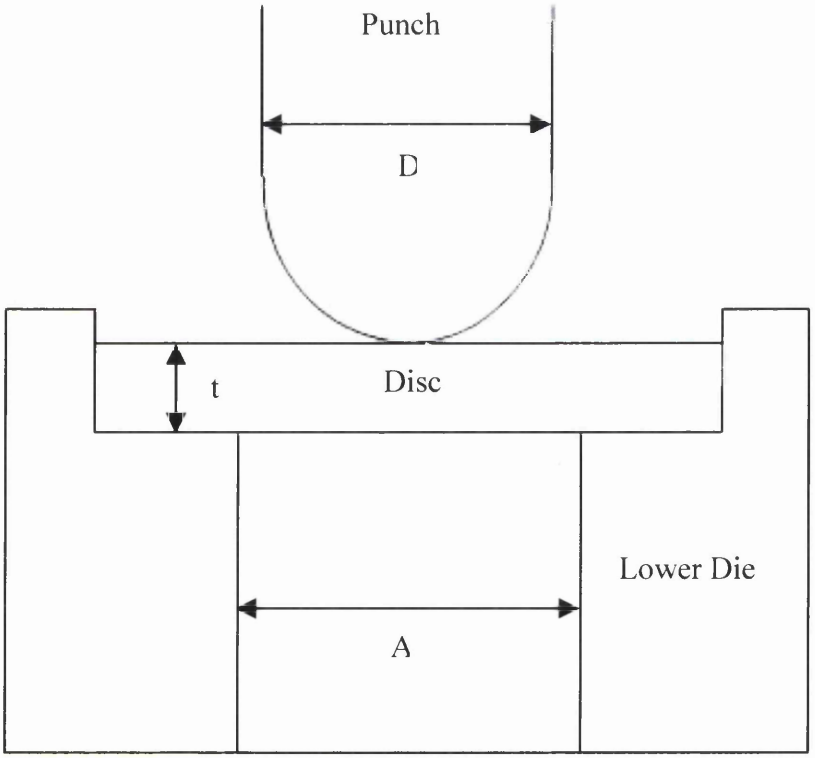

Figure 5.13. Schematic diagram of the punch, disc and lower die arrangement used in a miniature disc bend test.

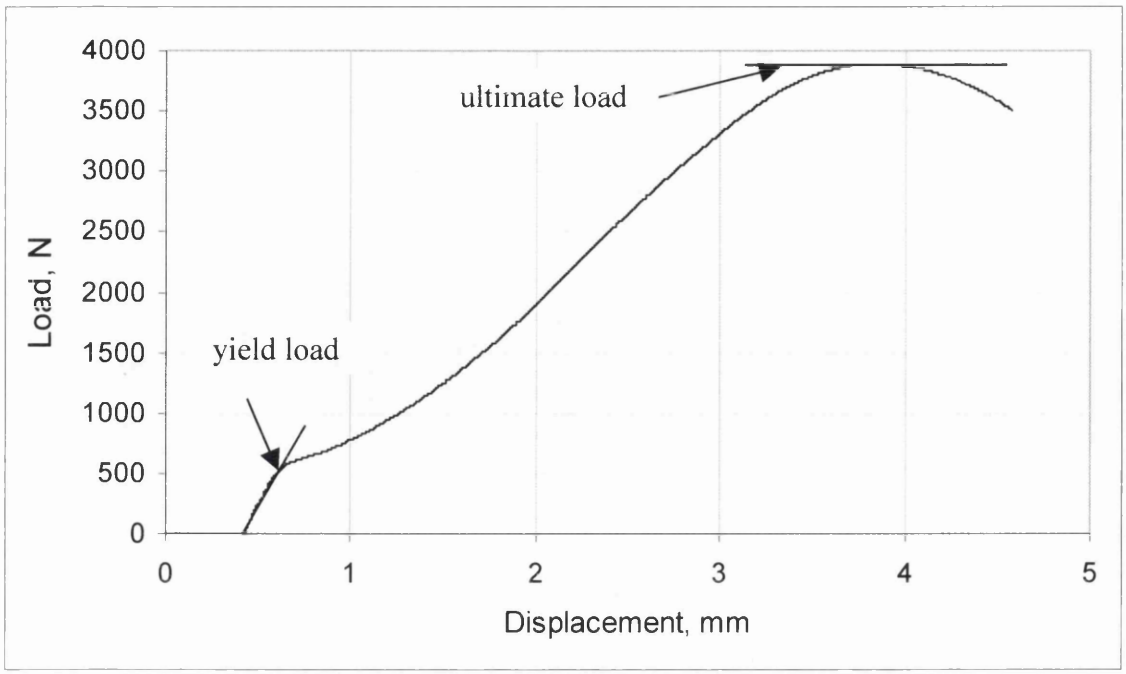

Figure 5.14. The load – displacement results from a miniature disc bend test using a 1mm disc of LCNb and a test speed of 1mm.min^{-1}. The yield and ultimate load are indicated.

Figure 5.15. Photograph of the failure of a 0.5mm thick disc of DP800 after testing at 1mm.min^{-1}. (Scale at side is mm)

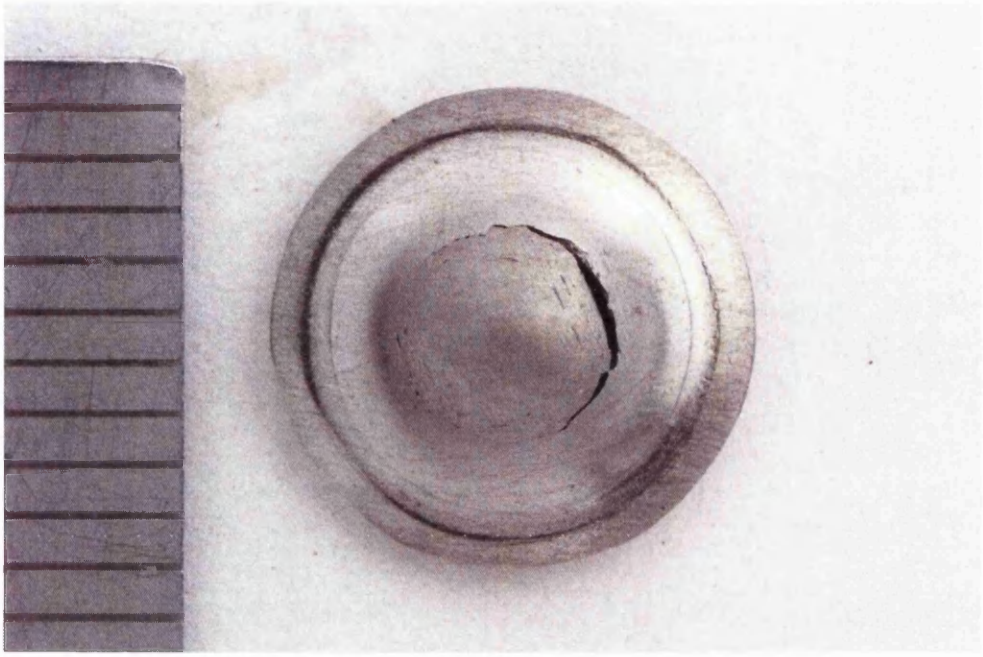

Figure 5.16. Photograph of the failure of a 1mm thick disc of DP800 after testing at 1mm.min^{-1}. (Scale at side is mm)

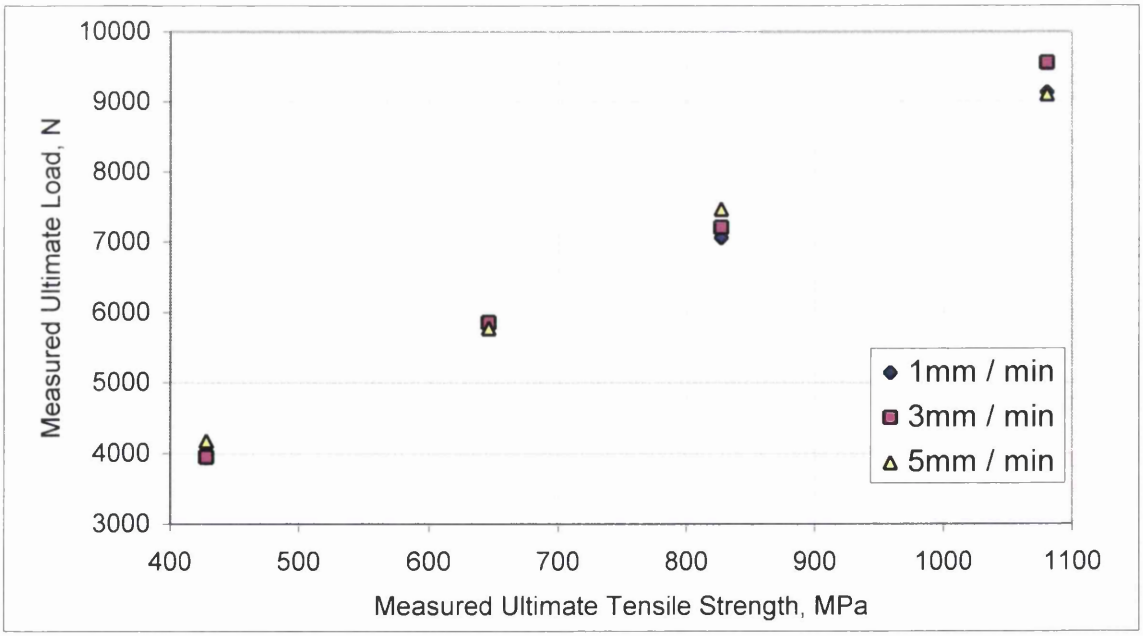

Figure 5.17. Relationship between the measured ultimate load and the measured ultimate tensile strength at 1, 3 and 5mm.min^{-1}.

Figure 5.18. Photograph of the failure of a 0.5mm thick disc of DP800 after testing at 3mm.min^{-1}. (Scale at side is mm)

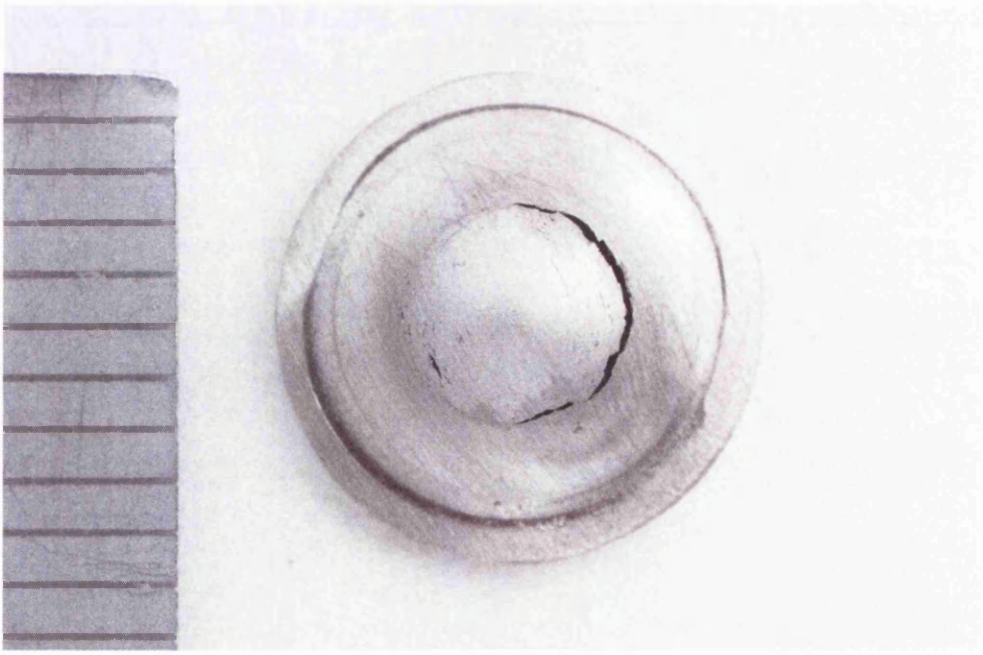

Figure 5.19. Photograph of the failure of a 1mm thick disc of DP800 after testing at 3mm.min^{-1}. (Scale at side is mm)

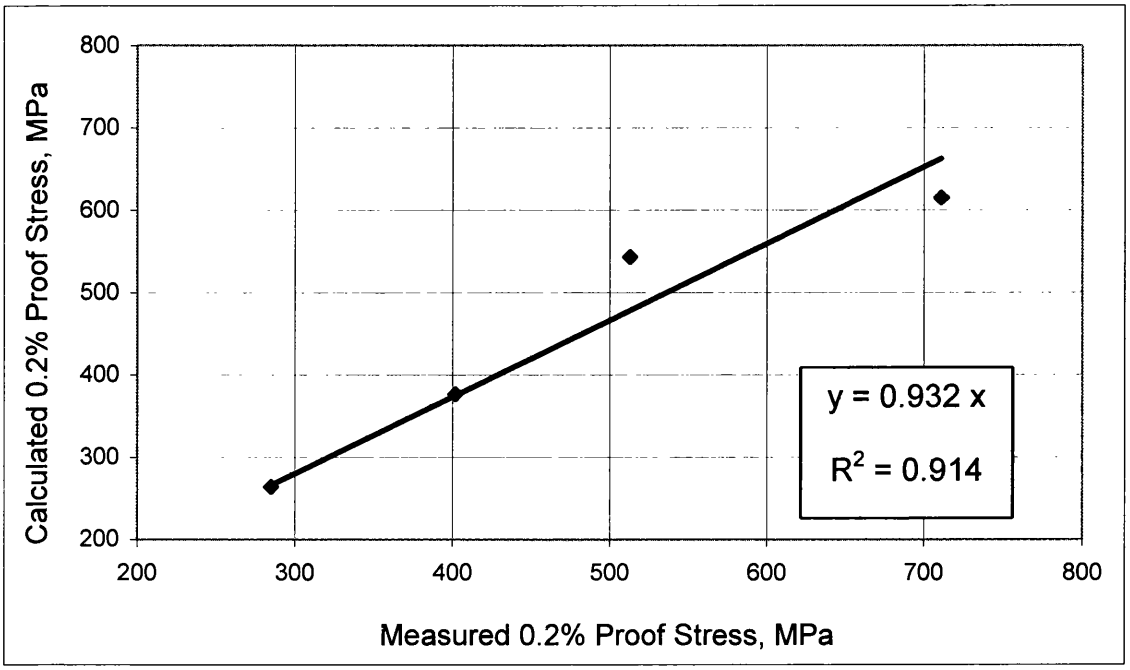

Figure 5.20. Relationship between the measured 0.2% proof stress and that predicted from the results of a miniature disc bend test.

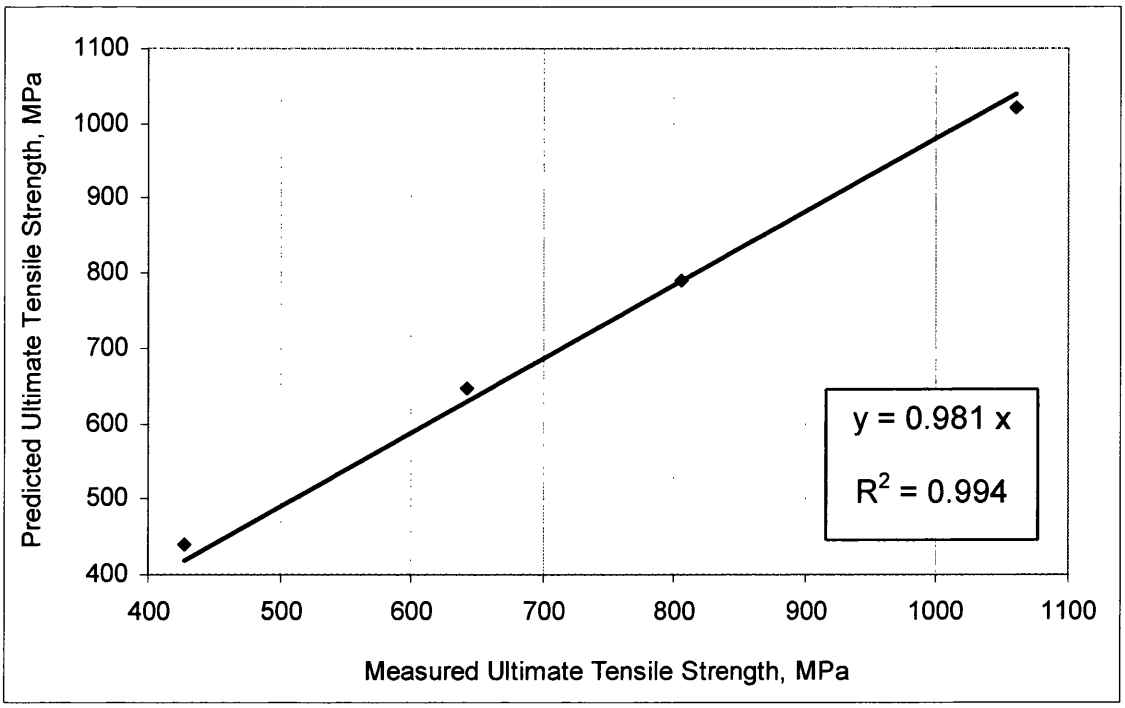

Figure 5.21. Relationship between measured ultimate tensile strength and that predicted from the results of a miniature disc bend test.

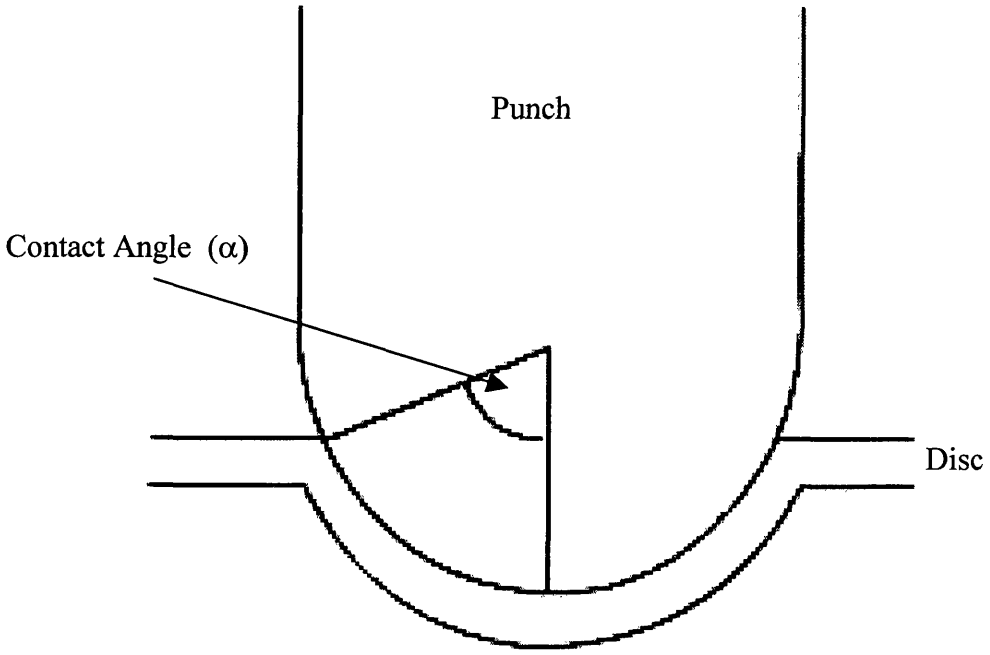

Figure 5.22. Schematic diagram showing the paraeters used to define the contact angle between punch and disc.

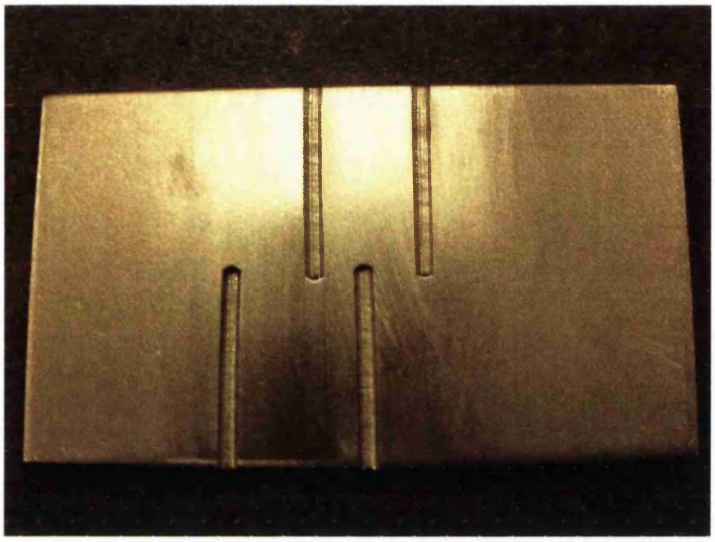

(a)

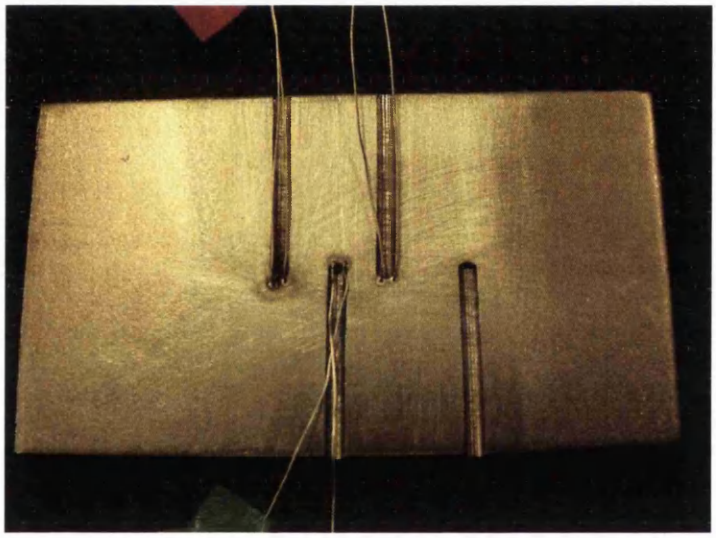

(b)

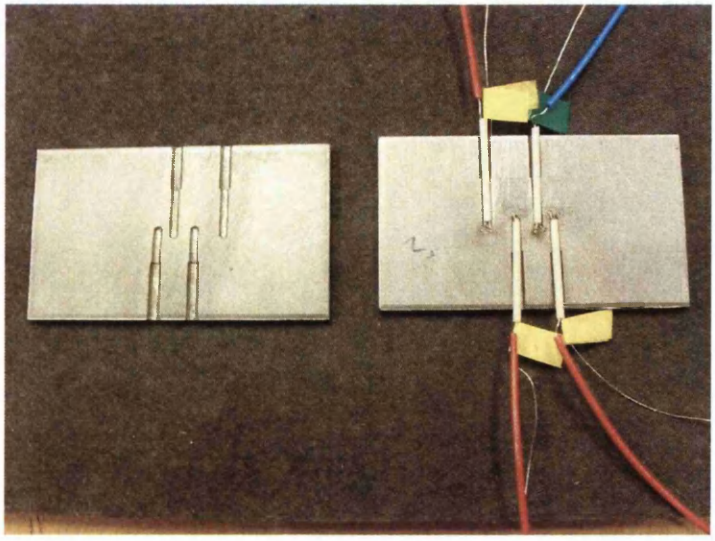

(c)

Figure 5.23 Photographs illustrating the steps in producing a weld coupon with attached thermocouples: (a) a sample with slots machined at fixed locations; (b) thermocouple wires attached to inside tips of each slot; (c) ceramic and polymer sheaths in place and identifying tags attached.

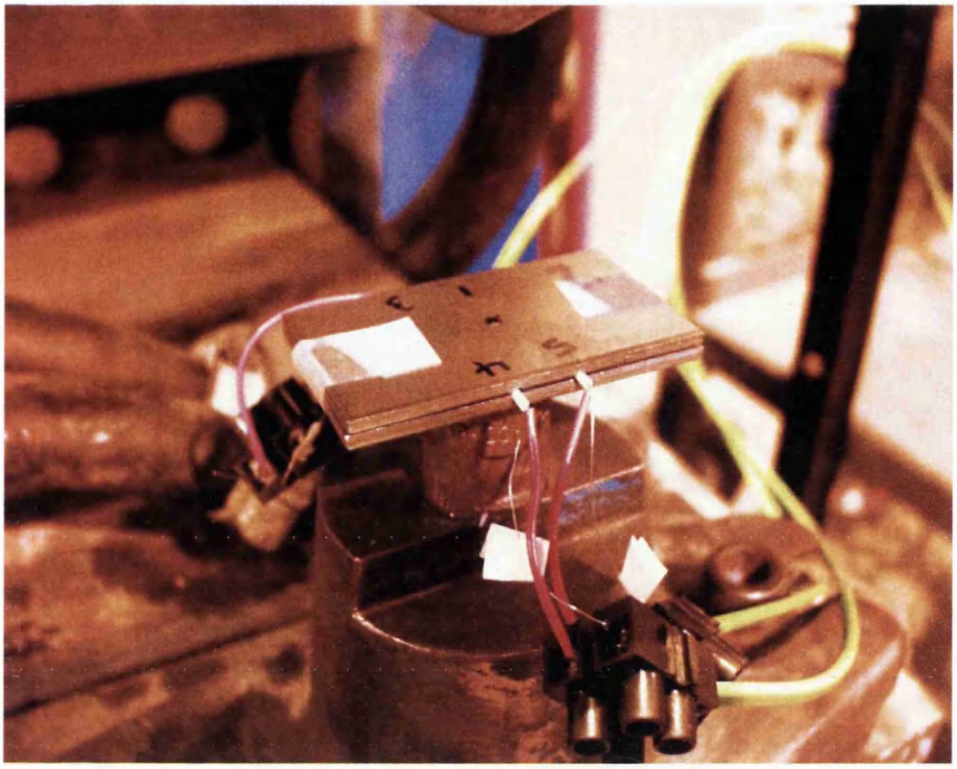

(a)

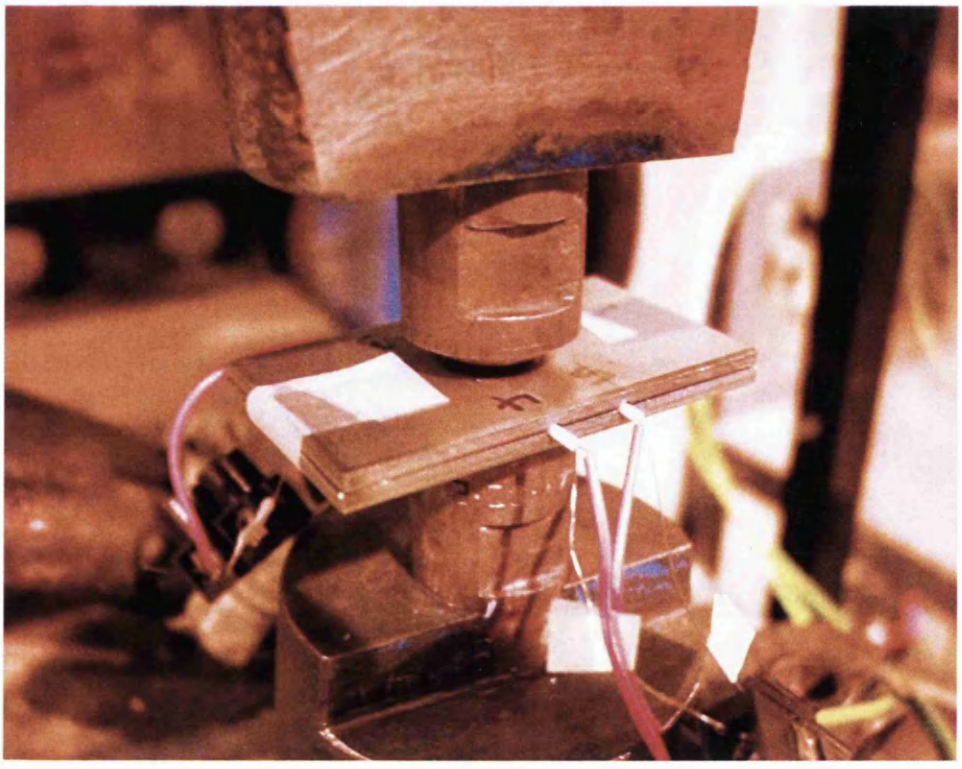

(b)

Figure 5.24. Detailed photographs showing the test specimen in position on the welding electrodes: (a) electrodes apart; (b) electrodes together.

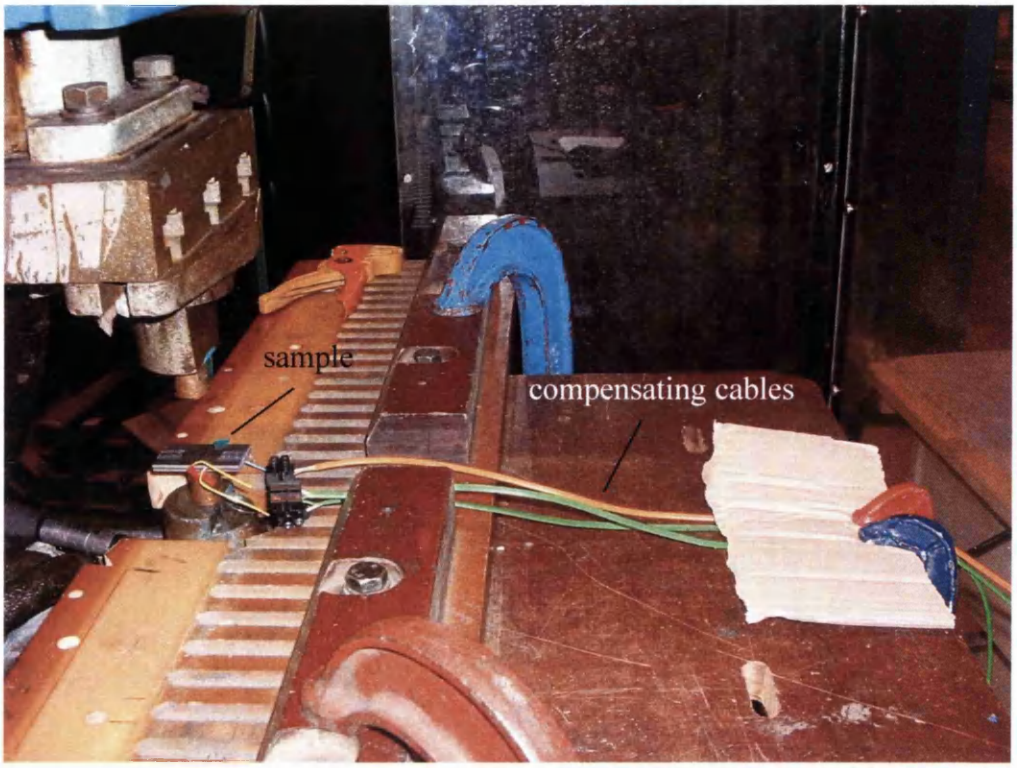

Figure 5.25. Detailed photograph of the weld test specimen and compensating cables.

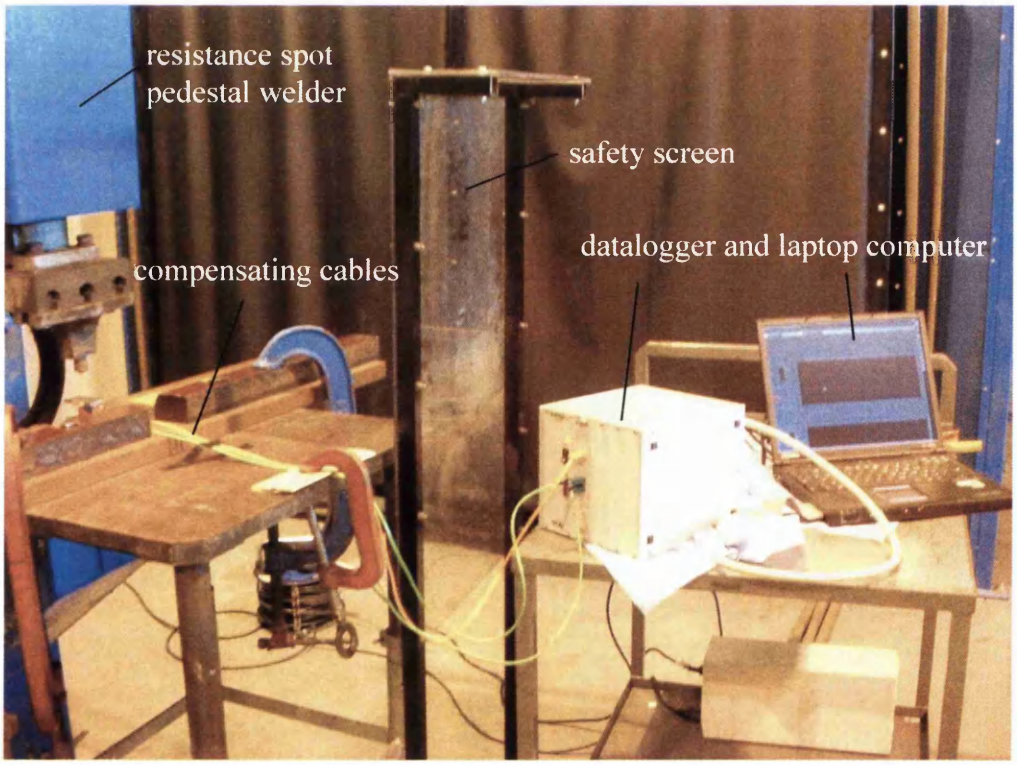

Figure 5.26 Photograph of the overall experimental setup for datalogging the thermocouple readings during resistance spot welding.

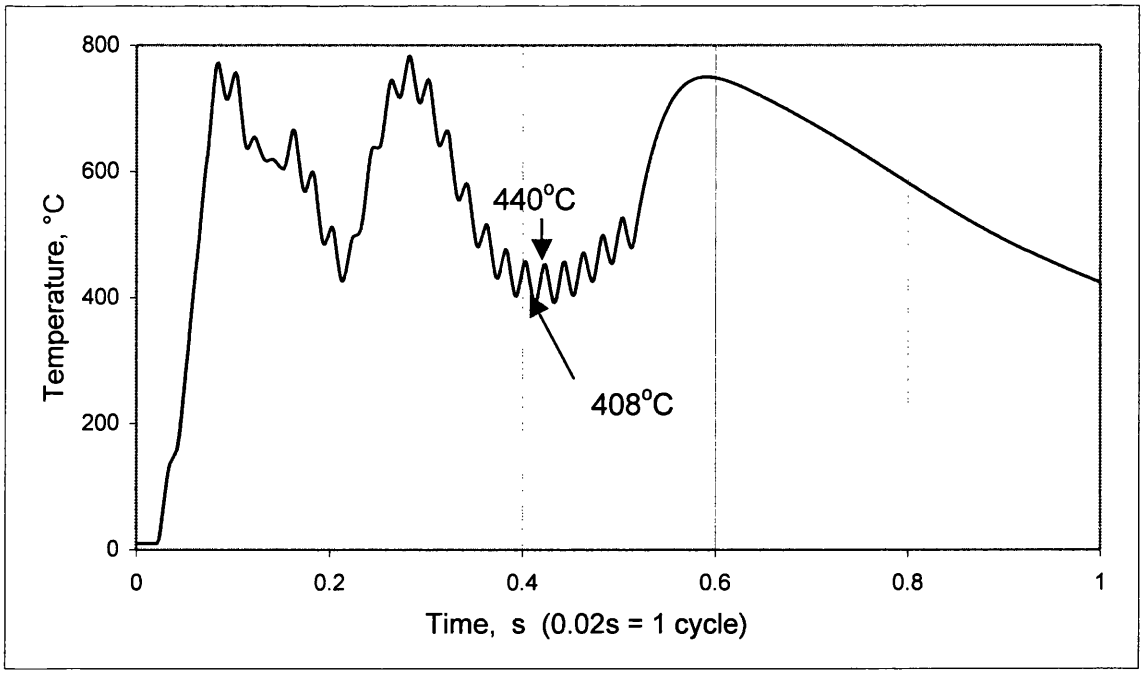

Figure 5.27 The variation in the temperature with time, measured by an R-type thermocouple, during a 25 cycle weld.

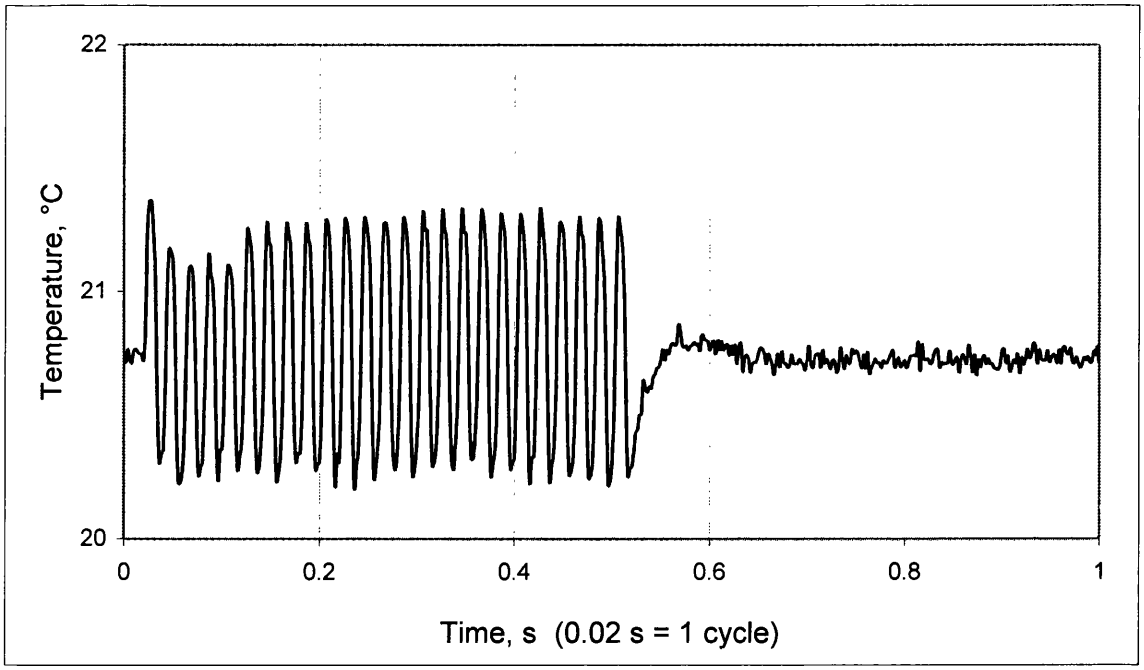

Figure 5.28 The variation in the temperature measured by an unattached thermocouple wire, lying parallel to an attached thermocouple, during a 25 cycle weld.

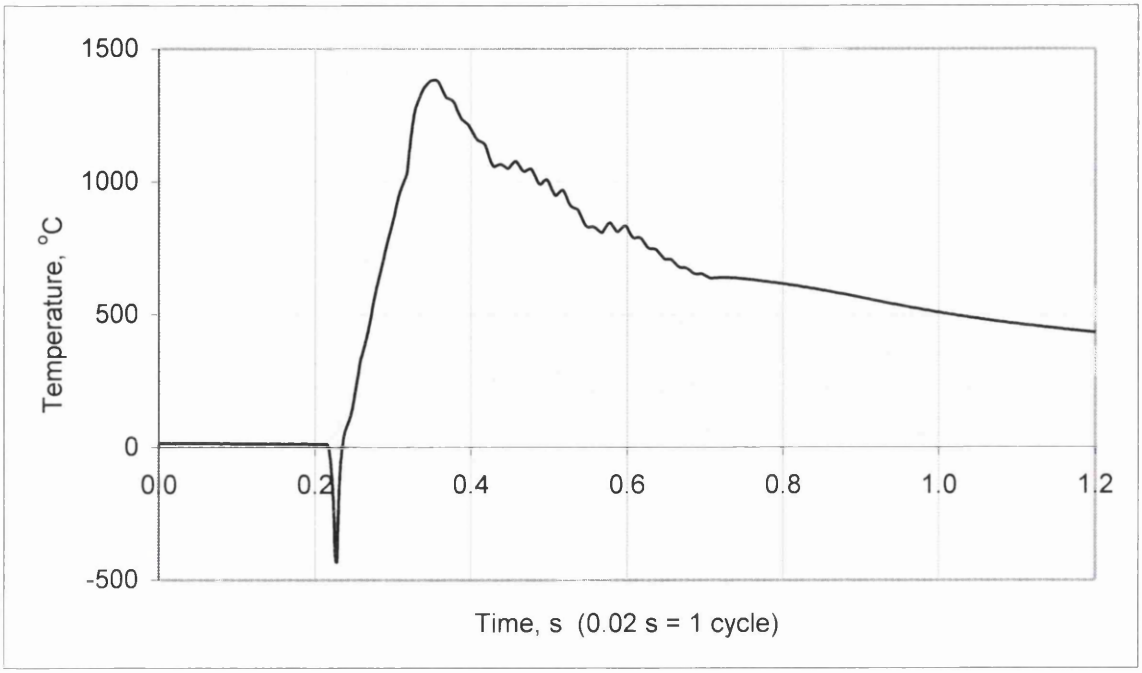

Figure 5.29. An example of the typical drop in temperature measured at the beginning of a welding cycle using a plain wire, R-type thermocouple.

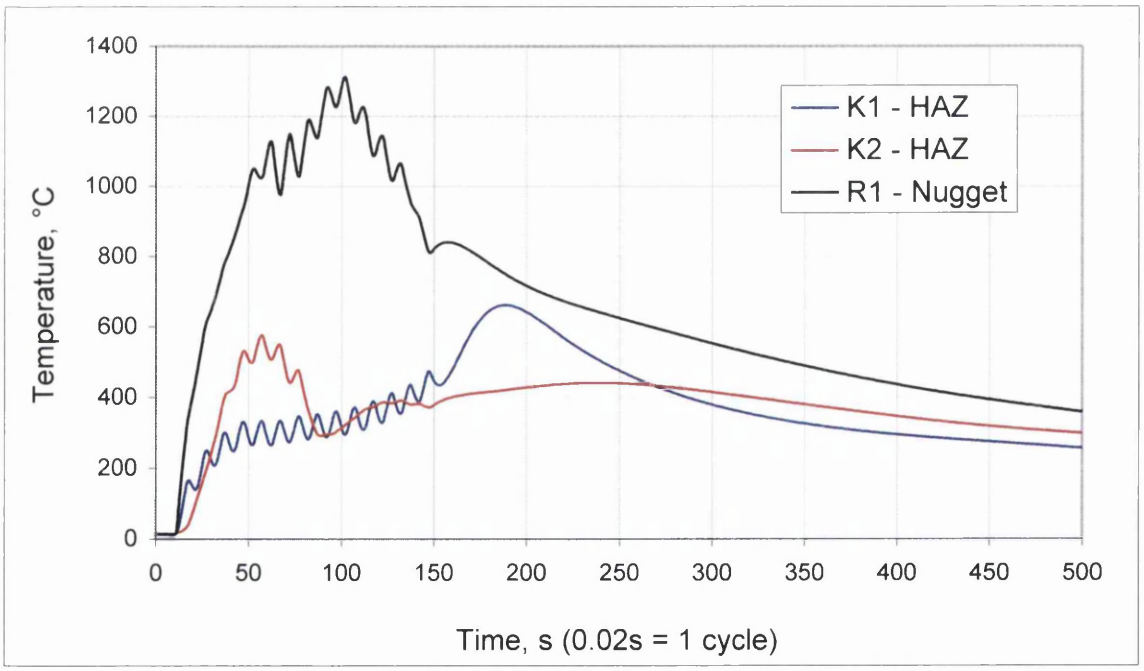

Figure 5.30. Example of time –temperature results showing the typical 'pull down' effect experienced by three plain wire thermocouples during a welding cycle.

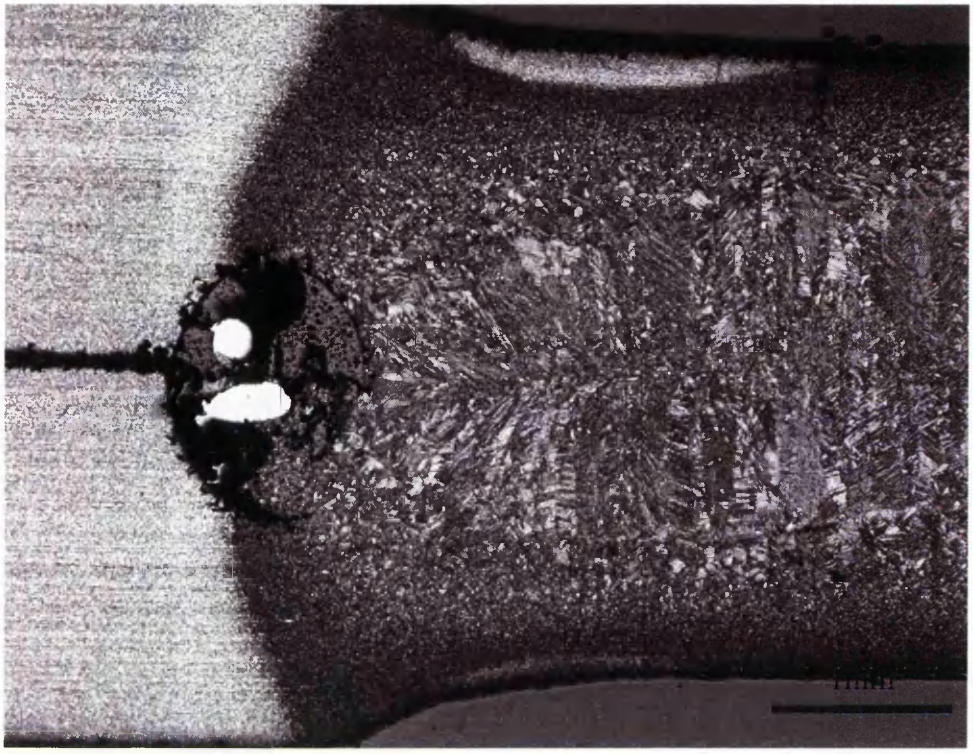

Figure 5.31. Micrograph showing microstructure around a thermocouple heat affected zone position. The thermocouple that can be seen is a type-K plain wire.

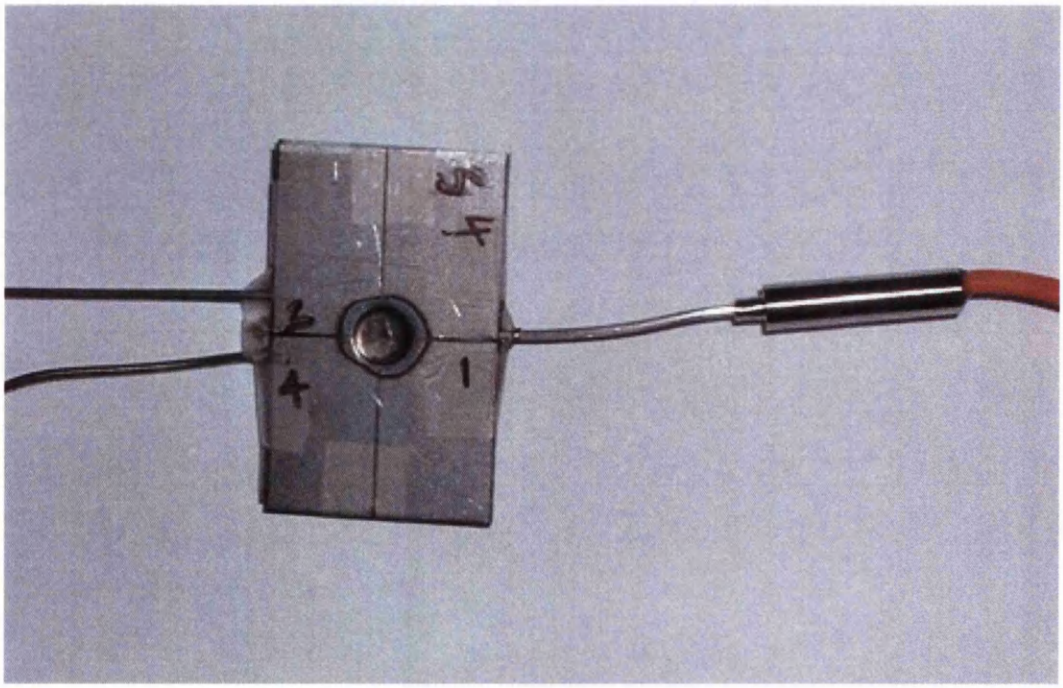

Figure 5.32. Photograph of a sample with sheathed thermocouples attached. Extra tape was used to maintain alignment of the two halves of the sample prior to welding.

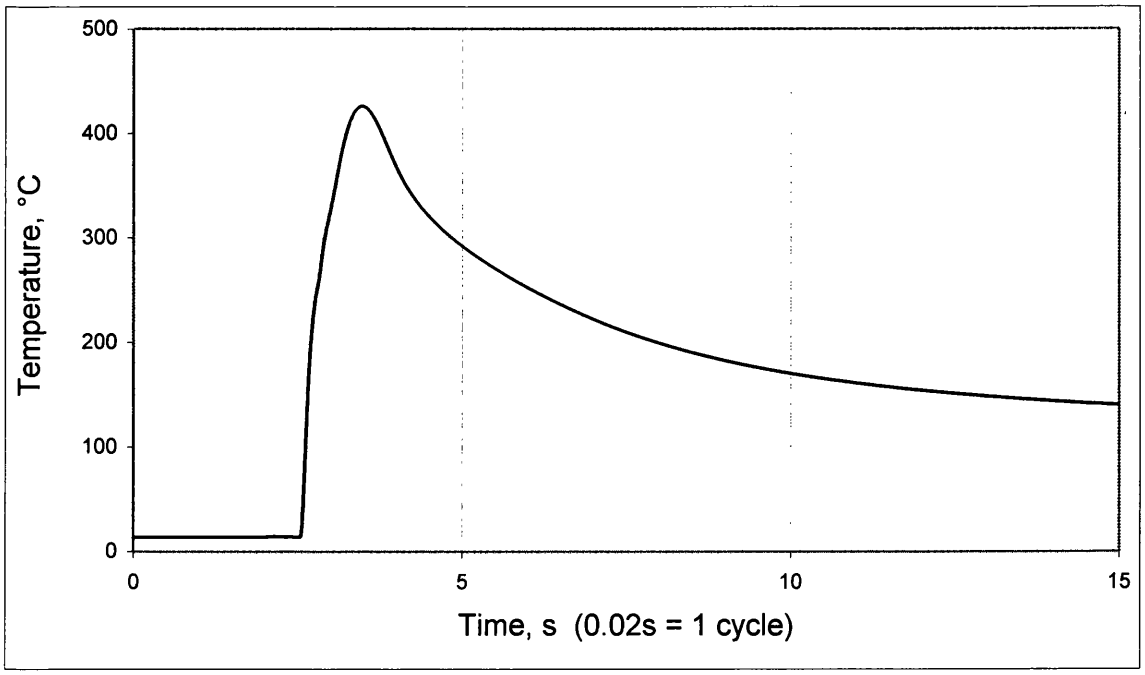

Figure 5.33. The thermal profile measured by a K-type sheathed thermocouple during resistance spot welding using 15 cycles of current, showing that there is no interference for this thermocouple type.

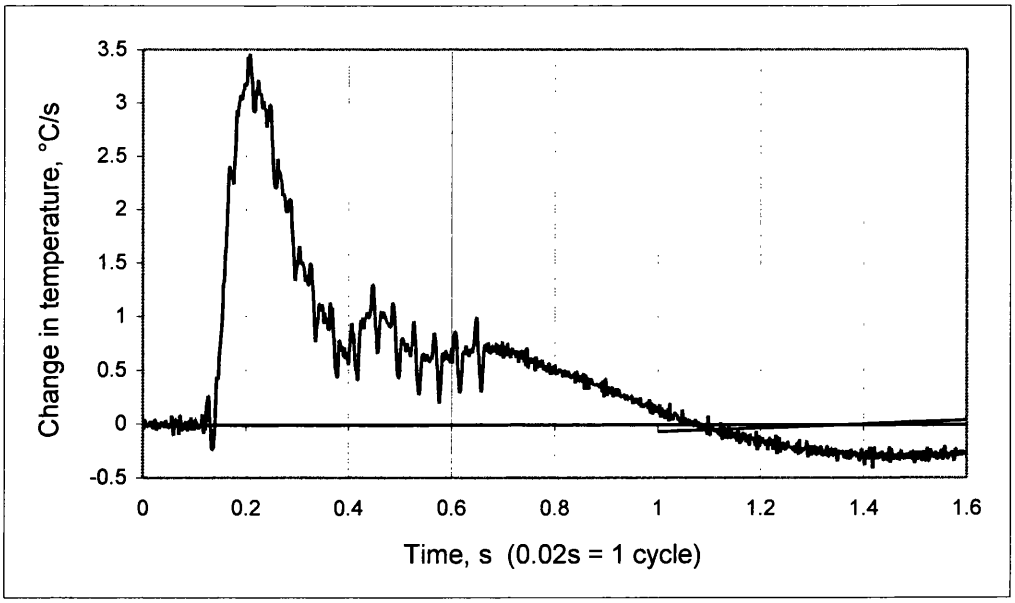

Figure 5.34. The rate of change of temperature measured by a sheathed K-type thermocouple during a resistance spot weld of 15 cycles of current.

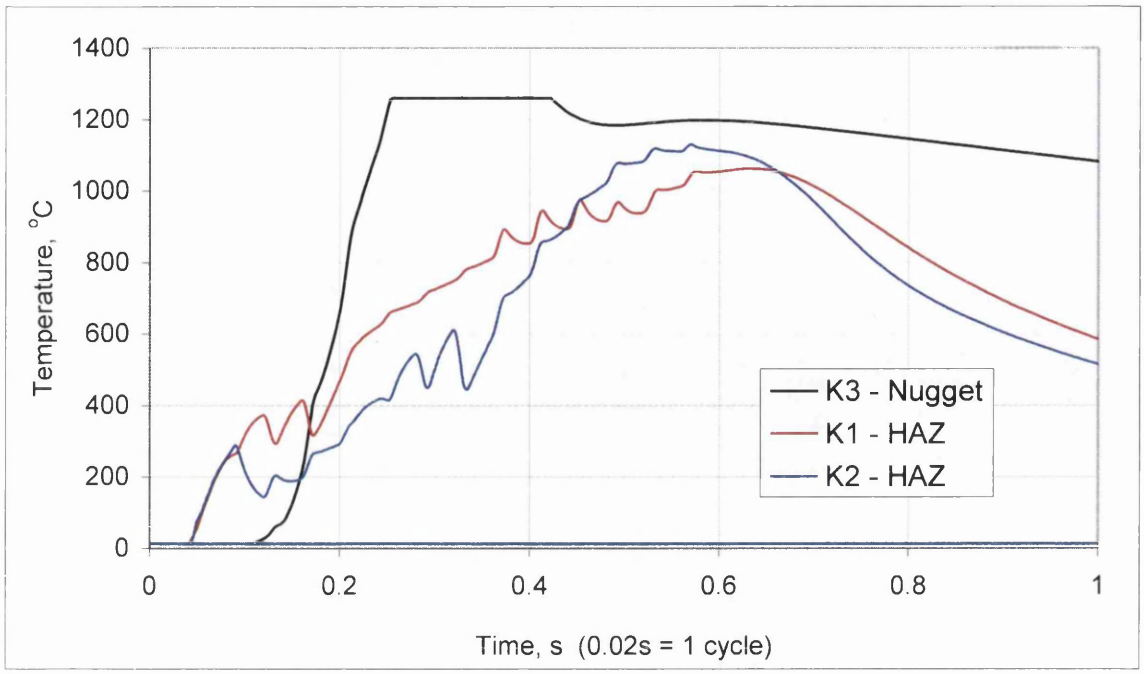

Figure 5.35. Thermal profile measured by three thermocouples during resistance spot welding. Thermocouple K3 (sheathed) demonstrates a lag behind the two plain wire thermocouples.

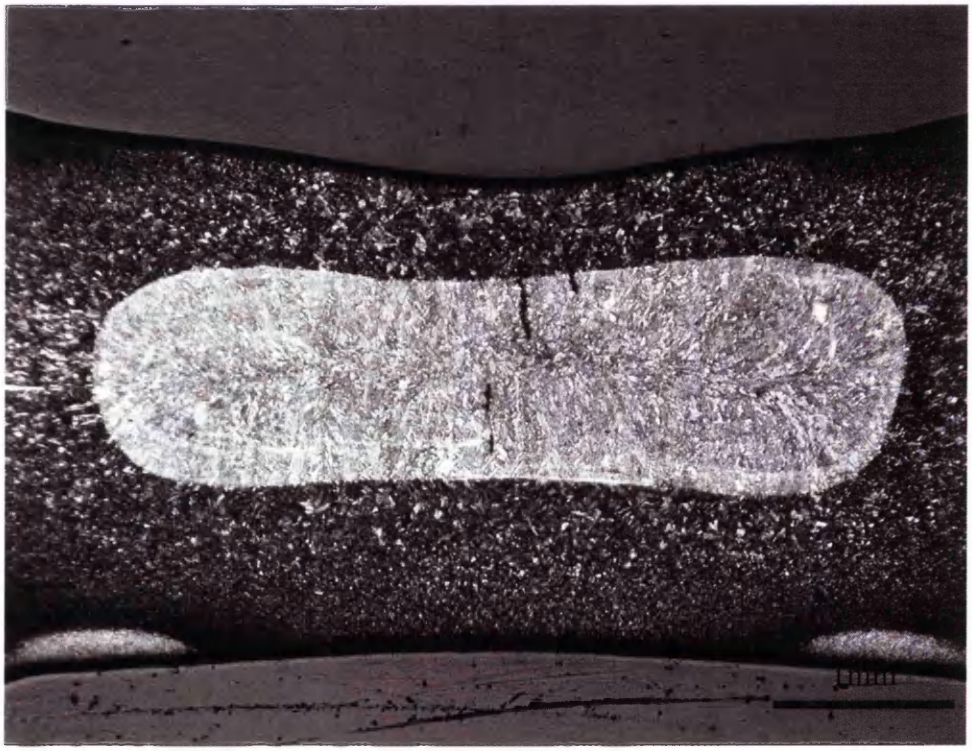

Figure 5.36. Micrograph indicating the weld microstructure following the use of sheathed thermocouples.

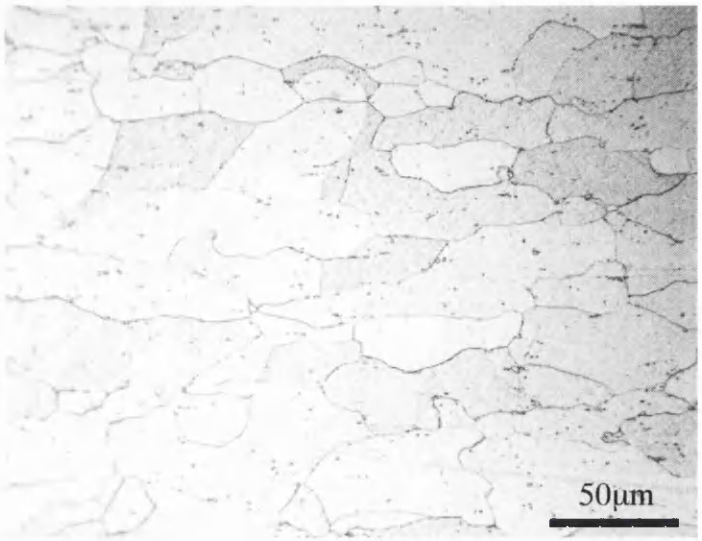

(a)

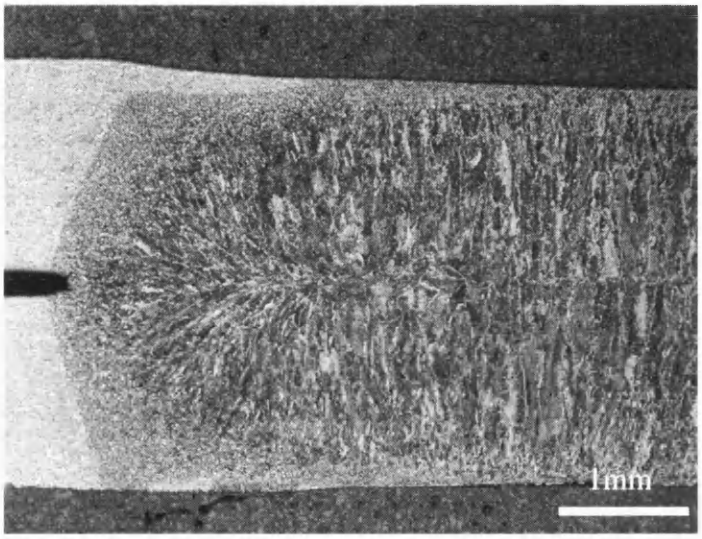

(b)

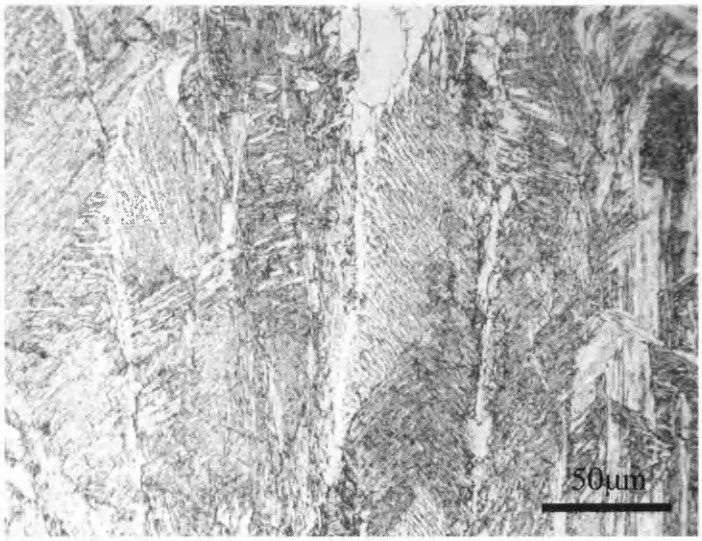

(c)

Figure 6.1. Micrographs of a 5√t spot weld made in alloy LC (CE - 0.04): (a) parent microstructure; (b) macro showing shape of weld and heat-affected zone; (c) columnar grains in the weld nugget.

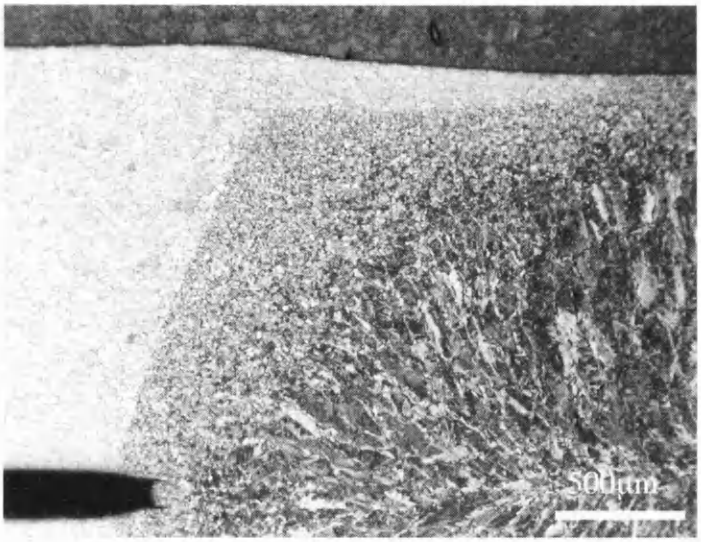

(d)

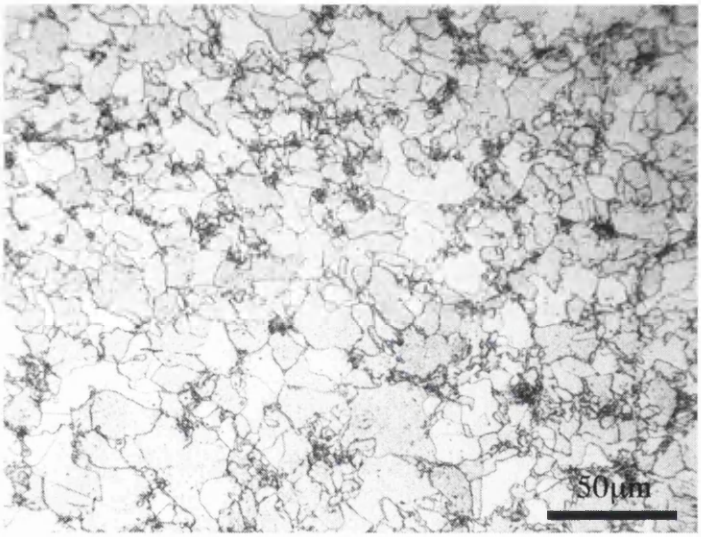

(e)

Figure 6.1. Micrographs of a 5√t spot weld made in alloy LC (CE - 0.04): (d) the variation in microstructure from the edge of the nugget through to the parent material; (e) heat-affected zone microstructure.

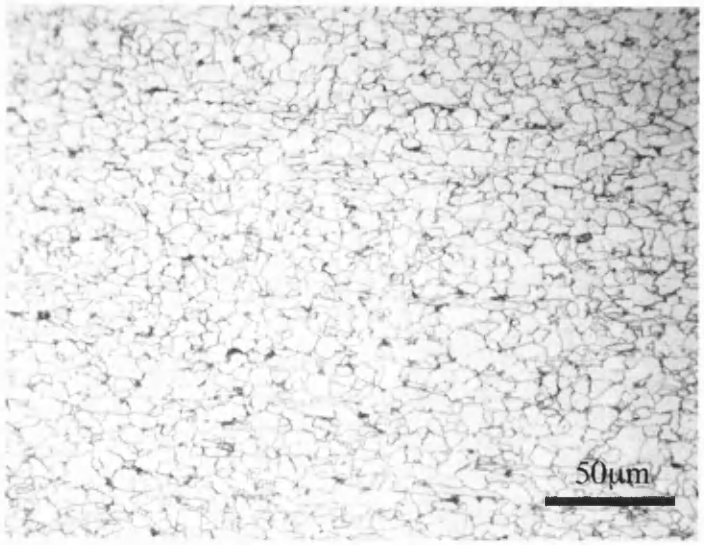

(a)

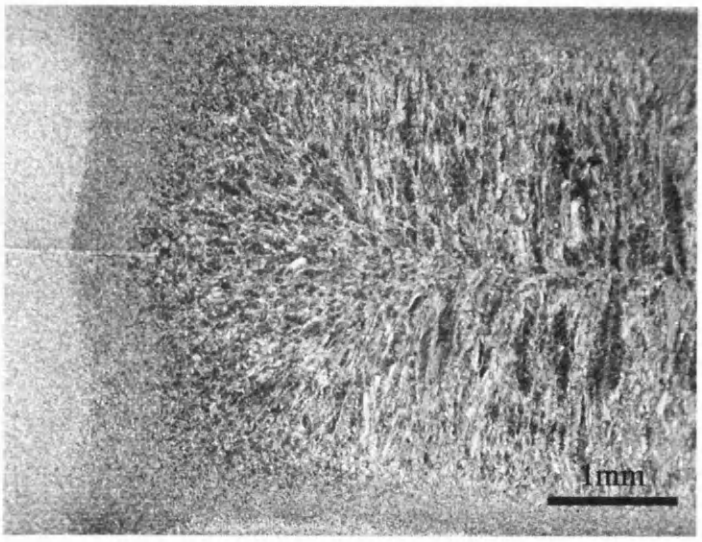

(b)

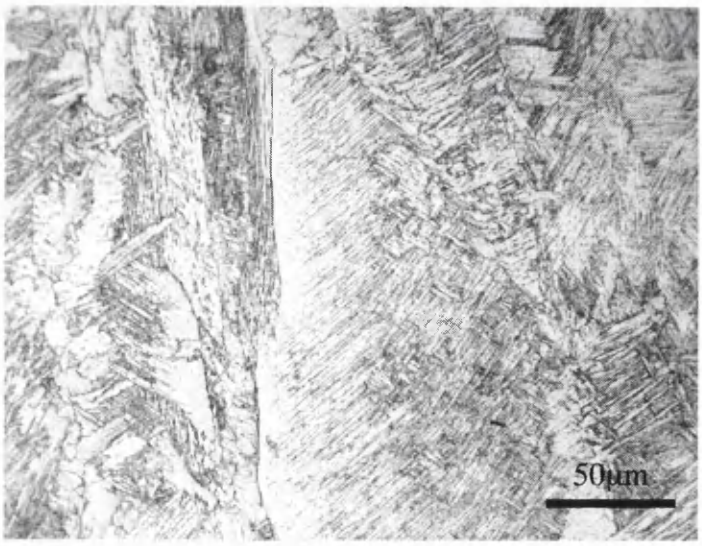

(c)

Figure 6.2. Micrographs of a 5√t spot weld made in alloy LCNb (CE - 0.07): (a) parent microstructure (b) macro showing shape of weld and heat-affected zone; (c) columnar grains in the weld nugget.

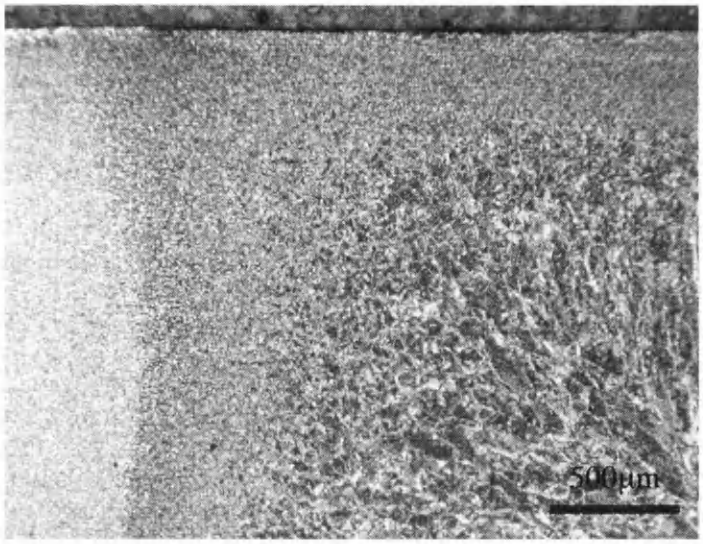

(d)

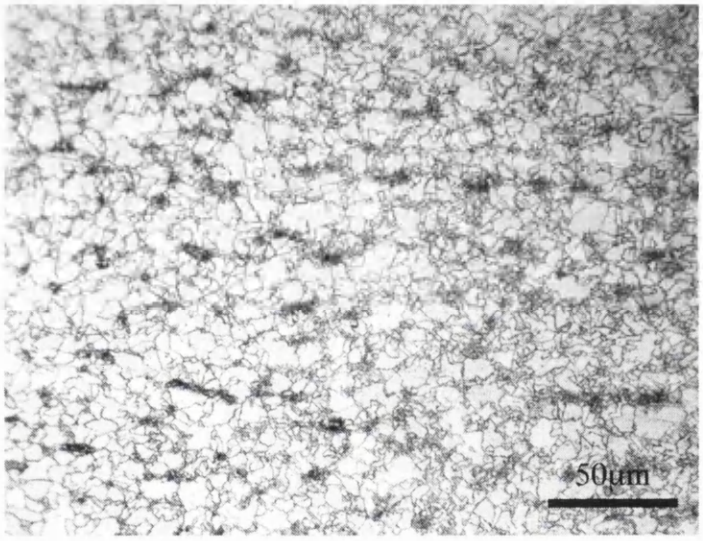

(e)

Figure 6.2. Micrographs of a 5√t spot weld made in alloy LCNb (CE - 0.07): (d) the variation in microstructure from the edge of the nugget through to the parent material; (e) heat-affected zone microstructure.

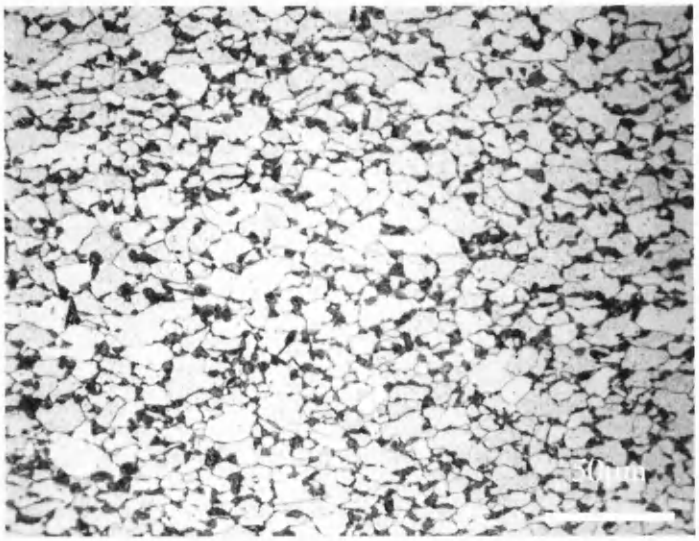

(a)

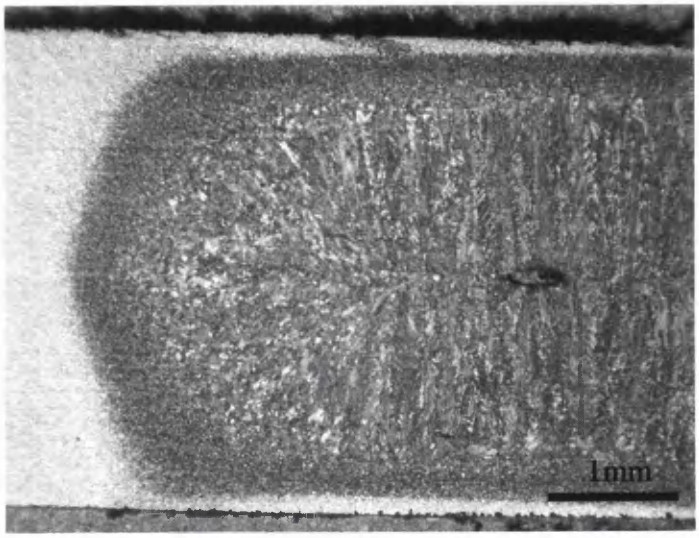

(b)

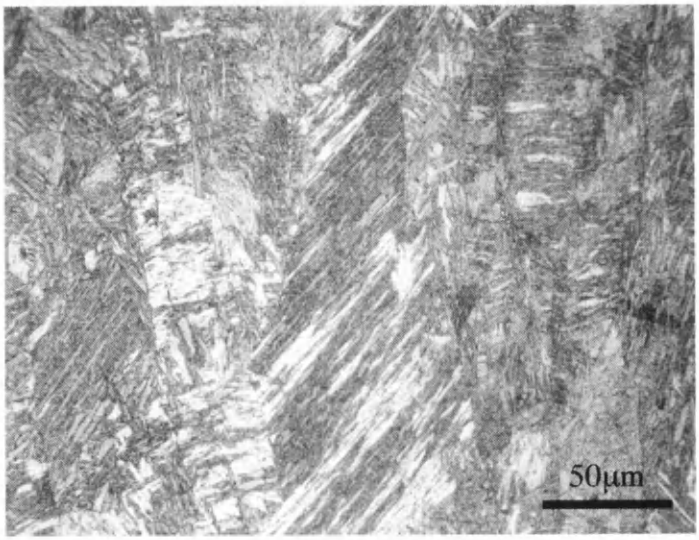

(c)

Figure 6.3. Micrographs of a 5√t spot weld made in alloy DP600 (CE - 0.14): (a) parent microstructure; (b) macro showing shape of weld and heat-affected zone; (c) columnar grains in the weld nugget.

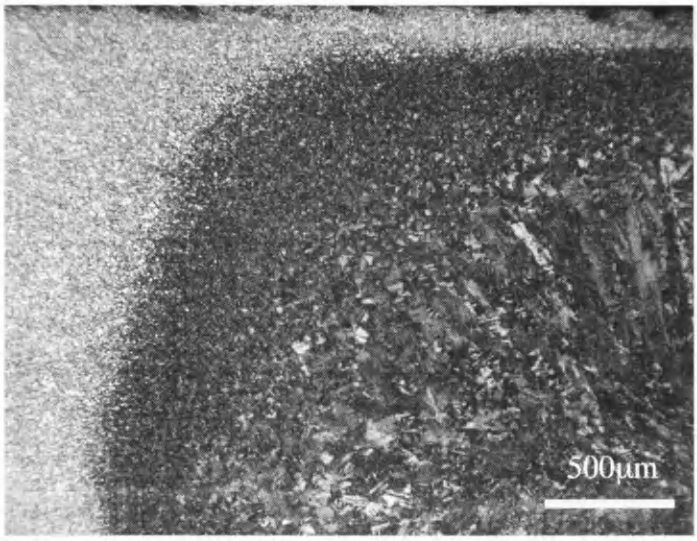

(d)

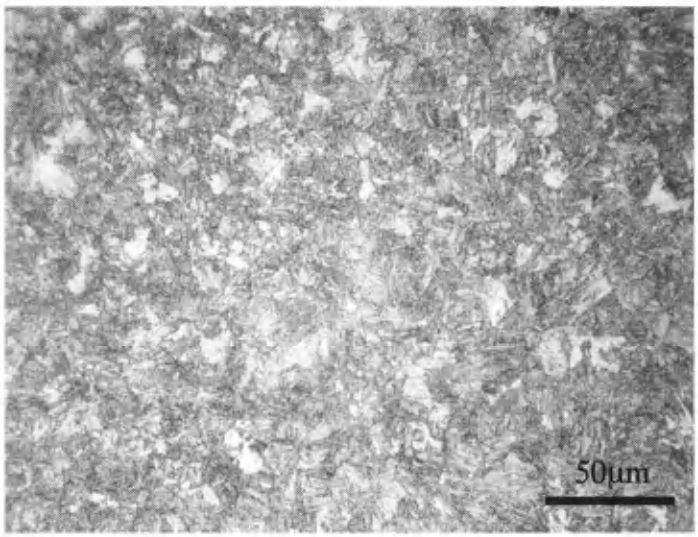

(e)

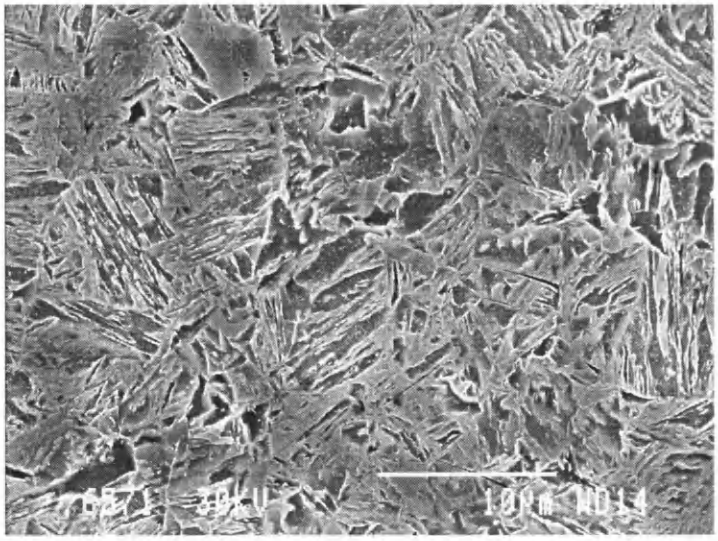

(f)

Figure 6.3. Micrographs of a 5√t spot weld made in alloy DP600 (CE - 0.14): (d) the variation in microstructure from the edge of the nugget through to the parent material; (e) heat-affected zone microstructure; (f) SEM micrograph of heat-affected zone microstructure.

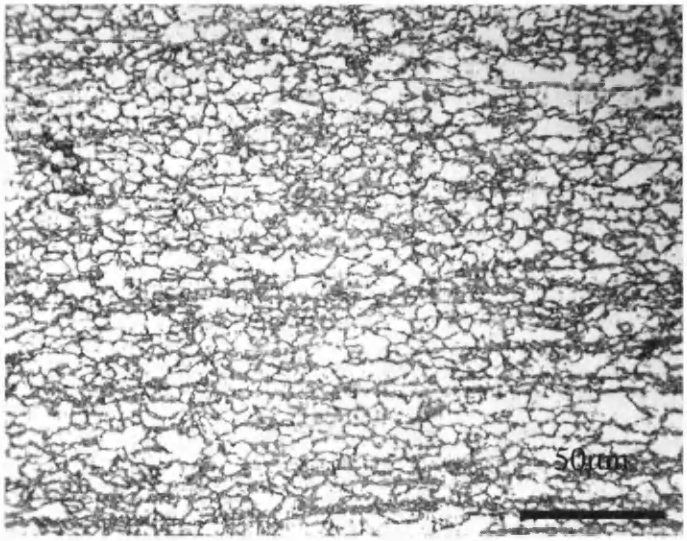

(a)

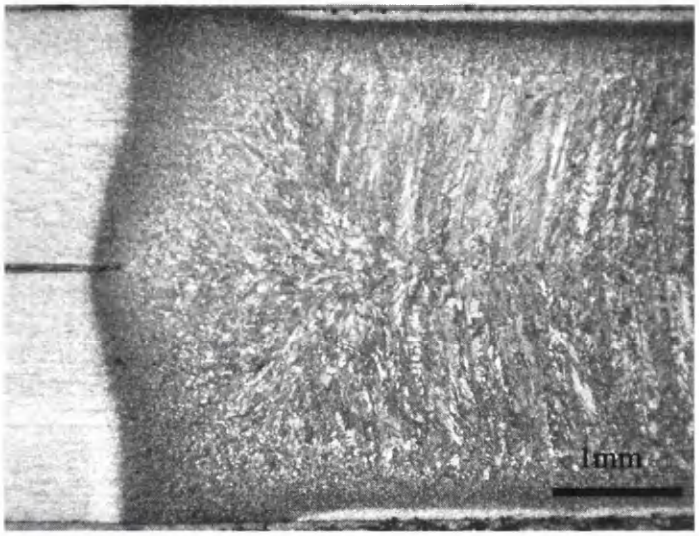

(b)

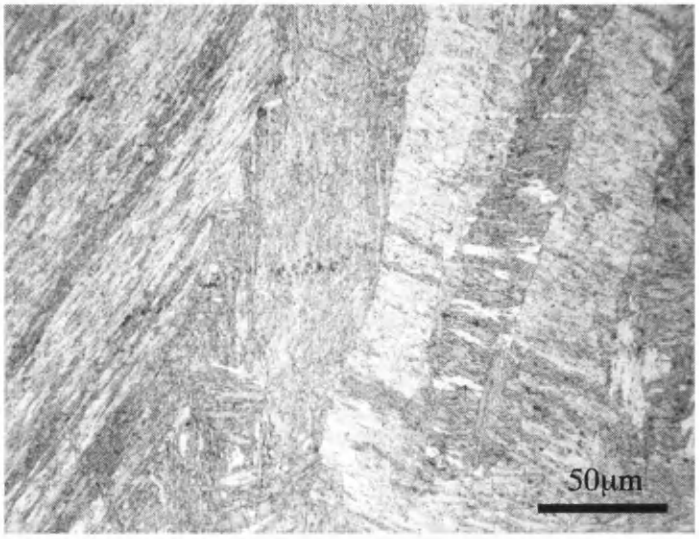

(c)

Figure 6.4. Micrographs of a 5√t spot weld made in alloy DP800 (CE - 0.22): (a) parent microstructure; (b) macro showing shape of weld and heat-affected zone; (c) columnar grains in the weld nugget.

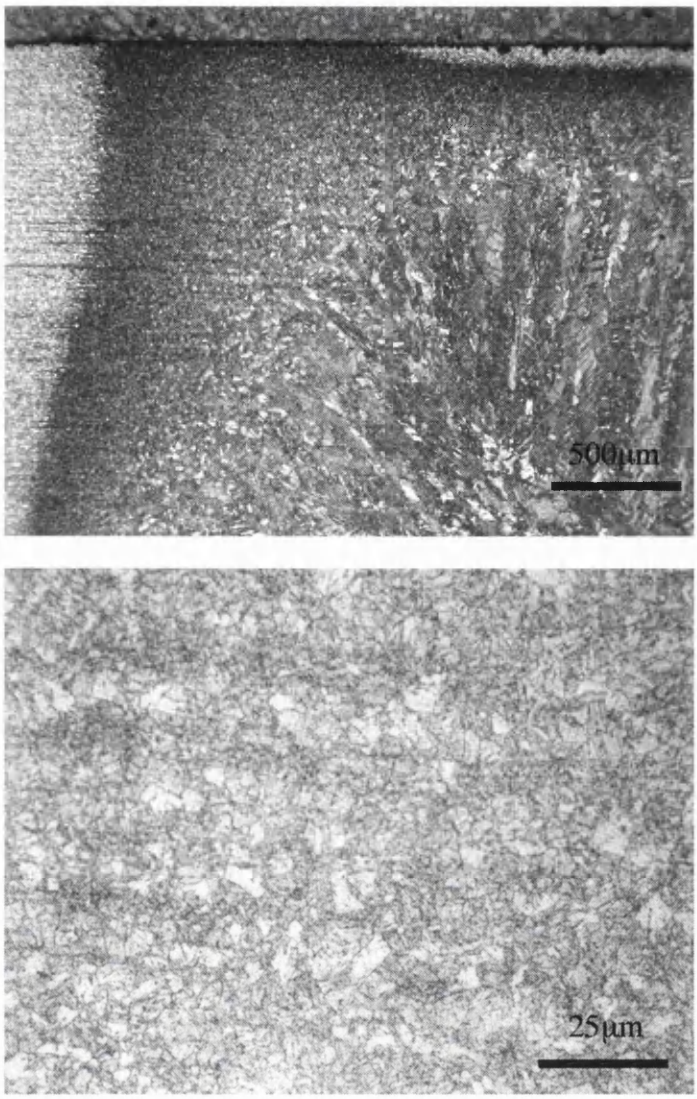

(d)

(e)

Figure 6.4. Micrographs of a 5√t spot weld made in alloy DP800 (CE - 0.22): (d) the variation in microstructure from the edge of the nugget through to the parent material; (e) heat-affected zone microstructure.

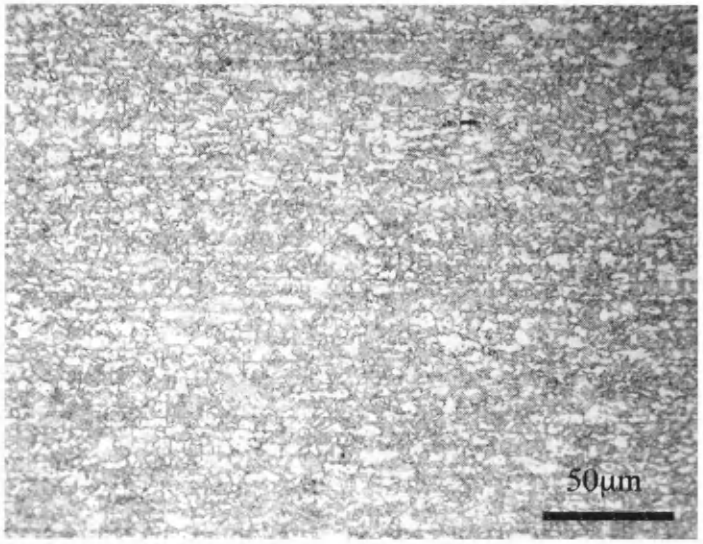

(a)

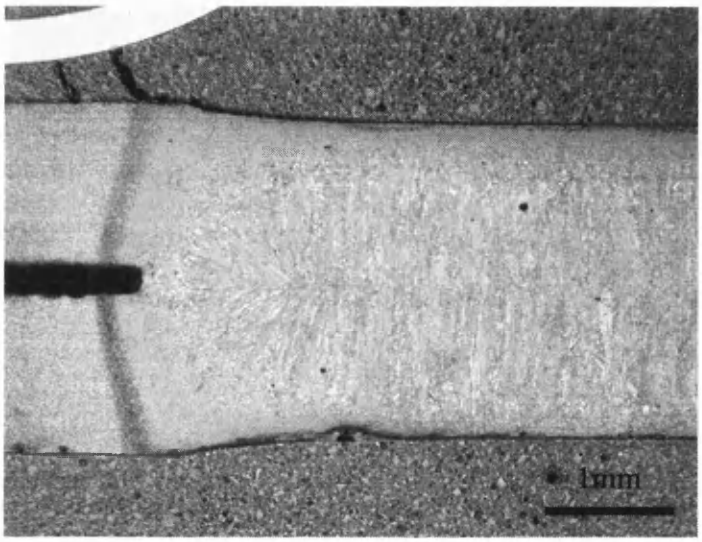

(b)

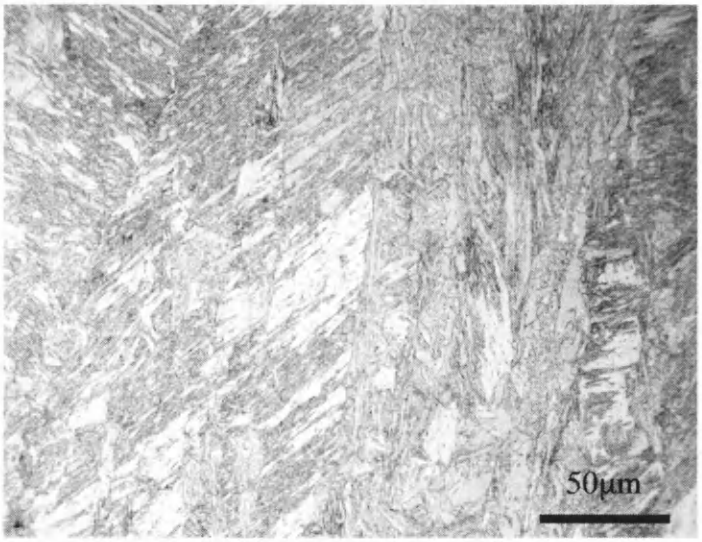

(c)

Figure 6.5. Micrographs of a 5√t spot weld made in alloy DP1000 (CE - 0.24): (a) parent microstructure; (b) macro showing shape of weld and heat-affected zone; (c) columnar grains in the weld nugget.

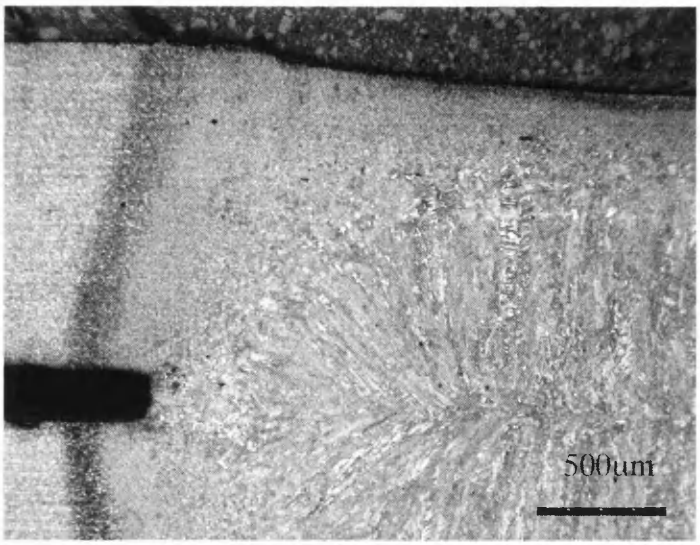

(d)

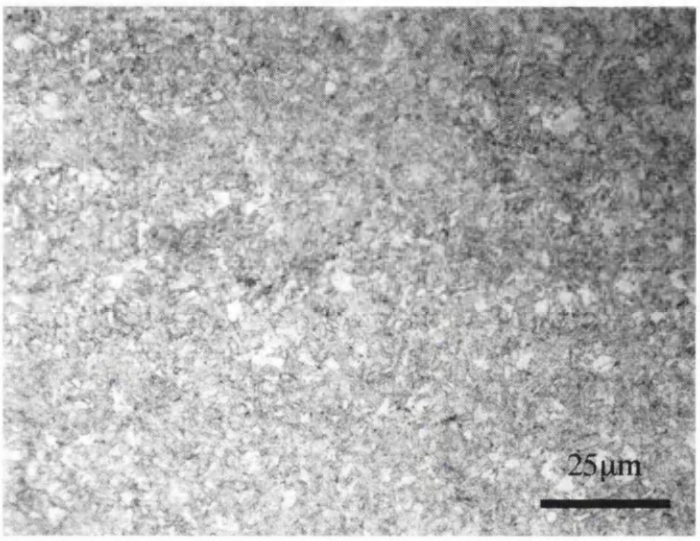

(e)

Figure 6.5. Micrographs of a 5√t spot weld made in alloy DP1000 (CE - 0.24): (d) the variation in microstructure from the edge of the nugget through to the parent material; (e) heat-affected zone microstructure.

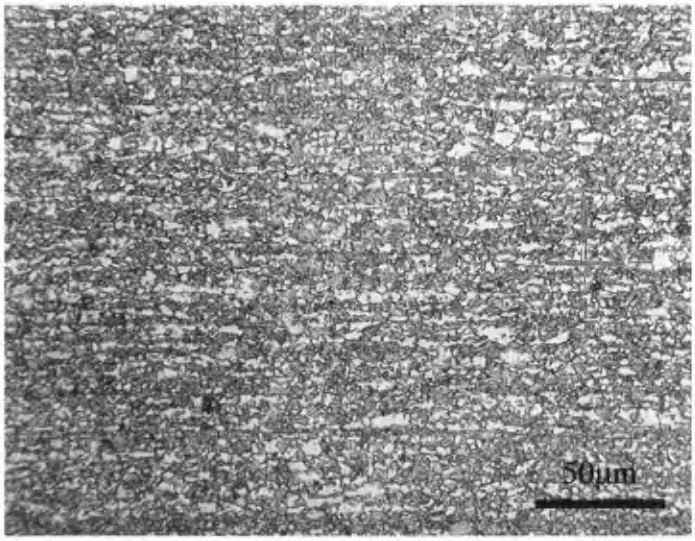

(a)

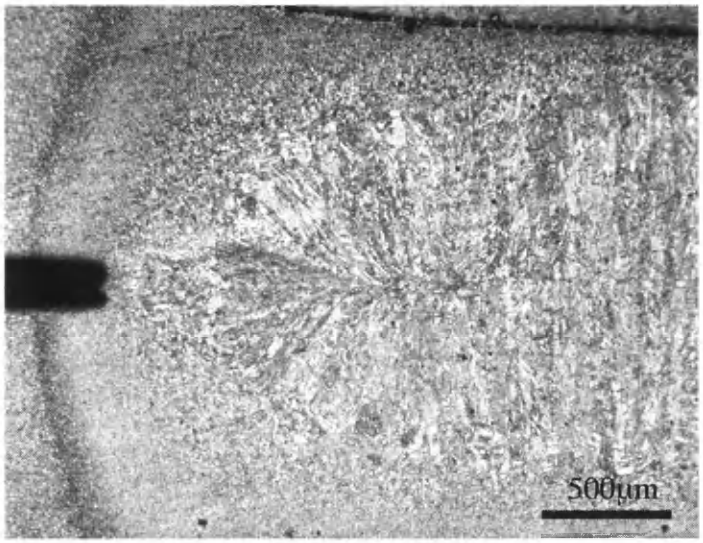

(b)

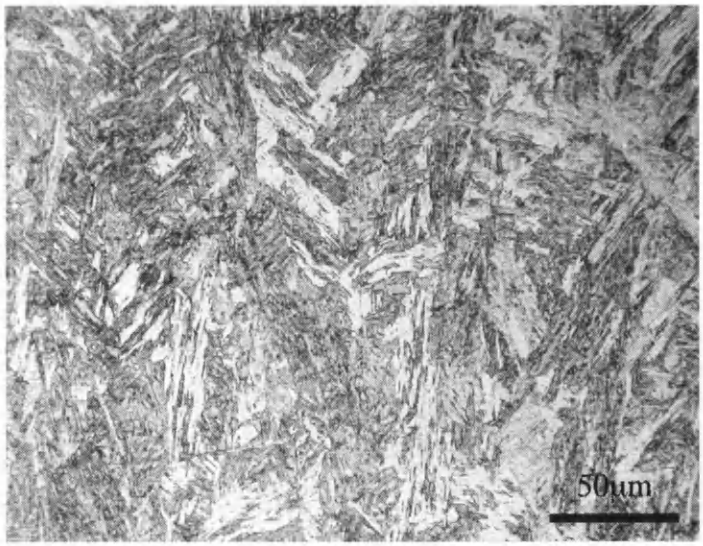

(c)

Figure 6.6. Micrographs of a 5√t spot weld made in alloy DP1400 (CE - 0.27): (a) parent microstructure; (b) macro showing shape of weld and heat-affected zone; (c) columnar grains in the weld nugget.

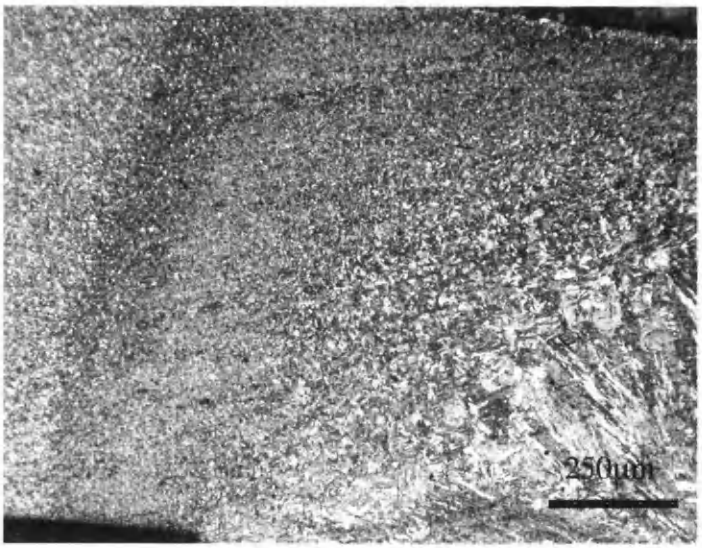

(d)

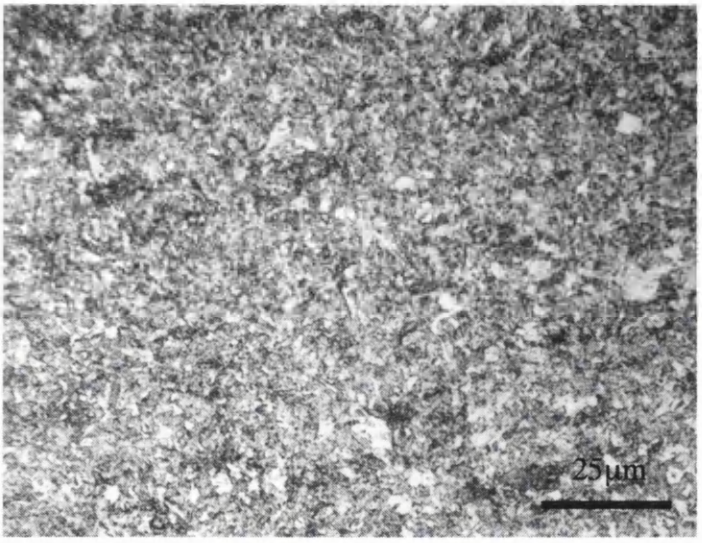

(e)

Figure 6.6. Micrographs of a 5√t spot weld made in alloy DP1400 (CE - 0.27): (d) the variation in microstructure from the edge of the nugget through to the parent material; (e) heat-affected zone microstructure.

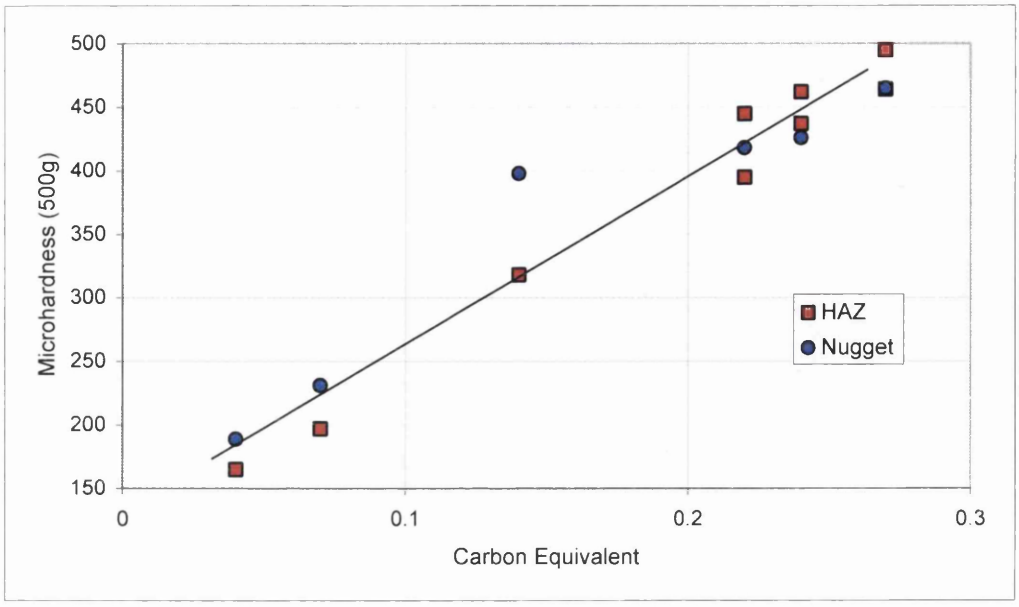

Figure 6.7. The relationship between the carbon equivalent of a steel grade and the microhardness of the nugget and heat affect zone in a 5√t resistance spot weld.

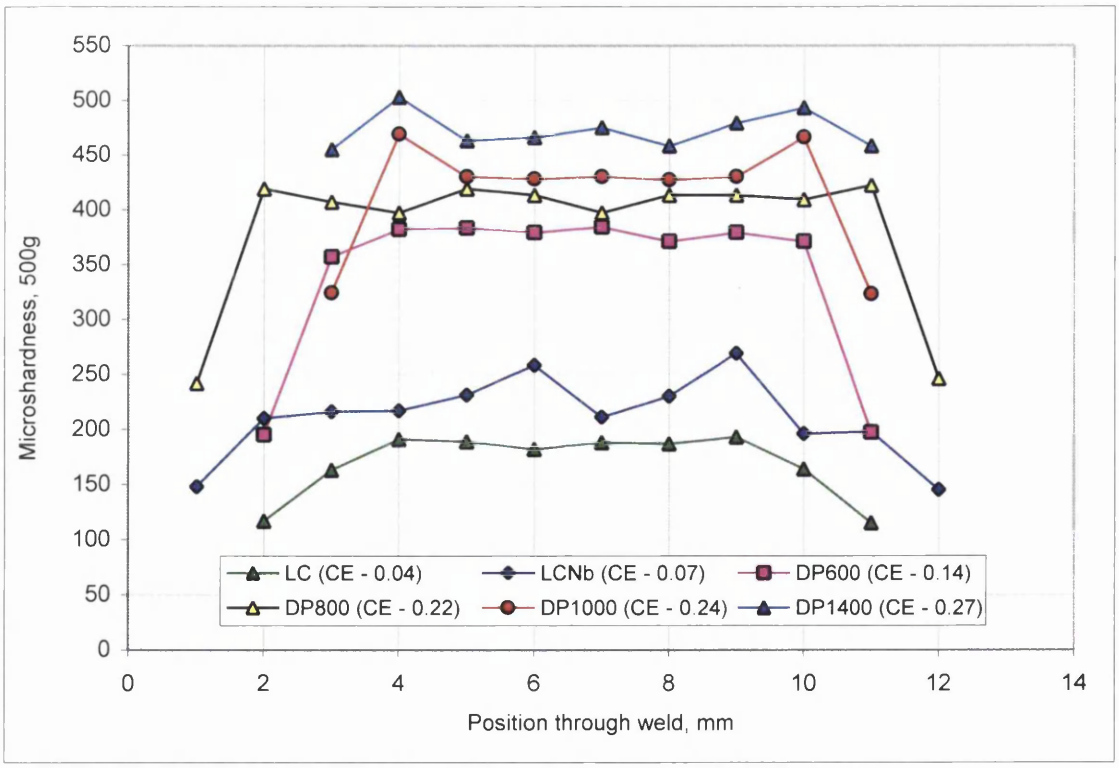

Figure 6.8. Microhardness profiles across 5√t welds made in each of the six steels in this investigation.

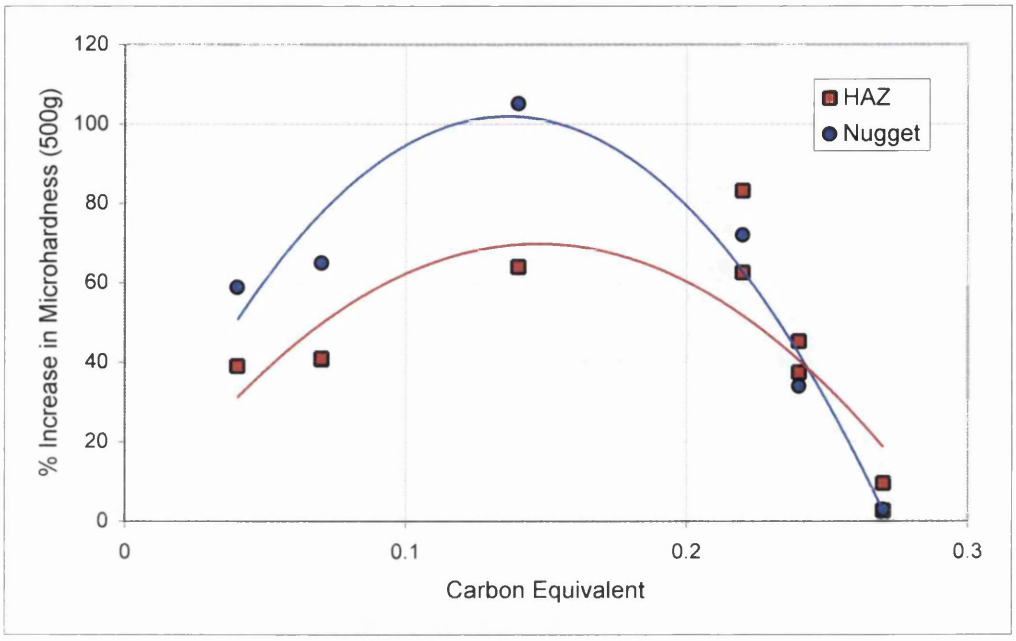

Figure 6.9. The relationship between the % increase in microhardness for the nugget and heat affected zone and the carbon equivalent.

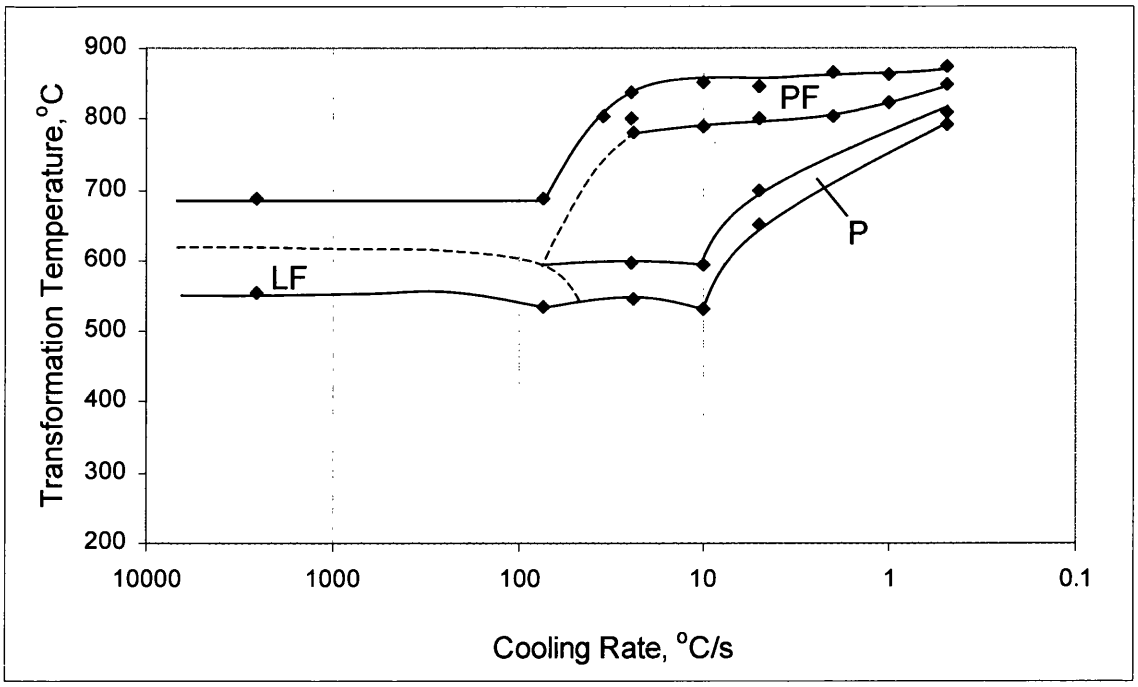

Figure 6.10. Continuous cooling transformation curve for steel grade: LC (CE – 0.04)

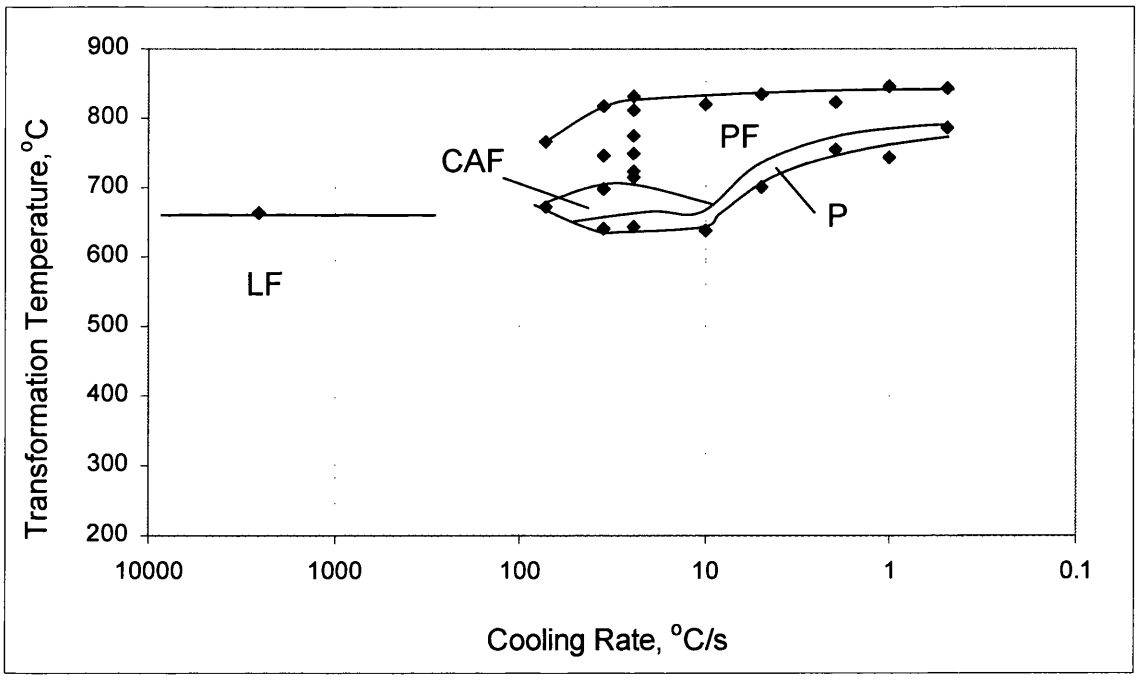

Figure 6.11. Continuous cooling transformation curve for steel grade: LCNb (CE – 0.07)

Key to all Figures:

PF – Polygonal Ferrite;	P – Pearlite;
CAF – Coarse Acicular Ferrite;	LF – Lath Ferrite;
B – Bainite;	M – Martensite.

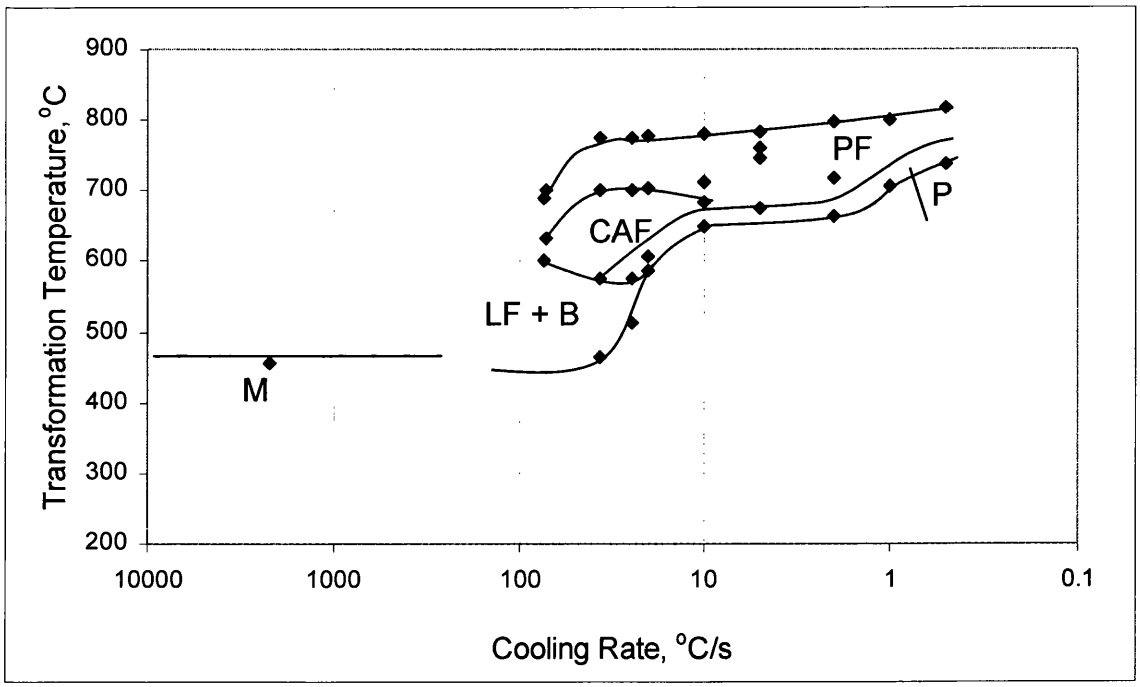

Figure 6.12. Continuous cooling transformation curve for steel grade: DP600 (CE – 0.14)

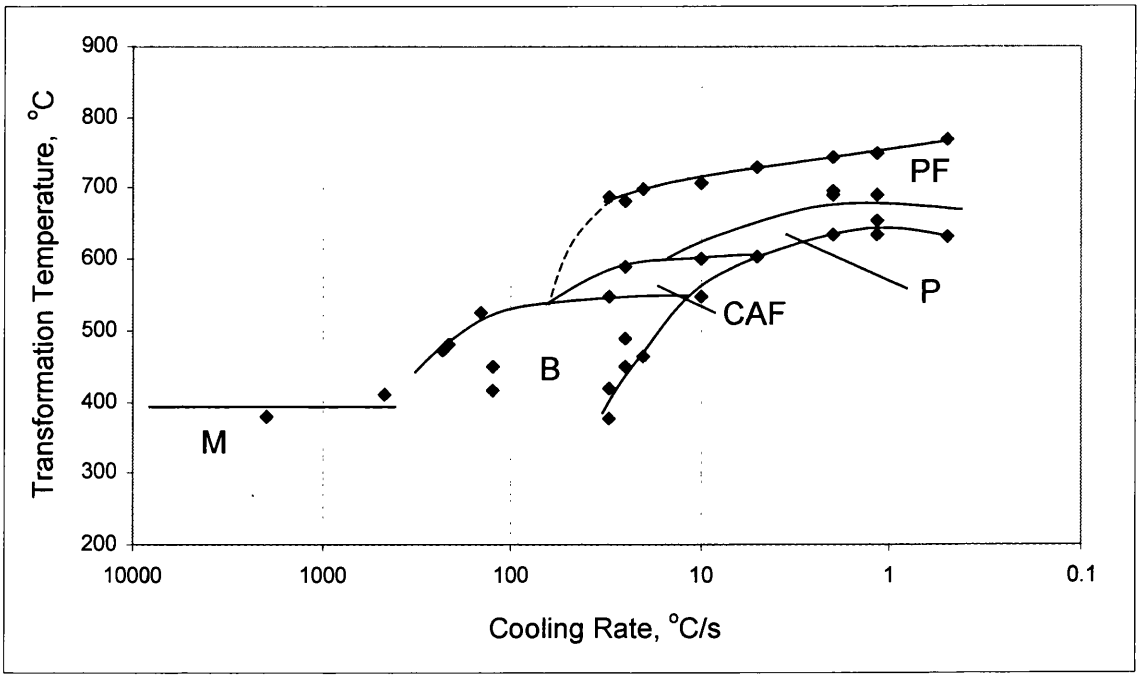

Figure 6.13. Continuous cooling transformation curve for steel grade: DP800 (CE – 0.22)

Key to all Figures:

PF – Polygonal Ferrite;
CAF – Coarse Acicular Ferrite;
B – Bainite;
P – Pearlite;
LF – Lath Ferrite;
M – Martensite.

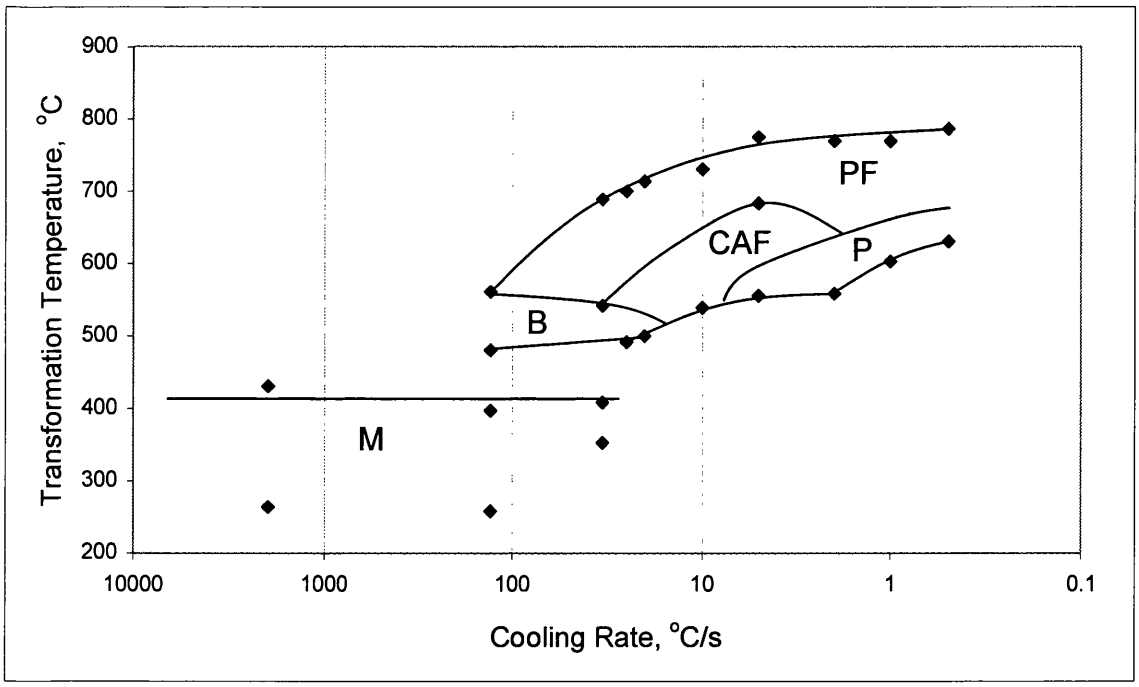

Figure 6.14. Continuous cooling transformation curve for steel grade: DP1000 (CE – 0.24)

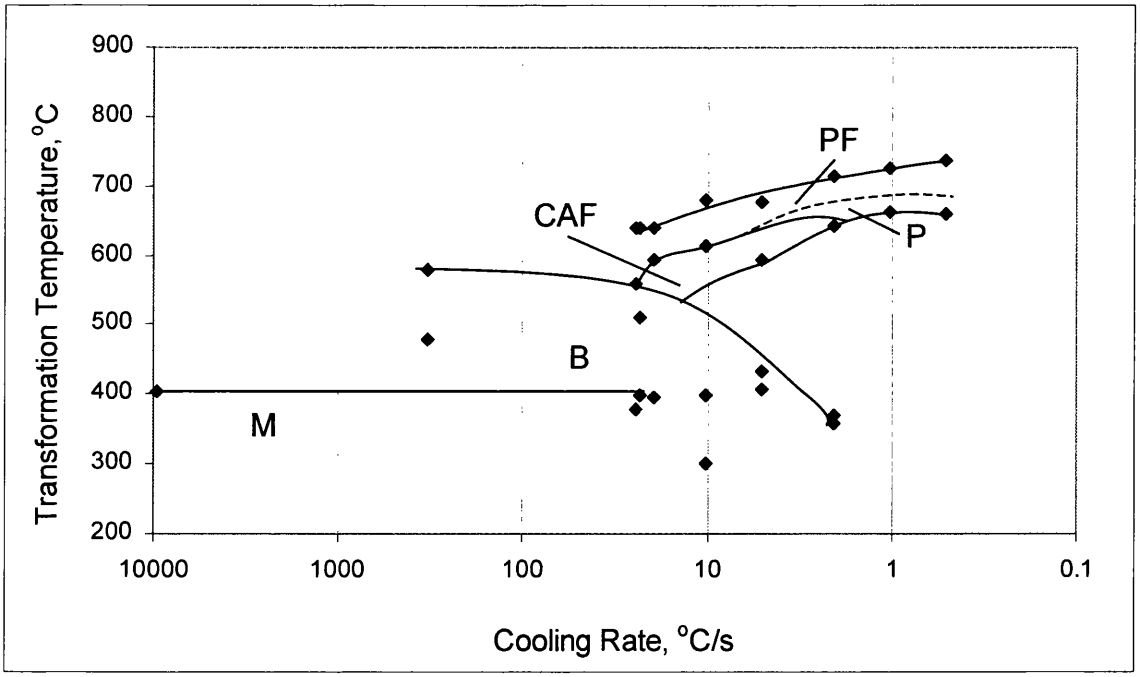

Figure 6.15. Continuous cooling transformation curve for steel grade: DP1400 (CE – 0.27)

Key to all Figures:

PF – Polygonal Ferrite;	P – Pearlite;
CAF – Coarse Acicular Ferrite;	LF – Lath Ferrite;
B – Bainite;	M – Martensite.

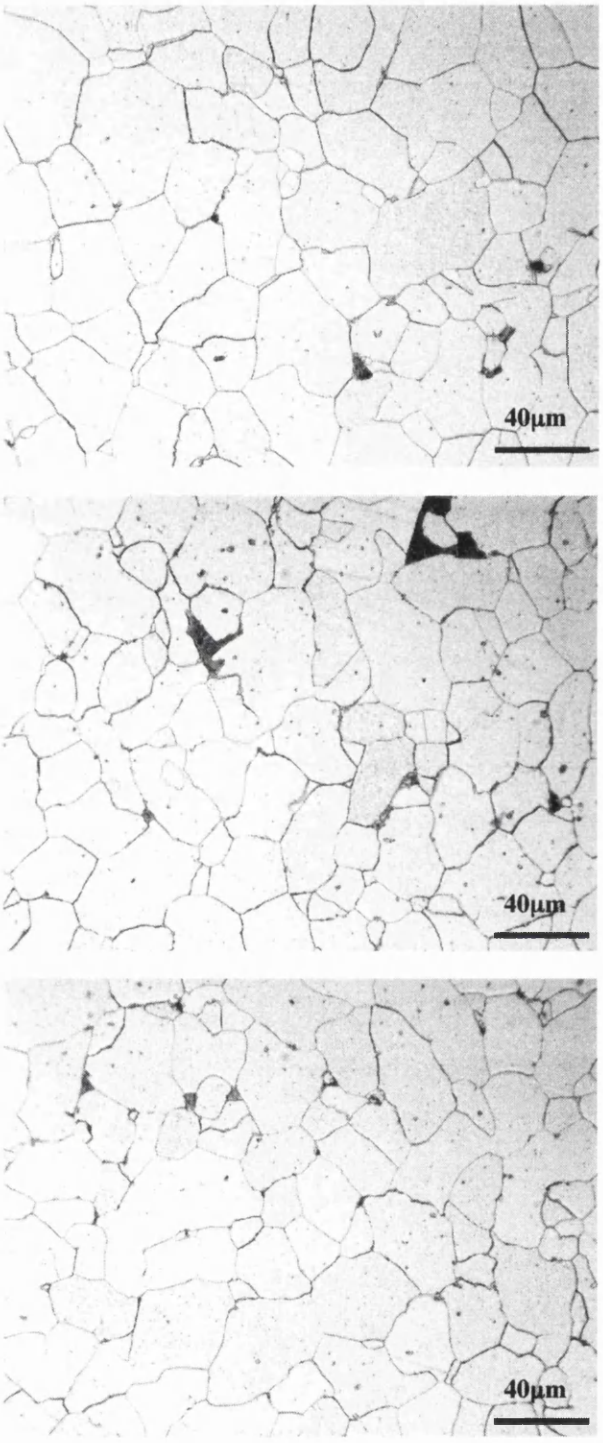

(a)

98.5% ferrite
1.5% pearlite

(b)

98.7% ferrite
1.3% pearlite

(c)

98.7% ferrite
1.3% pearlite

Figure 6.16. Typical micrographs from alloy LC (CE – 0.04) after normalizing and cooling using a Gleeble 1500. Cooling rate: (a) 0.5°C/s; (b) 1.0°C/s; (c) 2.0°C/s.

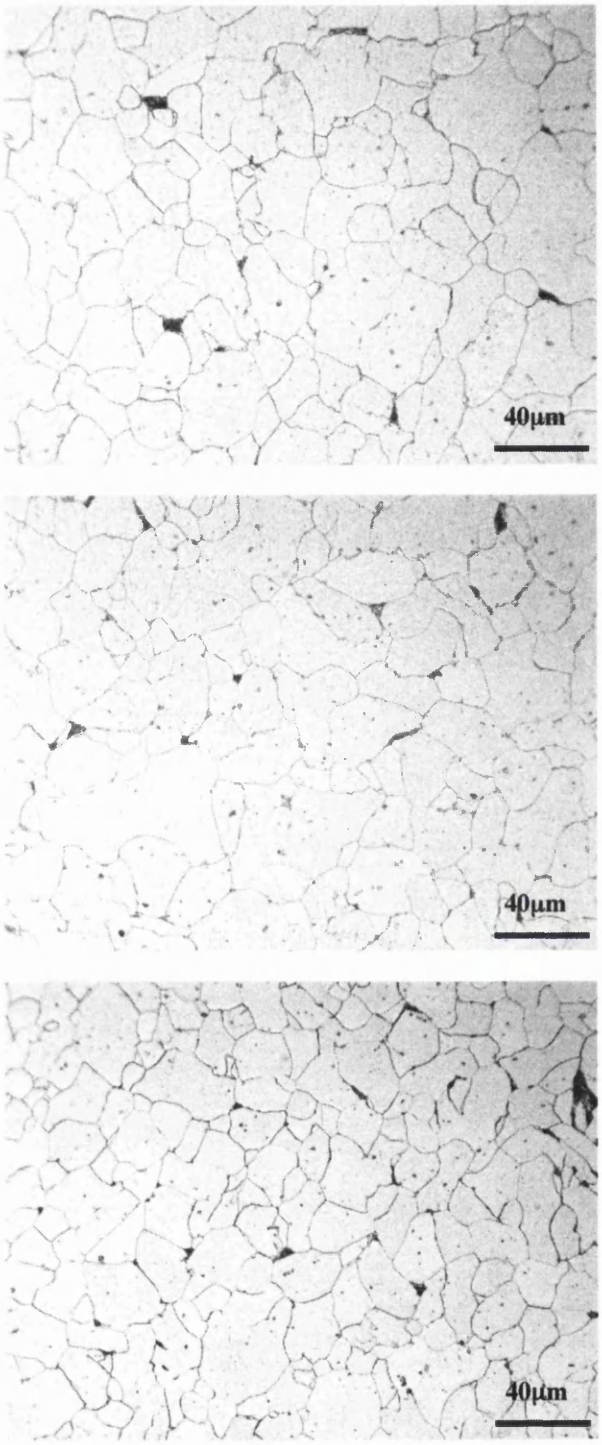

(d)

98.4% ferrite
1.6% pearlite

(e)

98.8% ferrite
1.2% pearlite

(f)

98.9% ferrite
1.1% pearlite

Figure 6.16. Typical micrographs from alloy LC (CE – 0.04) after normalizing and cooling using a Gleeble 1500. Cooling rate: (d) 5.1°C/s; (e) 10.5°C/s; (f) 23.4°C/s.

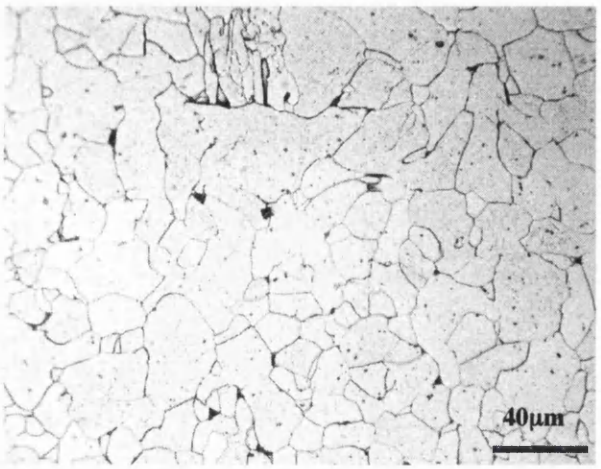

(g)

98.8% ferrite
1.2% pearlite

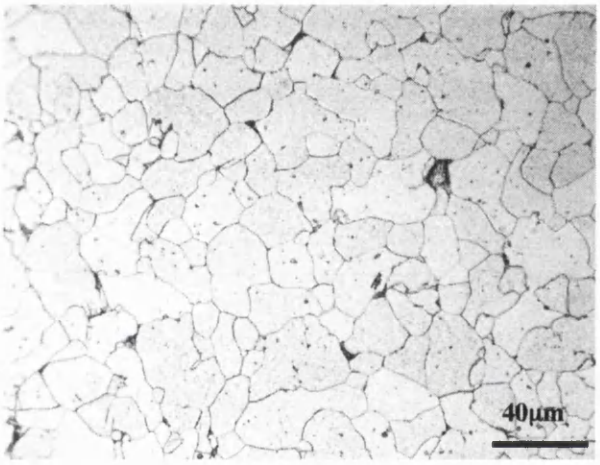

(h)

98.7% ferrite
1.3% pearlite

(i)

80.2% ferrite
29.8% lath ferrite

Figure 6.16. Typical micrographs from alloy LC (CE – 0.04) after normalizing and cooling using a Gleeble 1500. Cooling rate: (g) 26.7°C/s; (h) 26.6°C/s; (i) 392°C/s.

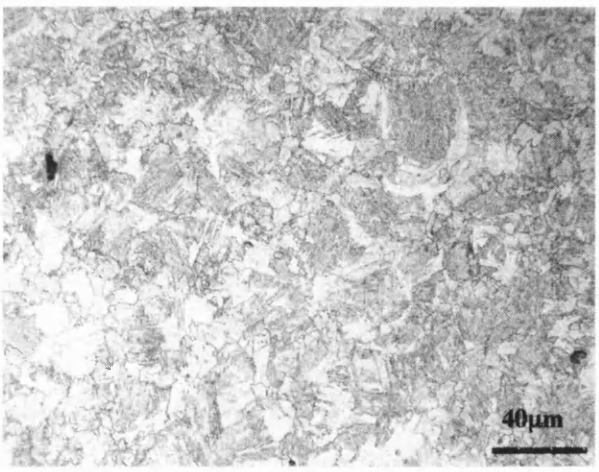

(j)

35.8% ferrite
64.2% lath ferrite

Figure 6.16. Typical micrographs from alloy LC (CE – 0.04) after normalizing and cooling using a Gleeble 1500. Cooling rate: (j) 3058°C/s.

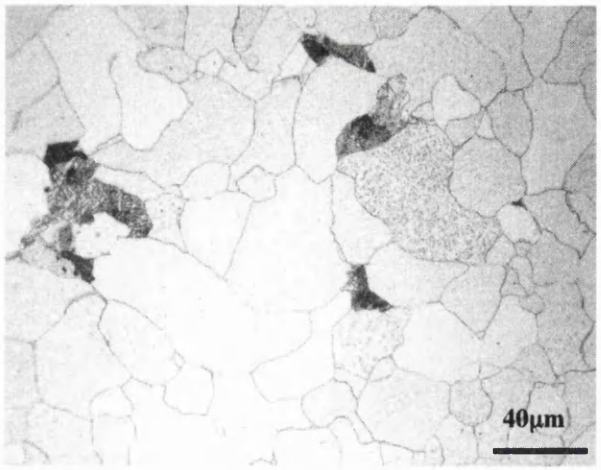

(a)

95.5% ferrite
4.5% pearlite

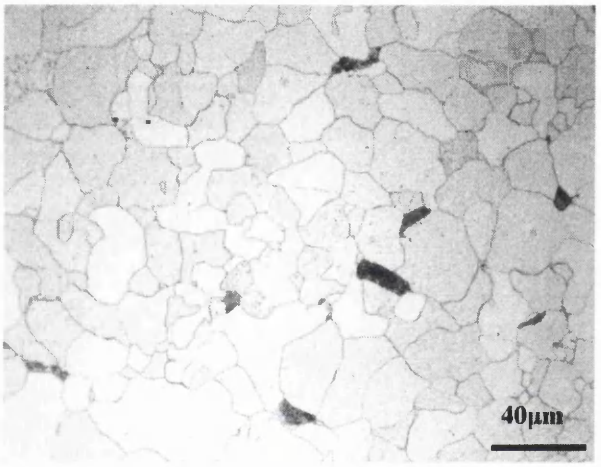

(b)

96.7% ferrite
3.3% pearlite

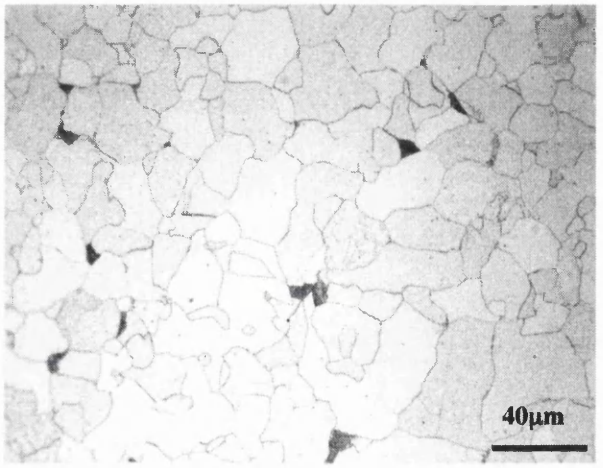

(c)

95.6% ferrite
4.4% pearlite

Figure 6.17. Typical micrographs from alloy LCNb (CE – 0.07) after normalizing and cooling using a Gleeble 3500. Cooling rate: (a) 0.5°C/s; (b) 1.0°C/s; (c) 2.0°C/s.

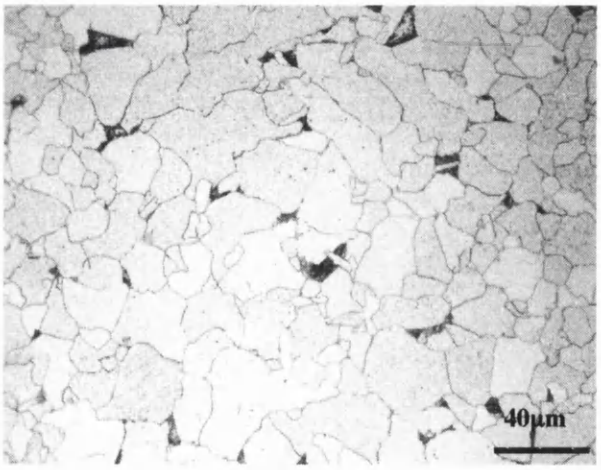

(d)

96.5% ferrite
3.5% pearlite

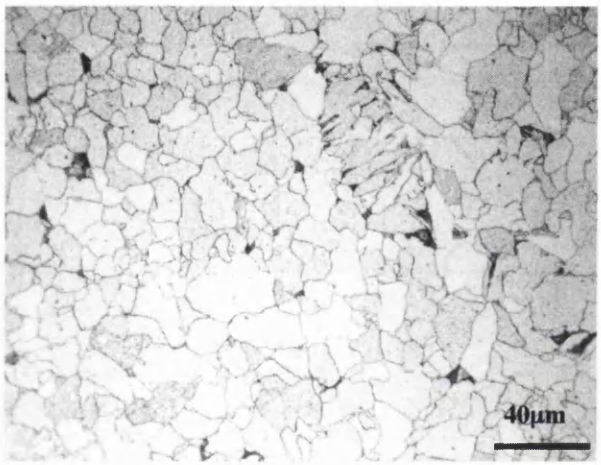

(e)

91.9% ferrite
4.5% pearlite
3.6% coarse acicular ferrite

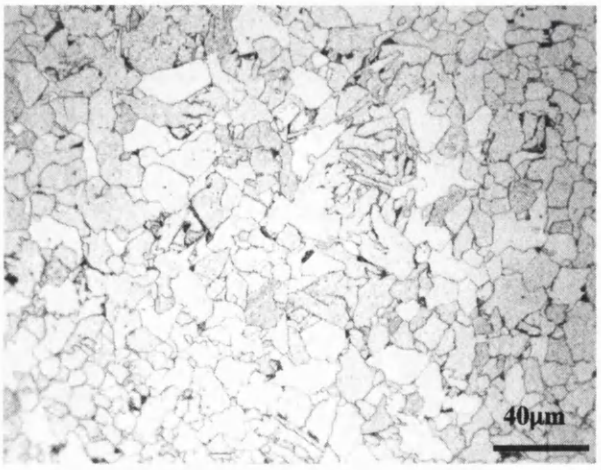

(f)

84.8% ferrite
2.5% pearlite
12.7% coarse acicular ferrite

Figure 6.17. Typical micrographs from alloy LCNb (CE – 0.07) after normalizing and cooling using a Gleeble 3500. Cooling rate: (d) 5.1°C/s; (e) 10.5°C/s; (f) 24.5°C/s.

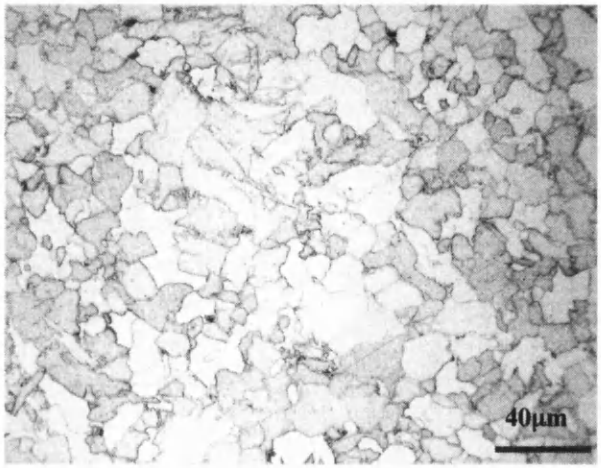

(g)

79.0% ferrite
2.5% pearlite
18.5% coarse acicular ferrite

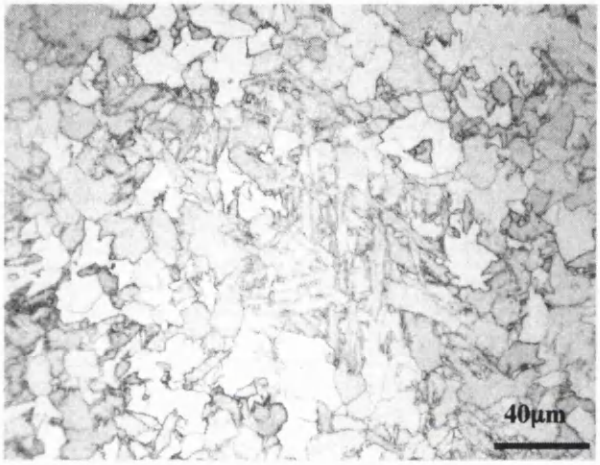

(h)

68.5% ferrite
31.5% coarse acicular ferrite

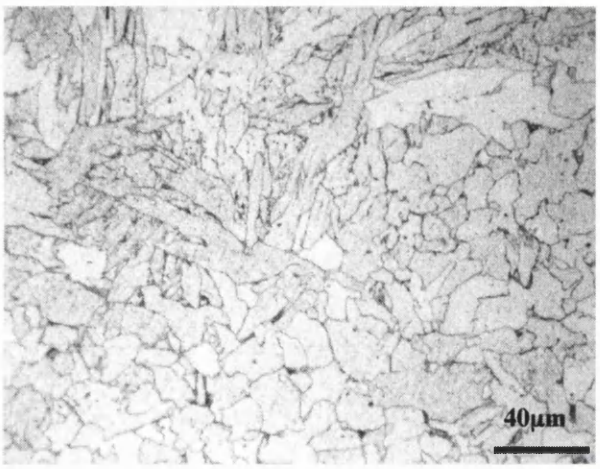

(i)

59.6% ferrite
40.4% coarse acicular ferrite

Figure 6.17. Typical micrographs from alloy LCNb (CE – 0.07) after normalizing and cooling using a Gleeble 3500. Cooling rate: (g) 24.3°C/s; (h) 35.3°C/s; (i) 73°C/s.

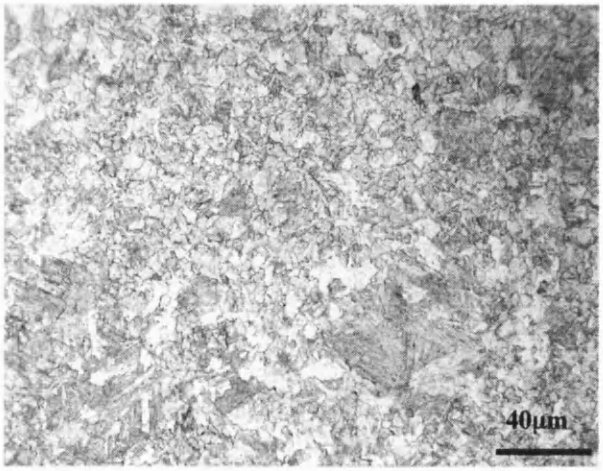

(j)

37.3% ferrite
62.7% lath ferrite

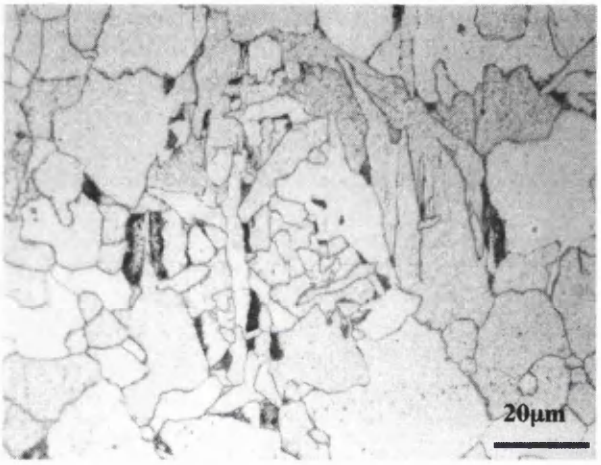

(k)

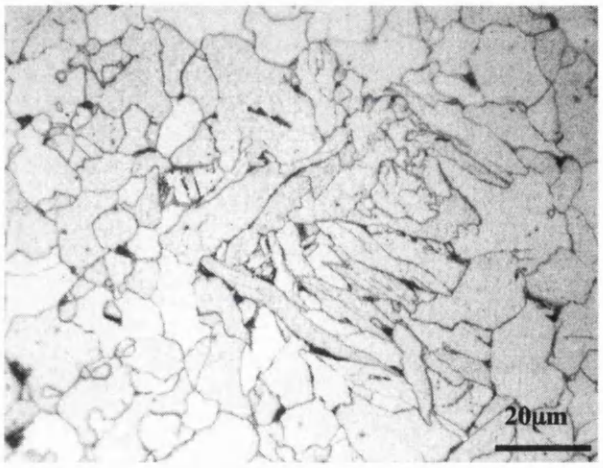

(l)

Figure 6.17. Typical micrographs from alloy LCNb (CE – 0.07) after normalizing and cooling using a Gleeble 3500. Cooling rate: (j) 2575°C/s.
Detailed micrographs of constituent termed coarse acicular ferrite. Cooling rate: (k) 10°C/s; (l) 24.5°C/s.

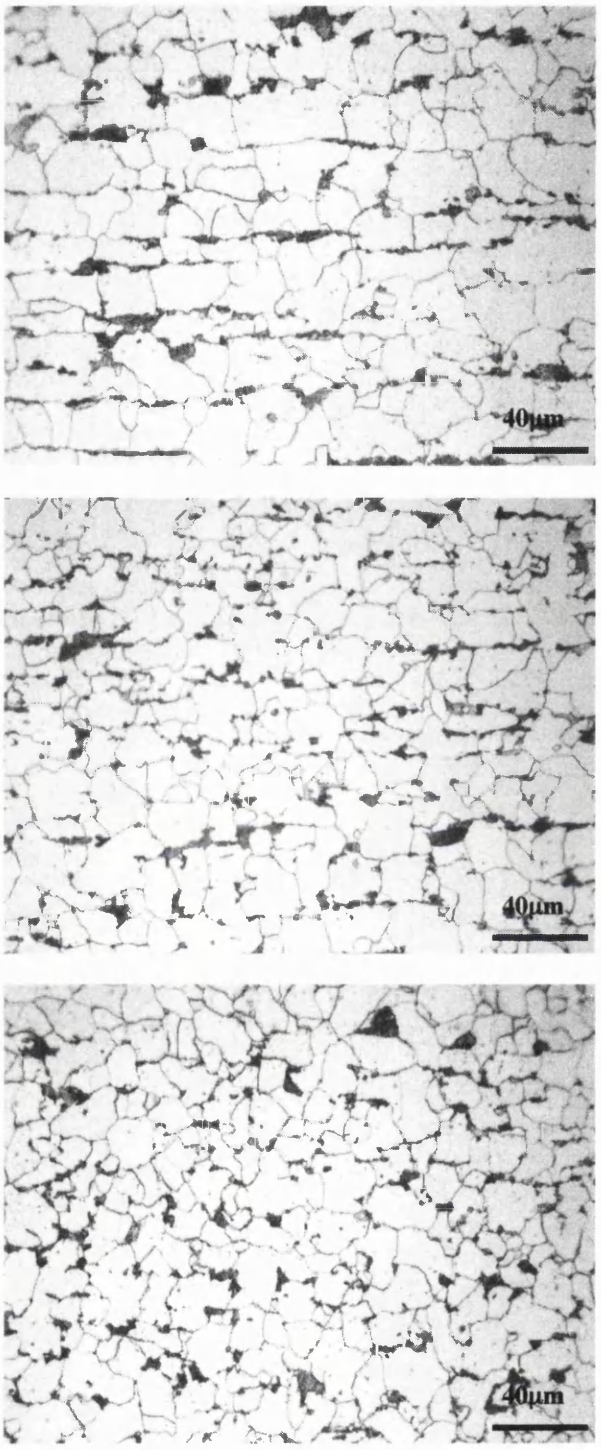

(a)

83.8% ferrite
16.2% pearlite

(b)

83.5% ferrite
16.5% pearlite

(c)

77.1% ferrite
22.9% pearlite

Figure 6.18. Typical micrographs from alloy DP600 (CE – 0.14) after normalizing and cooling using a Gleeble 3500. Cooling rate: (a) 0.5°C/s; (b) 1.0°C/s; (c) 2.0°C/s.

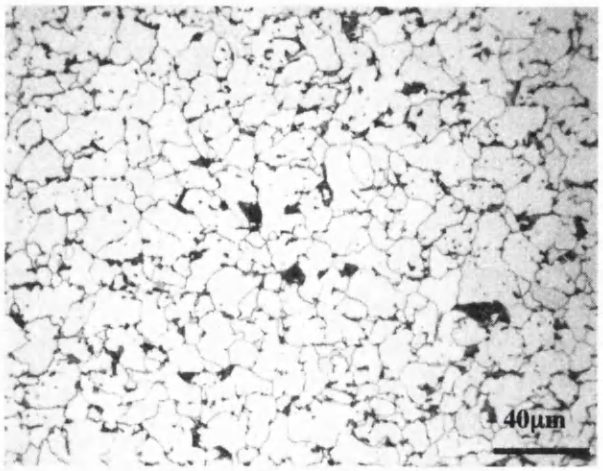

(d)

77.6% ferrite
22.4% pearlite

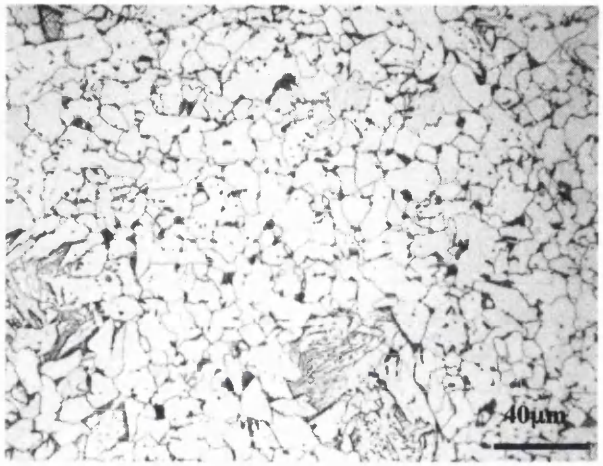

(e)

79.1% ferrite
9.9% pearlite
1.0% coarse acicular ferrite

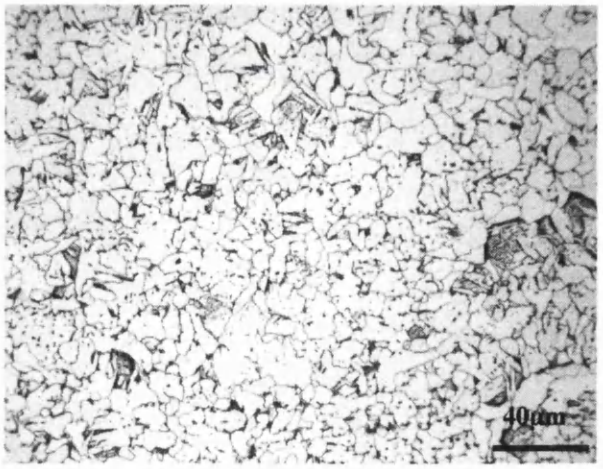

(f)

70.5% ferrite
15.9% pearlite
13.6% coarse acicular ferrite

Figure 6.18. Typical micrographs from alloy DP600 (CE – 0.14) after normalizing and cooling using a Gleeble 3500. Cooling rate: (d) 5°C/s; (e) 10°C/s; (f) 20.1°C/s.

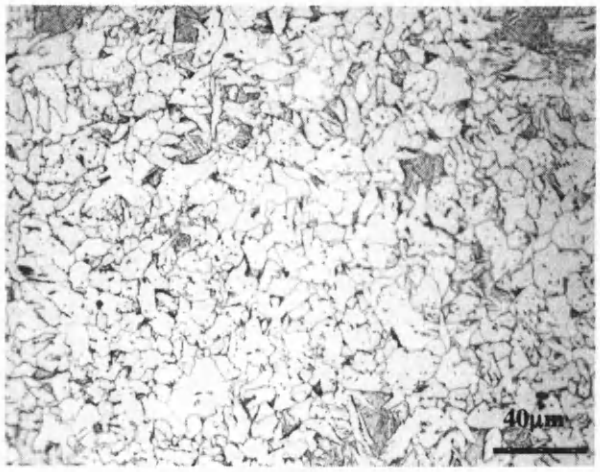

(g)

53.3% ferrite
6.9% pearlite
39.8% coarse acicular ferrite
+ bainite

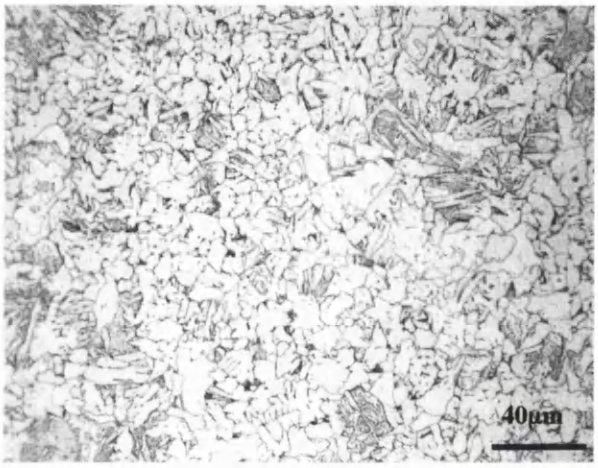

(h)

44.5% ferrite
3.8% pearlite
51.7% coarse acicular ferrite
+ bainite

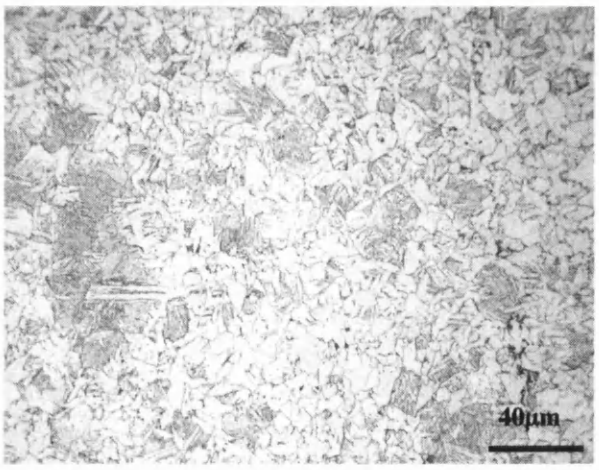

(i)

30.2% ferrite
69.8% coarse acicular ferrite
+ bainite

Figure 6.18. Typical micrographs from alloy DP600 (CE – 0.14) after normalizing and cooling using a Gleeble 3500. Cooling rate: (g) 24.9°C/s; (h) 36.3°C/s; (i) 72°C/s.

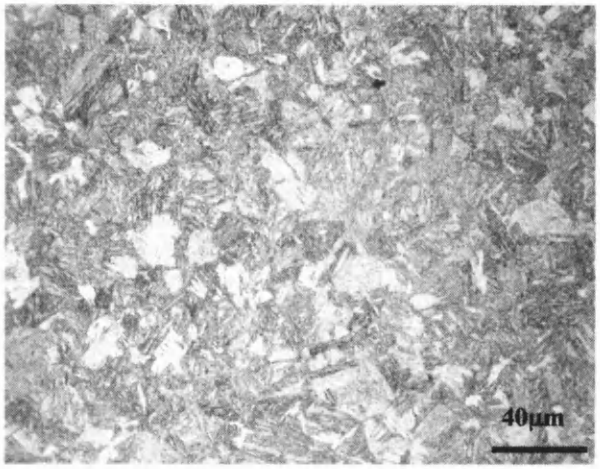

(j)

37.3% ferrite
62.7% lath ferrite

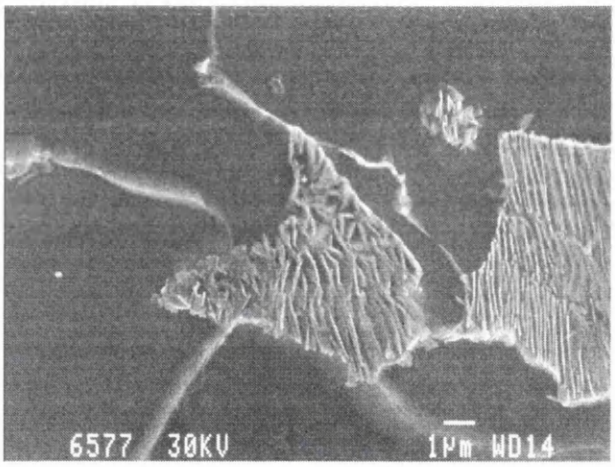

(k)

Figure 6.18. Typical micrographs from alloy DP600 (CE – 0.14) after normalizing and cooling using a Gleeble 3500. Cooling rate: (j) 2206°C/s.

Scanning electron micrograph of typical area of pearlite seen in slower cooled samples. Cooling rate: (k) 1°C/s.

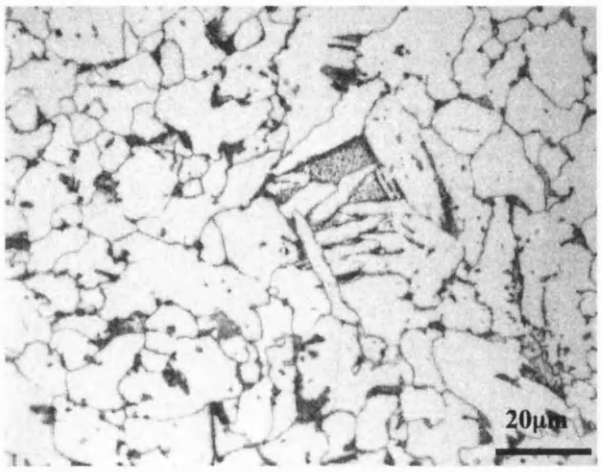

(l)

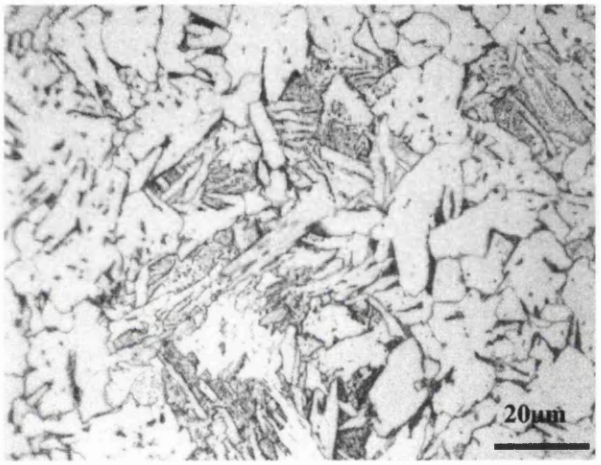

(m)

Figure 6.18. Detailed micrographs of alloy DP600 (CE – 0.14) after normalizing and cooling using a Gleeble 3500. Transformation constituents: (l) coarse acicular ferrite. Cooling rate: 10°C/s; (m) coarse acicular ferrite and bainite. Cooling rate: 24.9°C/s.

(a)

75.5% ferrite
25.5% pearlite

(b)

77.8% ferrite
22.2% pearlite

(c)

81.1% ferrite
18.9% pearlite

Figure 6.19. Typical micrographs from alloy DP800 (CE – 0.22) after normalizing and cooling using a Gleeble 3500. Cooling rate: (a) 0.5°C/s; (b) 1.0°C/s; (c) 2.0°C/s.

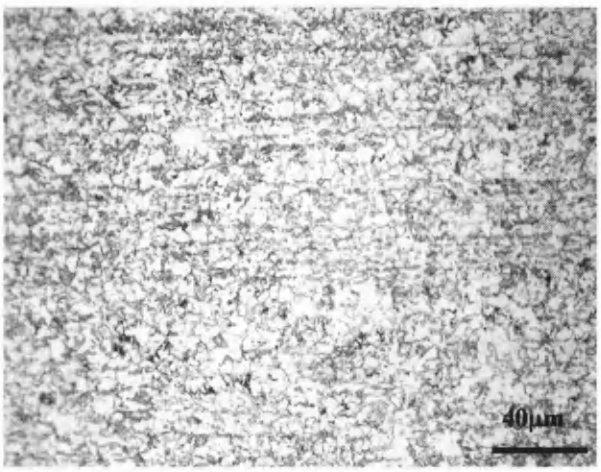

(d)

69.0% ferrite
17.3% pearlite
13.7% coarse acicular ferrite

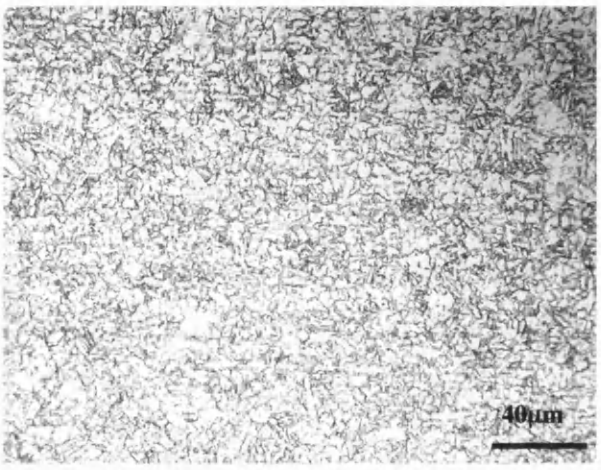

(e)

58.0% ferrite
11.2% pearlite
40.8% coarse acicular ferrite

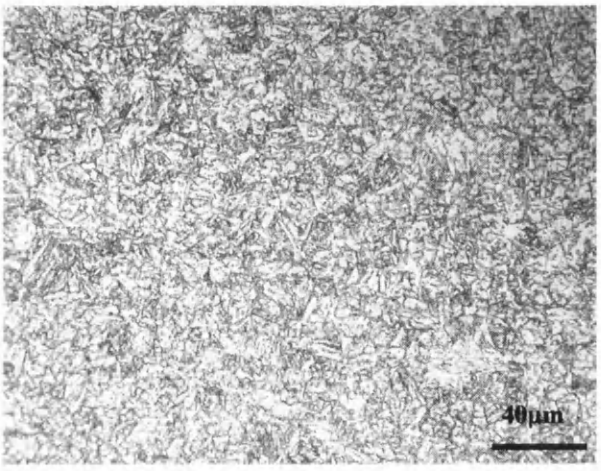

(f)

43.1% ferrite
56.9% coarse acicular ferrite
+ bainite

Figure 6.19. Typical micrographs from alloy DP800 (CE – 0.22) after normalizing and cooling using a Gleeble 3500. Cooling rate: (d) 5°C/s; (e) 10°C/s; (f) 20°C/s.

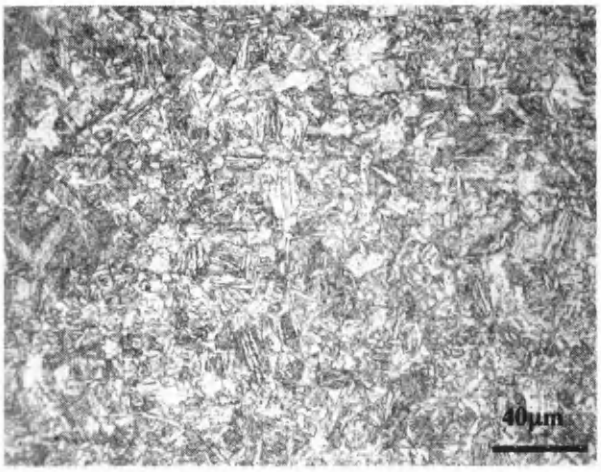

(g)

37.5% ferrite
62.5% 'needle ferrite' + bainite

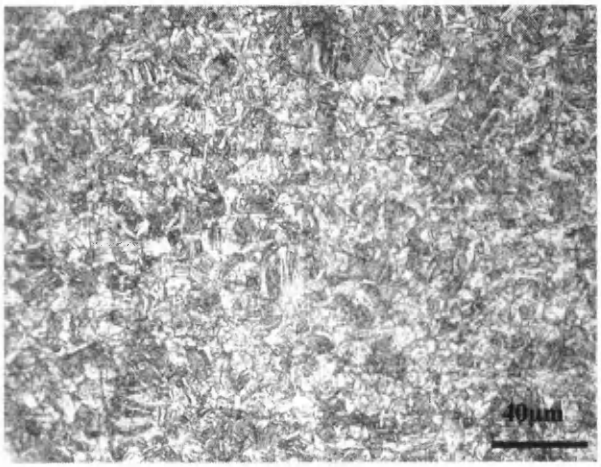

(h)

27.8% ferrite
58.2% 'needle ferrite' + bainite
14.0% martensite

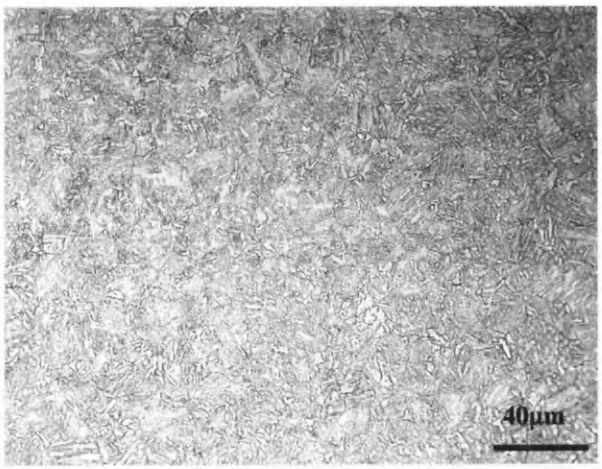

(i)

100% bainite + martensite

Figure 6.19. Typical micrographs from alloy DP800 (CE – 0.22) after normalizing and cooling using a Gleeble 3500. Cooling rate: (g) 25°C/s; (h) 35.7°C/s; (i) 119°C/s.

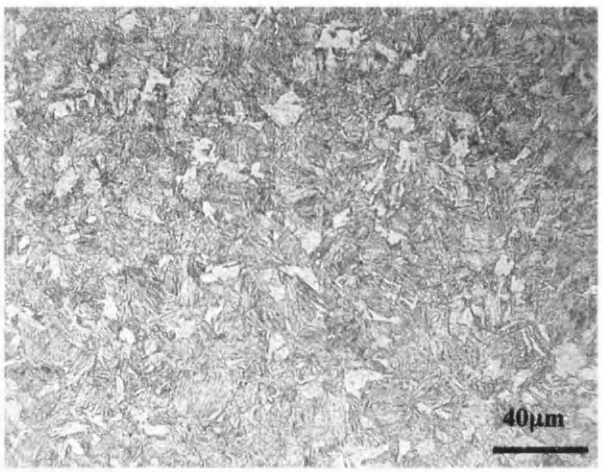

(j)

100% martensite

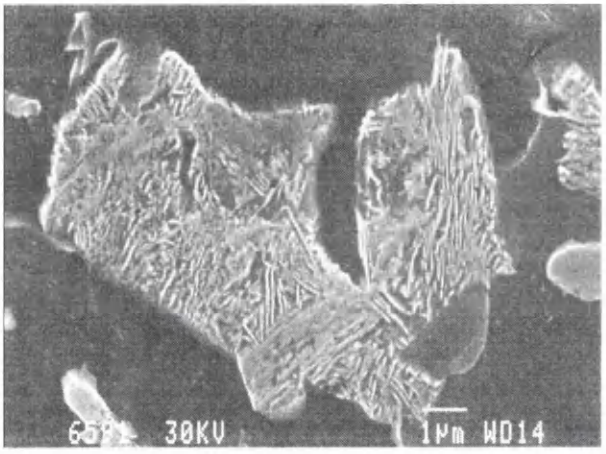

(k)

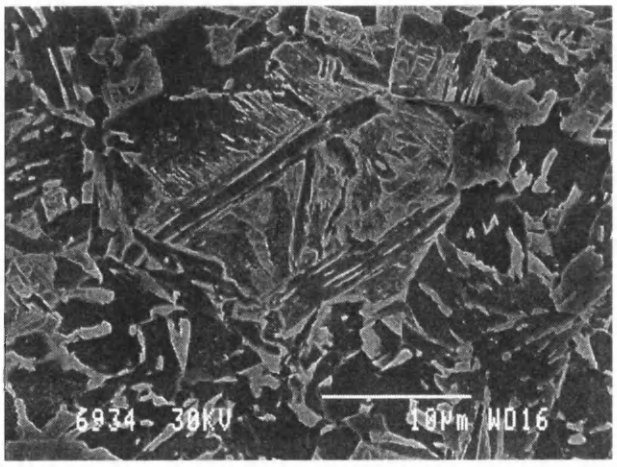

(l)

Figure 6.19. Typical micrographs from alloy DP800 (CE – 0.22) after normalizing and cooling using a Gleeble 3500. Cooling rate: (j) 1978°C/s.

Scanning electron micrographs of: (k) typical area of pearlite found in slower cooled samples. Cooling rate: 1°C/s; (l) detail of the needles seen in the darker areas of the micrograph in Figure 6.19(g).

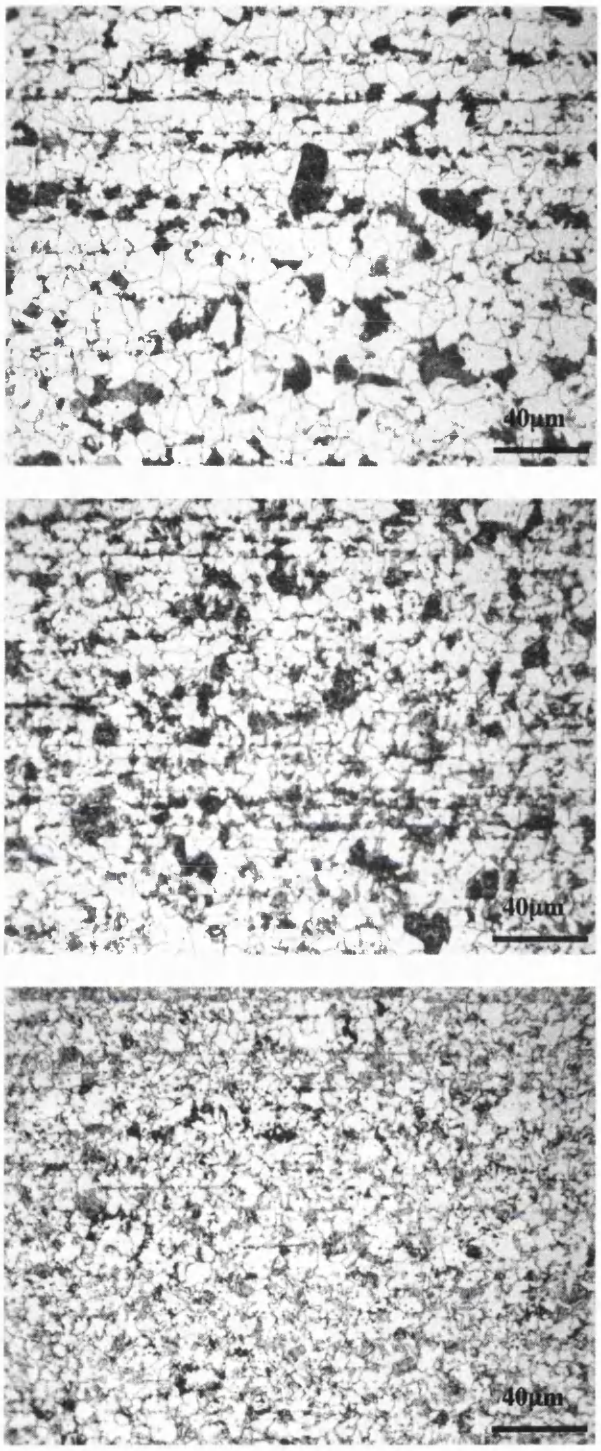

(a)

63.8% ferrite
36.2% pearlite

(b)

63.4% ferrite
36.6% pearlite

(c)

51.4% ferrite
20.0% pearlite
28.6% coarse acicular ferrite

Figure 6.20. Typical micrographs from alloy DP1000 (CE – 0.24) after normalizing and cooling using a Gleeble 3500. Cooling rate: (a) 0.5°C/s; (b) 1.0°C/s; (c) 2.0°C/s.

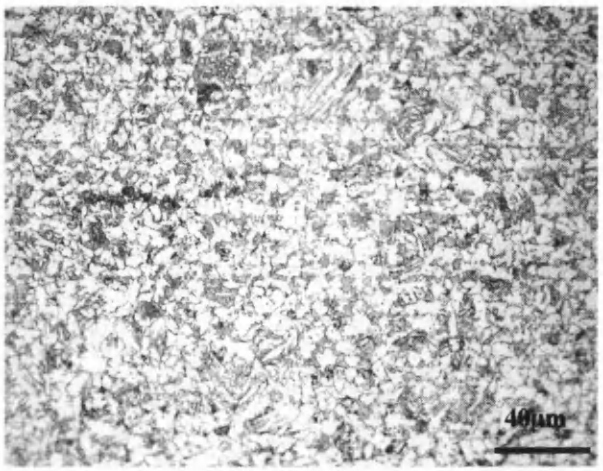

(d)

47.2% ferrite
5.5% pearlite
47.3% coarse acicular ferrite
+ bainite

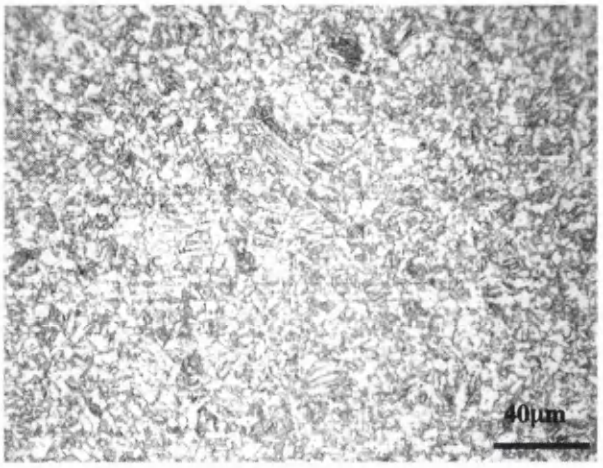

(e)

47.3% ferrite
52.7% coarse acicular ferrite
+ bainite

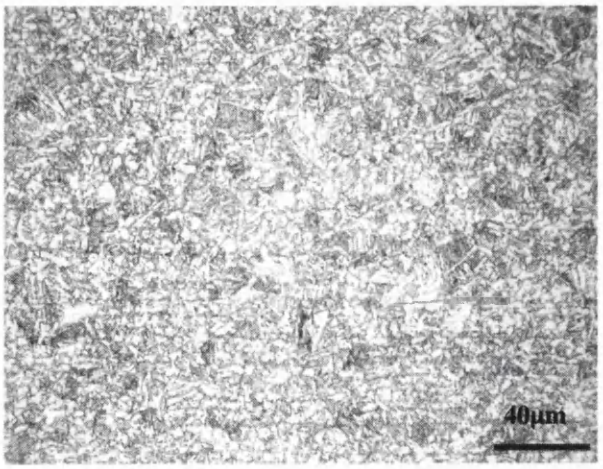

(f)

25.9% ferrite
74.1% coarse acicular ferrite
+ bainite

Figure 6.20. Typical micrographs from alloy DP1000 (CE – 0.24) after normalizing and cooling using a Gleeble 3500. Cooling rate: (d) 5°C/s; (e) 10°C/s; (f) 20°C/s.

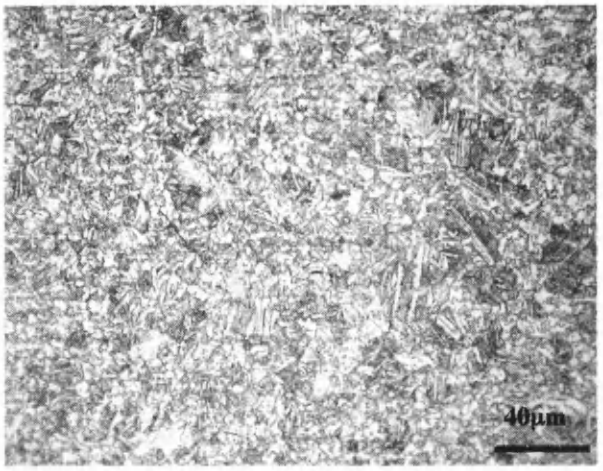

(g)

22.3% ferrite
61.8% coarse acicular ferrite
+ bainite
15.9% martensite

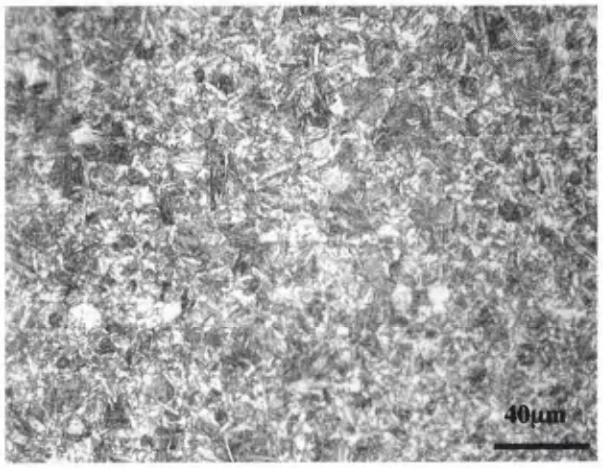

(h)

6.3% ferrite
65.1% coarse acicular ferrite
+ bainite
28.6% martensite

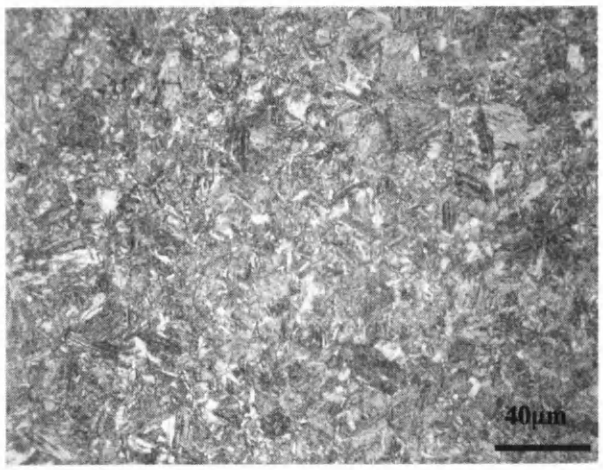

(i)

100% bainite and martensite

Figure 6.20. Typical micrographs from alloy DP1000 (CE – 0.24) after normalizing and cooling using a Gleeble 3500. Cooling rate: (g) 24.9°C/s; (h) 33.8°C/s; (i) 133°C/s.

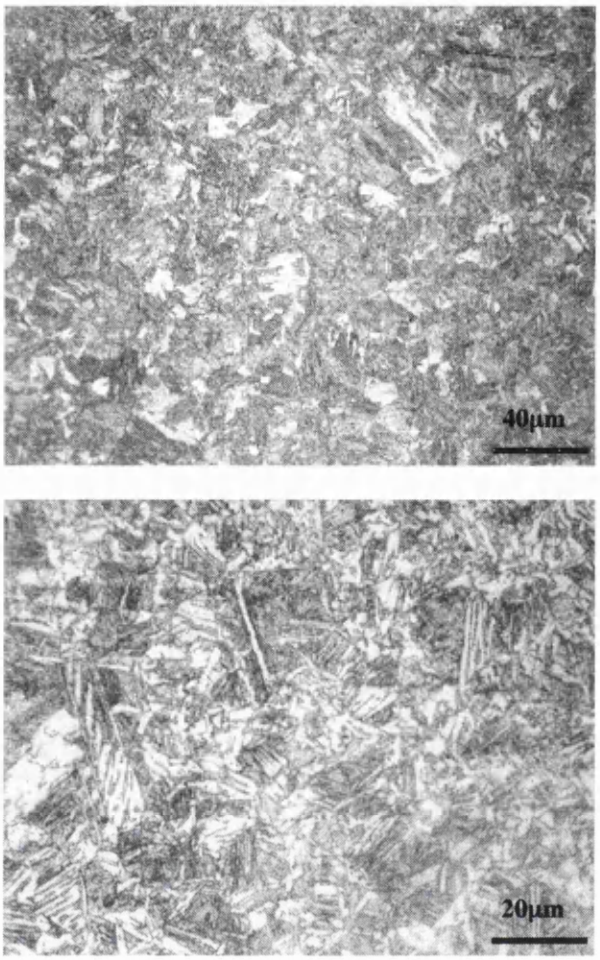

(j)

100% martensite

(k)

Figure 6.20. Typical micrographs from alloy DP1000 (CE – 0.24) after normalizing and cooling using a Gleeble 3500. Cooling rate: (j) 1950°C/s.

(k) Detailed micrograph of transformation constituents termed coarse acicular ferrite, bainite and martensite. Cooling rate: 35°C/s.

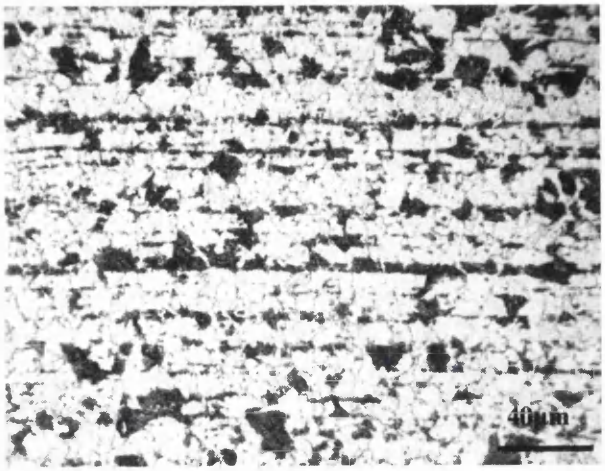

(a)

58.2% ferrite
42.8% pearlite

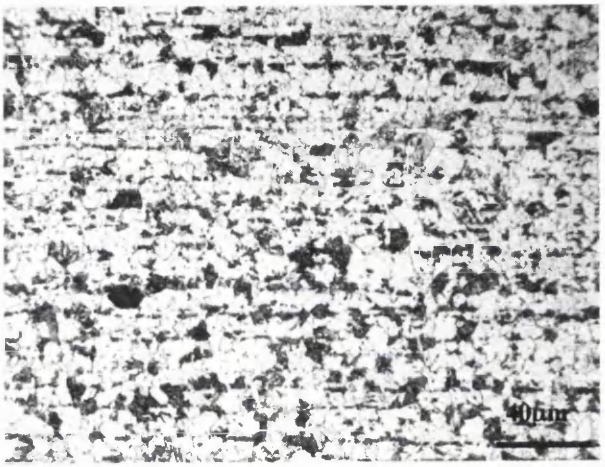

(b)

58.9% ferrite
42.1% pearlite

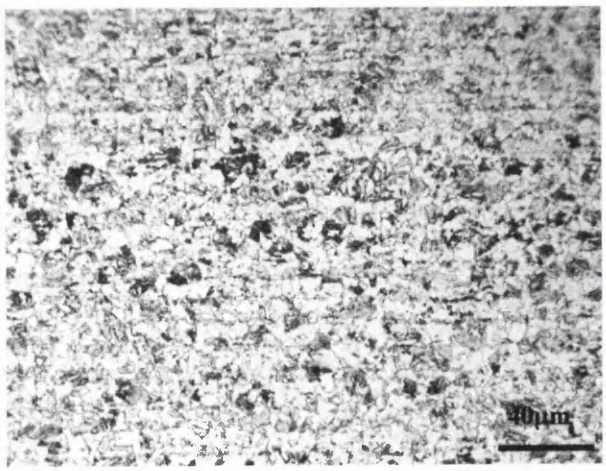

(c)

46.7% ferrite
18.9% pearlite
34.4% coarse acicular ferrite
+ bainite

Figure 6.21. Typical micrographs from alloy DP1400 (CE – 0.27) after normalizing and cooling using a Gleeble 1500. Cooling rate: (a) 0.5°C/s; (b) 1.0°C/s; (c) 2.0°C/s.

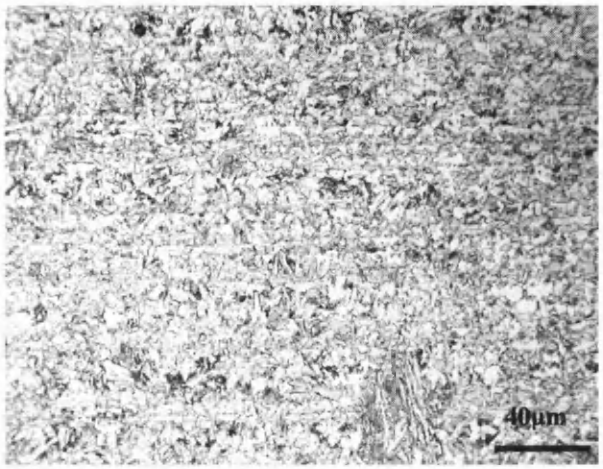

(d)

37.4% ferrite
5.2% pearlite
57.4% coarse acicular ferrite
+ bainite

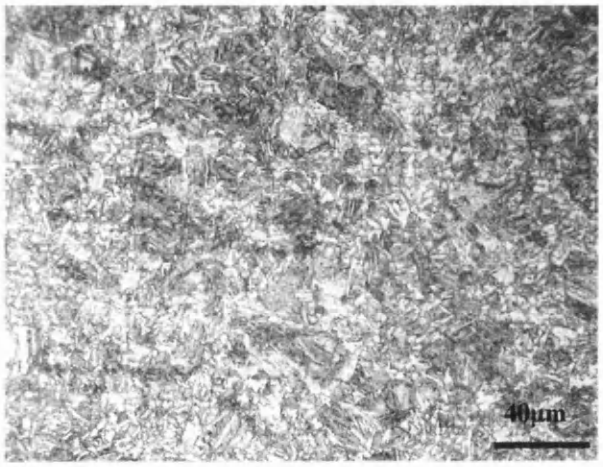

(e)

16.5% ferrite
83.5% coarse acicular ferrite
+ bainite

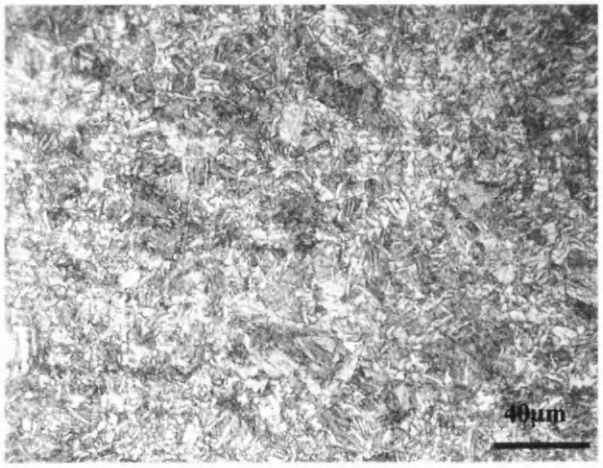

(f)

11.4% ferrite
71.2% coarse acicular ferrite
+ bainite
17.4% martensite

Figure 6.21. Typical micrographs from alloy DP1400 (CE – 0.27) after normalizing and cooling using a Gleeble 1500. Cooling rate: (d) 5.1°C/s; (e) 10.1°C/s; (f) 19.5°C/s.

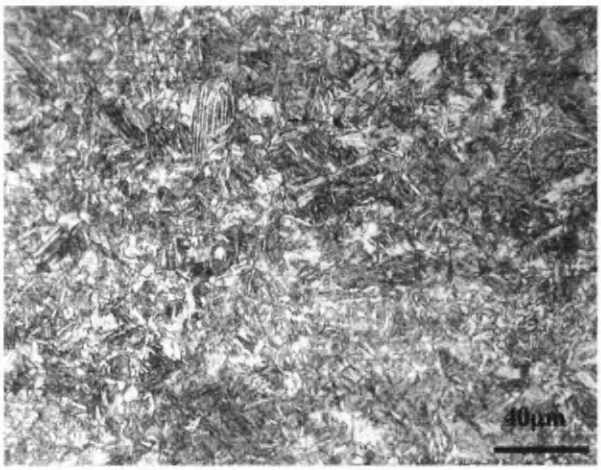

(g)

4.7% ferrite
95.3% bainite and martensite

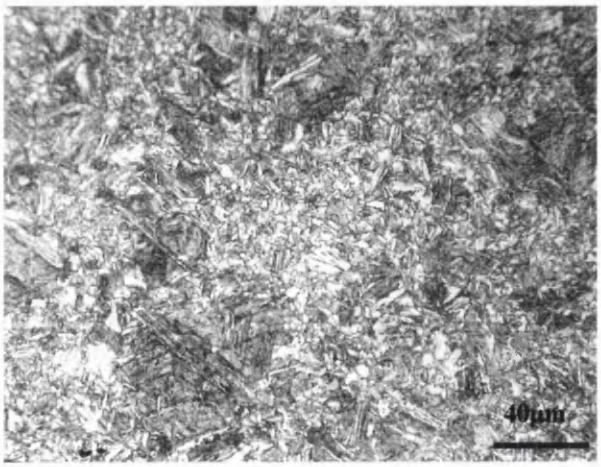

(h)

3.8% ferrite
96.2% bainite and martensite

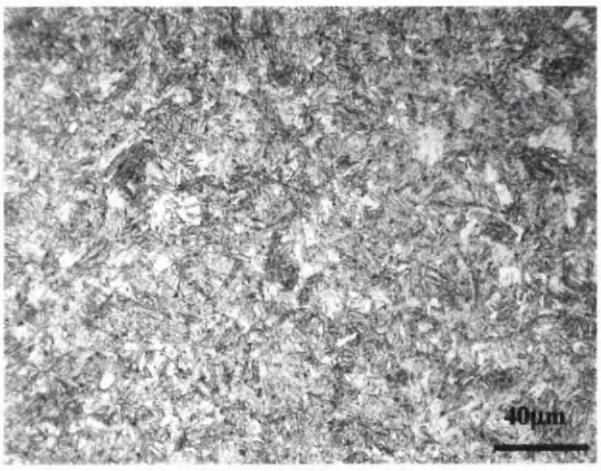

(i)

100% bainite and martensite

Figure 6.21. Typical micrographs from alloy DP1400 (CE – 0.27) after normalizing and cooling using a Gleeble 1500. Cooling rate: (g) 23.1°C/s; (h) 24.6°C/s; (i) 323°C/s.

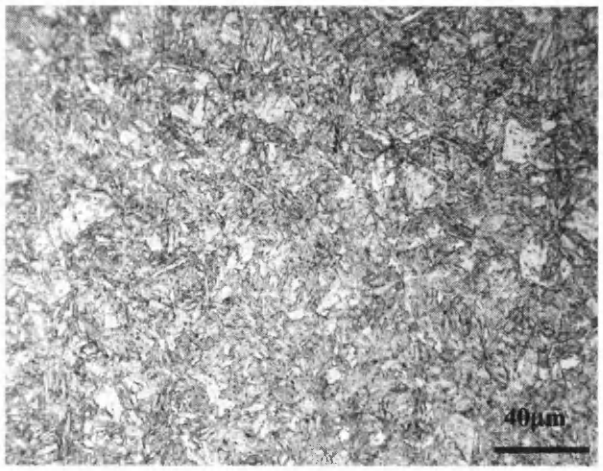

(j)

100% martensite

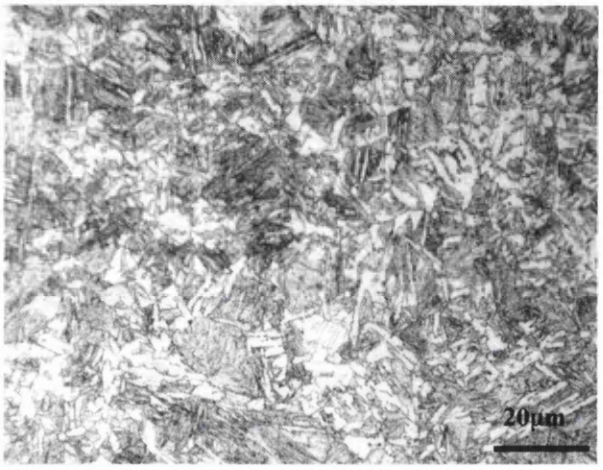

(k)

Figure 6.21. Typical micrographs from alloy DP1400 (CE – 0.27) after normalizing and cooling using a Gleeble 1500. Cooling rate: (j) 9450°C/s.

(k) Detailed micrograph of transformation constituents termed coarse acicular ferrite, bainite and martensite. Cooling rate: 19.5°C/s.

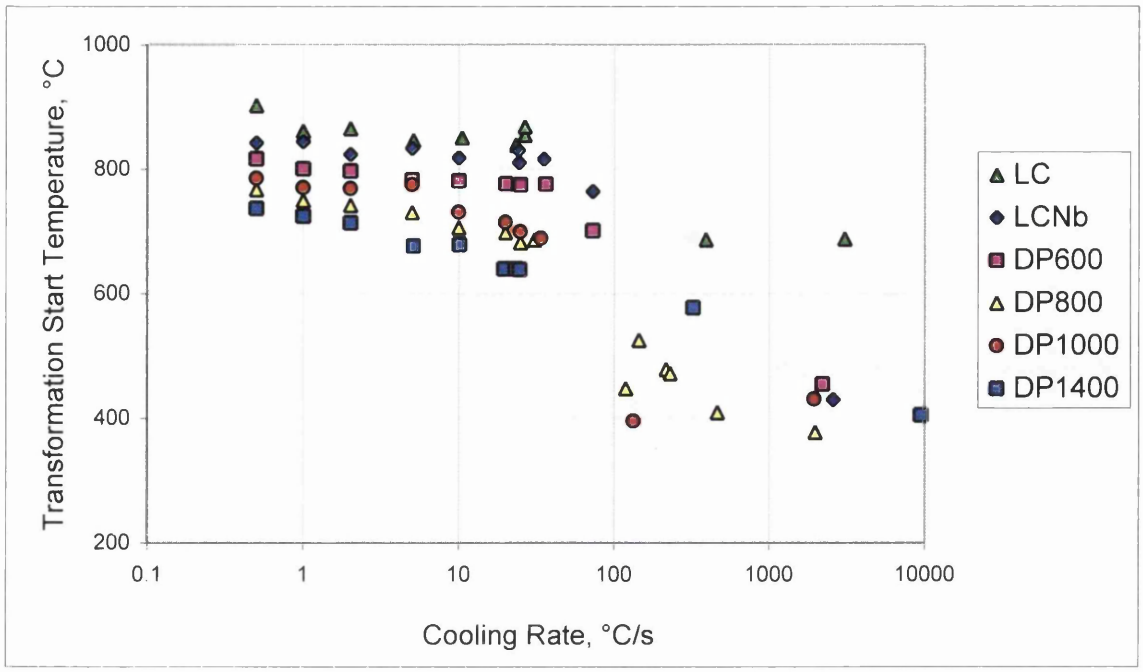

Figure 6.22. The relationship between the cooling rate and the transformation start temperature (AR_3), for the six steel studied.

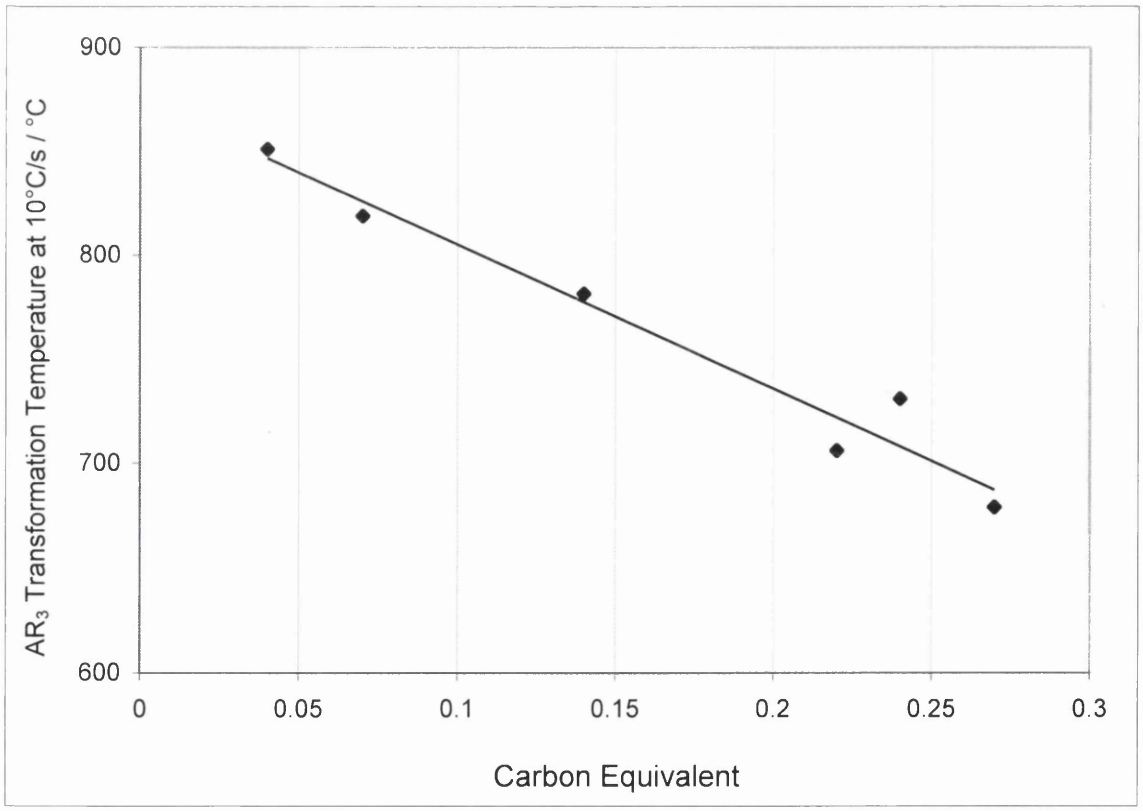

Figure 6.23. The relationship between the carbon equivalent and the transformation start temperature at a cooling rate of 10°C/s.

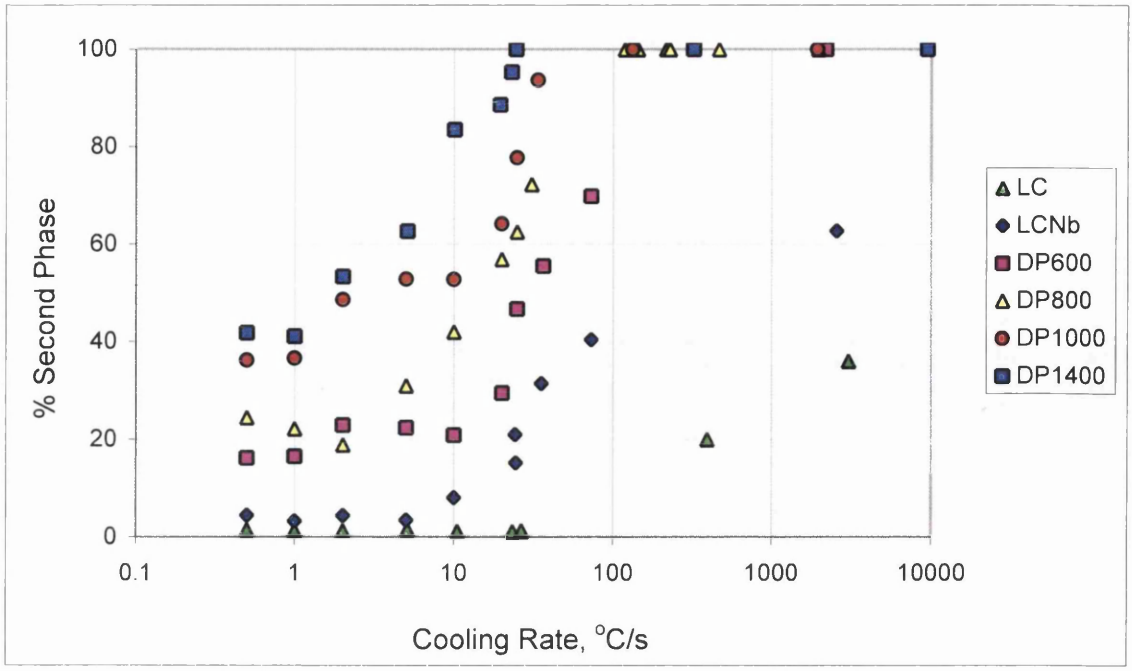

Figure 6.24. The relationship between the cooling rate and the percentage of second transformation product (that is, not pro-eutectoid ferrite), for the six steel grades studied.

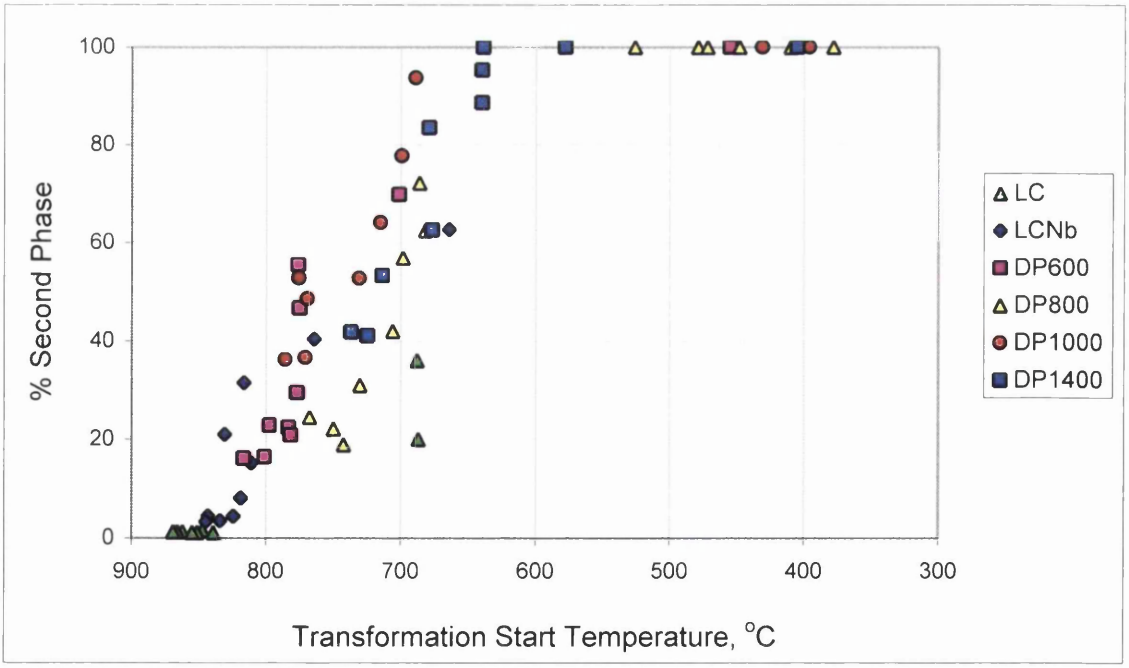

Figure 6.25. The relationship between the transformation start temperature (AR_3) and the percentage of second transformation product, for the six steel grades studied.

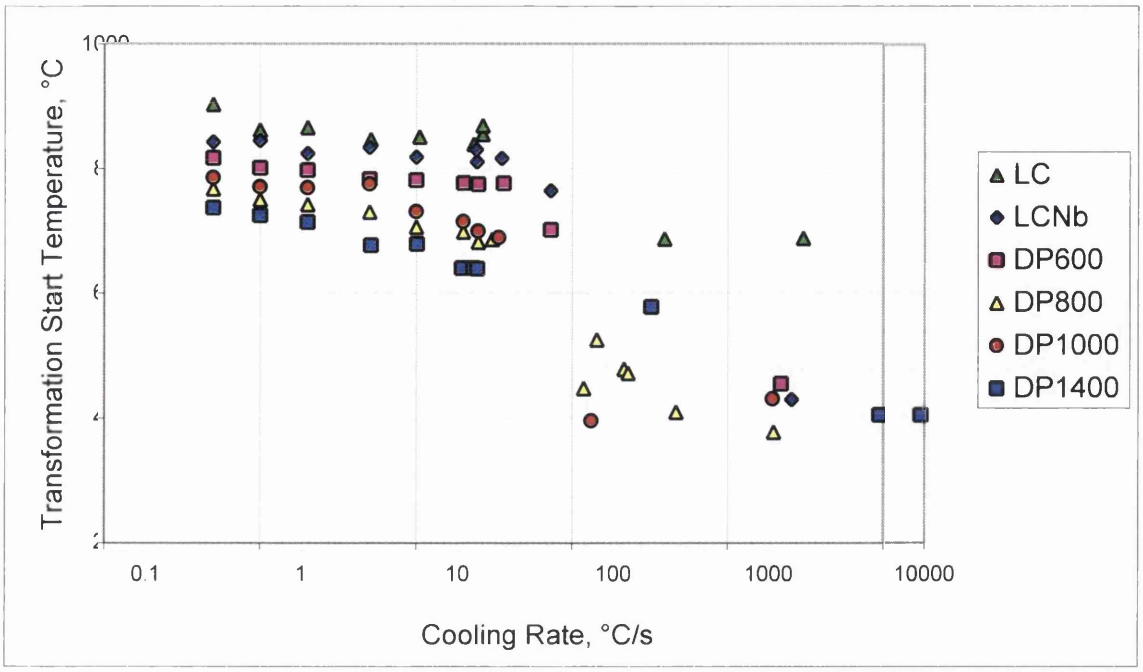

Figure 6.22. The relationship between the cooling rate and the transformation start temperature (AR_3), for the six steel studied.

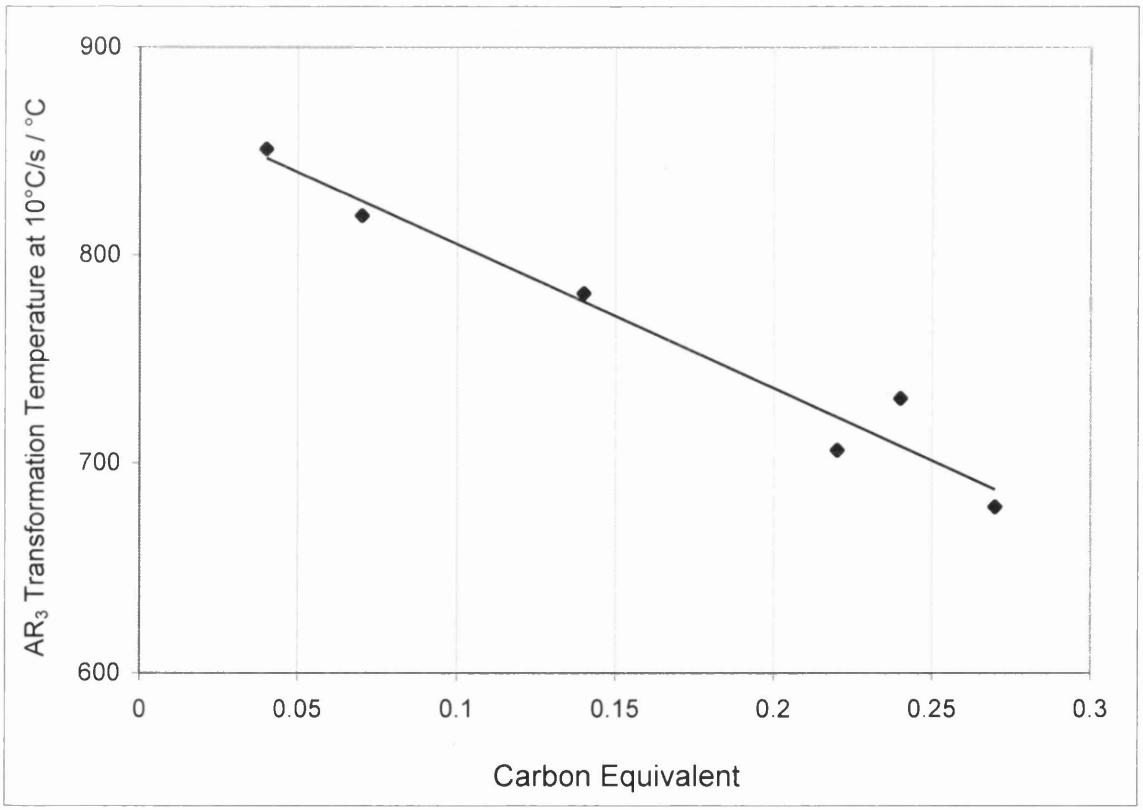

Figure 6.23. The relationship between the carbon equivalent and the transformation start temperature at a cooling rate of 10°C/s.

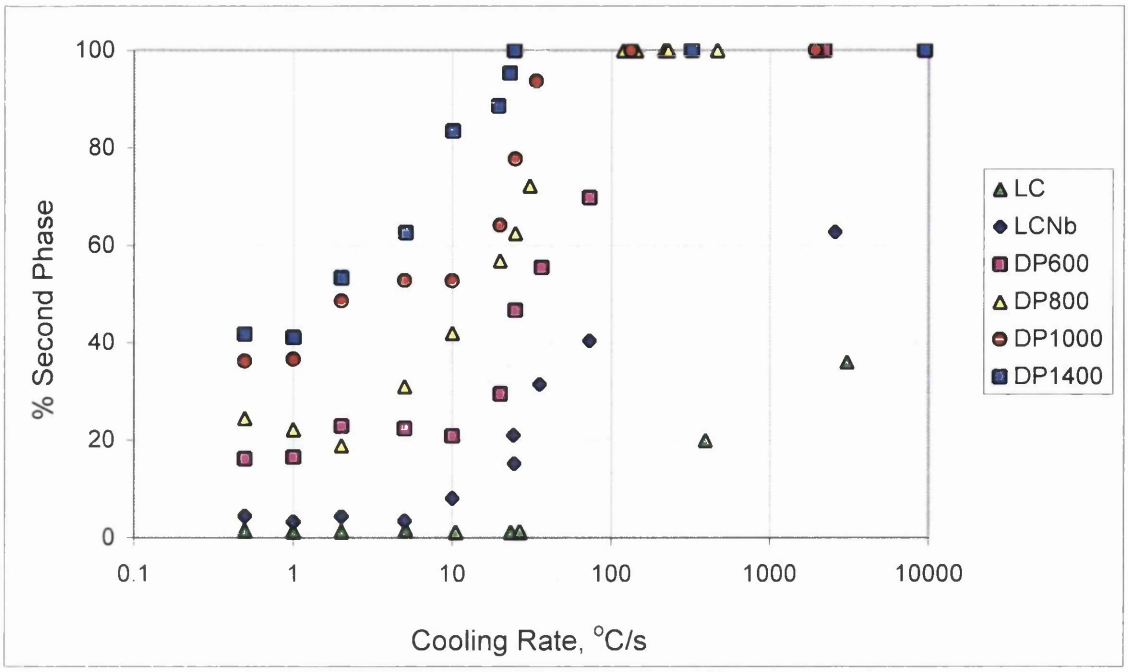

Figure 6.24. The relationship between the cooling rate and the percentage of second transformation product (that is, not pro-eutectoid ferrite), for the six steel grades studied.

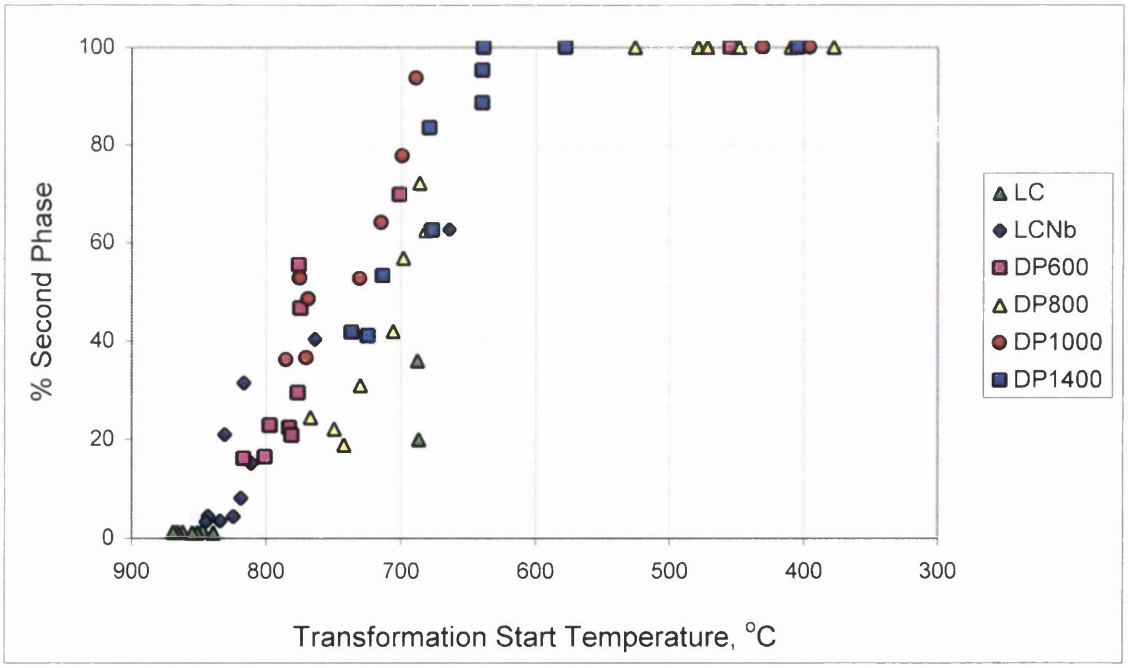

Figure 6.25. The relationship between the transformation start temperature (AR_3) and the percentage of second transformation product, for the six steel grades studied.

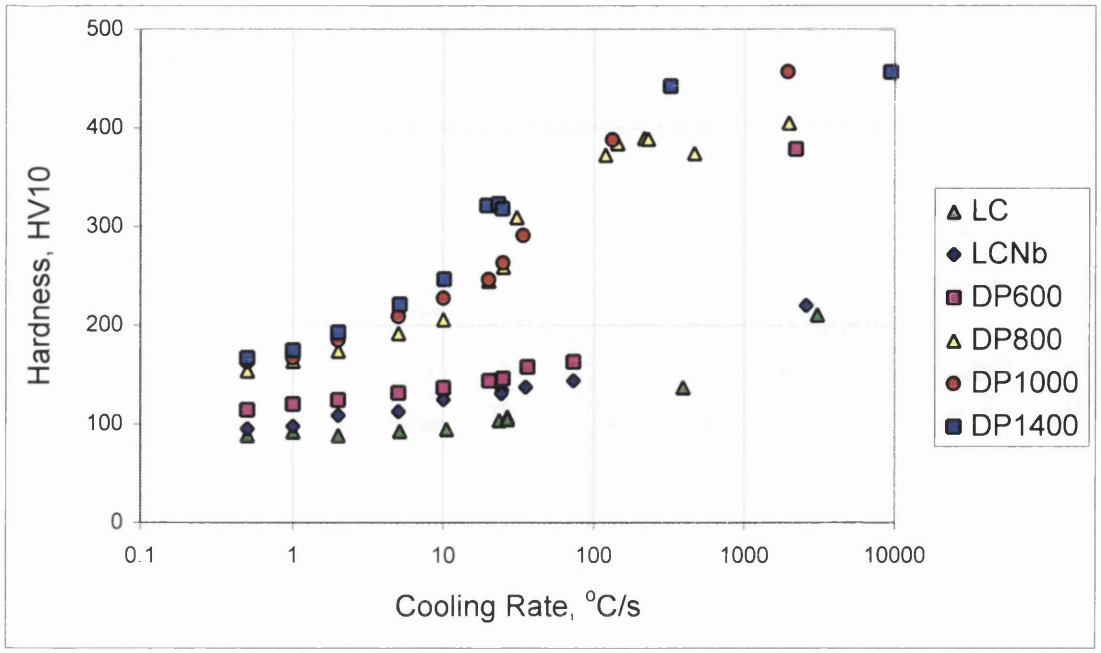

Figure 6.26. The relationship between the cooling rate and bulk Vickers hardness, for the six steel grades studied.

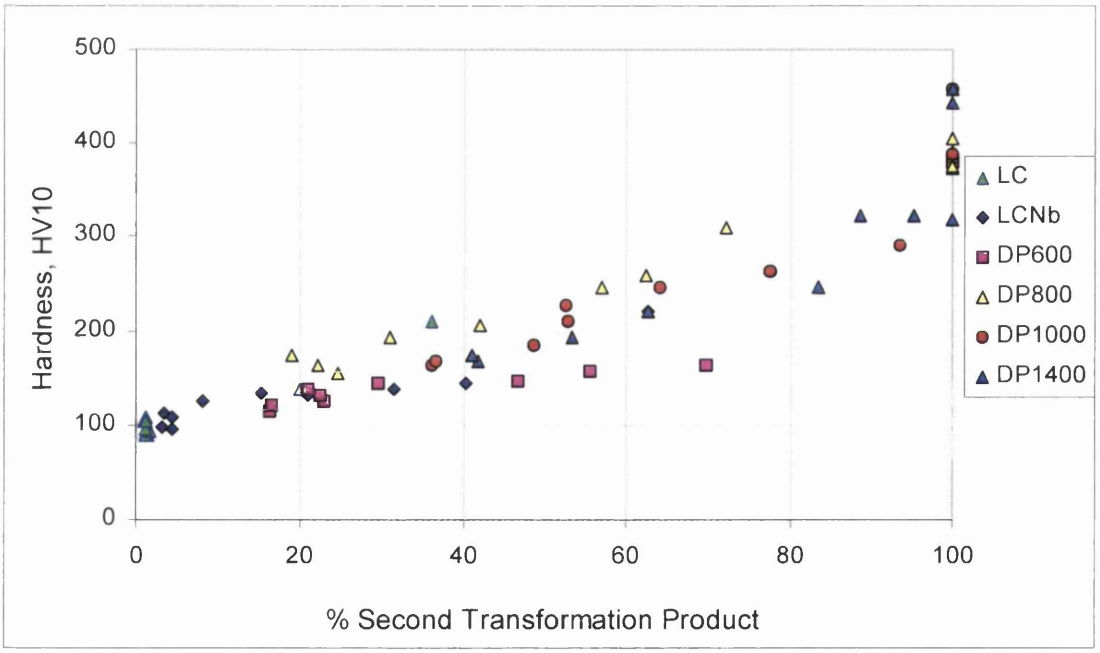

Figure 6.27. The relationship between the volume fraction of second transformation product and the bulk Vickers hardness, for the six steel grades studied.

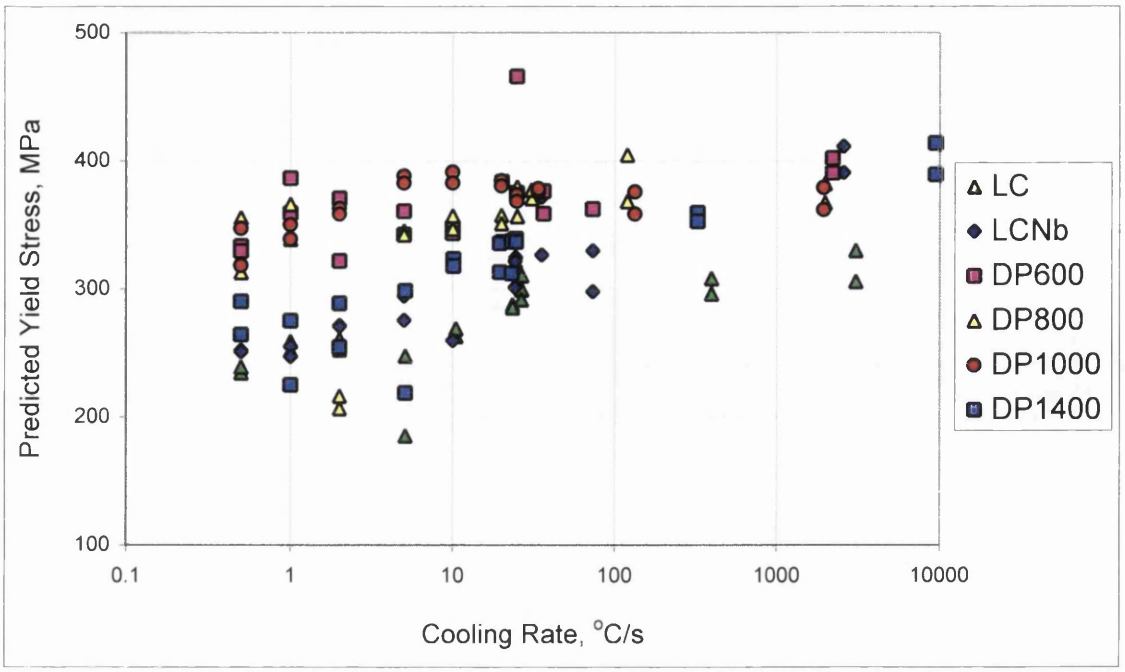

Figure 6.28. The relationship between the cooling rate and the yield stress predicted by miniature disc bend tests, for the six steel grades studied.

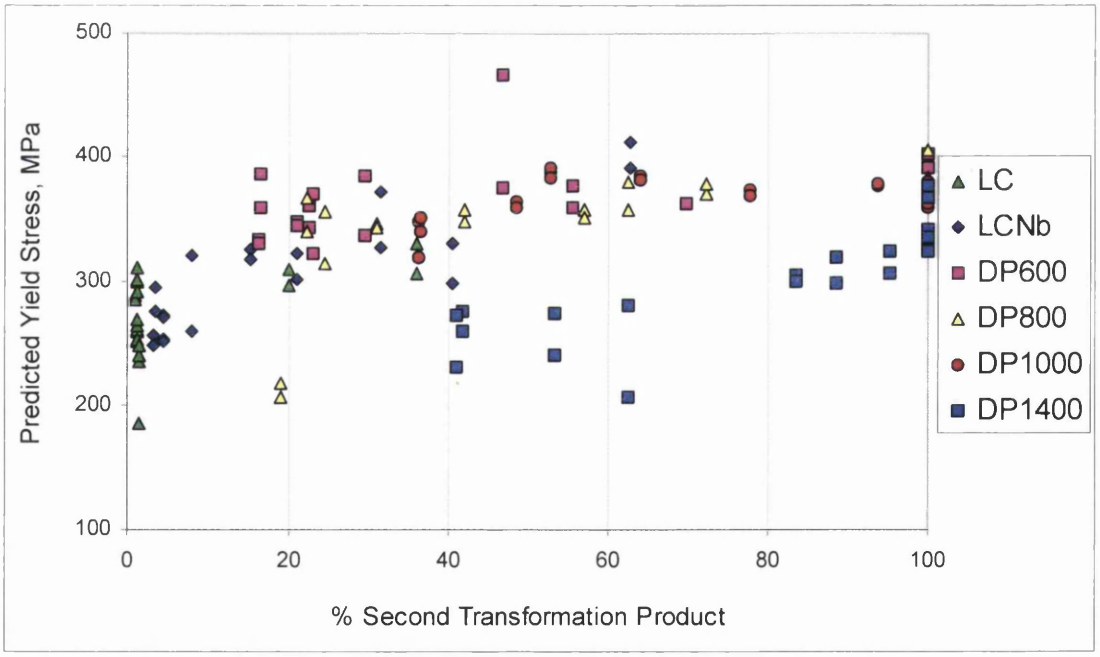

Figure 6.29. The relationship between the volume fraction of second transformation product and the yield stress predicted by miniature disc bend tests, for the six steel grades studied.

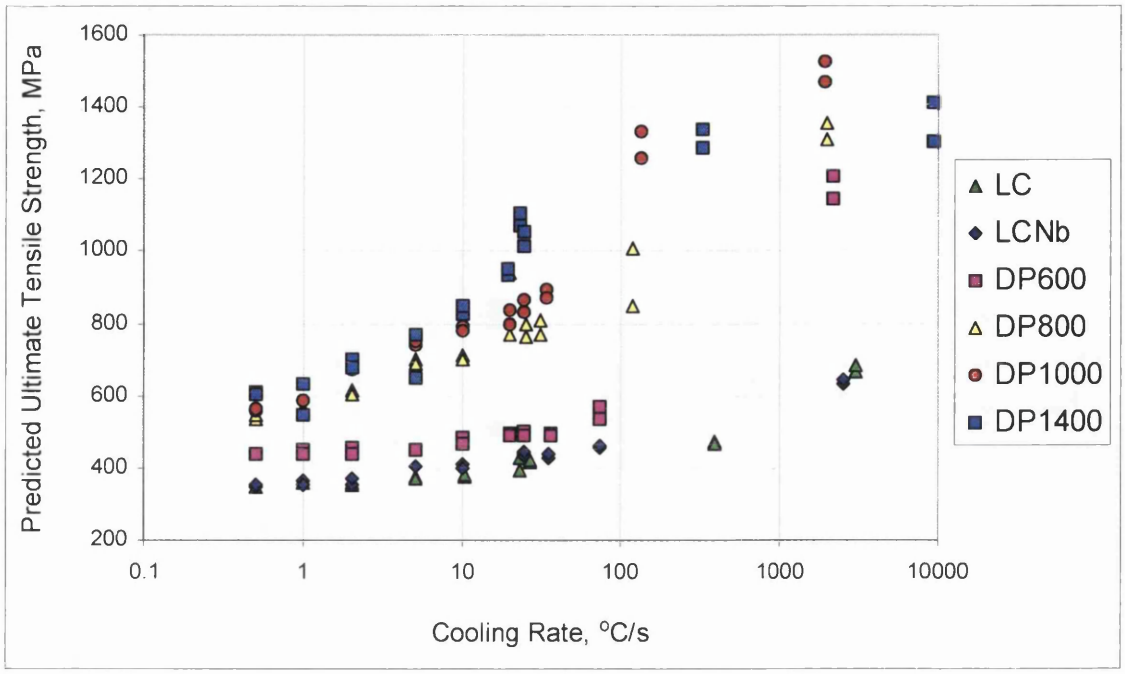

Figure 6.30. The relationship between the cooling rate and the ultimate tensile strength predicted by miniature disc bend tests, for the six steel grades studied.

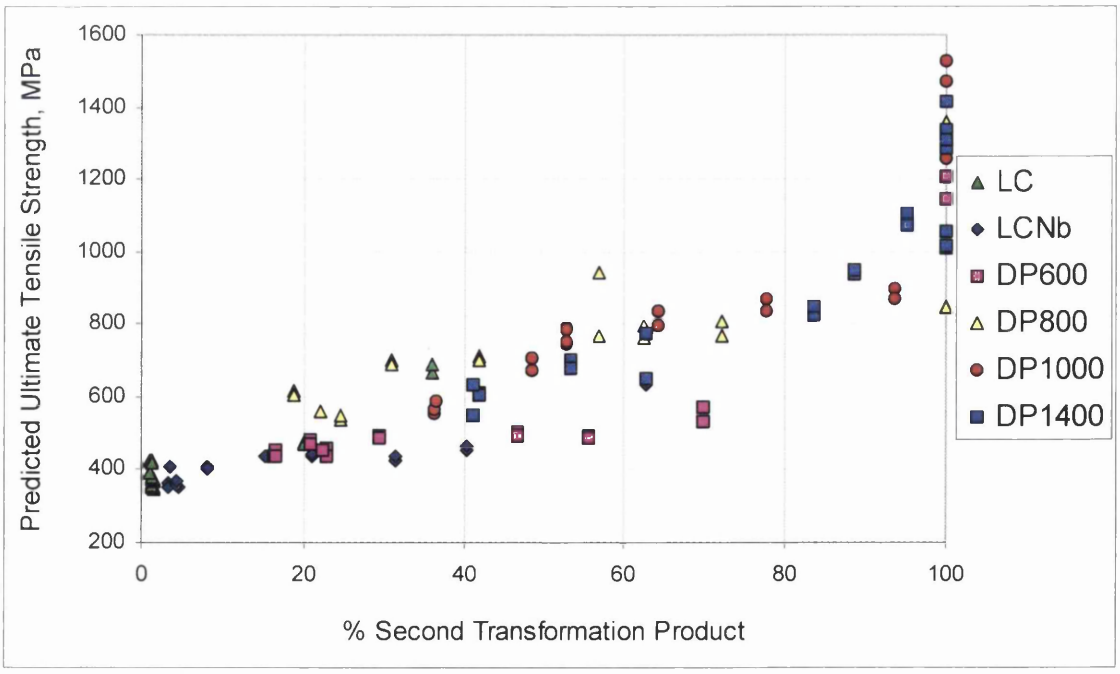

Figure 6.31. The relationship between the volume fraction of second transformation product and the ultimate tensile strength predicted by miniature disc bend tests, for the six steel grades studied.

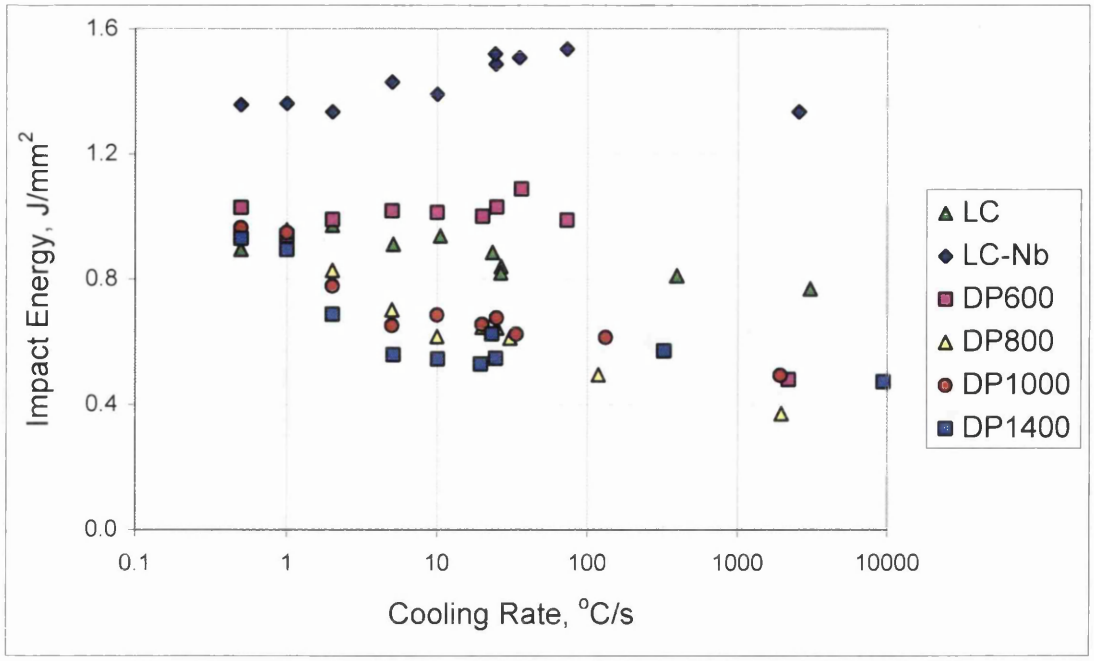

Figure 6.32. The relationship between the cooling rate and the impact energy measured by a miniature impact test, for the six steel grades studied.

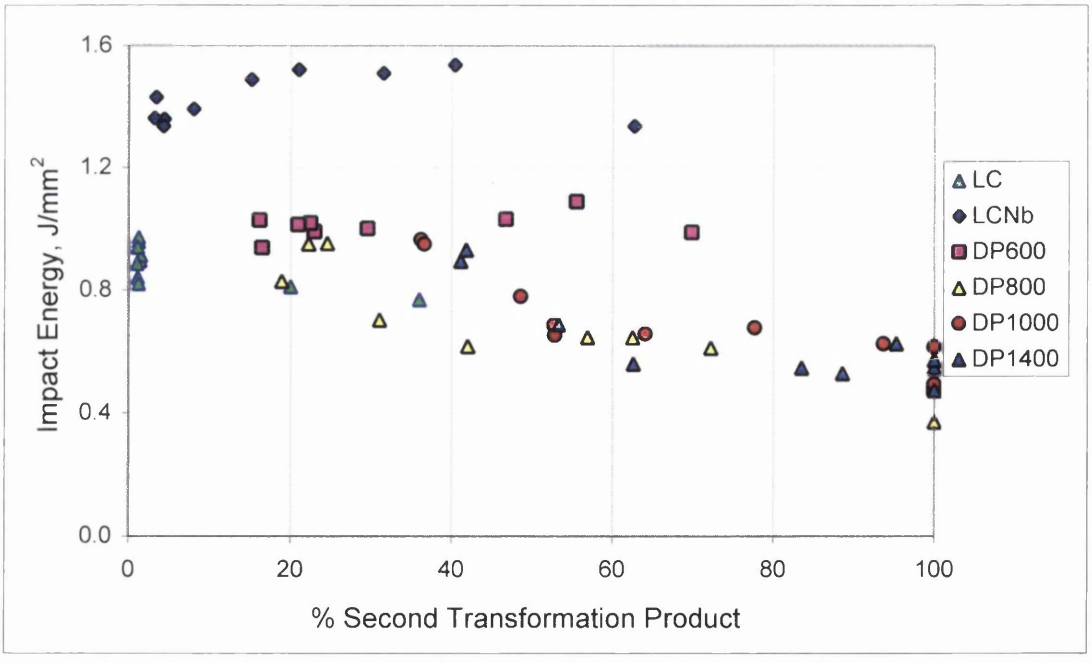

Figure 6.33. The relationship between the volume fraction of second transformation product and the impact energy measured by a miniature impact test, for the six steel grades studied.

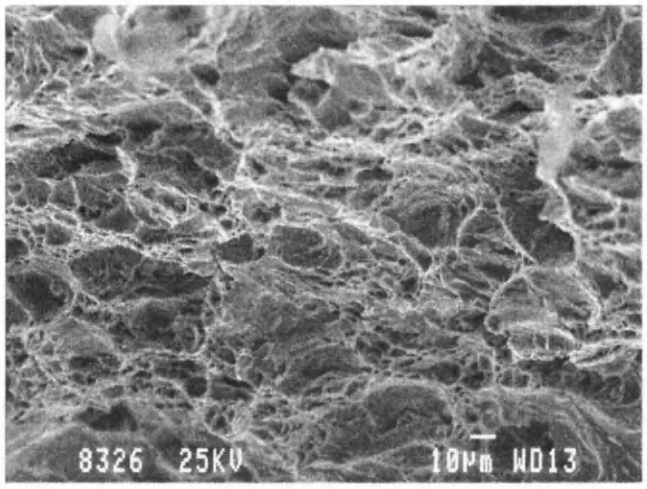

(a)

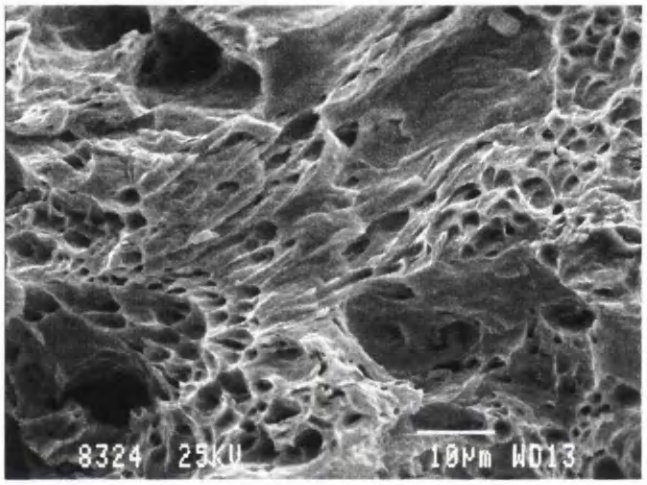

(b)

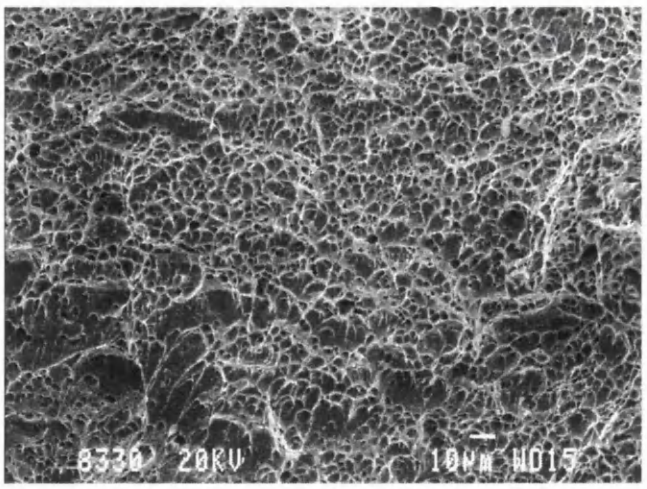

(c)

Figure 6.34. Typical scanning electron micrographs, from alloy LC (CE – 0.04), of the fracture surface of miniature impact tests. Cooling rate: (a) 0.5°C/s; (b) 0.5°C/s, detail of elongation of dimples prior to fracture; (c) 3058°C/s.

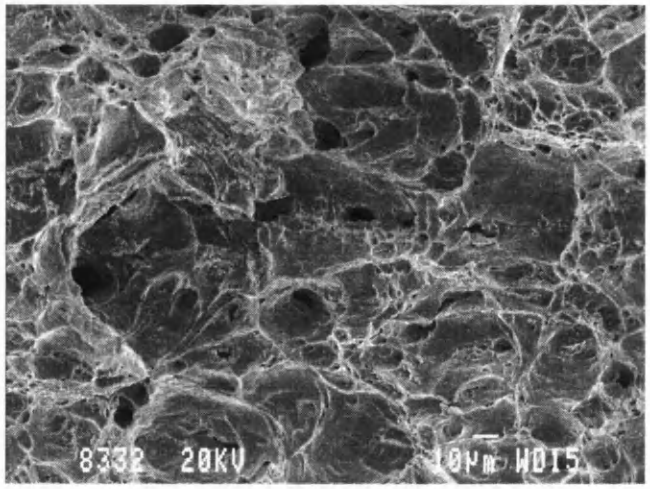

(a)

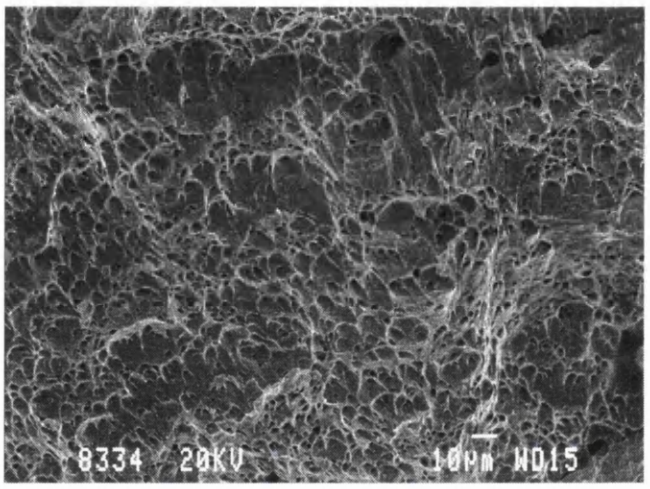

(b)

Figure 6.35. Typical scanning electron micrographs, from alloy LCNb (CE – 0.07), of the fracture surface of miniature impact tests. Cooling rate: (a) 0.5°C/s; (b) 2575°C/s.

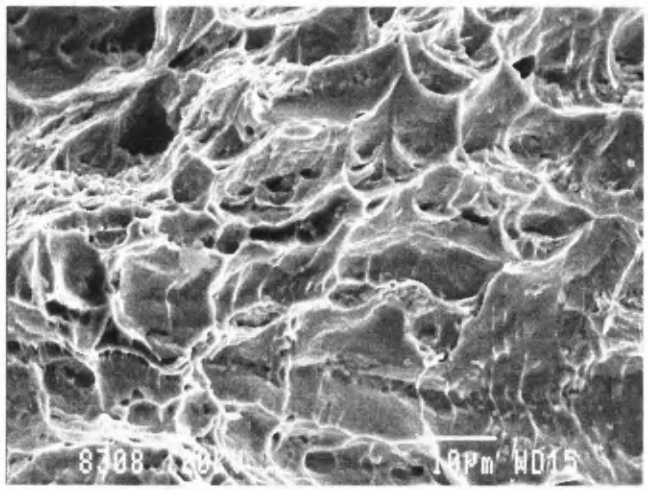

(a)

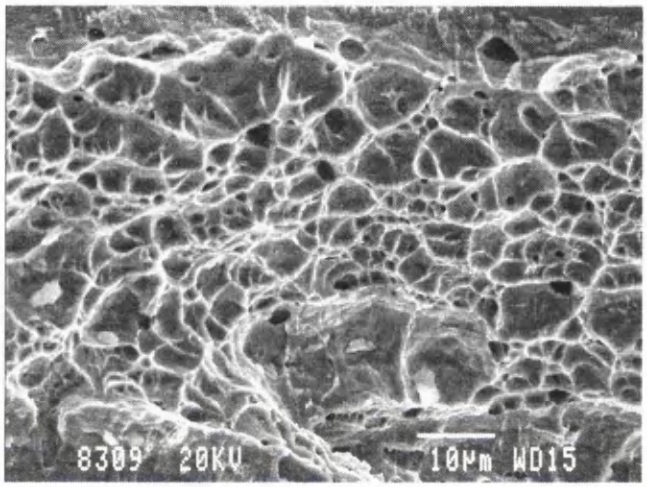

(b)

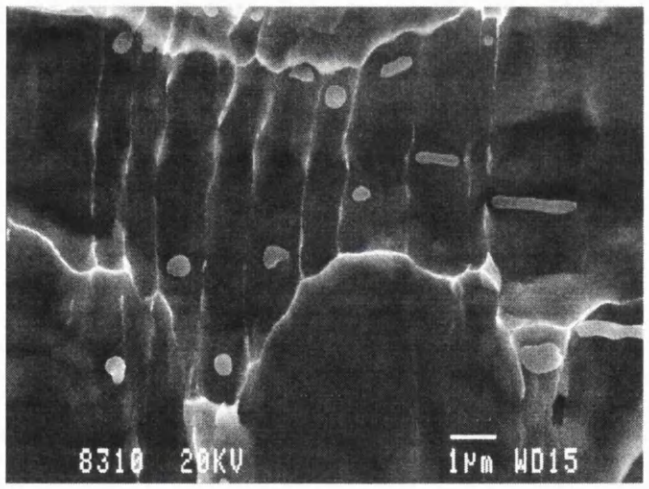

(c)

Figure 6.36. Typical scanning electron micrographs, from alloy DP600 (CE – 0.14), of the fracture surface of miniature impact tests. Cooling rate: (a) 0.5°C/s; (b) 2206°C/s; (c) 2206°C/s, detail of precipitates present in each rippled area from Figure 6.36(b).

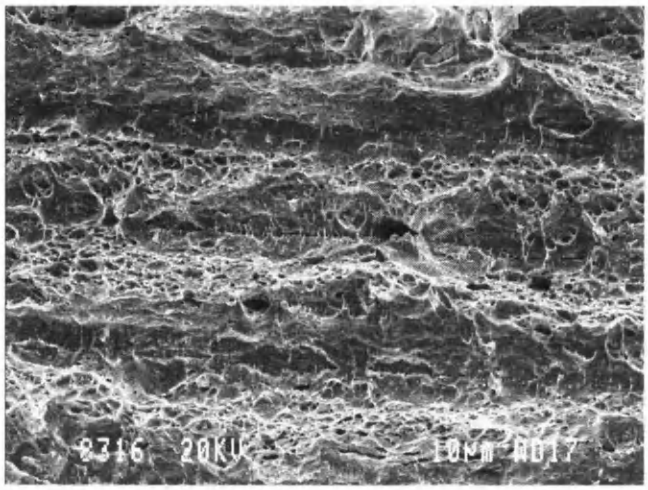

(a)

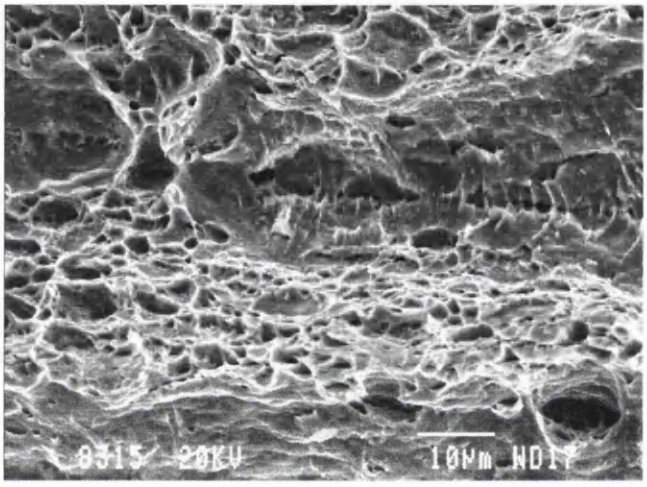

(b)

Figure 6.37 Typical scanning electron micrographs, from alloy DP800 (CE – 0.22), of the fracture surface of miniature impact tests. Cooling rate: (a) 0.5°C/s; (b) 0.5°C/s, detail seen within a flat area from Figure 6.37(a).

(c)

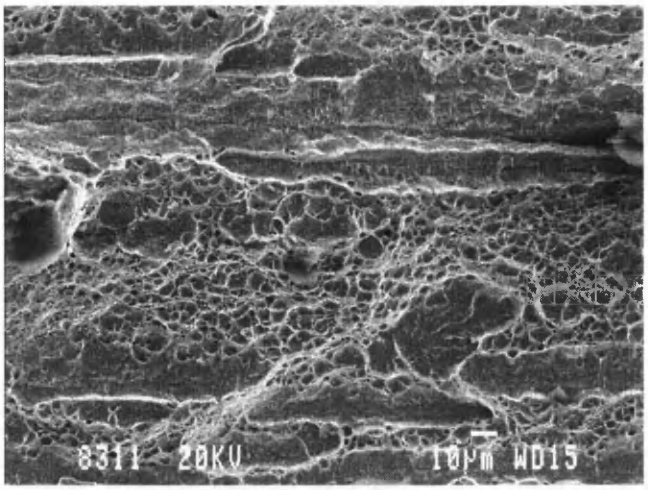

(c)

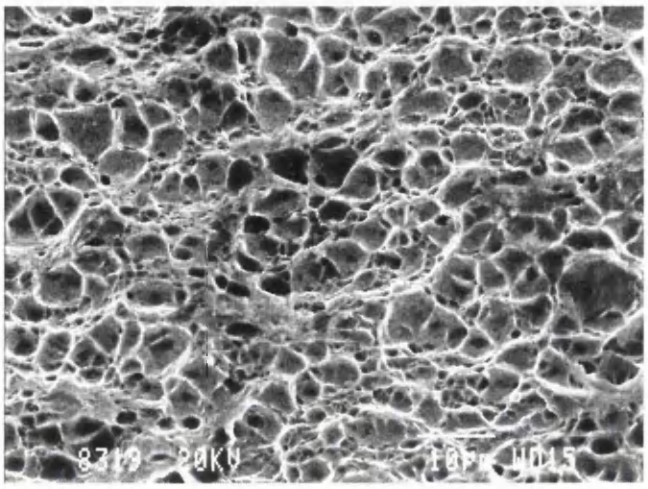

(d)

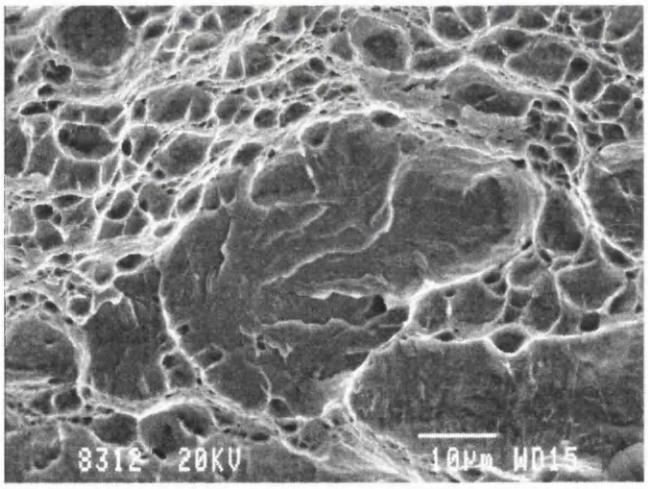

(e)

Figure 6.37 Typical scanning electron micrographs, from alloy DP800 (CE – 0.22), of the fracture surface of miniature impact tests. Cooling rate: (c) 1978°C/s; (d) 1978°C/s, detail of dimples from Figure 6.37(d); 1978°C/s, detail of flat area from Figure 6.37(d).

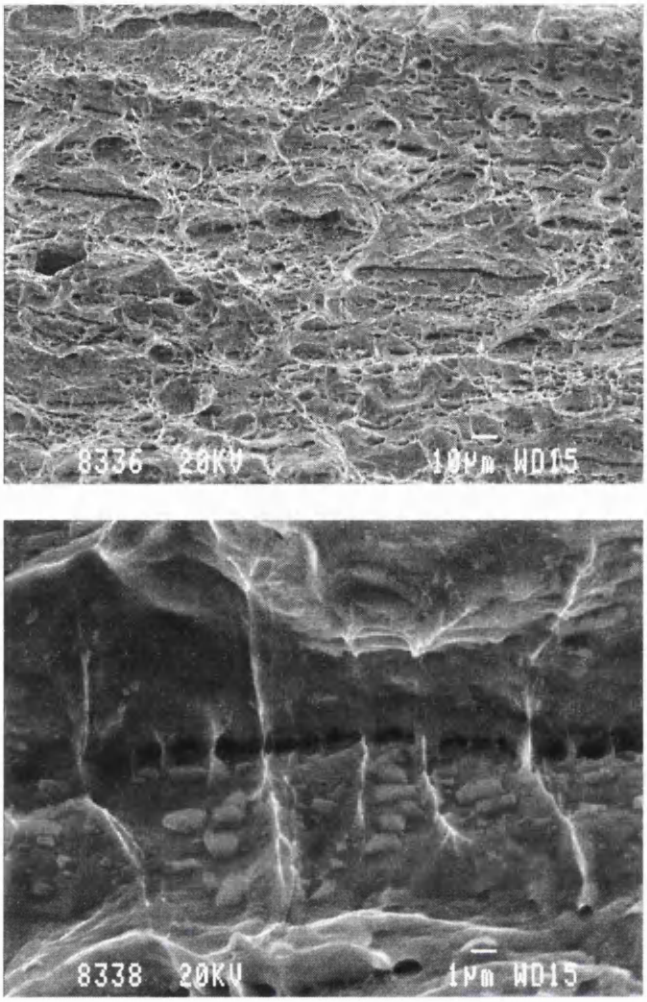

(a)

(b)

Figure 6.38 Typical scanning electron micrographs, from alloy DP1000 (CE – 0.24), of the fracture surface of miniature impact tests. Cooling rate: (a) 0.5°C/s; (b) 0.5°C/s, detail seen within a flat area from Figure 6.38(a).

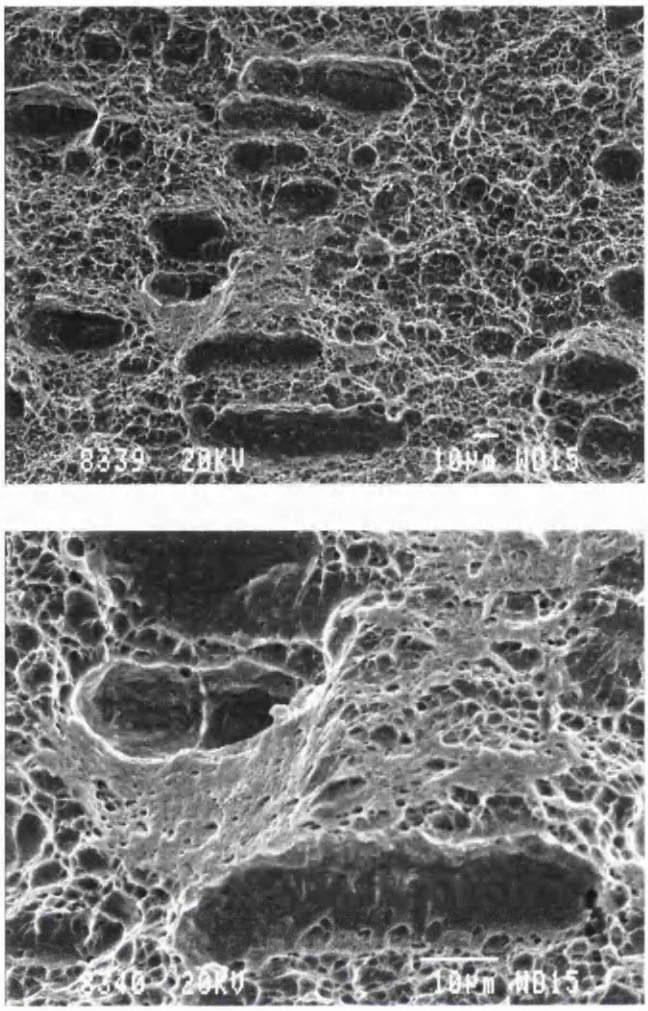

(c)

(d)

Figure 6.38 Typical scanning electron micrographs, from alloy DP1000 (CE – 0.24), of the fracture surface of miniature impact tests. Cooling rate: (c) 1950°C/s; (d) 1950°C/s, detail of flat area from Figure 6.38(c).

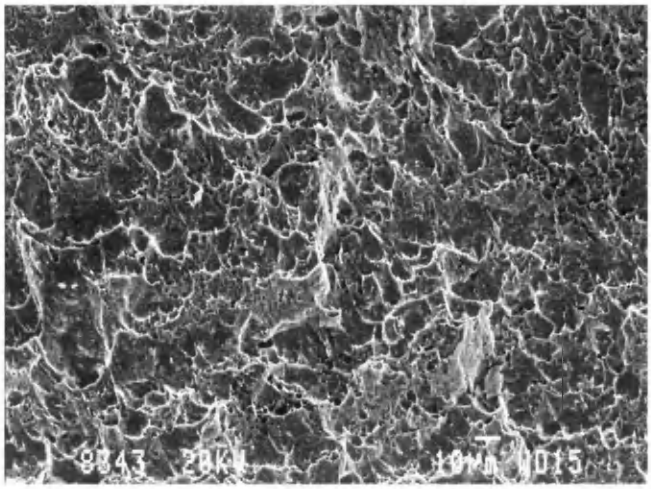

(a)

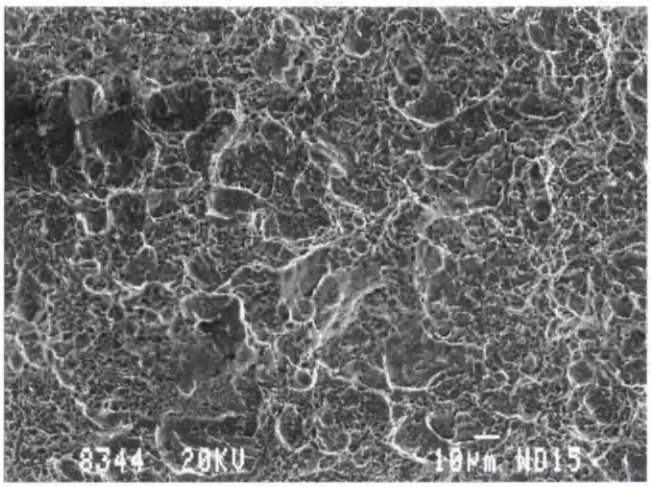

(b)

Figure 6.39 Typical scanning electron micrographs, from alloy DP1400 (CE – 0.27), of the fracture surface of miniature impact tests. Cooling rate: (a) 0.5°C/s; (b) 9450°C/s.

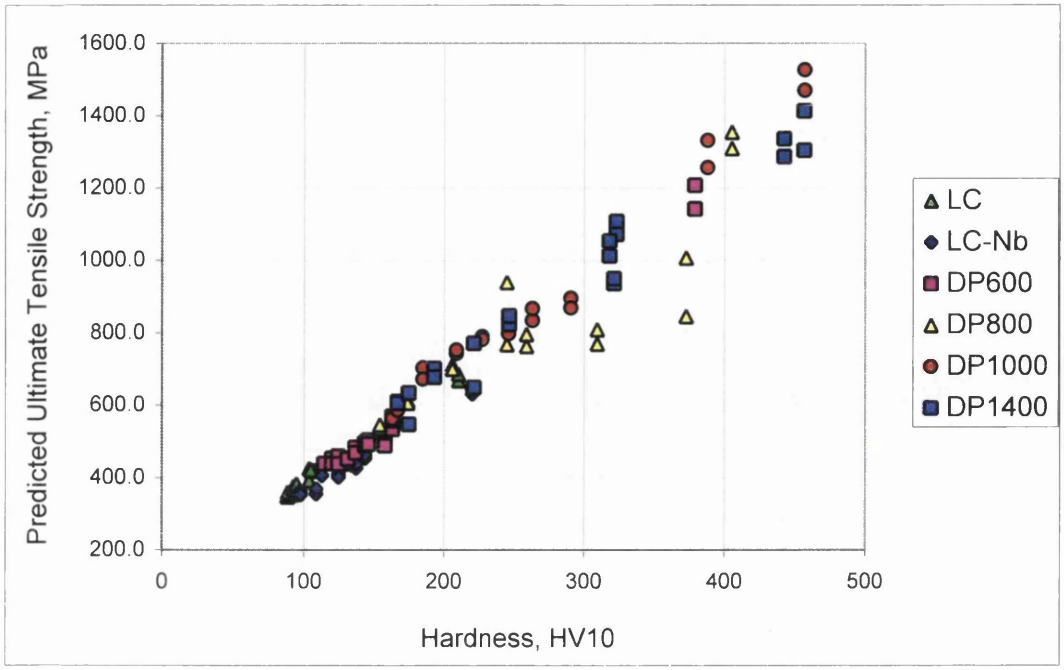

Figure 6.40. The relationship between the bulk Vickers hardness and the ultimate tensile strength predicted by a miniature disc bend test, for the six steel grades studied.

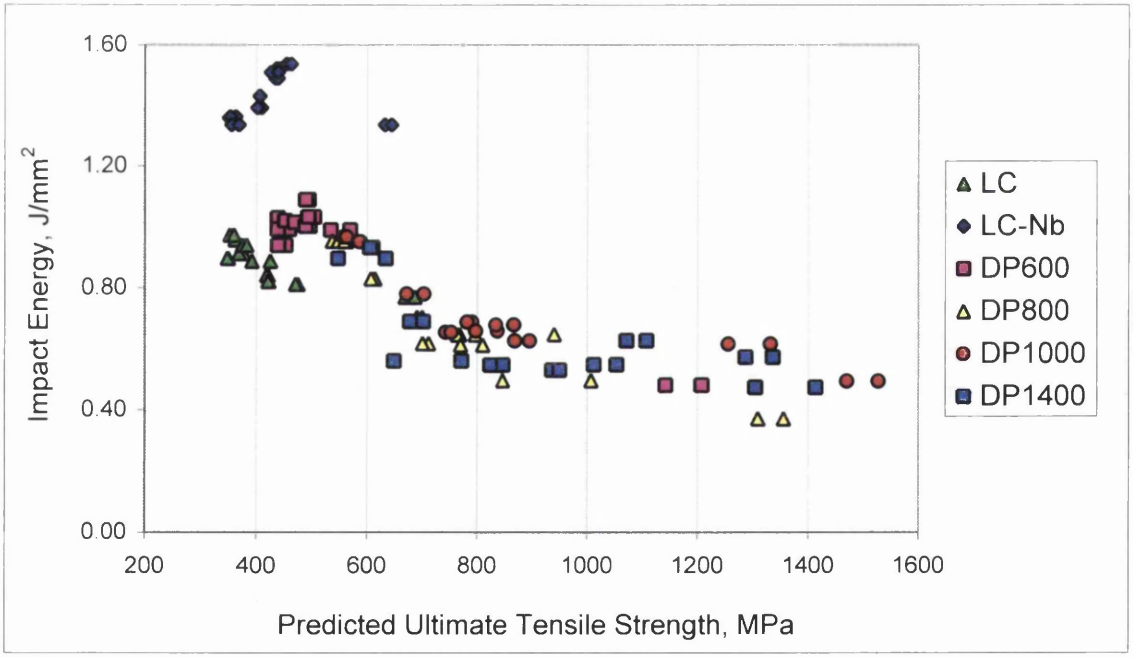

Figure 6.41. The relationship between the ultimate tensile strength predicted by a miniature disc bend test and the impact energy measured by a miniature impact test, for the six steel grades studied.

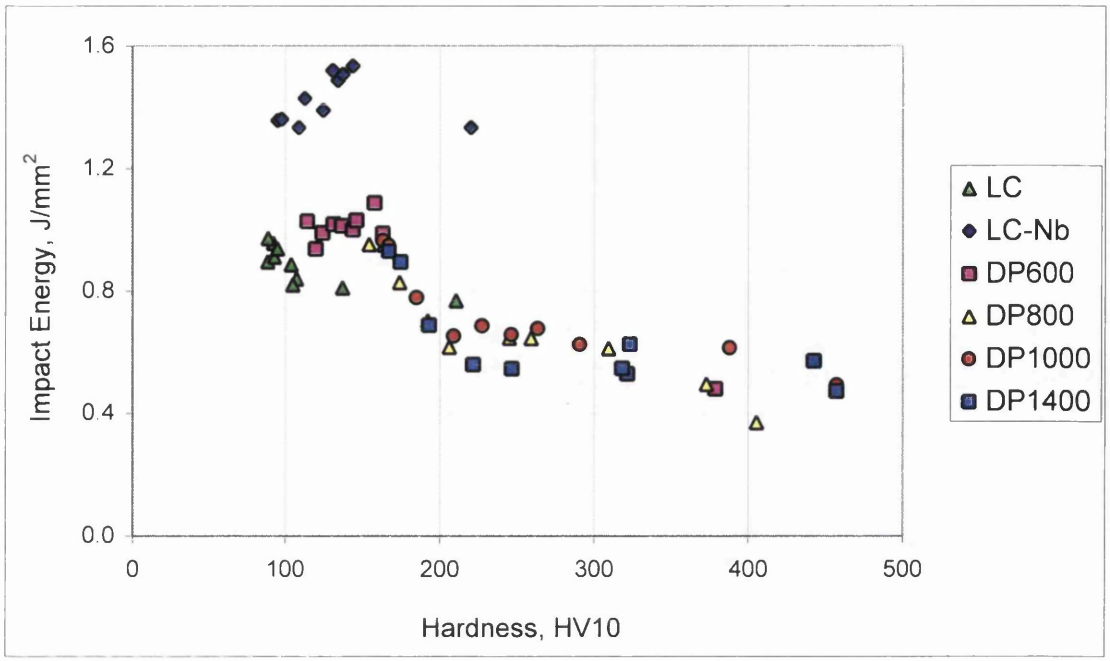

Figure 6.42. The relationship between the bulk Vickers Hardness and the impact energy measured by a miniature impact test, for the six steel grades studied.

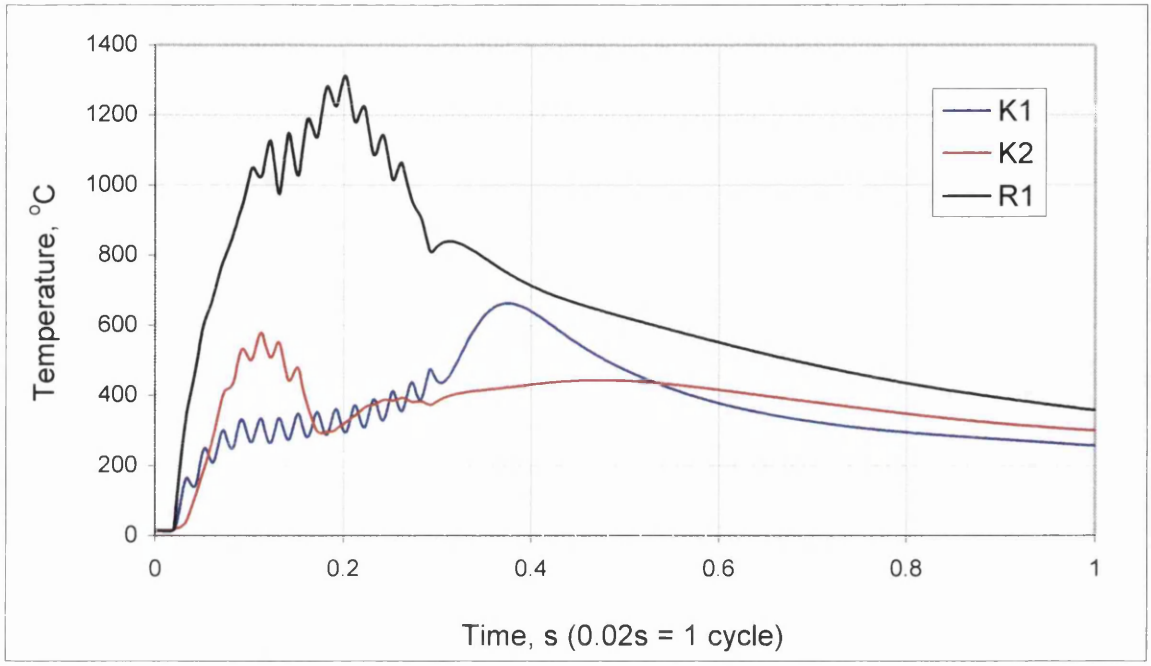

(a)

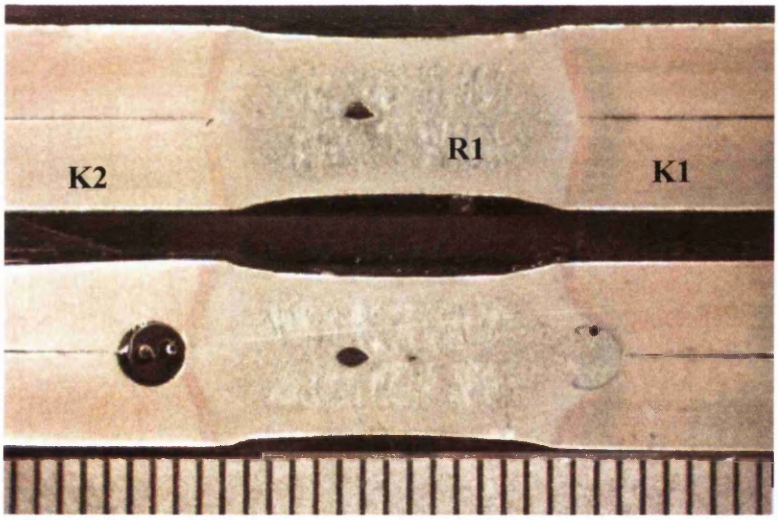

(b)

Figure 6.43 (a) The time – temperature profile measured for a for single pulse weld with plain wire thermocouples.
(b) The relative location of the thermocouples in the single pulse weld. Scale is in mm.

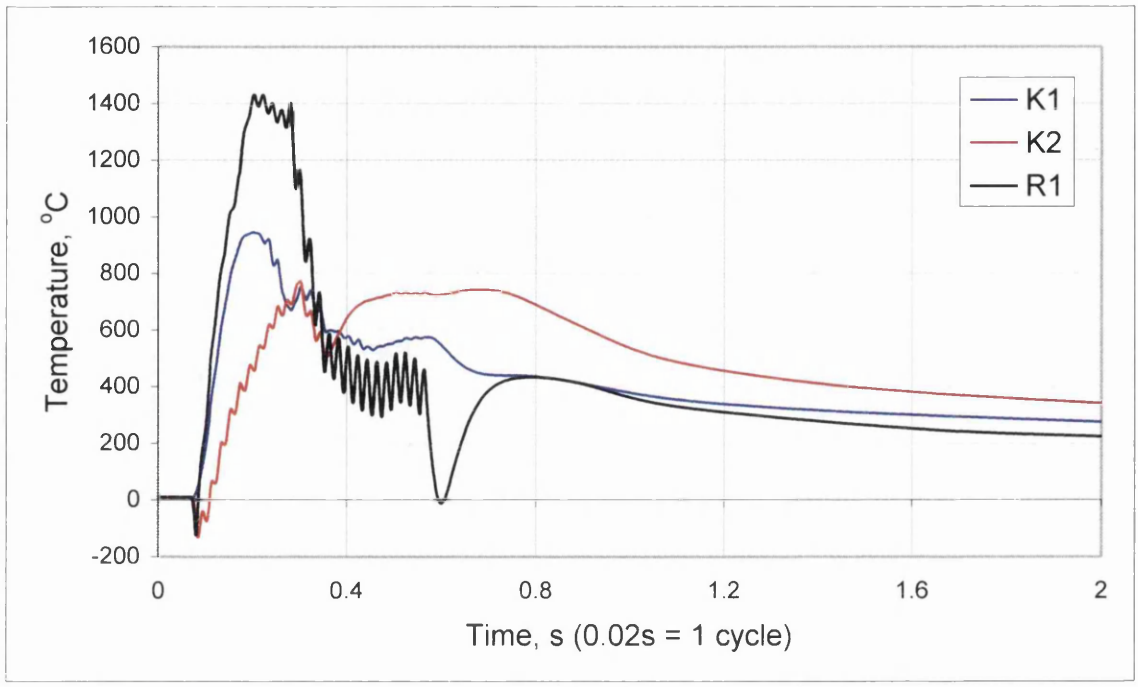

(a)

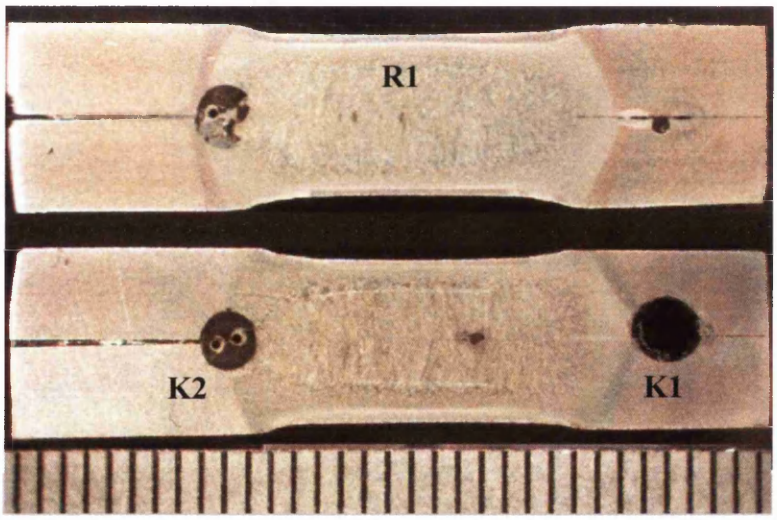

(b)

Figure 6.44 (a) The time – temperature profile for a for extended weld time weld – 25 cycles, measured using plain wire thermocouples.
(b) The relative location of the thermocouples in the 25 cycle weld. Scale is in mm.

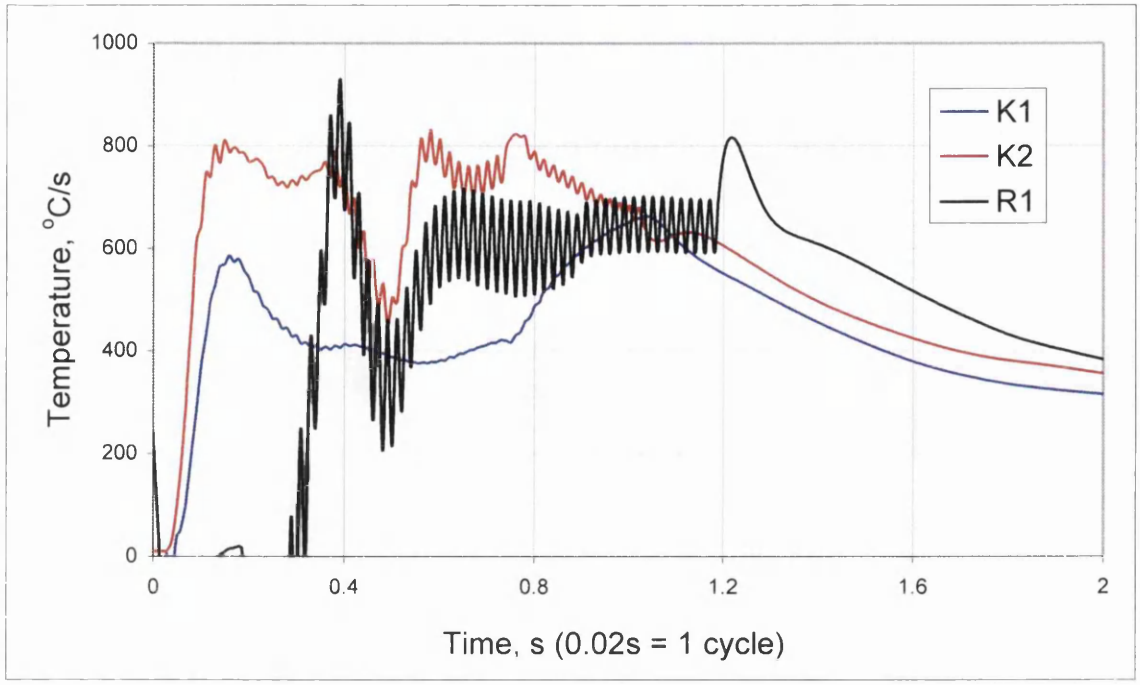

(a)

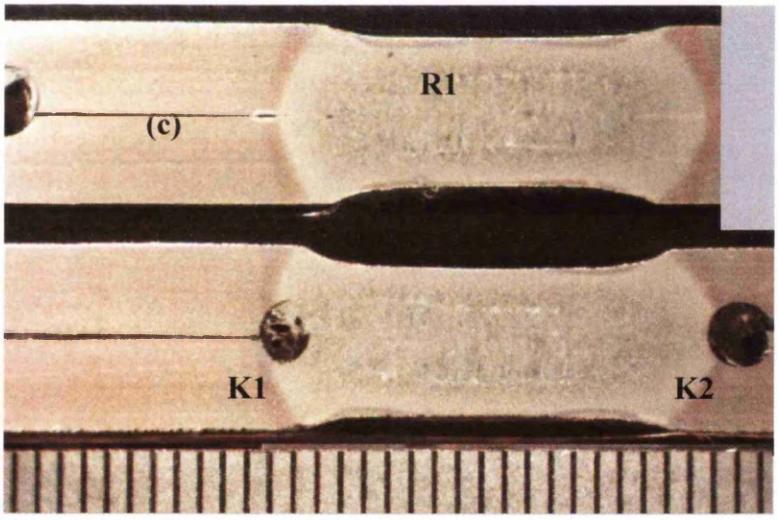

(b)

Figure 6.45 (a) The time – temperature profile for a for extended weld time weld – 50 cycles, measured using plain wire thermocouples.
(b) The relative location of the thermocouples in the 50 cycle weld. Scale is in mm.

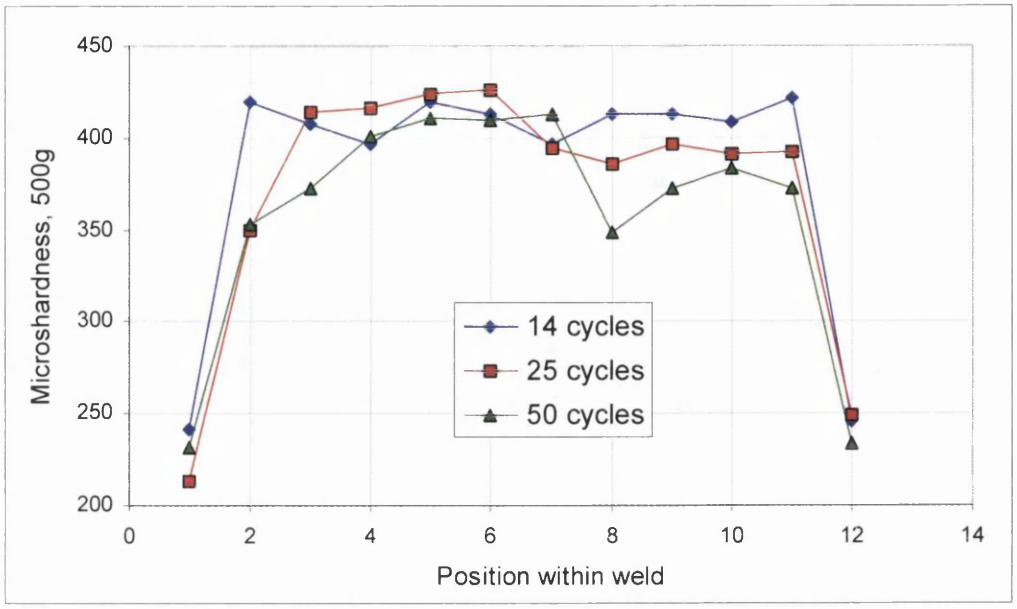

Figure 6.46. Microhardness profiles of welds produced using 14, 25 and 50 cycles of weld current produced in DP800.

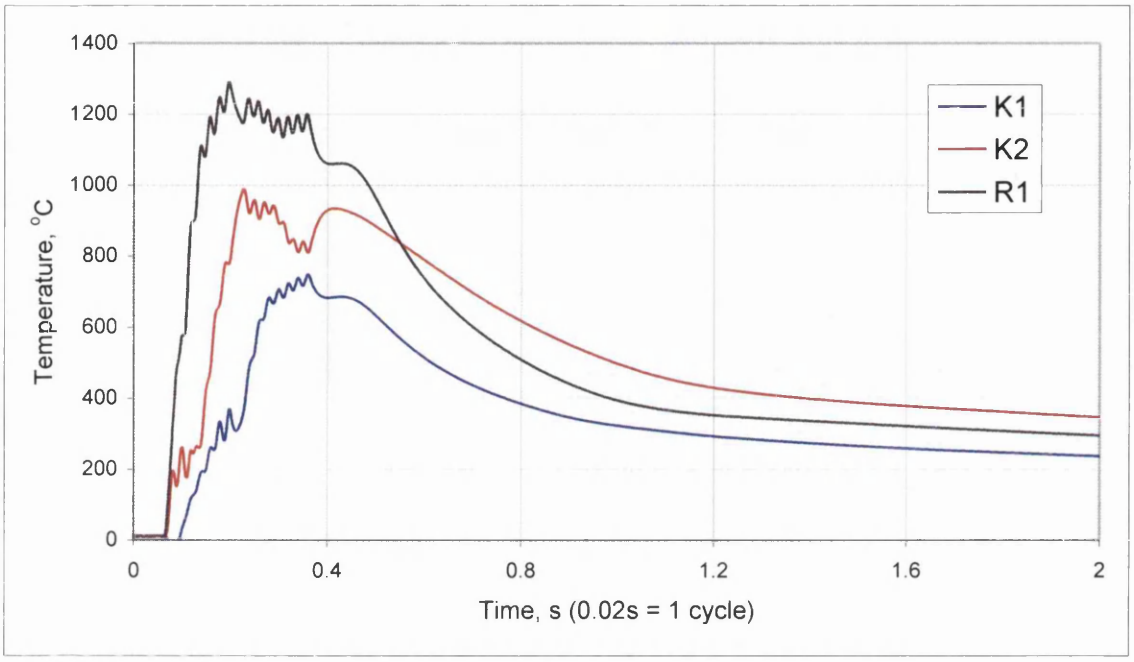

(a)

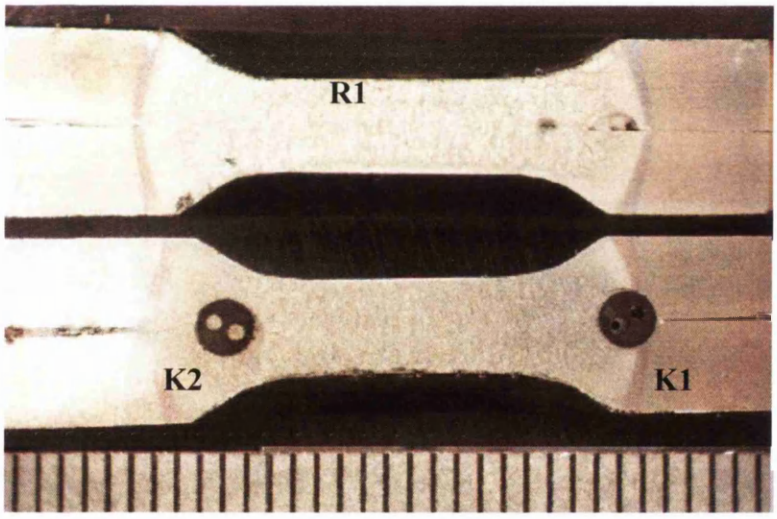

(b)

Figure 6.47 (a) The time – temperature profile for a pulsed weld – 2 x 7 cycles, measured using plain wire thermocouples.
(b) The relative location of the thermocouples in the 2 x 7 weld. Scale is in mm.

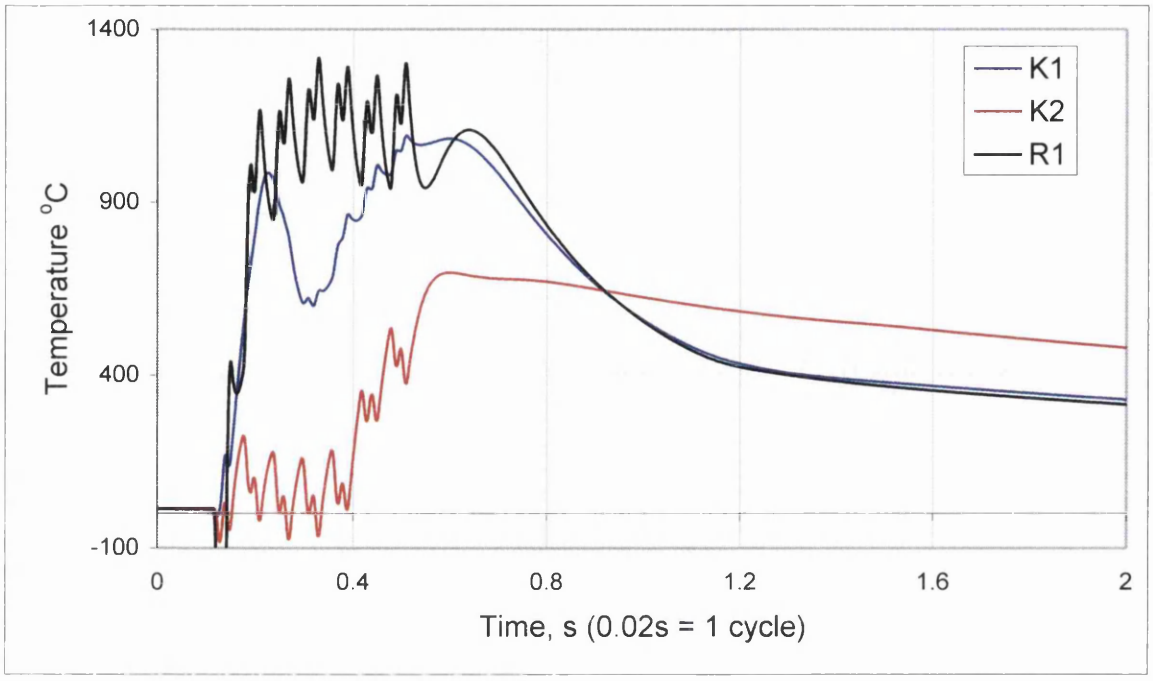

(a)

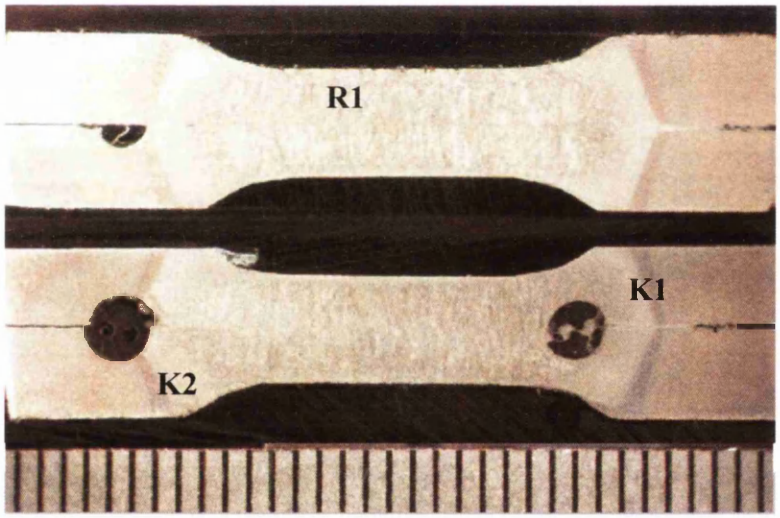

(b)

Figure 6.48 (a) The time – temperature profile for a pulsed weld – 7 x 2 cycles, measured using plain wire thermocouples.
(b) The relative location of the thermocouples in the 7 x 2 weld. Scale is in mm.

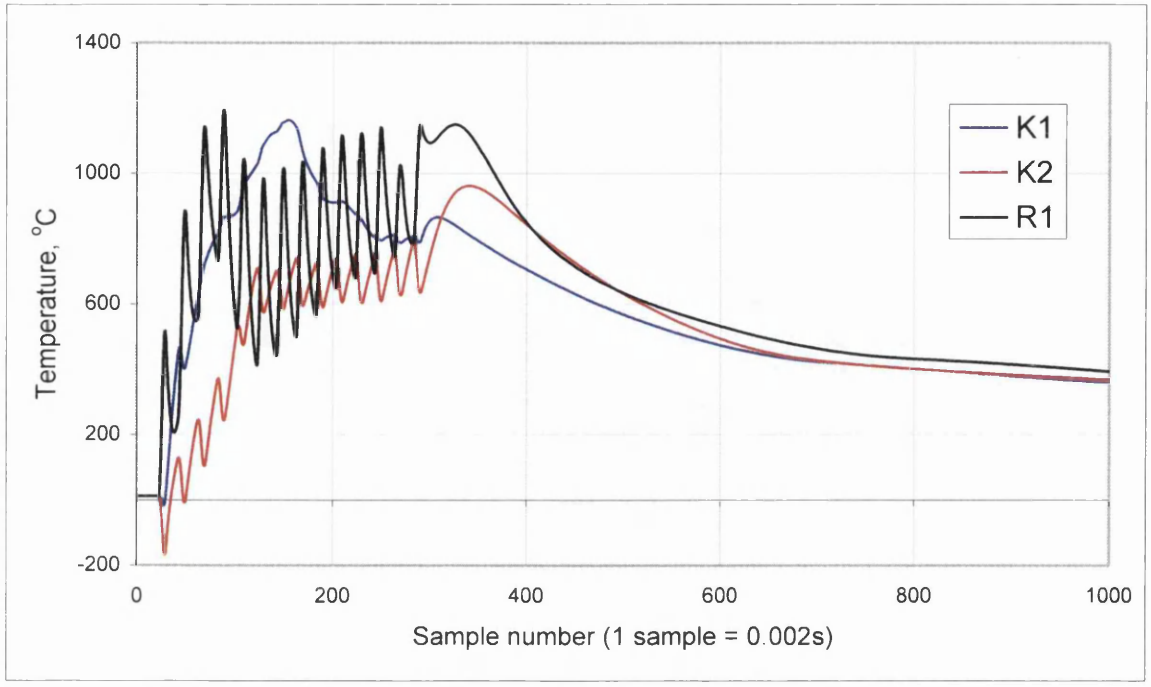

(a)

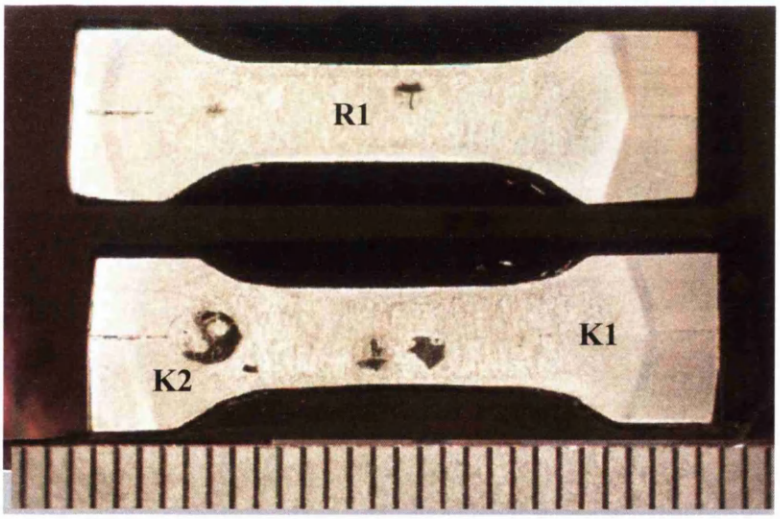

(b)

Figure 6.49 (a) The time – temperature profile for a pulsed weld – 14 x 1 cycles, measured using plain wire thermocouples.
(b) The relative location of the thermocouples in the 14 x 1 weld. Scale is in mm.

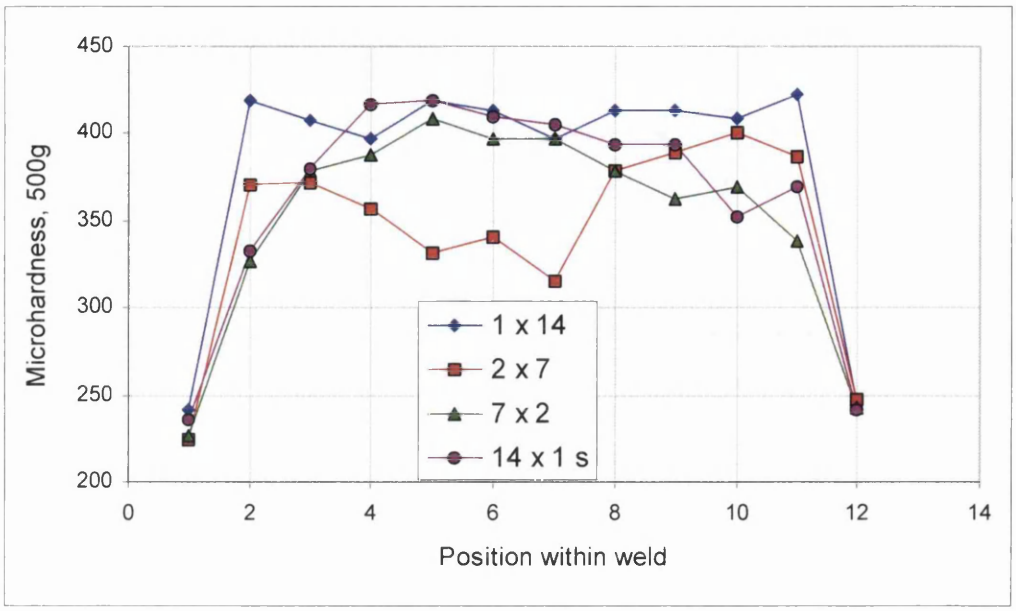

Figure 6.50. Microhardness profiles of welds produced using four different pulsed welding schedules: 1 x 14 cycles; 2 x 7 cycles; 7 x 2 cycles; and 14 x 1 cycles in DP800.

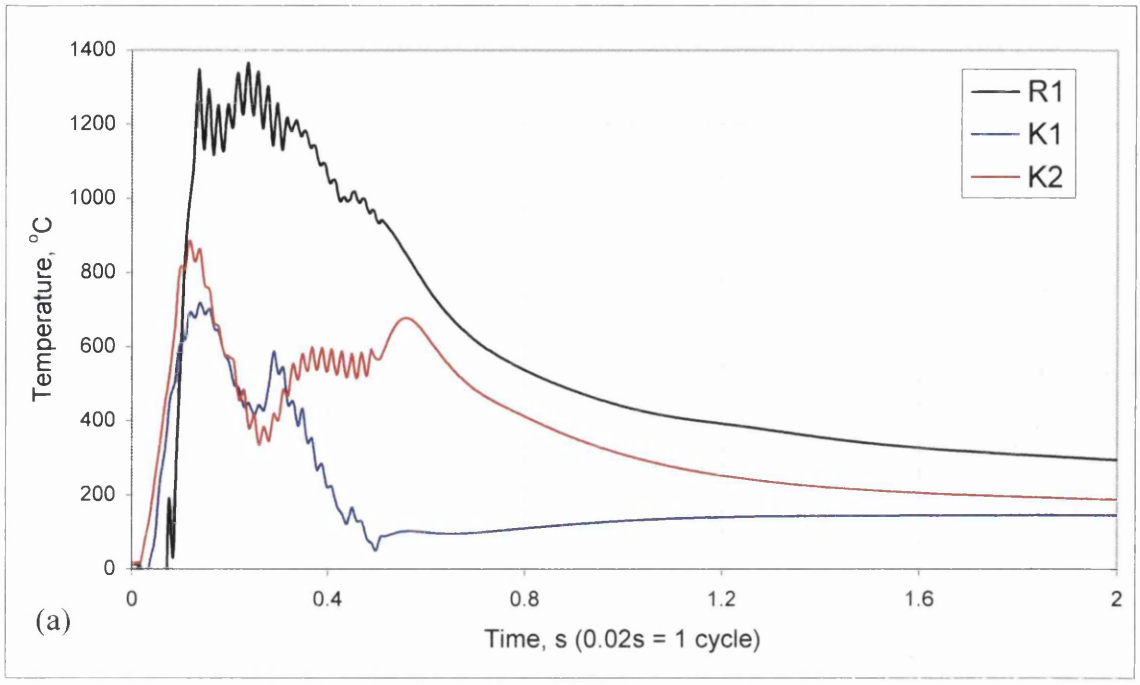

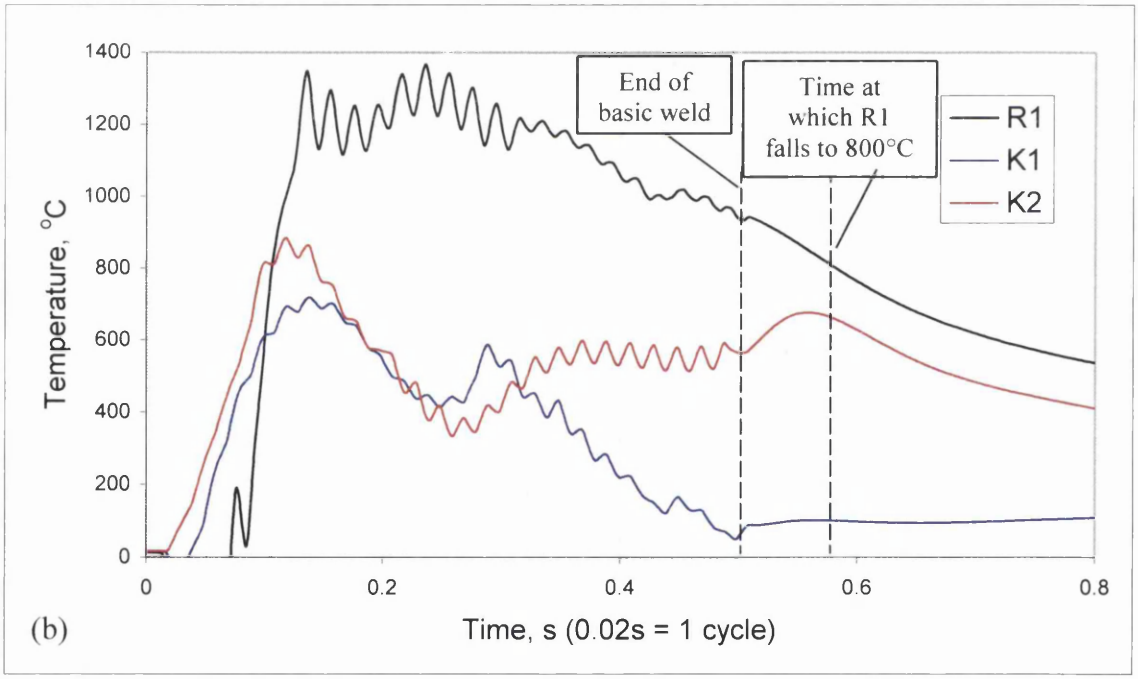

Figure 6.51 (a) The time - temperature profile for a single pulse weld - 25 cycles, measured using plain wire thermocouples.
(b) Selection of suitable time for application of second current pulse.

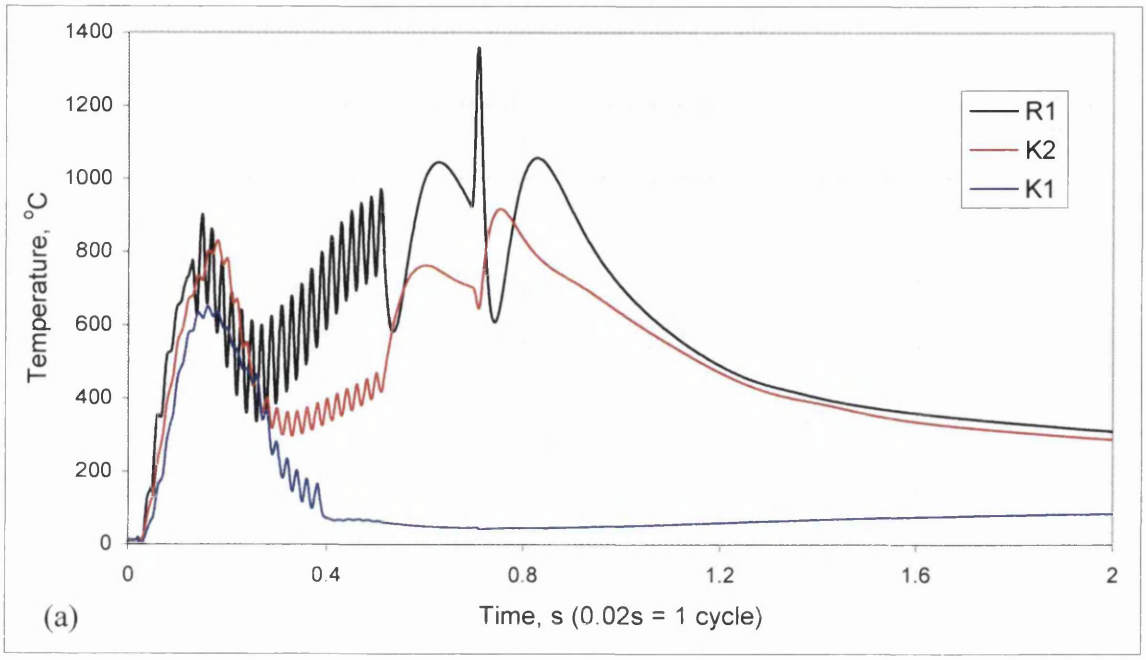

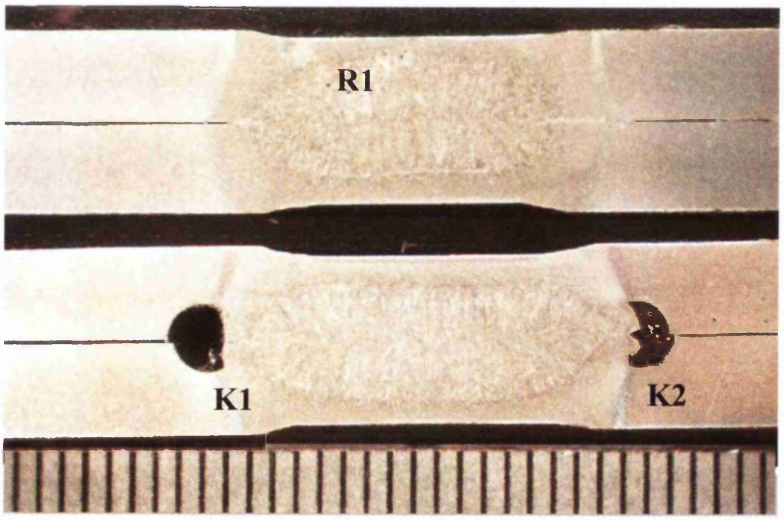

(b)

Figure 6.52 (a)The time - temperature profile for a single pulse weld - 25 cycles, with one post weld cooling pulse, measured using plain wire thermocouples.
(b) The relative location of the thermocouples in the controlled cooling weld. Scale is in mm.

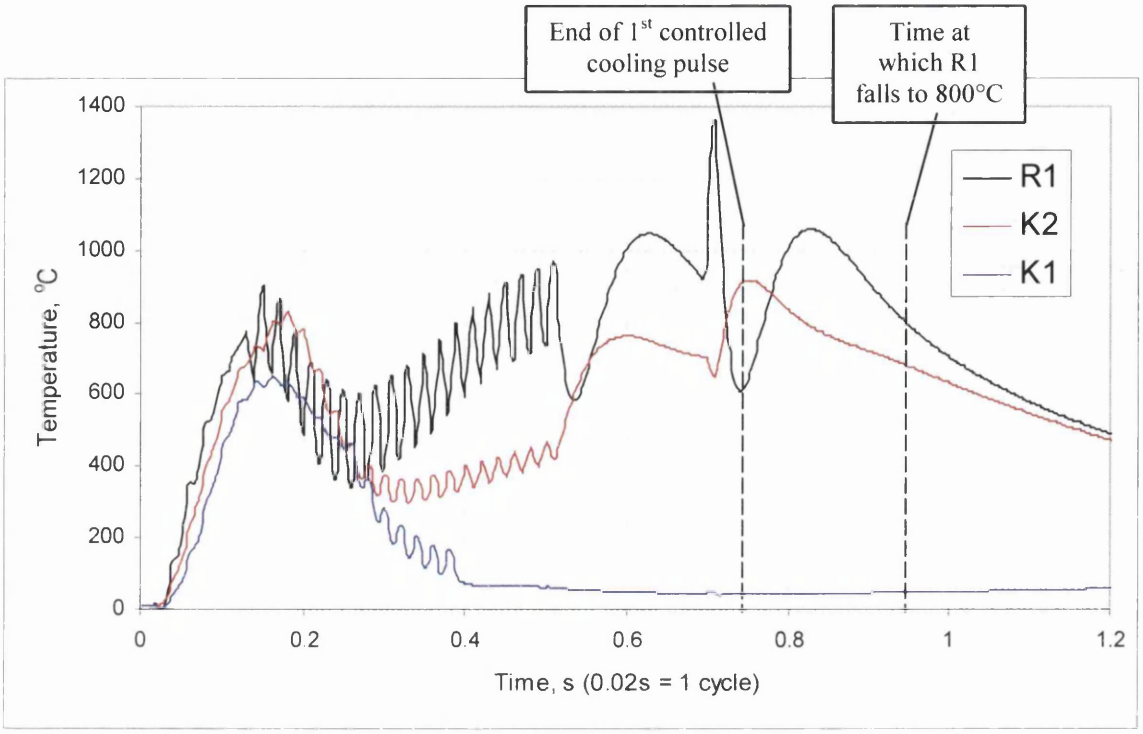

Figure 6.53 Selection of suitable time for application of third current pulse using the thermocouple output previously given in Figure 6.52(a).

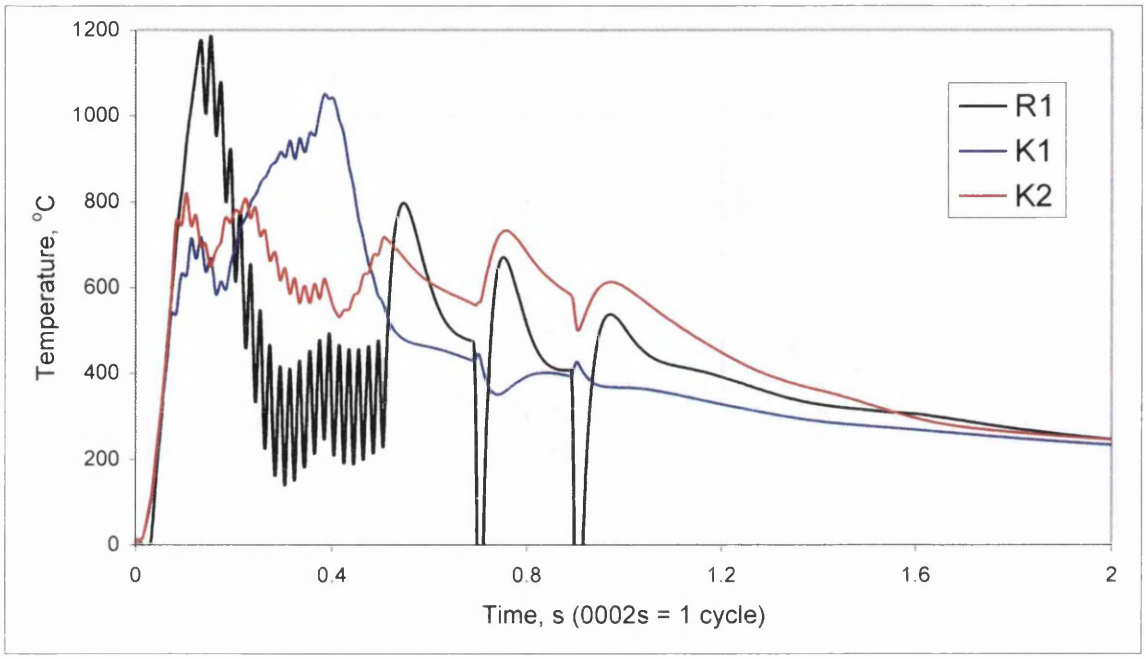

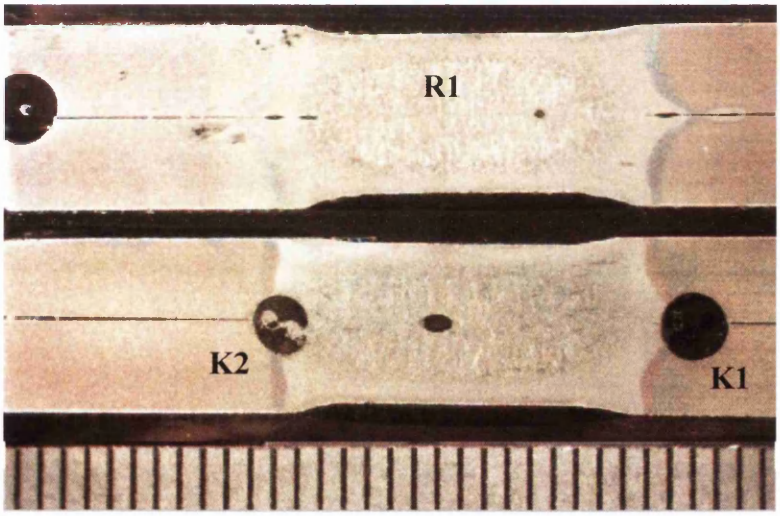

Figure 6.54 (a)The time - temperature profile for a single pulse weld - 25 cycles, with two post weld cooling pulses, measured using plain wire thermocouples.
(b) The relative location of the thermocouples in the controlled cooling weld. Scale is in mm.

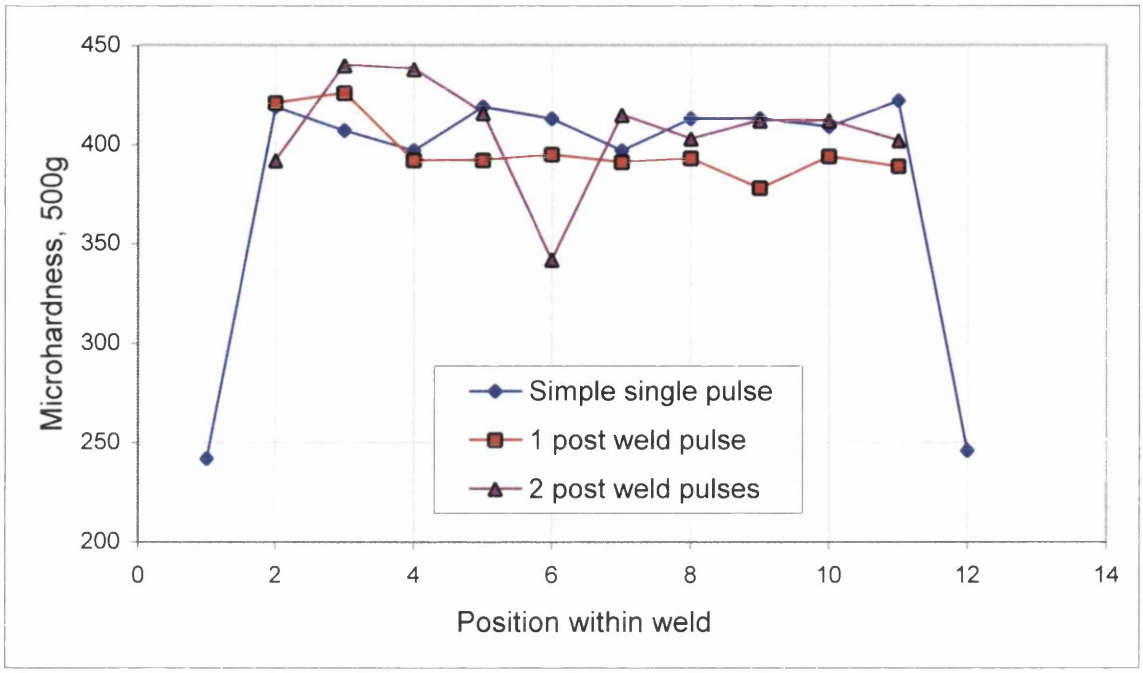

Figure 6.55. Microhardness profiles of welds subject to controlled cooling treatments produced in DP800. The legend refers to the treatments detailed in figures 6.52 and 6.54.

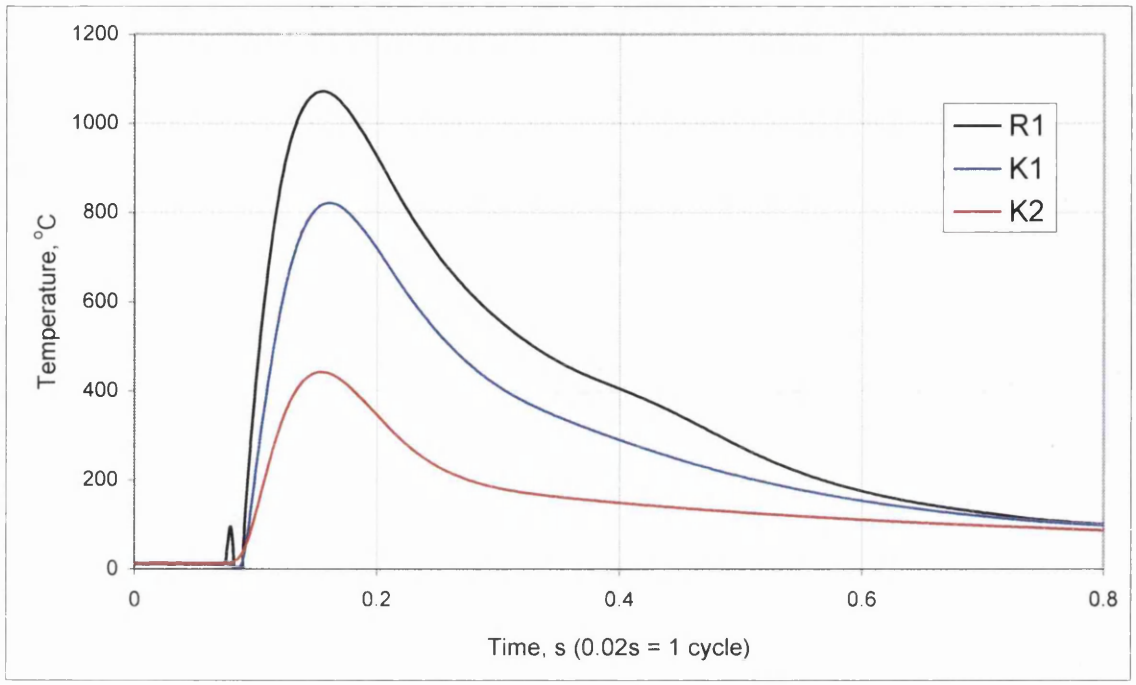

(a)

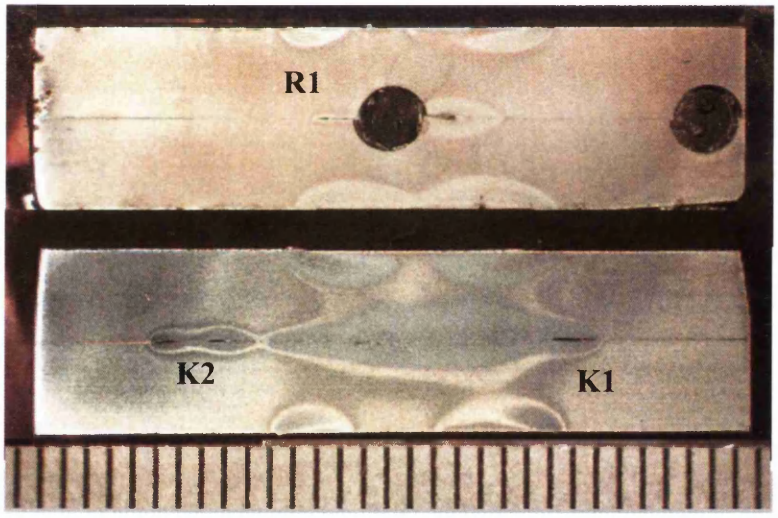

(b)

Figure 6.56 (a) The time – temperature profile for a single pulse of 1 cycle, measured using plain wire thermocouples.
(b) The relative location of the thermocouples in the single cycle pulse coupon. Scale is in mm.

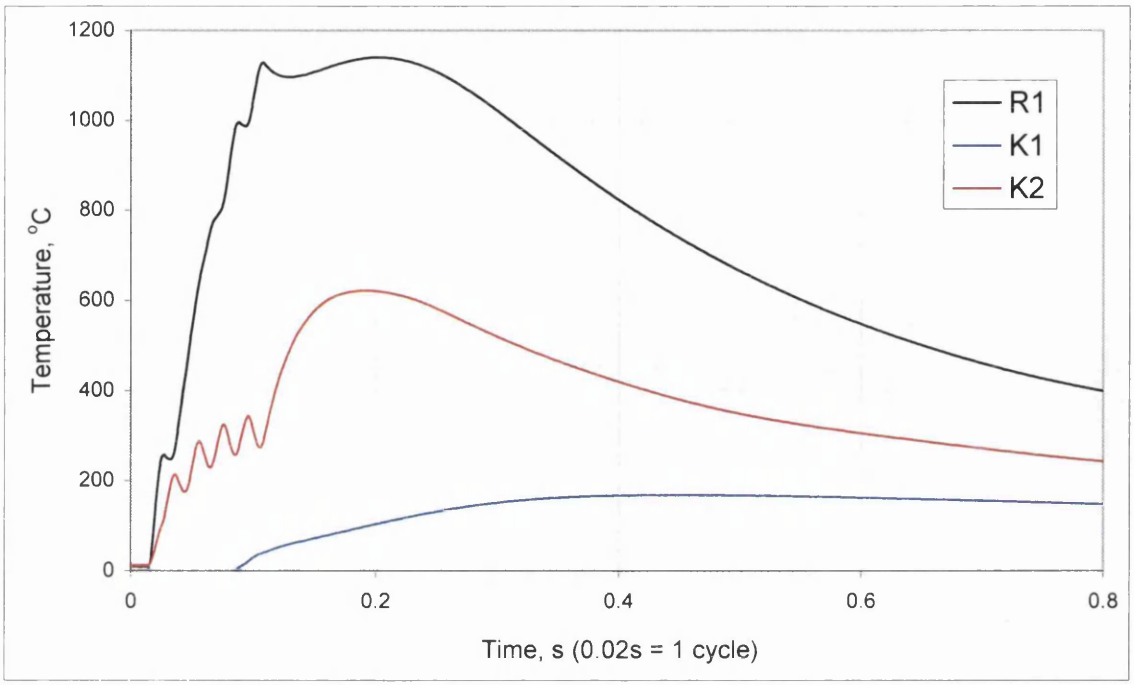

(a)

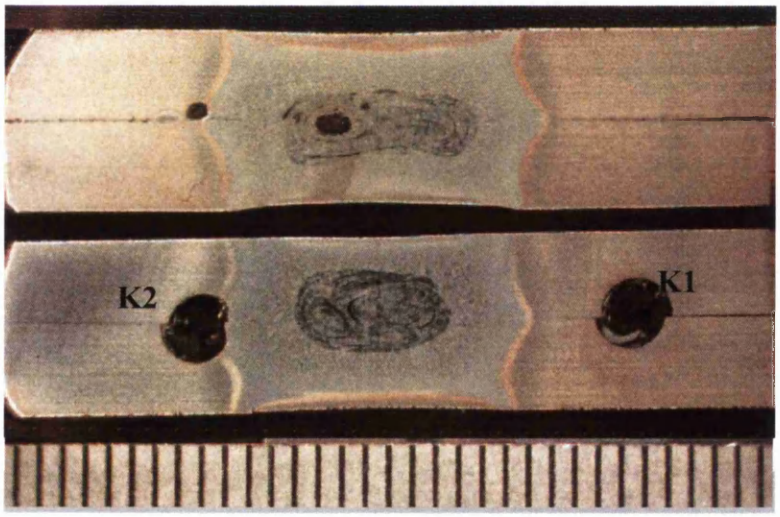

(b)

Figure 6.57 (a) The time – temperature profile for a single pulse of 5 cycles, measured using plain wire thermocouples.
(b) The relative location of the thermocouples in the single cycle pulse coupon. Scale is in mm.

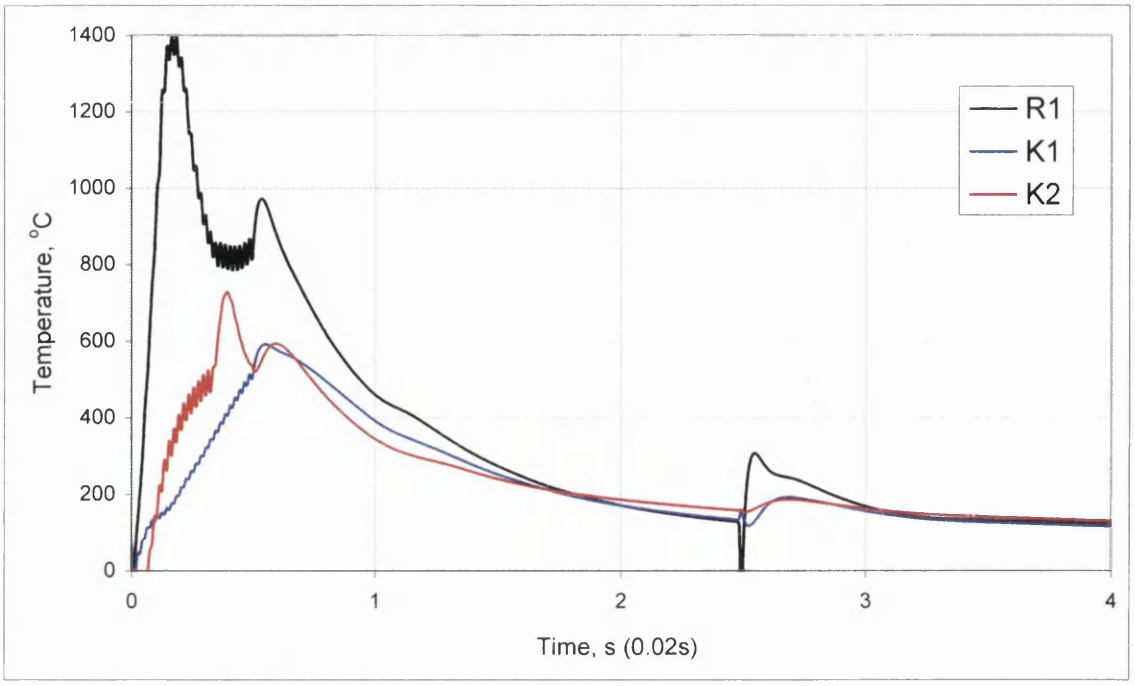

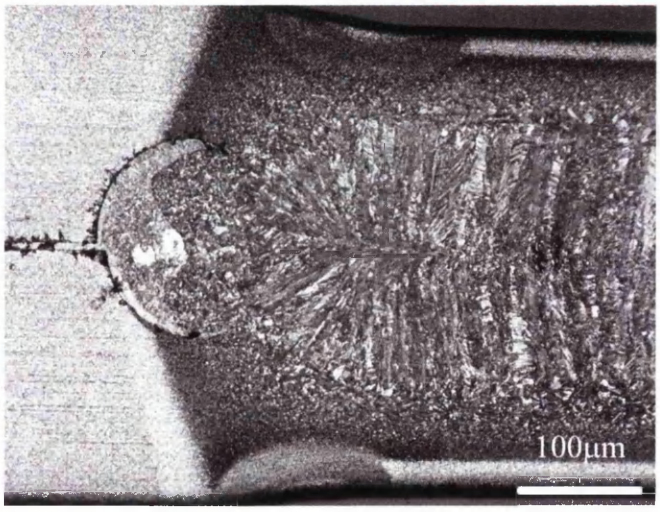

Figure 6.58 (a) The time – temperature profile for a single pulse weld – 25 cycles followed by one post weld tempering pulse, measured using plain wire thermocouples.

(b) An optical micrograph showing the thermal patterns visible after a post weld tempering pulse.

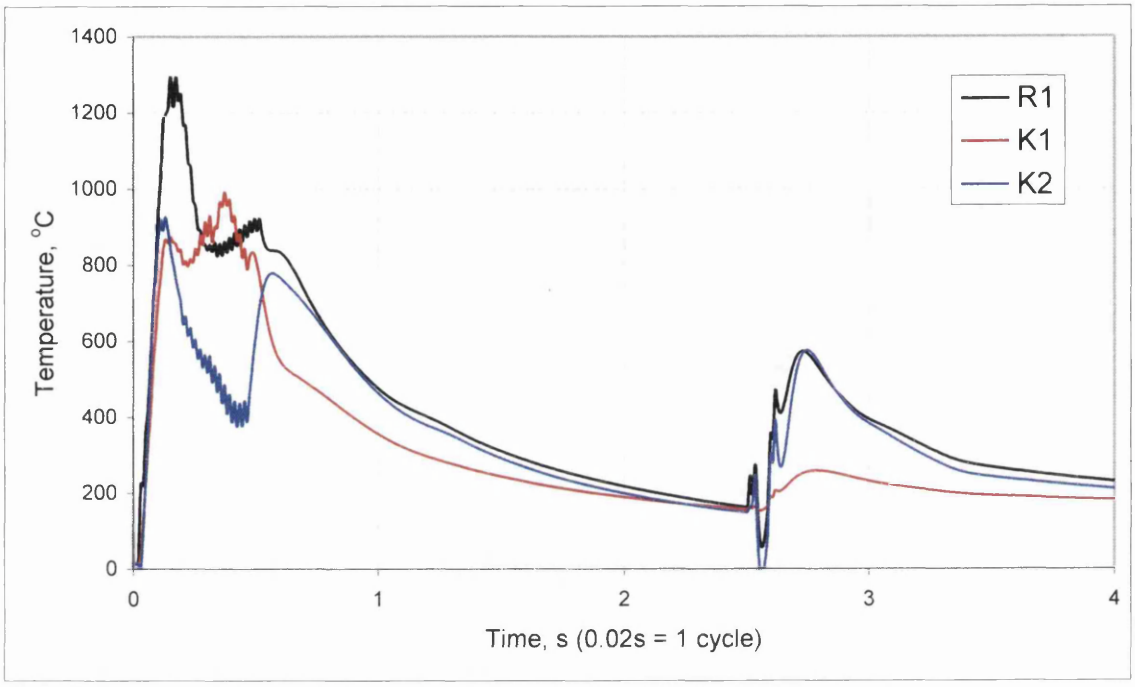

(a)

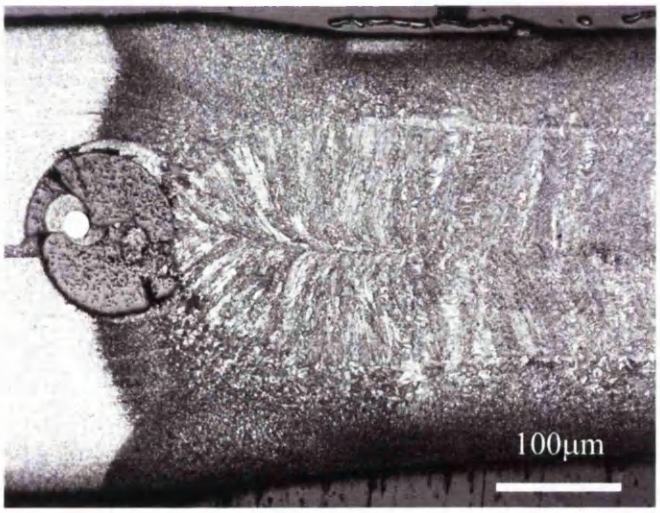

(b)

Figure 6.59 (a) The time – temperature profile for a single pulse weld – 25 cycles followed by two post weld tempering pulses (2 cycles each), measured using plain wire thermocouples.
(b) An optical micrograph showing the thermal patterns visible after post weld tempering.

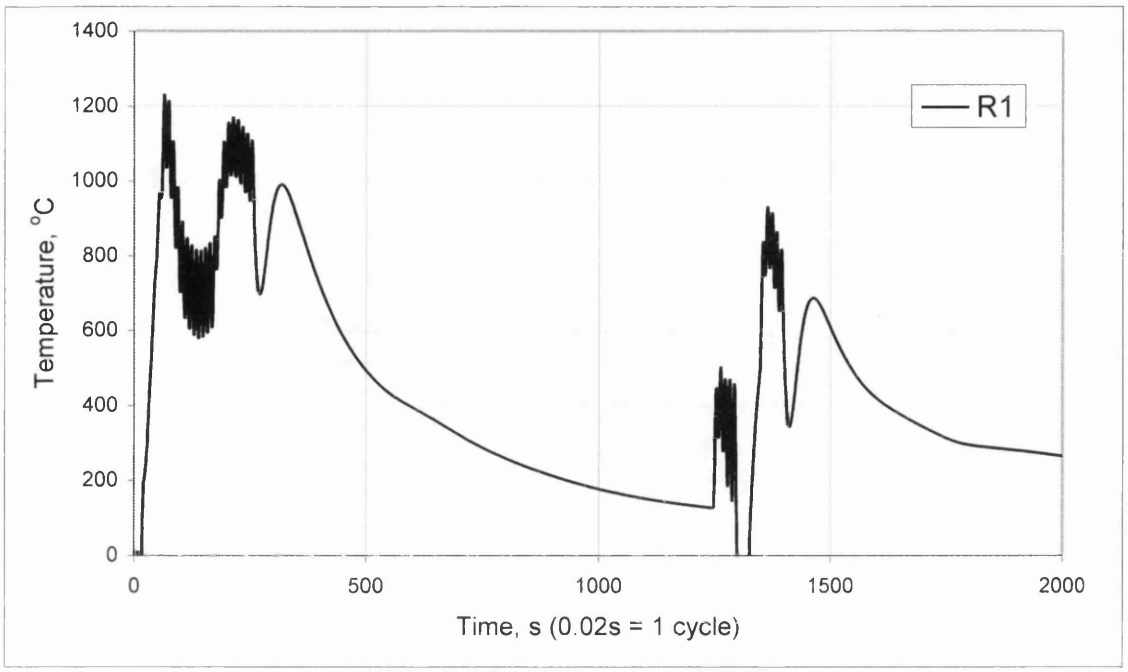

(a)

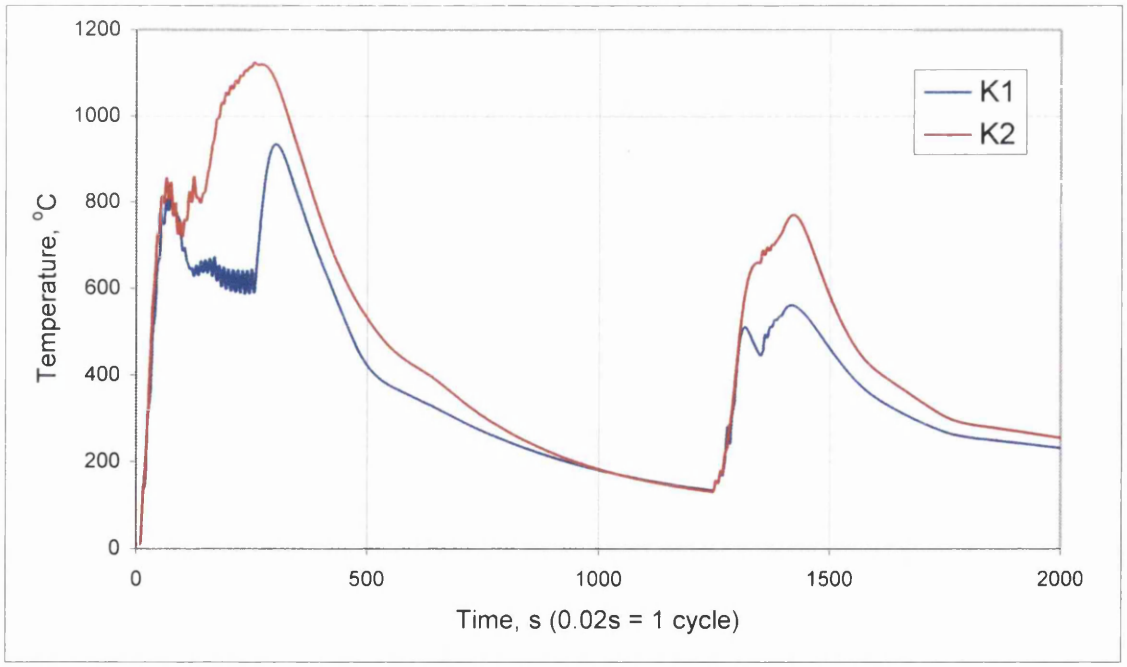

(b)

Figure 6.60 The time – temperature profile for a single pulse weld 25 cycles followed by two post weld tempering pulses (5 cycles each), measured using plain wire thermocouples: (a) R-type thermocouple results; (b) K-type thermocouple results

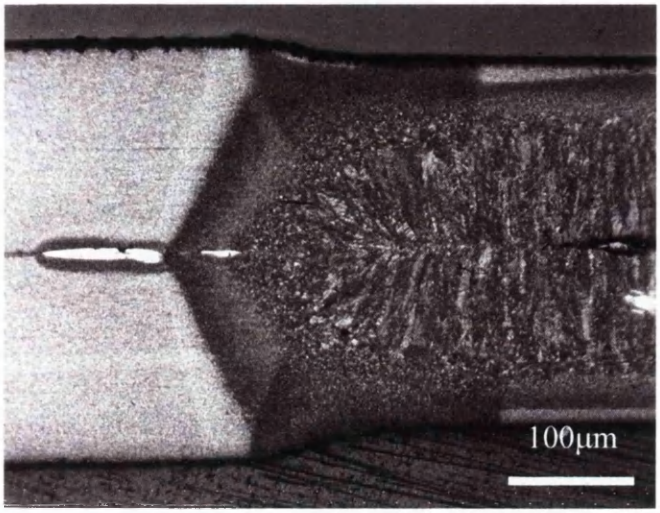

(c)

Figure 6.60 (c) An optical micrograph showing the thermal patterns visible after post weld tempering.

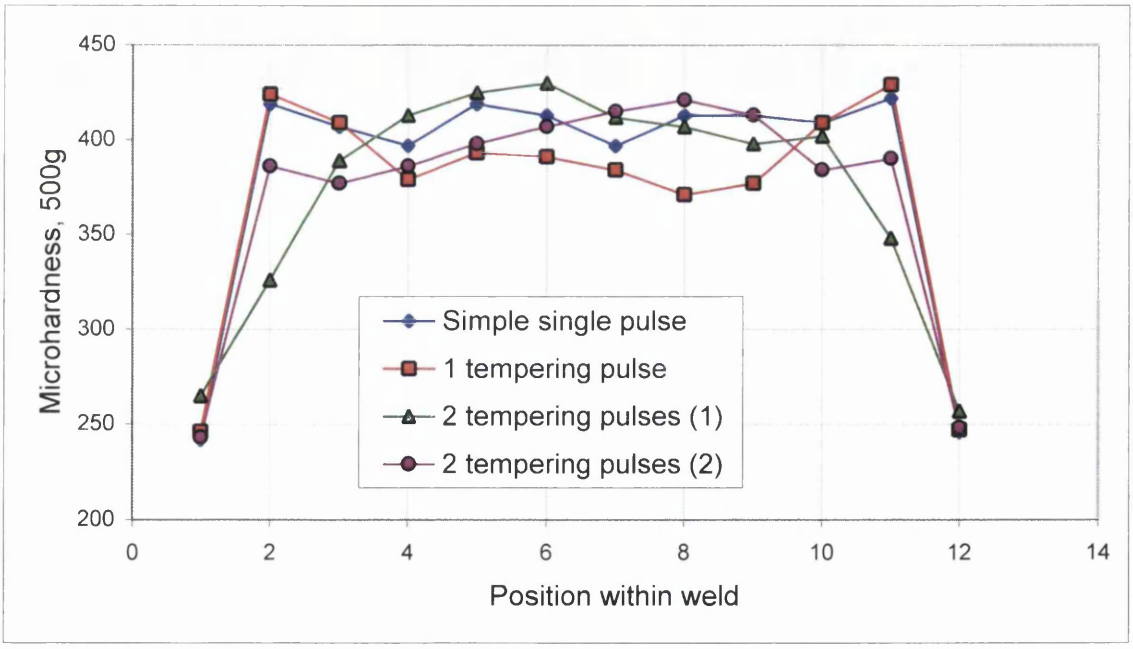

Figure 6.61. Microhardness profiles of three welds, made in DP800 and subject to tempering treatments. The legend refers to the treatments detailed in figures 6.58 to 6.60.

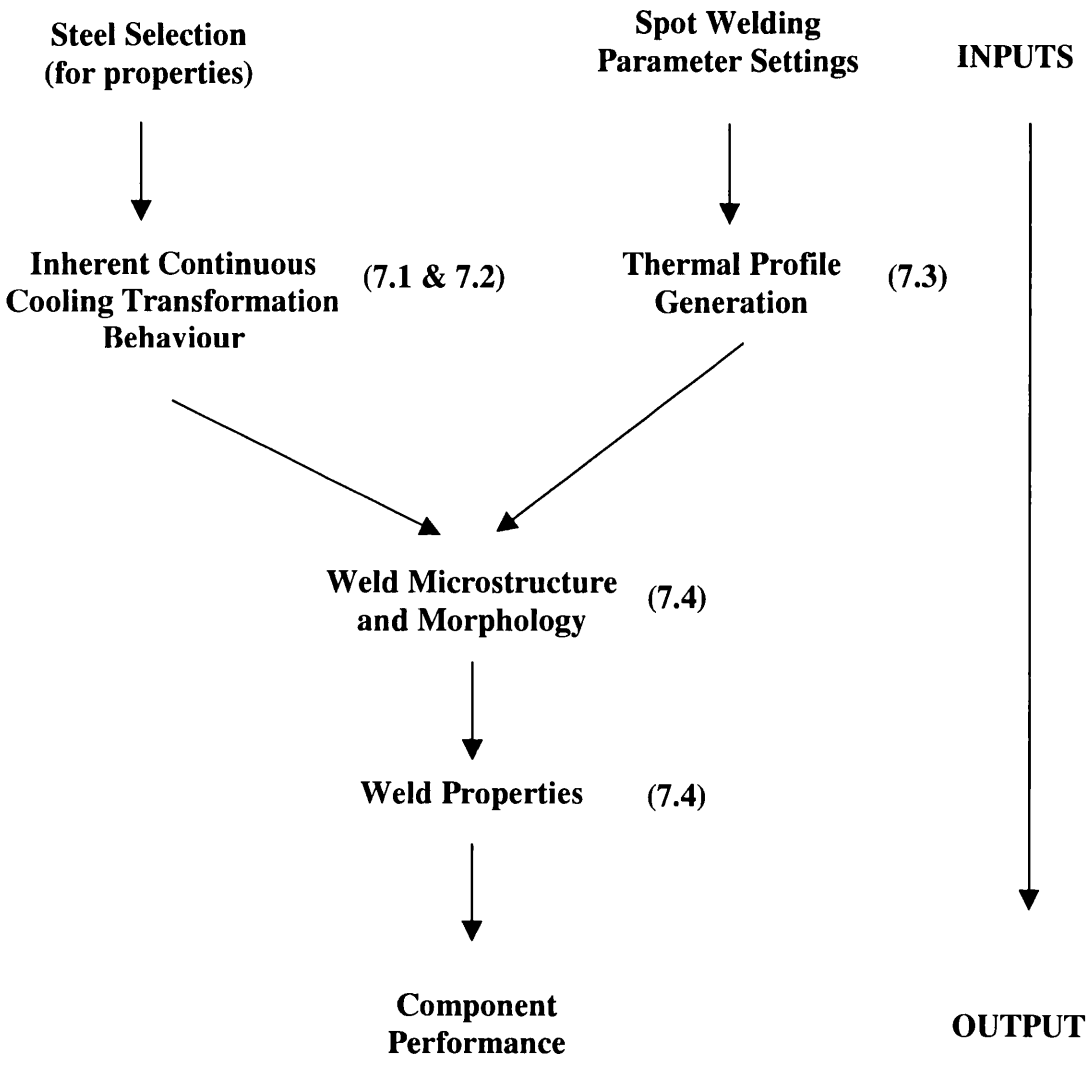

Figure 7.1. The welding process cycle. Numbers in brackets indicate the section concerned with the adjacent topic.